REPORT DOCUMENTATION PAGE

Form Approved
OMB No. 0704-0188

The public reporting burden for this collection of information is estimated to average 1 hour per response, including the time for reviewing instructions, searching existing data sources, gathering and maintaining the data needed, and completing and reviewing the collection of information. Send comments regarding this burden estimate or any other aspect of this collection of information, including suggestions for reducing the burden, to Department of Defense, Washington Headquarters Services, Directorate for Information Operations and Reports (0704-0188), 1215 Jefferson Davis Highway, Suite 1204, Arlington, VA 22202-4302. Respondents should be aware that notwithstanding any other provision of law, no person shall be subject to any penalty for failing to comply with a collection of information if it does not display a currently valid OMB control number.
PLEASE DO NOT RETURN YOUR FORM TO THE ABOVE ADDRESS.

1. REPORT DATE *(DD-MM-YYYY)*	2. REPORT TYPE	3. DATES COVERED *(From - To)*
15-01-2008	Final Technical Report	March 1, 2004-June 30 2007

4. TITLE AND SUBTITLE
Very High Performance Organic Photonic Devices

5a. CONTRACT NUMBER

5b. GRANT NUMBER
FA9550-04-1-0120

5c. PROGRAM ELEMENT NUMBER

6. AUTHOR(S)
Professor Stephen Forrest

5d. PROJECT NUMBER

5e. TASK NUMBER

5f. WORK UNIT NUMBER

7. PERFORMING ORGANIZATION NAME(S) AND ADDRESS(ES)
Princeton University, Princeton, NJ 08544

8. PERFORMING ORGANIZATION REPORT NUMBER

9. SPONSORING/MONITORING AGENCY NAME(S) AND ADDRESS(ES)
Air Force Office of Scientific Research
AFOSR/NA (Attn: Dr. Charles Lee)
875 North Randolph Street
Suite 325, Room 3112
Arlington, VA 22203

10. SPONSOR/MONITOR'S ACRONYM(S)

11. SPONSOR/MONITOR'S REPORT NUMBER(S)

12. DISTRIBUTION/AVAILABILITY STATEMENT
APPROVED FOR PUBLIC RELEASE

AFRL-SR-AR-TR-08-0044

13. SUPPLEMENTARY NOTES

14. ABSTRACT

The objective was to demonstrate very high efficiency, low cost organic solar cells on flexible substrates based on vapor-deposited thin film organic semiconductors. Our goal is to obtain solar power conversion efficiencies of >10% -- a value without precedent in over 30 years of science and engineering targeted at achieving practical organic solar energy conversion devices. A further objective is to demonstrate an electrically pumped organic thin film laser, again based on vapor-deposited molecular organic materials. The motivation for this investigation is the temperature independent wavelength and threshold characteristics of organic lasers. We will pursue two very promising and innovative approaches: employing high Q cavities where electrically pumped polaritons are generated, and the use of high intensity OLEDs to pump a low threshold light emitting film positioned in an integrated optical cavity.

15. SUBJECT TERMS

16. SECURITY CLASSIFICATION OF:			17. LIMITATION OF ABSTRACT	18. NUMBER OF PAGES	19a. NAME OF RESPONSIBLE PERSON
a. REPORT	b. ABSTRACT	c. THIS PAGE		81	Stephen R. Forrest
					19b. TELEPHONE NUMBER *(Include area code)* (734) 647-1147

Very High Performance Organic Photonic Devices

Final Report

Program Dates: March 1, 2004 to June 30, 2007

Grant No. FA9550-04-1-0120

P.I. Stephen Forrest
Department of Electrical Engineering
Princeton University
Princeton, NJ
forrest@princeton.edu

I. Objectives

The objective was to demonstrate very high efficiency, low cost organic solar cells on flexible substrates based on vapor-deposited thin film organic semiconductors. Our goal is to obtain solar power conversion efficiencies of >10% -- a value without precedent in over 30 years of science and engineering targeted at achieving practical organic solar energy conversion devices.

A further objective is to demonstrate an electrically pumped organic thin film laser, again based on vapor-deposited molecular organic materials. The motivation for this investigation is the temperature independent wavelength and threshold characteristics of organic lasers. We will pursue two very promising and innovative approaches: employing high Q cavities where electrically pumped *polaritons* are generated, and the use of high intensity OLEDs to pump a low threshold light emitting film positioned in an integrated optical cavity.

II. Significant Accomplishments

In the field of organic thin film solar cells, AFOSR funding has helped to propel our group into a *world leadership position.* This is apparent through the number of keynote, plenary and invited presentations that we have made on this subject at international meetings over the life span of this program. Also, all high efficiency organic cells currently being demonstrated in other laboratories, worldwide, employ either double heterjunctions or tandem cells, both of which were first demonstrated in our laboratories.

Our work has led to many breakthrough, foundation technologies in the area of organic photovoltaics (OPV), including in the generation of new and useful device architectures, understanding of the limiting factors to their performance, and in high volume film growth technologies based on organic vapor phase deposition. Among the highlights are the following:

1. We introduced, and demonstrated a novel, dual tandem cell configuration, and reported, record high solar power conversion efficiencies of 5.7% under 1 sun

20080131279

intensity, AM1.5G simulated solar radiation (no spectral correction). The cell fill factor exceeded 0.6, and Voc>1V was obtained, making this device competitive with inorganic, amorphous Si solar cells.

2. We introduced and demonstrated several new cell architectures, including the hybrid planar mixed cell employing the CuPc/C_{60} materials system, achieving 5% power conversion efficiency (no spectral correction).
3. We introduced the first bulk heterojunction structure in small molecular weight organic materials system. The so-called "controlled bulk HJ", grown by our proprietary technology of organic vapor phase deposition, increased the efficiency of the "traditional" CuPc/PTCBI system from 1% power conversion efficiency (PCE), to 2.7%.
4. We introduced the first all-organic nanocrystalline bulk HJ, again grown by OVPD, achieving 4.7% PCE (with solar correction). in demonstrating a bulk heterojunction cell based on small molecular weight materials using controlled growth of the heterojunction by organic vapor phase deposition.
5. We introduced new materials and structures leading to the highest reported efficiencies in the near infrared spectral regions based on CuPc and SnPc combinations. After the close of this program, this work led to the first demonstration of the multiple donor, "simultaneous HJ" organic solar cell structure.
6. Demonstration of high open circuit voltage organic PV cells based on a new class of acceptor molecules: the sub phthalocyanines.
7. We determined the fundamental origins of the low open circuit voltage typically observed in OPV cells, which is the largest source of loss of efficiency in these cells.

In the area of lasers, we have focused on the use of polariton emission as the route to coherent emission with the largest potential for success. In particular, our work has resulted in the following demonstrations and findings:

1. The first successful demonstration of strong coupling for a small molecular weight material in an optical microcavity. This was accomplished with a neat film of NTCDA inserted into a microcavity. The very large Rabi splittings suggest that this approach may be fruitful for eventually reaching lasing in such a cavity.
2. We demonstrated the strong coupling in organic phosphors could be used to measure the rate of critical transitions. In our case, we used it to measure the intersystem crossing rate in PtOEP.
3. We demonstrated the first strong coupling between a Frenkel exciton (in tetraphenyl porphorin) and a Wannier Mott exciton (in InGaP). This hybrid quasi-particle opens the door to obtaining coherent emission through the electrical pumping of the inorganic material, and then transferring energy between the inorganic and organic sections of the microcavity. This demonstration may eventually lead to *single photon lasing.*
4. We introduced a potential new means to induce coherent emission in electrically pumped organic thin films through the production of field-stabilized optically

generated geminate polaron pairs. This is analgous to Q-switching in conventional laser technologies, in that an inverted population is built up and then is allowed to recombine to result in a high density of photons exceeding threshold.

Accomplishments/New Findings

Highlights of the research accomplishments listed above in OPV and organic lasing are provided in the ATTACHMENT. These details are presented in select, publish papers fully detailing our results. A full listing of published results is provided in Sec. IV.

III. Personnel supported and/or associated with the research project

Graduate students: Jiangeng Xue (solar cells)
Barry Rand (solar cells)
Fan Yang (solar cells)
Rhonda Salzman (solar cells)
Richard Lunt (solar cells)
Russell Holmes (lasers)
Noel Geibink (lasers)
Stephane Kena-Cohen (lasers)

Post-docs: Yohai Roichman (solar cells)
Vinod Menon (lasers)

IV. Publications under AFOSR funding

1. "4.2% efficient organic photovoltaic cells with low series resistances", J. Xue, S. Uchida, B. P. Rand and S. R. Forrest, *Appl. Phys. Lett*, **84**, 3015 (2004).

2. "The Path to Ubiquitous and Low Cost Organic Electronic Appliances on Plastic", S. R. Forrest, *Nature* (London), invited, **428**, 911 (2004).

3. "Organic small molecule solar cells with a homogeneously mixed copper phthalocyanine: C_{60} active layer", S. Uchida, J. Xue, B. P. Rand and S. R. Forrest, *Appl. Phys. Lett*, **84**, 4218 (2004).

4. "Bipolar doping between a molecular organic donor-acceptor couple", J. Xue and S. R. Forrest, *Phys. Rev. B*, **69**, 245322 (2004).

5. "Exciton Formation Statistics Under Electrical Injection in Organic Semiconductor Thin Films", S. R. Forrest, *J. Luminescence*, invited, **110**, 378 (2004).

6. "Separation of geminate charge-pairs at donor-acceptor interfaces in disordered solids", P. Peumans and S. R. Forrest, *Chem. Phys. Lett.*, **398**, 27 (2004).

7. "Long-range absorption enhancement in organic tandem thin film solar cells containing silver nanoclusters," B. P. Rand, P. Peumans, and S. R. Forrest, *J. Appl. Phys.*, **96**, 7519 (2004).

8. "Strong exciton-photon coupling and exciton hybridization in a thermally evaporated polycrystalline film of an organic small molecule", R.J. Holmes and S.R. Forrest, *Phys. Rev. Lett.*, **93**, 186404 (2004).

9. "Asymmetric tandem organic photovoltaic cells with hybrid planar-mixed molecular heterojunctions", J. Xue, B. P. Rand, S. Uchida and S. R. Forrest, *Appl. Phys. Lett.*, **85**, 5757 (2004).

10. "Controlled growth of a molecular bulk heterojunction photovoltaic cell", F. Yang, M. Shtein, and S. R. Forrest, *Nat. Mater.*, **4**, 39 (2005).

11. "The limits to organic photovoltaic cell efficiency", S. R. Forrest, invited, *MRS Bulletin*, **30**, 28 (2005).

12. "A hybrid planar-mixed molecular heterojunction photovoltaic cell", J. Xue, B. P. Rand, S. Uchida and S. R. Forrest, *Adv. Mater.*, **17**, 66 (2005).

13. "Relationship between the ionization and oxidation potentials of molecular organic semiconductors", B. W. D'Andrade, S. Datta and S. R. Forrest, *Org. Electron.*, **6**, 11 (2005).

14. "Exciton-photon coupling in organic materials with large intersystem crossing rates and strong excited state molecular relaxation, R.J. Holmes and S.R. Forrest, *Phys. Rev. B*, **71**, 235203 (2005).

15. "Morphology control and material mixing by high-temperature organic vapor phase deposition and its application to thin-film solar cells", F. Yang, M. Shtein and S. R. Forrest, *J. Appl. Phys.*, **98,** 014906 (2005).

16. "Organic double-heterostructure photovoltaic cells employing thick tris(acetylacetonato) ruthenium(III) exciton blocking layers", B. P. Rand, J. Li, J. Xue, R. J. Holmes, M. E. Thompson, and S. R. Forrest, *Adv. Mat.*, **17**, 2714 (2005).

17. "Blue and Near-UV Phosphorescence from Iridium Complexes with Cyclometalated Pyrazolyl or N-Heterocyclic Carbene Ligands", T. Sajoto, P. I. Djurovich, A. Tamayo, M. Yousufuddin, R. Bau, M. E. Thompson, R. J. Holmes and S. R. Forrest, *Inorg. Chem.*, **44**, 7992 (2005).

18. "The effects of copper phthalocyanine purity on organic solar cell performance", R. F. Salzman, J. Xue, B. P. Rand, A. Alexander, M. E. Thompson, and S. R. Forrest, *Org. Electron. Lett.*, **6**, 242 (2005).

19. "Organic solar cells with sensitivity extending into the near-infrared", B. P. Rand, J. Xue, F. Yang and S. R. Forrest, *Appl. Phys. Lett.*, **87**, 233508 (2005).

20. "Mixed Donor-Acceptor Heterojunctions for Photovoltaic Applications. I. Materials Properties", B. P. Rand, J. Xue, S. Uchida and S. R. Forrest, *J. Appl. Phys.*, **98**, 124902, (2005).

21. "Mixed Donor-Acceptor Heterojunctions for Photovoltaic Applications. II. Device Applications", B. P. Rand, J. Xue, S. Uchida and S. R. Forrest, *J. Appl. Phys.*, **98**, 124903 (2005).

22. "Semitransparent Organic Photovoltaic Cells", R. Bailey-Salzman, B. P. Rand and S. R. Forrest, *Appl. Phys. Lett.*, **88**, 233502 (2006).

23. "Organic solar cells using transparent SnO_2:F anodes", F. Yang and S. R. Forrest, *Adv. Mater.*, **18**, 2018 (2006).

24. "Enhanced Open Circuit Voltage in Subphthalocyanine/C_{60} Organic Photovoltaic Cells", K.L. Mutolo, E. I. Mayo, B. P. Rand, S. R. Forrest and M. E. Thompson, *J. Am. Chem. Soc.*, **128**, 8108 (2006).

25. "Accumulation of electric-field-stabilized geminate polaron pairs in an organic semiconductor to attain high excitation density under low intensity pumping", N. C. Giebink and S. R. Forrest, *Appl. Phys. Lett.* **89**, 193502 (2006).

26. "Strong coupling and hybridization of Frenkel and Wannier-Mott excitons in an organic-inorganic optical microcavity", R. J. Holmes, S. Kéna-Cohen, V.M. Menon and S.R. Forrest, *Phys. Rev. B*, **74**, 235211 (2006).

27. "Strong exciton-photon coupling in organic materials" R. J. Holmes and S. R. Forrest, invited, *Organic Electron.*, **8**, 77 (2007).

28. "Offset energies at organic semiconductor heterojunctions and their influence on the open-circuit voltage of thin-film solar cells", B. P. Rand, D. P. Burk and S. R. Forrest, *Phys. Rev. B*, **75**, 115327 (2007).

29. "Real-time Monitoring of Organic Vapor-Phase Deposition of Molecular Thin Films Using High-Pressure Reflection High-Energy Electron Diffraction ", R. Lunt, J. B. Benziger and S. R. Forrest, *Appl. Phys. Lett.*, **90**, 181932 (2007).

30. "Near-infrared sensitive small molecule organic photovoltaic cells based on chloroaluminum phthalocyanine", R. F. Bailey-Salzman, B. P. Rand, and S. R. Forrest, *Appl. Phys. Lett.*, **91**, 013508 (2007).

31. "Gallium doped zinc oxide films as transparent electrodes for organic solar cell applications", V. Bhosle, J. T. Prater, D. Pendergrast, S.R. Forrest, J. Narayan, *J. Appl. Phys.*, **102**, 023501 (2007).

32. "Green polariton photoluminescence using the red-emitting phosphor PtOEP", S. Kéna-Cohen and S.R. Forrest, *Phys. Rev. B*, **76**, 075202 (2007).

33. "The limits to accumulation of electric field-stabilized geminate polaron-pairs in an organic semiconductor thin film", N.C. Giebink, S.R. Forrest, *Phys. Rev. B*, **76**, 075318 (2007).

34. "Growth of an ordered crystalline organic heterojunction", R. R. Lunt, J. B. Benziger and S. R. Forrest, *Adv. Mater.*, **19**, 4229 (2007).

35. "Efficient solar cells using all-organic nanocrystalline networks", F. Yang, K. Sun, and S. R. Forrest, *Adv. Mater.*, **19**, 4166 (2007).

Presentations at meetings

1. "Organic small molecule solar cells with a homogeneously mixed copper phthalocyanine:C_{60} active layer", S. Uchida, J. Xue, B. P. Rand and S. R. Forrest, MRS Spring Mtg., Paper S3.11, San Francisco (April, 2004).

2. "How High Can We Get? The Limits to Solar Energy Conversion Efficiency in Organic Photovoltaic Cells", S. R. Forrest, 6th Int. Symp. On Functional Pi-Electron Systems, plenary lecture, Paper E0.7, Cornell U. (June, 2004).

3. "The role of triplet excitons in organic electronic devices", S. R. Forrest, invited, W. E. Haerus Symposium on Condensed Matter Physics, Bad Honnef (May, 2004).

4. "The role of triplet excitons in organic electronic devices", S. R. Forrest, invited, 20th Annual Conference of the European Phys. Soc., Condensed Matter Div., Prague (July, 2004).

5. "How High Can We Get? The Limits to Solar Energy Conversion Efficiency in Organic Photovoltaic Cells", S. R. Forrest, plenary lecture, SPIE 49th Ann. Mtg., Conf. 5520, Organic Photovoltaics V, Denver (Aug., 2004).

6. "Organic double-heterostructure photovoltaic cells employing thick tris(acetylacetonato) ruthenium (III) exciton blocking layers", B. P. Rand, J. Li, J. Xue, R. J. Holmes, M. E. Thompson and S. R. Forrest, Paper D5.7, *MRS Fall Mtg.*, Boston (Nov., 2005).

7. "Effects of copper phthalocyanine purity on organic solar cell performance", R. F. Salzman, J. Xue, B. P. Rand, A. Alexander, M. E. Thompson and S. R. Forrest, Paper D5.8, *MRS Fall Mtg.*, Boston (Nov., 2005).

8. "Efficient infrared-absorbing organic solar cells employing a tin phthalocyanine donor layer", B. P. Rand, J. Xue and S. R. Forrest, Paper D6.3, *MRS Fall Mtg.*, Boston (Nov., 2005).

9. "Hybridization of Frenkel and Wannier-Mott excitons in an optical microcavity", S. Kéna-Cohen, R. J. Holmes, V. Menon. and S. R. Forrest, Conf. on Lasers and Electrooptics, 2006, Baltimore (May, 2006).

10. "Energy level matching in organic photovoltaics", E. I. Mayo, B. P. Rand, C. Schlenker, S. R. Forrest and M. E. Thompson, *16th Int. Conf. on Photochemical Conversion and Storage of Solar Energy*, Paper W4-P-38, Uppsala, (July 2-7, 2006).

11. "Strategies for Achieving High Efficiency Organic Solar Cells", S. R. Forrest, *16th Int. Conf. on Photochemical Conversion and Storage of Solar Energy*, plenary, Uppsala, (July 2-7, 2006).

12. "Organic photovoltaic cells: Strategies for increasing solar energy conversion efficiencies", B. P. Rand and S. R. Forrest, invited, *Am. Chem. Soc. Mtg.*, Denver, (Sept., 2006).

13. "Accumulation of Electric-field stabilized geminate polar pair states to attain high excitation density with a low pump intensity,", N. C. Giebink and S. R. Forrest, *Mater. Res. Ann. Mtg.*, Paper S1.10, Boston (Nov., 2006).

14. "The source of the maximum open circuit voltage in molecular photovoltaic devices and implications for efficiency improvements", B. P. Rand, D. Pendergrast and S. R. Forrest, *Mater. Res. Ann. Mtg.*, Paper CC2.8, Boston (Nov., 2006).

15. "Progress in vapor deposited photovoltaic cells", S. R. Forrest, invited, *Mater. Res. Ann. Mtg.*, Paper CC3.3, Boston (Nov., 2006).

16. "Organic photovoltaic cells exhibiting increased V_{oc} with subphthalocyanine donor-like materials", K. L. Mutolo, E. L. Morrison, E. I. Mayo, B. P. Rand, S. R. Forrest, and M. E. Thompson, *Mater. Res. Ann. Mtg.*, Paper CC4.11, Boston (Nov., 2006).

17. "Organic solar cells using transparent SnO_2:F anodes", F. Yang and S. R. Forrest, *Mater. Res. Ann. Mtg.*, Paper CC4.12, Boston (Nov., 2006).

18. "Very low dark current double heterojunction solar cells employing chloraluminum phthalocyanine as a donor", R. F. Bailey-Salzman, B. P. Rand and S. R. Forrest, *Mater. Res. Ann. Mtg.*, Paper 6.37, Boston (Nov., 2006).

19. "Gallium doped zinc oxide films as transparent electrodes for organic solar cell applications", V. Bhosle, J. Prater, D. Pendergrast, S. R. Forrest and J. Narayan, *Mater. Res. Ann. Mtg.*, Paper CC10.21, Boston (Nov., 2006).

20. "Thin Film Organic Solar Cells: Control of Morphology and Device Architecture to Achieve High Energy", S. R. Forrest, invited, *Gordon Research Conf.*, Renewable Energy: Solar Fuels, Ventura, CA (Jan., 2007).

21. "Controlling nanostructure in organic films to achieve high photovoltaic efficiency", S. R. Forrest, 2007 *Am. Phys. Soc. March Mtg.*, invited, Paper L2.04, Denver (March, 2007).

22. "Nanocrystalline organic solar cells", F. Yang, K. Sun and S. R. Forrest, 2007 *Am. Phys. Soc. March Mtg.*, Paper P24.07, Denver (March, 2007).

23. "Real-time monitoring of organic thin film morphology by organic vapor phase deposition", R. Lunt, J. B. Benziger and S. R. Forrest, 2007 *Am. Phys. Soc. March Mtg.*, Paper P42.09, Denver (March, 2007).

24. "Green polariton photoluminescence in organic microcavities containing the red-emitting phosphor PtOEP", S. Kena-Cohen and S. R. Forrest, *Am. Phys. Soc. March Mtg.*, Paper N24.01, Denver (March, 2007).

25. "Organic Thin Film Photovoltaics: A Low Cost Solution to Solar Energy Conversion?" S. R. Forrest, Keynote, 2007 NREL Solar Program, Denver (April, 2007).

IV. Consulting with AF Labs

Several discussions were held with Mike Gerhold and Paul Haugssen at AFRL to determine the type of solar cell samples that aree needed for their testing applications.

V. Transitions

Throughout this program we have had close interactions with two companies who are attempting to bring to commercialization the results of our research. These are Universal Display Corporation (lasers), with the POC Dr. Julie Brown, CTO of the corporation; and Global Photonic Energy Corporation (solar cells), with the POC Mr. Aaron Waddell, President of the corporation. Both entities are direct spin offs from the laboratory of the PI. and have therefore had a long standing and productive relationship that makes technology transition particularly simple. All IP generated in this program is exclusively licensed to these two companies through prior agreements with Princeton University. In addition, we have worked closely with Aixtron AG who is manufacturing OVPD tools for use by the organic electronics (in particular for display production) industry. We have acted as advisors to help design both manufacturing and laboratory scale OVPD tools.

VI. New Discoveries

Several patent disclosures and filings have been made in the course of this program. These are provided separately due to their confidential nature. Patents issued in the areas investigated during the course of the program are listed below. We note that all patents listed are only those granted from the USPTO. However, all are filed internationally, and at this time many of those international filings have also resulted in granted patents. All patents have been licensed to either UDC and/or GPEC. All contained technologies have been successfully transitioned.

1. 7,314,773 Low resistance thin film organic solar cell electrodes

2. 7,242,703 Organic injection laser
3. 7,230,269 Organic photosensitive cells having a reciprocal-carrier exciton blocking layer
4. 7,205,585 Organic photosensitive optoelectronic device with an exciton blocking layer
5. 7,196,835 Aperiodic dielectric multilayer stack
6. 7,196,366 Stacked organic photosensitive devices
7. 7,194,173 Organic devices having a fiber structure
8. 7,179,543 Doping of organic opto-electronic devices to extend reliability
9. 7,173,369 Transparent contacts for organic devices
10. 7,151,217 Organic photosensitive optoelectronic devices with transparent electrodes
11. 7,061,011 Bipolar organic devices
12. 7,026,187 Method of manufacturing high-mobility organic thin films using organic vapor phase deposition
13. 7,026,041 Organic photosensitive optoelectronic device with an exciton blocking layer

VII. Honors/Awards

- IEEE and OSA: Fellow
- National Academy of Engineering: Member
- 2006: Jan Rajchman Prize, Soc. Information Display, for "insights into exciton generation and diffusion that led to the discovery of phosphorescent OLEDs, quadrupling efficiency".
- 2007: IEEE Daniel E. Noble Prize for "innovations in organic light emitting devices"

ATTACHMENT

Detailed Result Highlights of work sponsored by AFOSR.

The selected publications are listed below:

Organic Photovoltaic Cells

1. "The Path to Ubiquitous and Low Cost Organic Electronic Appliances on Plastic", S. R. Forrest, *Nature* (London), invited, **428**, 911 (2004).

2. "Asymmetric tandem organic photovoltaic cells with hybrid planar-mixed molecular heterojunctions", J. Xue, B. P. Rand, S. Uchida and S. R. Forrest, *Appl. Phys. Lett.*, **85**, 5757 (2004).

3. "Controlled growth of a molecular bulk heterojunction photovoltaic cell", F. Yang, M. Shtein, and S. R. Forrest, *Nat. Mater.*, **4**, 39 (2005).

4. "A hybrid planar-mixed molecular heterojunction photovoltaic cell", J. Xue, B. P. Rand, S. Uchida and S. R. Forrest, *Adv. Mater.*, **17**, 66 (2005).

5. "Organic solar cells with sensitivity extending into the near-infrared", B. P. Rand, J. Xue, F. Yang and S. R. Forrest, *Appl. Phys. Lett.*, **87**, 233508 (2005).

6. "Mixed Donor-Acceptor Heterojunctions for Photovoltaic Applications. I. Materials Properties", B. P. Rand, J. Xue, S. Uchida and S. R. Forrest, *J. Appl. Phys.*, **98**, 124902, (2005).

7. "Semitransparent Organic Photovoltaic Cells", R. Bailey-Salzman, B. P. Rand and S. R. Forrest, *Appl. Phys. Lett.*, **88**, 233502 (2006).

8. "Enhanced Open Circuit Voltage in Subphthalocyanine/C_{60} Organic Photovoltaic Cells", K.L. Mutolo, E. I. Mayo, B. P. Rand, S. R. Forrest and M. E. Thompson, *J. Am. Chem. Soc.*, **128**, 8108 (2006).

9. "Offset energies at organic semiconductor heterojunctions and their influence on the open-circuit voltage of thin-film solar cells", B. P. Rand, D. P. Burk and S. R. Forrest, *Phys. Rev. B*, **75**, 115327 (2007).

10. "Efficient solar cells using all-organic nanocrystalline networks", F. Yang, K. Sun, and S. R. Forrest, *Adv. Mater.*, **19**, 4166 (2007).

Organic Lasers

11. "Strong exciton-photon coupling and exciton hybridization in a thermally evaporated polycrystalline film of an organic small molecule", R.J. Holmes and S.R. Forrest, *Phys. Rev. Lett.*, **93**, 186404 (2004).

12. "Exciton-photon coupling in organic materials with large intersystem crossing rates and strong excited state molecular relaxation, R.J. Holmes and S.R. Forrest, *Phys. Rev. B*, **71**, 235203 (2005).

13. "Accumulation of electric-field-stabilized geminate polaron pairs in an organic semiconductor to attain high excitation density under low intensity pumping", N. C. Giebink and S. R. Forrest, *Appl. Phys. Lett.* **89**, 193502 (2006).

14. "Strong coupling and hybridization of Frenkel and Wannier-Mott excitons in an organic-inorganic optical microcavity", R. J. Holmes, S. Kéna-Cohen, V.M. Menon and S.R. Forrest, *Phys. Rev. B*, **74**, 235211 (2006).

Stephen R. Forrest

Princeton Institute for the Science and Technology of Materials (PRISM), Department of Electrical Engineering, Princeton University, Princeton, New Jersey 08544, USA

Organic electronics are beginning to make significant inroads into the commercial world, and if the field continues to progress at its current, rapid pace, electronics based on organic thin-film materials will soon become a mainstay of our technological existence. Already products based on active thin-film organic devices are in the market place, most notably the displays of several mobile electronic appliances. Yet the future holds even greater promise for this technology, with an entirely new generation of ultralow-cost, lightweight and even flexible electronic devices in the offing, which will perform functions traditionally accomplished using much more expensive components based on conventional semiconductor materials such as silicon.

Interest in organic electronics stems from the ability to deposit organic films on a variety of very-low-cost substrates such as glass, plastic or metal foils, and the relative ease of processing of the organic compounds that are currently being engineered by hundreds of chemists. The most advanced organic electronic systems already in commercial production are high-efficiency, very bright and colourful thin displays based on organic light-emitting devices[1] (OLEDs). Significant progress is also being made in the realization of thin-film transistors[2–4] (TFTs) and thin-film organic photovoltaic cells[5–8] for low-cost solar energy generation. Yet the ultimate test of this technology lies less in the reliability and performance of the organic components, which in some cases has already approached or even exceeded the requirements of a particular application, but rather in the ability to manufacture products at very low-cost. Although the cost of the organic materials used in most thin-film devices is low, in electronics the materials cost rarely determines that of the end product, where fabrication and packaging costs typically dominate. Hence, the successful application of this interesting materials platform will depend on capturing its low-cost potential through the innovative fabrication of devices on inexpensive, large-area substrates.

This suggests that conventional semiconductor device fabrication technologies need to be adapted to handle the large-area substrates spanned by organic macroelectronic circuits, and to be compatible with the physical and chemical properties of these fascinating compounds. Also, solids based on organic compounds are typically bonded by weak van der Waals forces that decrease as $1/R^6$, where R is the intermolecular spacing. This is in contrast to inorganic semiconductors that are covalently bonded, whose strength falls off as $1/R^2$. Hence, organic electronic materials are soft and fragile, whereas inorganic semiconductors are hard, brittle, and relatively robust when exposed to adverse environmental agents such as moisture and the corrosive reagents and plasmas commonly used in device fabrication. The apparent fragility of organic materials has also opened the door to a suite of innovative fabrication methods that are simpler to implement on a large scale than has been thought possible in the world of inorganic semiconductors. Many processes involve direct printing through use of contact with stamps, or alternatively via ink-jets and other solution-based methods.

Here I describe several recent advances in organic electronic devices, focusing particularly on the specialized processing techniques used in their realization. The discussion begins with a description of the unique electronic and optical properties of organic materials that make them interesting as technological substances. This is followed by a discussion of the methods of film deposition and patterning using techniques that have been developed to maintain the very low costs inherent in these material systems. The promise of organic electronics through the production of ubiquitous, low-cost and robust devices filling niches not occupied by silicon-based electronics should become readily apparent through the understanding of the unique properties that characterize these potentially high-performance materials.

Like all organic materials, organic semiconductors are carbon-rich compounds with a structure tailored to optimize a particular function, such as charge mobility or luminescent properties. Organic electronic materials (Fig. 1) can be classified into three categories: 'small molecules', polymers and biological materials. 'Small molecule' is a term broadly used to refer to those compounds with a well-defined molecular weight. The material shown, Pt-octaethylporphyrin (PtOEP), is a metallorganic complex that has

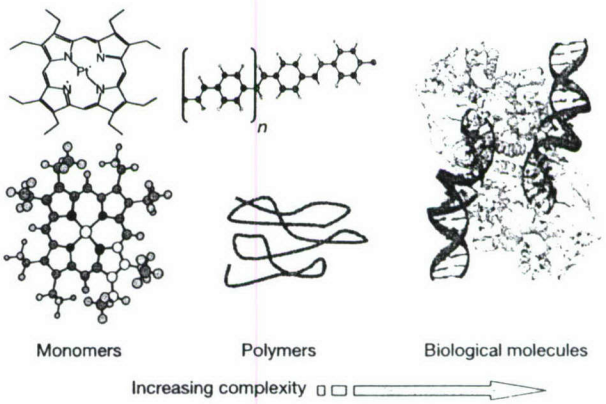

Figure 1 Various types of organic electronic materials, ranged in order of increasing complexity from left (simplest) to right (most complex). Monomeric compounds (left), typified by the metallorganic phosphor PtOEP shown here, are single compact molecular units with a well-defined molecular weight that are generally, although not always, deposited in vacuum. Dendrimers are larger variants of small-molecular-weight compounds. Next in complexity are polymers (centre), forming chains of repeating monomeric units. The chains are not of a well-defined length, and thus their molecular weight varies over a considerable range. Polymers are generally, although not always, deposited from liquid solution. Finally, the most complex materials are of biological origin (right), consisting of proteins and strands of DNA. Currently, there are no clear demonstrations of the utility of these complex structures for use in electronic applications.

©2004 Nature Publishing Group

been optimized to provide deep red phosphorescent emission when placed in an OLED[9]. Other small-molecular-weight materials include low-generation dendrimers and other oligomers[10,11]. In contrast, polymers are long-chain molecules consisting of an indeterminate number of molecular repeat units. The molecule shown is poly(*p*-phenylene vinylene), or PPV. Like PtOEP, PPV is an emissive organic semiconductor used in OLEDs[12–14]. At the high end of the complexity scale are organic materials of biological origin (in contrast to PtOEP and PPV, which are synthetic). As yet there are no clear applications that exploit the optical or electronic properties of these most complicated structures, although considerable investigation into the understanding and utilization of photosynthetic complexes is currently under way[15,16]. This Review concerns only monomeric and polymeric materials, as they are in the most advanced state of development for electronic and photonic applications.

Although much emphasis has been placed on the differences between the properties of small-molecular-weight organic thin films and polymers for organic electronic applications, there are in general more similarities than differences in both their electronic and optical properties, with the main distinction being in the methods of thin-film deposition and device preparation. In both polymers and small molecules, the excitonic state dominates their optical properties[17]. Here, an exciton is a molecular excited state that is mobile within the solid—that is, it can hop from molecule to molecule, or in the case of polymers, from chain to chain as well as along the polymer backbone until it recombines, generating either light (in a radiative process) or heat (under non-radiative circumstances). The most dominant species in organic electronic devices is the Frenkel exciton—a tightly bound (~1-eV binding energy) electron–hole pair that is generally localized on a single molecule at a time[18]. In addition, in highly ordered molecular crystals, more weakly bound charge-transfer (CT) excitons are found in the optical spectra. These equally mobile states are generally spread over one or more neighbouring molecules, and owing to their larger diameters, are more weakly bound (~10–100 meV) than Frenkel states.

Similarly, charge carrier (electron or hole) transport can occur via hopping between molecular sites, or from chain to chain. In this case, the carrier mobilities are quite low compared with inorganic semiconductors whose room temperature values typically range from 100 to $10^4\,cm^2\,V^{-1}\,s^{-1}$ (ref. 19). In contrast, in highly ordered molecular materials where charges hop between closely spaced molecules forming a crystalline stack, mobilities of $\mu \approx 1\,cm^2\,V^{-1}\,s^{-1}$ have been observed at room temperature[20–22]. This apparently is an approximate upper bound, with the mobility ultimately limited by thermal motion between neighbouring molecules. In more disordered molecular systems and polymers, the mobilities are only 10^{-3} to 10^{-5} times this upper limit[23–25]. However, deposition (generally by spinning) of polymers onto substrates prepared by rubbing or other 'direction-inducing' processes can lead to alignment of the chains, thus increasing the charge mobility over that of completely randomly disordered films[26]. A further strategy for reducing disorder in molecular systems as well as in polymers is by templating ordered epitaxy-like growth using crystalline substrates that impose their lattice order onto the adsorbed organic films[27,28]. However, this latter approach may also result in a prohibitive increase of device fabrication complexity, or may be limited to only a few organic materials and substrates that are not necessarily optimal for use in a particular application.

The low mobility leads to low electrical conductivity σ, given by $\sigma = ne\mu$, where n is the charge carrier density and e is the electronic charge. Thus, typical conductivities of organic materials are $\sigma \approx 10^{-6}\,S\,cm^{-1}$. In addition to low conductivity, low mobility also results in a very low charge carrier velocity, $v = \mu F \approx 10\,cm\,s^{-1}$, where F is the electric field of $\sim 10^5\,V\,cm^{-1}$, typical of many devices[29,30].

Owing to the low conductivity and carrier velocities that are intrinsic to organic thin-film semiconductors, one would expect that very-low-bandwidth operation of common optoelectronic devices such as transistors, OLEDs and photodetectors would provide a significant, if not fatal, limitation to their application in modern electronic systems. Although in many cases this is indeed true, the applications open to organic electronics are not targeted at simply replacing conventional electronics niches served by materials such as crystalline silicon. For example, very-low-bandwidth (~10-kHz) organic thin-film transistors (OTFTs) may find application in display back planes or low-cost 'disposable' electronics, such as building entry cards and other radio-frequency identification inventory control devices[31,32]. In addition, by using the thin vertical dimension (normal to the substrate plane) and the high crystalline order inherent in some molecular thin-film systems, very short carrier transit distances, and hence response times, can be obtained, leading to surprisingly high bandwidths. This has recently been demonstrated using multiple-layer organic photodetectors with bandwidths approaching 450 MHz (ref. 33). Further possibilities for exploiting the short vertical dimensions have also been demonstrated in polymer OTFTs by depositing polythiophene derivatives into a 'V'-shaped channel microcut into a flexible poly(ethylene terephthalate) substrate[34].

The viability of organic electronics, therefore, lies not in the displacement of existing applications niches currently filled by conventional semiconductors, *per se*, but rather in capturing the low cost and enormous variability inherent in organic systems that are otherwise not accessible. Success in achieving very-low-cost electronics hinges almost entirely on the ability to deposit and fabricate organic electronic devices using methods that represent a revolutionary departure from those commonly used by the current high-performance electronics industry. Hence, a great deal of current research has focused on depositing films and patterning devices on a large scale (leading to 'macroelectronic' applications), avoiding the need for labour-intensive techniques such as photolithography that today dominate the cost structure of conventional electronics.

It is commonly observed that the purity of the starting material is central to assuring high-performance and high-reliability electronic device operation. In organic electronics, the types of impurities and their effect on performance may differ substantially from those affecting inorganic semiconductor devices. Substitutional lattice impurities such as boron or phosphorous can change the conductivity of the host inorganic semiconductor (for example, silicon) by several orders of magnitude if introduced at only the parts per billion level, because each impurity atom disrupts the valence states of the neighbouring lattice atoms. However, no equivalent ordered lattice or bond-sharing exists in organic solids. The van der Waals forces that bond organic crystals, and also provide the cohesive force between neighbouring polymer chains, do not involve sharing of electrons between nearest-neighbour molecules[35]. Thus, impurities do not necessarily form electrically active substitutional defects. Yet, impurities may act as deep traps, extracting charge or acting as recombination sites within the thin film, or if ionic, they may still contribute charge to the surrounding crystal. Hence, although impurities act in remarkably different ways compared to an ordered inorganic semiconductor, they nevertheless can strongly influence the conductive properties of an organic material.

Indeed, intentional doping of molecular organic materials using the n-type dopants Pyronin B (ref. 36), 4-phenanthridinolato-Li (ref. 37) or Li (ref. 38), and p-type dopants such as F_4-TCNQ and $FeCl_3$ (refs 39–41), have been shown to increase the conductivity of small-molecular-weight films by several orders of magnitude compared with undoped organic layers. More frequently, however, dopants such as oxygen or even water can enter the organic film through unintentional exposure to the environment, leading to

©2004 Nature Publishing Group

degradation of the device performance over extended periods of operation[42–46]. Also, molecular impurities such as fractions that are co-deposited with the desired organic semiconductor can disrupt the molecular stacking order, resulting in a significant reduction in charge carrier mobility.

Because polymer chains in solution have a dispersity of molecular weights whose mean values are often $>10^5$, depending on the length of the polymer chain, there are few strategies for purifying the material based on molecular weight alone. Chromatography and other 'distillation' processes are commonly used to achieve the highest level of purity[47], although attaining $<1\%$ impurity concentrations remains a challenge. In contrast, small-molecule materials have well-defined molecular weights, allowing for straightforward separation of the host from the impurities. One common means for accomplishing this is via thermal gradient sublimation[27], whereby the organic source material is heated in a vacuum furnace, and then allowed to condense downstream in a cooler region of the furnace. The low- and high-molecular-weight impurities each condense in a different temperature zone from the desired source material, making separation of these components possible. Using sublimation techniques, fractional impurity concentrations as low as 10^{-4} are potentially achievable, although it remains an important challenge to measure this quantity precisely because of the complex role that impurities play in affecting the properties of the host material.

As noted previously, the principal distinction between polymers and small-molecular-weight organic thin films is the different methods used in their deposition and patterning.

In general, polymers are solution processed, uniformly applied across the entire wafer substrate by spin-on or spray-on methods. The solvent is then 'driven off' by evaporation after deposition. This technique can lead to very uniform films ~100 nm thick, as required in most devices such as OLEDs and OTFTs. Although there are several advantages to this method of film application, such as very-high-speed deposition over large substrate areas, there are also potential shortcomings. Primarily, the solvents used for one polymer layer can, and often do, attack previously applied layers, thereby limiting the complexity (and often as a consequence, the performance) of the structure that can be achieved[48]. This limitation is most frequently overcome by functionalizing or blending polymers to perform the many different tasks required to meet all of the performance criteria demanded by a particular application. For example, in an OLED where both charge conductivity and luminescence efficiency must be simultaneously maximized, the polymer can itself be functionalized, or it can be blended with other polymers (or even small-molecular-weight materials and dendrimers) to achieve both properties in a single layer[49]. Unfortunately, this can often lead to compromises, in which one performance parameter is traded off against another in the interest of low cost and fabrication simplicity.

A more serious shortcoming of full-surface deposition is the inability to locally pattern the electronic device. An example where substantial in-plane patterning must be applied is in fabricating colour displays based on a triad of closely spaced red (R), green (G) and blue (B) polymer OLEDs. The R, G and B sub-pixels must be separately contacted and energized such that their intensities can be individually controlled to achieve both the desired colour and intensity grey-scale[50]. Unfortunately, using spin-on or spray-on methods, the entire substrate is coated with only a single material, requiring different strategies for such a lateral functionalization. One emerging patterning strategy is ink-jet printing[51–54]. Micrometre-high polymer walls are prepatterned onto the substrate surface, thereby forming a region that defines the ~50–100-μm pixel diameter (Fig. 2). This is followed by ejecting a droplet of the solvated polymer from a micrometre-scale nozzle from a modified ink-jet printer. The droplet lands at the base of the well, spreading out to form a structure of dimensions determined by the well itself. This is done for each of the three colour sub-pixels, with adjacent wells in the triad each filled with polymers that are functionalized to produce the desired R, G and B colour emission (see Fig. 2). The process can be very rapid, generating a mobile phone display in only a few seconds.

Ink-jet printing requires precise control of the polymer chemistry to satisfy all the electrical and optical demands of a high-performance display. In addition, the polymer ink must have the appropriate mechanical properties, such that there is uniform coverage across the well diameter, as the applied voltage across the OLED, and hence the local current density, is strongly dependent on layer thickness. The process, therefore, places additional demands on the polymer inks over those for materials applied by conventional solution processing. Yet, early results with ink-jet printing of organic electronic devices have been quite promising[53]. For example, Toshiba has recently demonstrated its application to the fabrication of a full-colour polymer display with a 17-inch diagonal dimension. Although several problems related to pixel yield and operational lifetime of the display require further work before practical, cost-effective components can be realized, the demonstration of the

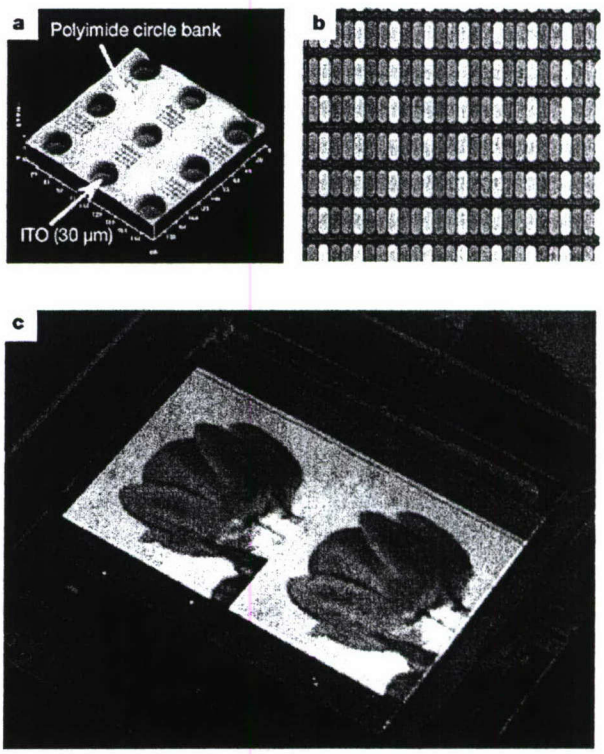

Figure 2 Ink-jet printing and the fabrication of full-colour polymer organic light-emitting device (OLED) displays. **a**, An atomic force micrograph of the polymer dams, or 'circle banks' prepatterned onto the substrate to receive and confine the polymer droplet from the ink-jet head, thereby forming a well defined polymer light-emitting device pixel, in this case with a diameter of 30 μm. Accurate positioning of the ink-jet nozzle to ensure hitting the circle bank 'target' that contains the indium tin oxide (ITO) anode (30 μm diameter), thereby forming the OLED, remains a challenge. From ref. 53. **b**, Three-colour triad of ink-jet-printed pixels, forming a prototype full-colour display (**c**). The individual 66 × 200 μm pixels in (**b**) are shown emitting fluorescent light after optical excitation. The full colour, 2-inch-diagonal ink-jet-printed display consists of a 128 × 160 array of polymer pixels, each pixel having dimensions of 60 × 200 μm. Images in **b** and **c** courtesy of Philips Electronics.

©2004 Nature Publishing Group

patterning technology over such a large spatial scale suggests that ink-jet printing offers many possibilities for fabricating very-large-scale and complex organic electronic circuits that will be produced at a cost unapproachable using conventional semiconductor device fabrication methods.

Thermal sublimation in vacuum is the most common means for depositing small-molecular-weight thin films[27]. This process involves the heating of the source material in a vacuum chamber, with the substrate located several centimetres distant, usually placed above the source. This 'bottom up' geometry prevents the source material from spilling out of the sublimation boat, and also avoids contamination of the substrate by flaking of material previously deposited onto the vacuum chamber wall, thereby creating dust that would ordinarily land on the substrate surface if a 'top down' deposition geometry were used. Vacuum thermal evaporation (VTE) is widely used in the processing of inorganic semiconductor devices because of the precision with which layer thicknesses can be controlled (typically to within ± 0.5 nm), and the relative simplicity of the process. One particular advantage of VTE is its ability to grow an unlimited number of layers, each optimized for a different function, to complete the device structure. This flexibility in device design is an inherent feature of 'dry processing'—that is, the several material layers that are deposited to form a device structure do not physically interact because there is no solvent that might transport material and chemically attack the predeposited film. This compatibility between layers provides for enormous flexibility in choosing materials and structures to be used in complex, modern electronic devices.

Nevertheless, there are several shortcomings to VTE: it can be wasteful of material, and it is difficult to maintain a uniform deposition rate because the organic material sources are typically thermally insulating. Hence, they are only heated in regions where the organic source is in contact with the resistively heated boat, creating pockets in the source powder that occasionally collapse under gravity, resulting in spitting or rapid changes in evaporation rate. Nevertheless, commercial production of organic displays is primarily based on VTE, and very-large-area full-colour displays (with 20-inch-diagonal displays recently announced by IBM, and 13-inch-diagonal displays demonstrated by Sony, among others) have been demonstrated using this process. One such display is shown in Fig. 3a, along with a conceptual view of a future 'universal communication device' consisting of computer and communication electronics contained in a very compact appliance also containing a lightweight and rugged display deposited on a flexible substrate[55,56]. Indeed, the ability to deposit organics onto a wide range of substrates without regard for the lattice-matching conditions that limit the materials choices of conventional semiconductor devices opens up many opportunities for applications based on this technology.

To avoid many of the shortcomings of VTE, an alternative method for depositing molecular organic thin films called organic vapour phase deposition (OVPD) has recently been introduced[57,58]. This technique differs from VTE in that evaporation occurs in a hot-walled reactor vessel in the presence of an inert carrier gas such as nitrogen or argon that is also maintained at a temperature sufficiently high to induce evaporation of the source material (see Fig. 4). These apparently simple differences from VTE have numerous consequences: evaporation in the presence of a carrier gas transforms the pickup of material into an equilibrium process, as opposed to the non-equilibrium conditions extant in VTE. That is, in VTE, the rate of material evaporation (and hence arrival rate of molecules at the substrate surface) follows an exponential dependence, $r = r_o \exp(-\Delta H_{vap}/kT_{cell})$, where ΔH_{vap} is the enthalpy of vaporization of the source organic, k is Boltzmann's constant, and T_{cell} is the source cell temperature. In contrast, in OVPD the carrier gas becomes saturated with the organic source material, which is then carried downstream to the cooled substrate where it enters a boundary layer of nearly stagnant flow. Depending on the pressure and temperature within the reactor, transport can be 'diffusion limited', whereby the molecule entering the thick boundary region suffers many collisions in a purely random process before reaching the substrate surface where physisorption occurs. At lower molecular partial pressures or higher gas flow velocities, the boundary layer thickness is decreased, and transport becomes 'kinetically limited'—that is, the rate of arrival of the molecules at the substrate is determined by the flow field of the gas that entrains them towards the surface.

Differences in molecular kinetic energy and momentum inherent in the diffusive and kinetic regimes lead to considerable differences in, and hence control over, the resulting thin-film morphology. For example, in the channels of pentacene OTFTs grown by OVPD, the crystallite size of the pentacene can vary from only a few tens of nanometres when grown under highly kinetic conditions, to several micrometres when grown in the diffusive regime[4] (Fig. 4). This variability arises because under equilibrium diffusive growth, molecules arriving at the surface can find their lowest-energy configuration with respect to neighbouring molecules, thus forming an ordered, self-assembled crystal structure. Under kinetic growth conditions, the molecules arrive rapidly at an aggressively cooled substrate, and are forced to 'stick' in positions that they assume at the time of arrival, hence leading to greater crystalline disorder. The result of this control is an increase in transistor field-effect hole

Figure 3 Organic emissive displays in the present and the future. **a**, A full colour, 13-inch diagonal small-molecular-weight OLED display. The display is only 2 mm thick, and uses top emitting OLEDs on an active transistor matrix backplane. The display supports full motion video images, and can be viewed at very oblique angles (right) without incurring a significant change in colour or contrast. Images courtesy of Sony Corp. A principal advantage of organic electronic devices is their ability to be deposited onto any substrate, including flexible and robust plastic sheets. **b**, A conceptual view of a future organic electronic flexible display that when not in use is rolled up into a pen-like device containing computational and wireless communication electronics. This lightweight and potentially low-cost electronic appliance is enabled by the high-resolution flexible display technology now being developed by the organic electronics community. Images courtesy of Universal Display Corp.

©2004 Nature Publishing Group

mobility under diffusion-limited growth by over an order of magnitude when compared to that obtained for kinetically grown crystals. Indeed, the highest hole mobilities obtained for pentacene TFTs grown by both OVPD and VTE are $\mu_{eff} \approx 1.5\,cm^2\,V^{-1}\,s^{-1}$, comparable to electron mobilities in amorphous silicon TFTs[3,4].

As well as allowing the control of crystalline morphology by the saturated pickup of the source material, OVPD is also a relatively dust-free process, because the chamber walls are maintained at a temperature high enough to prevent readsorption. This also leads to very-high-efficiency material use, as the only cold region in the reactor where molecular adsorption can occur is the substrate. Finally, none of the non-uniformities in evaporation rate common to VTE affect growth by OVPD, simply because the source material is infused with the carrier gas, making the entire source isothermal, independent of its thermal conductivity.

As in the solution-based application of polymers, simple deposition either by VTE or OVPD results in the full surface of the substrate being uniformly coated. In both OVPD and VTE, therefore, the most common means for achieving patterned growth as required for display pixellation is to deposit the material through a shadow mask placed in close (~1 μm) proximity to the substrate surface. The mask has an array of apertures whose dimensions match that of the desired deposit diameter, with the minimum feature size approximately equal to that of the mask thickness (for example, ~20–75 μm). Indeed, under highly controlled conditions, the smallest features achieved using shadow masks are[59] 1–5 μm.

An analogue to ink-jet printing, known as organic vapour-jet printing (OVJP), has also been proposed and developed for use with small-molecular-weight materials[59,60]. Like OVPD, the solvent is a hot inert carrier gas that vaporizes the organic source, creating a flow of volatilized molecules. These molecules pass through a nozzle, after which they are deposited onto a cold substrate surface placed in close proximity (~10–100 μm) to the nozzle tip. This process replaces the liquid solvent used in ink-jet printing with an inert carrier gas, thereby eliminating many of the mechanical properties of the liquid (such as meniscus formation leading to thickness non-uniformities), and does not require polymer wells to be formed on the substrate to spatially contain the liquid droplet. Like ink-jet printing, OVJP is at its very earliest stages of development, and as yet there are no clear demonstrations that this technology will eventually find use in the large-scale production of low-cost organic electronic circuits and systems.

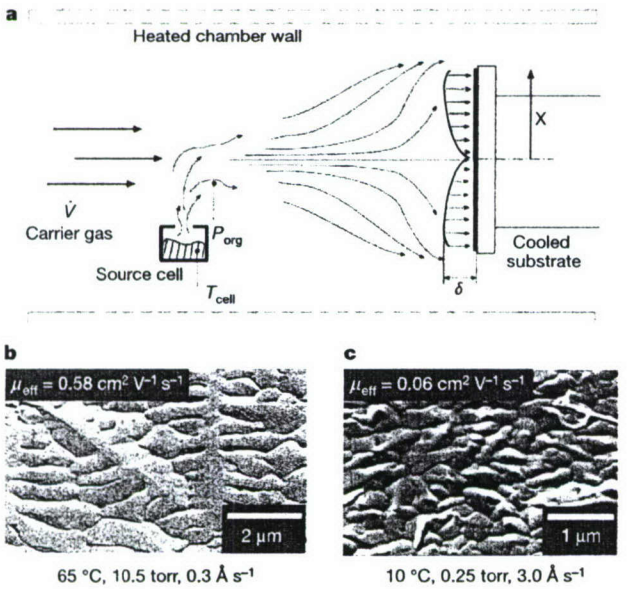

Figure 4 The process of organic vapour-phase deposition (OVPD) for the growth of organic electronic devices. **a**, A schematic cross-section of a hot-walled OVPD reactor showing the growth process. Growth occurs by infusing a hot boat containing the organic source material with an inert carrier gas. The gas becomes saturated with the organic vapours and carries them downstream to a cooled substrate where they physisorb onto its surface. Shown immediately in front of the substrate is a hydrodynamic boundary layer of thickness δ. Depending on the reactor pressure and rate of molecular pickup by the carrier gas, the boundary layer thickness can be varied from very thin (in which case the growth rate is considered kinetically limited, whereby the nearly 'ballistic' transport of molecules to the surface dominates) to several millimetres thick (corresponding to diffusion-limited growth, whereby the molecules suffer many collisions within the boundary layer, thereby controlling the growth process). Because the walls of the chamber are hot, adsorption occurs only on the substrate, resulting in extremely high-efficiency use of materials. Further, the pickup of molecular species results in saturation of the inert carrier gas, resulting in highly controlled growth rates. Here, $\dot{V}$ is the gas volumetric flow velocity, P_{org} is the partial pressure of the organic material in the gas stream, T_{cell} is the temperature of the organic source cell, and X is the position as a function of distance from the substrate axis. **b**, **c**, The growth regime affects the morphology of a pentacene film. The conditions in **b** correspond to diffusion-limited growth (high substrate temperature and chamber pressure, slow growth rate) resulting in very large crystalline domains. In a thin-film transistor, these domains can span the entire device active region from source to drain contacts, leading to a high field-effect hole mobility of $\mu_{eff} = 0.58\,cm^2\,V^{-1}\,s^{-1}$. For kinetically grown films (**c**) (low substrate temperature and chamber pressure, and high growth rate), the crystallite size is considerably smaller than in **b**. In this case, transport from source to drain is primarily limited by scattering from grain boundaries between the individual crystallites, resulting in a tenfold decrease in hole mobility. From refs 4 and 58.

Patterned deposition is based on the thermal imaging dry transfer (using, for example, a laser or other localized heat source) of a

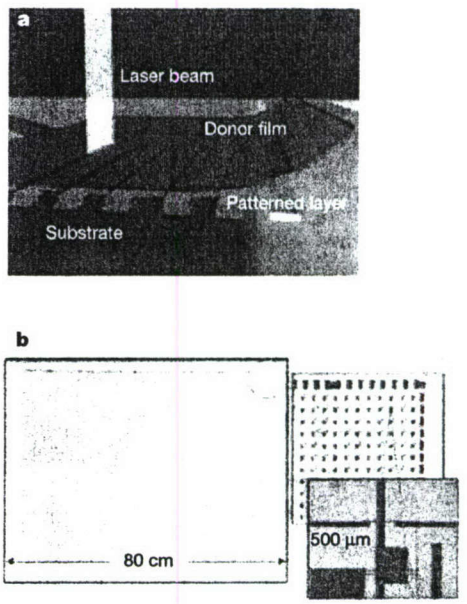

Figure 5 Laser-induced thermal imaging transfer of active organic semiconductor materials to a substrate. **a**, A 'donor' film is pre-loaded with the organic thin film, which is then locally transferred by thermal ablation using a laser. From ref. 63. **b**, Micrograph of a 50 × 75 cm array of pentacene organic thin-film transistors whose source and drain contacts were patterned using laser-induced thermal imaging. The various images show different magnifications from (clockwise) the full panel, a small segment containing approximately 100 TFTs, and a single TFT with a gate length of ~20 μm. From ref. 52.

©2004 Nature Publishing Group

polymer or small-molecular-weight material from a 'donor' or material source sheet, to the 'receiver' or target substrate, and is also attracting interest[61]. The transfer occurs by ablation of materials that are predeposited onto the donor sheet held in contact with the substrate (Fig. 5). In one demonstration of this method, high-conductivity, 5 × 2.7 μm, polymer contacts loaded with single-walled carbon nanotubes used for the source and drain of a pentacene transistor were transferred using an infrared diode laser as the ablation source[62]. The pentacene channel was applied by routine VTE deposition, thereby spanning the gap between source and drain. A 50 × 75 cm printed transistor backplane has been fabricated using thermal imaging, suggesting its utility for producing large-area organic circuits (Fig. 5). This technique, however, is not confined to the deposition of contacts, but can be applied to the transfer of the active semiconductor layer as well[63]. For example, a blend of a blue-light-emitting polymer and a hole transport layer was transferred to a receiving substrate using laser ablation, creating well-formed and high-resolution blue-emitting OLEDs. The transferred material must be optimized such that its resistance to thermal degradation and mechanical properties are suitable for this so-called laser-induced thermal imaging process. Although this optimization can lead to compromises in device performance, laser-induced thermal transfer of organics is showing early promise as a route for realizing practical macroelectronic integrated circuits.

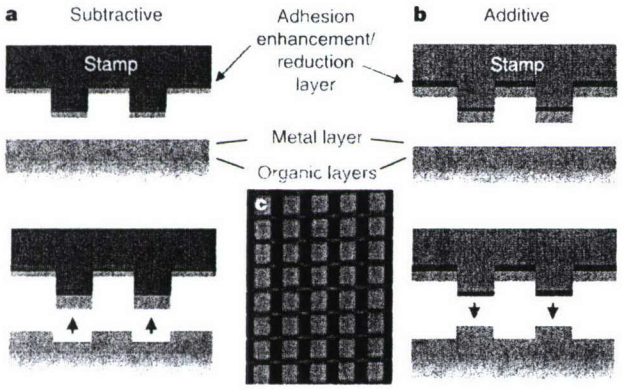

Figure 6 Direct micro/nanopatterning of an organic electronic device by cold welding. In the subtractive process (**a**), the organic layers comprising the active electronic device are deposited across the full substrate surface, followed by the deposition of the unpatterned metallic contact. A hard 'stamp' is then fabricated, whose raised regions correspond to the regions of the finished device where cathode metal is removed. The stamp is first coated with an adhesion 'enhancement' layer, followed by deposition of the same metal used as a contact metal to the organic electronic device. The stamp is then brought into a pressure contact with the substrate, such that the metal on the stamp and substrate form an intimate metallic bond, or cold weld. Pressing harder causes the metal at the edge of the stamp to fracture, allowing for lift-off of the metal under the stamp when it is separated from the substrate. The amount of pressure that needs to be applied to cause a fracture at the edge of the stamp increases with the thickness of the metal. Note that no pressure is applied to a device whose active region is under the metal contact (for example, a detector or an OLED). In the additive process (**b**), the metal layer that is predeposited onto the organic layer surface is very thin (typically ~5 nm). This is the 'strike layer'. Unlike the subtractive process, the desired thickness of the metal contact is deposited onto the stamp itself, not the organic layers. Further, before deposition on the stamp, the stamp surface is coated with an 'adhesion reduction layer' that ensures that the metal can easily lift away from the stamp after separation from the substrate. The stamp and substrate are then brought into pressure contact where cold welding once more occurs and the metal on the stamp is left behind, directly forming the contact pattern. The thin residual strike layer between the contacts is then removed by gentle etching by a reactive gas or by simple sputtering. Using soft stamps, this process requires very low pressures that are not dependent on metal thickness (no fracture is required). The pattern definitions achievable using these processes are <10 nm in many cases. In **c** is shown a segment of a passive matrix OLED display patterned using the subtractive process. The green regions are pixels emitting light when electrically addressed. From refs 68 and 69.

To capture the low-cost potential of organic thin films inherent in their low-temperature deposition on substrates such as glass, plastic or metal foils, it is imperative that these processes be complemented by similarly inexpensive device patterning and fabrication methods. For this reason, researchers have long sought innovative and fault-tolerant methods for patterning thin organic films that are simple and do not result in the destruction of these often fragile or environmentally sensitive materials.

In addition to patterning during deposition using techniques such as ink-jet or OVJP, methods have also been developed to pattern the organics into circuits after deposition. These methods include direct nanoimprinting of the polymer[64], lithographically induced self assembly[65], microcutting of the cathode metal after deposition onto the underlying active organic materials[66], photo-crosslinking of polymer regions to form conducting contacts to organic thin-film transistors, followed by creating vertical interconnects between circuit levels (or 'vias') using metal 'pins'[32], lamination of contacts onto the organic surface from soft rubber stamps[67], and cathode formation by cold welding from stamps[68,69].

Cold welding is the binding of two clean surfaces, each containing a film of the same metal, on contact or on application of a moderate pressure (Fig. 6). To pattern contacts and interconnects, one starts by forming a 'stamp' in a soft material such as poly(dimethylsiloxane) (PDMS), where the desired pattern is embossed onto the stamp surface[68]. Then an adhesion-preventing coating is placed on the stamp, followed by the deposition of the metal at a thickness needed for the cathode or other metallic interconnect. Before the cold-welding step, the organic layers forming the desired electronic device are deposited across the full surface of the substrate in the normal sequence. This is capped with a very thin (~5 nm)

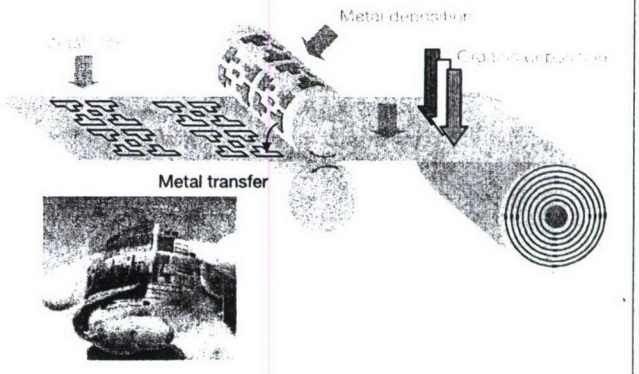

Figure 7 Conceptual diagram of continuous and very-low-cost manufacture of organic electronic devices. Starting with a roll of plastic substrate, the organic materials forming the device active regions are first deposited either from the liquid or vapour phase, and then a metal 'strike layer' (such as in Fig. 6) is deposited. The film is then passed between rollers with an embossed pattern representing the ultimate electrode scheme required on their surfaces. These rollers then directly pattern the electrodes, again as in Fig. 6. In the final step, the strike layer metal is removed by dry etching, completing the circuit. The sheets are eventually coated to eliminate degradation from exposure to the environment, and then packaged to suit the desired application. The lower photograph shows a fully processed wafer foil containing all-polymer transistors and integrated circuits, showing recent progress in achieving this vision of the future. Photograph courtesy of T. Jackson, Pennsylvania State University.

©2004 Nature Publishing Group

unpatterned metal film, such as LiF/Al/Au, that ultimately forms part of the injecting cathode into the organic heterostructure. This thin layer is known as the 'strike layer'.

In bringing the stamp and substrate into contact and under weak pressure (typically 1 atm), the metal on the stamp cold-welds to the same metal which is also used for the strike layer (Fig. 6). Here, noble metals are preferred, as they do not form thick oxides that might prevent bonding when brought into contact with the second metal surface. As the stamp is lifted away from the surface, its thick metal layer is left behind, bonded to the strike layer owing to the cold weld. Finally, the strike layer between the metal pattern remaining after stamping is removed, using a plasma or other light etching step. This technique has been shown to result in high-quality organic electronic devices with pattern resolutions approaching 10 nm.

The opportunities for the use of organic thin films in modern electronic circuits are rapidly expanding, based on the very high-performance and unique functionality offered by these principally carbon-containing semiconductors. However, their practical implementation in electronic applications will ultimately be decided by the ability to produce devices and circuits at a cost that is significantly below that needed to manufacture conventional electronic circuits based on, for example, silicon. If successful, these low-cost fabrication processes will ultimately result in the 'printing' of large-area organic electronic circuits using roll-to-roll or web-based methods, where low-temperature deposition of the organics is followed by metal deposition and patterning in a continuous, high-speed process analogous, perhaps, to processes used in the printing of documents or fabrics (Fig. 7). However, much work must be done before such an ambitious goal can be realized. Although many innovative technologies have been developed relating to the fabrication of thin-film organic devices with high performance and long operational lifetime, very few of these technologies have left the laboratory and found their way into a manufacturing environment. Indeed, only the simplest fabrication technologies have so far been implemented on manufacturing lines: spin-coating of polymers over broad substrate surfaces to create monochrome displays, or in the case of small molecules, vacuum deposition through shadow masks resulting in full colour displays. Yet even these early demonstrations are impressive. As the more sophisticated and versatile methods currently being developed in the laboratory make their way into the manufacturing environment, we can expect that organic electronic circuits whose functions are only now being envisioned will one day revolutionize the technological world in which we live. □

doi:10.1038/nature02498.

1. Vaeth, K. M. OLED-display technology. *Inform. Display* **19,** 12–17 (2003).
2. Lin, Y. Y., Gundlach, D. J., Nelson, S. F. & Jackson, T. N. in *55th Annu. Dev. Res. Conf.* 60 (Electron Device Society, Ft Collins, Colorado, 1997).
3. Gundlach, D. J., Lin, Y. Y. & Jackson, T. N. Pentacene organic thin film transistors—molecular ordering and mobility. *IEEE Electron. Dev. Lett.* **18,** 87–89 (1997).
4. Shtein, M., Mapel, J., Benziger, J. B. & Forrest, S. R. Effects of film morphology and gate dielectric surface preparation on the electrical characteristics of organic vapor phase deposited pentacene thin-film transistors. *Appl. Phys. Lett.* **81,** 268–270 (2002).
5. Peumans, P. & Forrest, S. R. Very high efficiency double heterostructure copper phthalocyanine/C_{60} photovoltaic cells. *Appl. Phys. Lett.* **79,** 126–128 (2001).
6. Granstrom, M. *et al.* Laminated fabrication of polymeric photovoltaic diodes. *Nature* **395,** 257–260 (1998).
7. Peumans, P., Uchida, S. & Forrest, S. R. Efficient bulk heterojunction photovoltaic cells based on small molecular weight organic thin films. *Nature* **425,** 158–162 (2003).
8. Shaheen, S. E. *et al.* 2.5% efficient organic plastic solar cells. *Appl. Phys. Lett.* **78,** 841–843 (2001).
9. Baldo, M. A. *et al.* High efficiency phosphorescent emission from organic electroluminescent devices. *Nature* **395,** 151–154 (1998).
10. Anthopoulos, T. D. *et al.* Highly efficient single-layer dendrimer light-emitting diodes with balanced charge transport. *Appl. Phys. Lett.* **82,** 4824–4826 (2003).
11. Ma, D. G. *et al.* Bright electroluminescence from a new conjugated dendrimer. *Synth. Met.* **137,** 1125–1126 (2003).
12. Lee, C.-L., Lee, K. B. & Kim, J.-J. Polymer phosphorescent light emitting devices doped with tris(2-phenylpyridine) iridium as a triplet emitter. *Appl. Phys. Lett.* **77,** 2280–2282 (2000).
13. Burroughes, J. H. *et al.* Light-emitting diodes based on conjugated polymers. *Nature* **347,** 539–541 (1990).
14. Braun, D. & Heeger, A. J. Visible light emission from semiconducting polymer diodes. *Appl. Phys. Lett.* **58,** 1982–1984 (1991).
15. Greenbaum, E., Blankinship, S. L., Lee, J. W. & Ford, R. M. Solar photobiochemistry: Simultaneous photoproduction of hydrogen and oxygen in a confined bioreactor. *J. Phys. Chem. B* **105,** 3605–3609 (2001).
16. Greenbaum, E., Lee, I. & Lee, J. W. Functional 3D nanoscale imaging of a single-molecule photovoltaic structure. *Biophys. J. Part 2* **82,** 206–207 (2002).
17. Pope, M. & Swenberg, C. E. *Electronic Processes in Organic Crystals* (Clarendon, Oxford, 1982).
18. Silinsh, E. A. in *Organic Molecular Crystals* (ed. Queisser, H.-J.) Ch. 1 (Springer, Berlin, 1980).
19. Sze, S. M. *Physics of Semiconductor Devices* (John Wiley, New York, 1981).
20. Warta, W., Stehle, R. & Karl, N. Ultrapure, high mobility organic photoconductors. *Appl. Phys. A* **36,** 163–170 (1985).
21. Karl, N. Studies of organic semiconductors for 40 years. III. *Mol. Cryst. Liq. Cryst.* **171,** 31–51 (1989).
22. Forrest, S. R., Kaplan, M. L. & Schmidt, P. H. Organic-on-inorganic semiconductor contact barrier diodes. II. Dependence on organic film and metal contact properties. *J. Appl. Phys.* **56,** 543–551 (1984).
23. Campbell, A. J., Bradley, D. D. C. & Antoniadis, H. Dispersive electron transport in an electroluminescent polyfluorene copolymer measured by the current integration time-of-flight method. *Appl. Phys. Lett.* **79,** 2133–2135 (2001).
24. Blom, P. W. M., de Jong, M. J. M. & vanMunster, M. G. Electric-field and temperature dependence of the hole mobility in poly(p-phenylene vinylene). *Phys. Rev. B* **55,** R656–R659 (1997).
25. Bulovic, V., Burrows, P. E. & Forrest, S. R. in *Electroluminescence I* (ed. Mueller, G.) 262 (Academic, New York, 2000).
26. Sirringhaus, H. *et al.* Mobility enhancement in conjugated polymer field-effect transistors through chain alignment in a liquid-crystalline phase. *Appl. Phys. Lett.* **77,** 406–408 (2000).
27. Forrest, S. R. Ultrathin organic films grown by organic molecular beam deposition and related techniques. *Chem. Rev.* **97,** 1793–1896 (1997).
28. van de Craats, A. M. *et al.* Meso-epitaxial solution-growth of self organizing discotic liquid-crystalline semiconductors. *Adv. Mat.* **15,** 495–499 (2003).
29. Burrows, P. E. & Forrest, S. R. Electroluminescence from trap-limited current transport in vacuum deposited organic light emitting devices. *Appl. Phys. Lett.* **64,** 2285–2287 (1994).
30. Parker, I. D. Carrier tunneling and device characteristics in polymer light emitting diodes. *J. Appl. Phys.* **75,** 1656–1666 (1994).
31. Gelinck, G. H., Geuns, T. C. T. & de Leeuw, D. M. High-performance all-polymer integrated circuits. *Appl. Phys. Lett.* **77,** 1487–1489 (2000).
32. Drury, C. J., Mutsaers, C. M. J., Hart, C. M., Matters, M. & de Leeuw, D. M. Low-cost all-polymer integrated circuits. *Appl. Phys. Lett.* **73,** 108–110 (1998).
33. Peumans, P., Bulovic, V. & Forrest, S. R. Efficient, high-bandwidth organic multilayer photodetectors. *Appl. Phys. Lett.* **76,** 3855–3857 (2000).
34. Stutzmann, N., Friend, R. H. & Sirringhaus, H. Self-aligned vertical-channel polymer field effect transistors. *Science* **299,** 1881–1884 (2003).
35. Kitaigorodsky, A. I. *Molecular Crystals and Molecules* (Academic, New York, 1973).
36. Werner, A. G. *et al.* Pyronin B as a donor for n-type doping of organic thin films. *Appl. Phys. Lett.* **82,** 4495–4497 (2003).
37. Fukase, A. & Kido, J. Organic electroluminescent devices having self-doped cathode interface layer. *Jpn. J. Appl. Phys. 2* **41,** L334–L336 (2002).
38. Kido, J. & Matsumoto, T. Bright organic electroluminescent devices having a metal-doped electron-injecting layer. *Appl. Phys. Lett.* **73,** 2866–2868 (1998).
39. Endo, J., Matsumoto, T. & Kido, J. Organic electroluminescent devices with a vacuum-deposited Lewis-acid-doped hole-injecting layer. *Jpn. J. Appl. Phys. 2* **41,** L358–L360 (2002).
40. Gao, W. & Kahn, A. Controlled p-type doping of an organic molecular semiconductor. *Appl. Phys. Lett.* **79,** 4040–4042 (2001).
41. Pfeiffer, M., Forrest, S. R., Leo, K. & Thompson, M. E. Electrophosphorescent p-i-n organic light emitting devices for very high efficiency flat panel displays. *Adv. Mater.* **14,** 1633–1636 (2002).
42. Do, L. M. *et al.* Observation of degradation processes of Al electrodes in organic electroluminescence devices by electroluminescence microscopy, atomic force microscopy, scanning electron microscopy and Auger electron spectroscopy. *J. Appl. Phys.* **76,** 5118–5121 (1994).
43. Aziz, H. *et al.* Degradation processes at the cathode/organic interface in organic light emitting devices with Mg:Ag cathodes. *Appl. Phys. Lett.* **72,** 2642–2644 (1998).
44. Burrows, P. E. *et al.* Reliability and degradation of organic light emitting devices. *Appl. Phys. Lett.* **65,** 2922–2924 (1994).
45. Kwong, R. C. *et al.* High operational stability of electrophosphorescent devices. *Appl. Phys. Lett.* **81,** 162–164 (2002).
46. Xu, G. Fighting OLED degradation. *Inform. Display* **19,** 18–21 (2003).
47. Gutmann, F. & Lyon, L. E. *Organic Semiconductors* Part A (R. E. Krieger Publishing, Malabar, Florida, 1981).
48. Wu, C. C., Sturm, J. C., Register, R. A. & Thompson, M. E. Integrated three color organic light emitting devices. *Appl. Phys. Lett.* **69,** 3117–3119 (1996).
49. Jiang, X. Z. *et al.* Effect of carbazole-oxadiazole excited-state complexes on the efficiency of dye-doped light-emitting diodes. *J. Appl. Phys.* **91,** 6717–6724 (2002).
50. Gu, G. & Forrest, S. R. Design of flat panel displays based on organic light emitting devices. *IEEE J. Sel. Top. Quant. Electron.* **4,** 83–99 (1998).
51. Hebner, T. R. & Sturm, J. C. Local tuning of organic light-emitting diode color by dye droplet application. *Appl. Phys. Lett.* **73,** 1775–1777 (1998).
52. Sirringhaus, H. *et al.* High-resolution inkjet printing of all-polymer transistor circuits. *Science* **290,** 2123–2126 (2000).
53. Shimoda, T., Morii, K., Seki, S. & Kiguchi, H. Inkjet printing of light-emitting polymer displays. *Mater. Res. Soc. Bull.* **28,** 821–827 (2003).
54. Hebner, T. R., Wu, C. C., Marcy, D., Lu, M. H. & Sturm, J. C. Ink-jet printing of doped polymers for organic light emitting devices. *Appl. Phys. Lett.* **72,** 519–521 (1998).
55. Gustafsson, G. *et al.* Flexible light-emitting diodes made from soluble conducting polymers. *Nature* **357,** 477–479 (1992).
56. Gu, G., Burrows, P. E., Venkatesh, S., Forrest, S. R. & Thompson, M. E. Vacuum-deposited,

©2004 Nature Publishing Group

non-polymeric flexible organic light emitting devices. *Opt. Lett.* **22,** 175–177 (1997).
57. Burrows, P. E. *et al.* Organic vapor phase deposition: a new method for the growth of organic thin films with large optical nonlinearities. *J. Cryst. Growth* **156,** 91–98 (1995).
58. Shtein, M., Gossenberger, H. F., Benziger, J. B. & Forrest, S. R. Material transport regimes and mechanisms for growth of molecular organic thin films using low-pressure organic vapor phase deposition. *J. Appl. Phys.* **89,** 1470–1476 (2001).
59. Shtein, M., Peumans, P., Benziger, J. B. & Forrest, S. R. Micropatterning of organic thin films for device applications using organic vapor phase deposition. *J. Appl. Phys.* **93,** 4005–4016 (2003).
60. Shtein, M., Peumans, P., Benziger, J. & Forrest, S. R.. Direct, mask- and solvent-free printing of molecular organic semiconductors. *Adv. Mater.* (in the press).
61. Karnakis, D. M., Lippert, T., Ichinose, N., Kawanishi, S. & Fukumura, H. Laser induced molecular transfer using ablation of a triazeno-polymer. *Appl. Surf. Sci.* **127–129,** 781–786 (1998).
62. Blanchet, G. B., Loo, Y.-L., Rogers, J. A., Gao, F. & Fincher, C. R. Large area, high resolution dry printing of conducting polymers for organic electronics. *Appl. Phys. Lett.* **82,** 463–465 (2003).
63. Suh, M. C., Chin, B. D., Kim, M.-H., Kang, T. M. & Lee, S. T. Enhanced luminance of blue light-emitting polymers by blending with hole transporting materials. *Adv. Mater.* **15,** 1254–1258 (2003).
64. Wang, J., Sun, X., Chen, L. & Chou, S. Y. Direct nanoimprint of submicron organic light-emitting structures. *Appl. Phys. Lett.* **75,** 2767–2769 (1999).
65. Chou, S. Y., Zhuang, L. & Guo, L. Lithographically induced self-construction of polymer microstructures for resistless patterning. *Appl. Phys. Lett.* **75,** 1004–1006 (1999).
66. Stutzmann, N., Tervoort, T. A., Bastiaansen, K. & Smith, P. Patterning of polymer-supported metal films by microcutting. *Nature* **407,** 613–616 (2000).
67. Zaumseil, J. *et al.* Nanoscale organic transistors that use source/drain electrodes supported by high resolution rubber stamps. *Appl. Phys. Lett.* **82,** 793–795 (2003).
68. Kim, C. & Forrest, S. R. Fabrication of organic light-emitting devices by low pressure cold welding. *Adv. Mater.* **15,** 541–545 (2003).
69. Kim, C., Burrows, P. E. & Forrest, S. R. Micropatterning of organic electronic devices by cold-welding. *Science* **288,** 831–833 (2000).

Acknowledgements The author is indebted to his many students, and in particular M. Thompson, for many discussions over the years. He is also grateful to the Air Force Office of Scientific Research, the Defense Advanced Research Projects Agency, the National Science Foundation and Universal Display Corporation for their financial support of this work.

Competing interests statement The author declares that he has no competing financial interests.

Correspondence and requests for materials should be addressed to the author (forrest@princeton.edu).

©2004 Nature Publishing Group

HTML ABSTRACT + LINKS

Asymmetric tandem organic photovoltaic cells with hybrid planar-mixed molecular heterojunctions

Jiangeng Xue, Soichi Uchida,[a] Barry P. Rand, and Stephen R. Forrest[b]
Department of Electrical Engineering, and Princeton Institute for the Science and Technology of Materials (PRISM), Princeton University, Princeton, New Jersey 08544

(Received 29 July 2004; accepted 18 October 2004)

We demonstrate high-efficiency organic photovoltaic cells by stacking two hybrid planar-mixed molecular heterojunction cells in series. Absorption of incident light is maximized by locating the subcell tuned to absorb long-wavelength light nearest to the transparent anode, and tuning the second subcell closest to the reflecting metal cathode to preferentially absorb short-wavelength solar energy. Using the donor, copper phthalocyanine, and the acceptor, C_{60}, we achieve a maximum power conversion efficiency of $\eta_P=(5.7\pm0.3)\%$ under 1 sun simulated AM1.5G solar illumination. An open-circuit voltage of $V_{OC}\leq 1.2$ V is obtained, doubling that of a single cell. Analytical models suggest that power conversion efficiencies exceeding 6.5% can be obtained by this architecture. © *2004 American Institute of Physics*. [DOI: 10.1063/1.1829776]

Organic photovoltaic (PV) cells have the potential for providing a practical solution to solar energy conversion due to their low material cost, ease of processing, and compatibility with flexible substrates.[1,2] The power conversion efficiency (η_P) of organic PV cells has steadily improved through the use of new materials and device structures.[3–13] Performance of early organic bilayer heterojunction (HJ) PV cells was limited by the ability of excitons to diffuse to the donor–acceptor (D–A) interface, since their diffusion length (typically $L_D\leq 100$ Å)[1] is much shorter than the optical absorption length ($L_A\approx 1000$ Å). The efficiency has been improved by using the acceptor material C_{60} with a long exciton diffusion length ($L_D\approx 400$ Å),[1,6] or by forming a bulk HJ.[4,5] By combining these two approaches, we have recently demonstrated $\eta_P=5\%$ under simulated AM1.5G solar illumination in a copper phthalocyanine (CuPc)/C_{60} organic PV cell incorporating a mixed D–A layer sandwiched between homogeneous donor and acceptor layers (called a "hybrid planar-mixed heterojunction," or PM-HJ).[13]

Yakimov and Forrest[8] demonstrated a more than doubling of individual CuPc/PTCBI (or 3, 4, 9, 10-perylenetetracarboxylic bisbenzimidazole) cell efficiencies of $\eta_P=1\%$ to $\eta_P=2.5\%$ by stacking[14] two thin cells in series, with Ag nanoclusters between the subcells providing both optical field enhancement and efficient recombination sites for the photogenerated charges. The photovoltage of this "tandem" cell was twice that of each individual cell (or subcell). Here, we show that by stacking two CuPc/C_{60} hybrid PM-HJ cells in series with optimized optical absorption, $\eta_P=(5.7\pm0.3)\%$ under 1 sun$=100$ mW/cm^2 simulated AM1.5G solar illumination is achieved, representing ~15% increase from a single hybrid PM-HJ cell.[13] Furthermore, the open circuit voltage, V_{OC}, of the tandem cell is twice that of a single PV cell, reaching up to 1.2 V under high intensity illumination. In particular, we show that without including antireflection coatings on the substrates, organic PV cells with solar power conversion efficiencies exceeding 6.5% are possible using optimized tandem structures of this type.

The structure of a CuPc/C_{60} hybrid PM-HJ tandem cell is schematically shown in Fig. 1(a). A transparent, conducting indium-tin-oxide (ITO) layer on a glass substrate is used as the anode, while a 1000 Å thick thermally evaporated Ag electrode serves as the cathode. The photoactive region of each subcell consists of a hybrid PM-HJ,[13] i.e., a mixed CuPc:C_{60} layer sandwiched between homogeneous CuPc and C_{60} layers, which combines the good transport of photogenerated charge carriers to their respective electrodes charac-

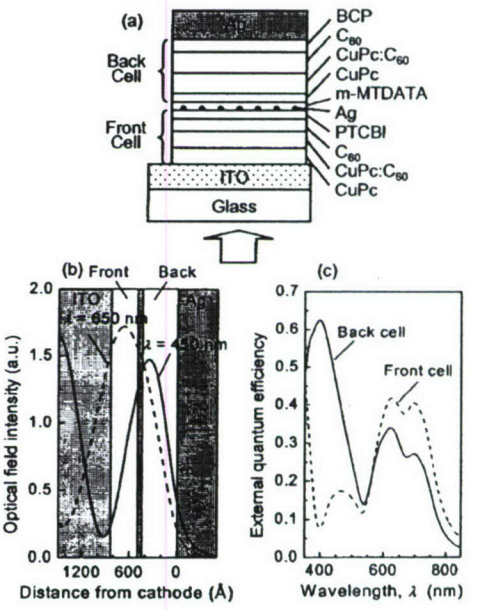

FIG. 1. (a) Structure of an organic tandem PV cell formed by stacking two hybrid PM-HJ cells in series. Each subcell (front or back, with respect to the incident light direction as indicated) employs a mixed CuPc:C_{60} layer sandwiched between homogeneous CuPc and C_{60} layers as the photoactive region, with a PTCBI (front) or BCP (back) layer serving as the EBL. (b) Optical field intensities at $\lambda=450$ nm (solid line) and $\lambda=650$ nm (dashed line) calculated as functions of the distance from the cathode in an asymmetric organic tandem cell (B in Table I). (c) Calculated external quantum efficiencies for the front (dashed line) and back (solid line) subcells of cell B. The asymmetric spectral responses from the two subcells result from the placement of the layers within the asymmetric tandem cell structure.

[a]Currently on leave from Central Technical Research Laboratory, Nippon Oil Corporation, 8 Chidori-cho, Naka-ku, Yokohama, 230-0815 Japan.
[b]Electronic mail: forrest@princeton.edu

 © 2004 American Institute of Physics
Downloaded 12 Jan 2008 to 141.213.8.105. Redistribution subject to AIP license or copyright; see http://apl.aip.org/apl/copyright.jsp

TABLE I. Layer thicknesses (in Å) of three asymmetric tandem organic PV cells as well as their predicted performance (short-circuit current density J_{SC}, open-circuit voltage V_{OC}, fill factor FF, and power conversion efficiency η_P) and measured efficiency $\eta_{P,exp}$, under 1 sun AM1.5G solar illumination. The charge recombination zone in each tandem cell consists of a 5 Å thick Ag nanocluster layer and a 50 Å thick m-MTDATA doped with 5 mol % F_4-TCNQ. Parameters used in the model are[a] J_s=35 nA/cm^2, R_s=0.25Ω cm^2, n=1.6, L_{c0}=400 Å, V_{bi}=0.65 V, and the exciton diffusion length in CuPc, C_{60}, and PTCBI is L_D=80 Å, 400 Å, and 30 Å, respectively.

	Front cell				Back cell								
Cell label	CuPc	CuPc:C_{60}	C_{60}	PTCBI	CuPc	CuPc:C_{60}	C_{60}	BCP	J_{SC} (mA/cm^2)	V_{OC} (V)	FF	η_P (%)	$\eta_{P,exp}$ (%)
A	100	180	20	50	20	130	250	75	9.4	1.03	0.54	5.2	5.4±0.3
B	75	125	80	50	60	130	160	75	9.7	1.03	0.59	5.9	5.7±0.3
C	90	110	0	50	50	100	210	100	10.3	1.04	0.61	6.5	5.0±0.3

[a]See Refs. 1, 11, and 13.

teristic of homogeneous materials, with the high exciton diffusion efficiency in mixed regions.[13] Thin layers of PTCBI and bathocuproine (BCP) are used as the exciton-blocking layer (EBL)[15] in the front (nearest the ITO) and back (nearest the cathode) subcells, respectively, thereby forming a high-efficiency double HJ PV structure.[15] The two subcells are connected in series by a charge recombination zone for electrons generated in the front cell and holes generated in the back cell. The recombination centers are Ag nanoclusters[8] (~5 Å average thickness) buried in a 50 Å thick 4, 4′, 4″-tris(3-methyl-phenyl-phenyl-amino)triphenylamine (m-MTDATA) p-doped[12] with 5 mol % tetrafluoro-tetracyanoquinodimethane. Device fabrication procedures and methods of characterization have been described elsewhere.[10]

The previously demonstrated CuPc/PTCBI tandem cell[8] has a symmetric spectral response from each of the two subcells. The optical interference between the incident light and that reflected from the metal cathode leads to a maximum optical intensity at a distance of $\lambda/4n$ from the organic/cathode interface, where λ is the incident light wavelength and n is the average refractive index of the intervening organic layers. Improved performance is therefore expected from an "asymmetric" tandem cell with a front cell having peak absorption tuned to the long-wavelength spectral region, and a back cell efficiently absorbing at shorter wavelengths. Considering that CuPc absorbs between λ=550 nm and 750 nm, and C_{60} between λ=350 nm and 550 nm, an asymmetric CuPc/C_{60} hybrid PM-HJ tandem cell structure is obtained when the front cell has a thicker homogeneous CuPc layer and a thinner C_{60} layer than the back cell. A tradeoff between the homogeneous and mixed layer thicknesses is also required to balance the photocurrent in the two subcells, considering the short exciton diffusion lengths in the homogeneous layers, and the low charge mobilities in the mixed layers.[13]

Optimization of the CuPc/C_{60} hybrid PM-HJ tandem cell efficiency begins by modeling the current density versus voltage (J–V) characteristics of subcell i (i=1, 2 denoting the front and back cell, respectively) following:[13]

$$J_i(V_i) = J_{d,i}(V_i) + J_{\mathrm{Ph},i}(V_i) = J_{s,i}\left\{\exp\left[\frac{q(V_i - J_i R_{s,i})}{n_i kT}\right] - 1\right\} + J^0_{\mathrm{ph},i}\eta_{CC,i}(V_i), \quad (1)$$

where $J_{d,i}$ and $J_{\mathrm{ph},i}$ are the dark and photocurrent densities, respectively, $J_{s,i}$ is the reverse-bias saturation current, n_i is the ideality factor, $R_{S,i}$ is the cell series resistance, q is the electron charge, k is Boltzmann's constant, and T is the temperature. Using a model that considers both optical interference and exciton diffusion,[1,16] we obtain the photocurrent density $J^0_{\mathrm{Ph},i}$ under an incident optical power density P_O, assuming all photogenerated charges are collected at the electrodes. This assumption does not hold for a cell with a mixed layer, where molecular intermixing leads to charge carrier mobilities that are significantly reduced from those in polycrystalline homogeneous regions,[13] thereby leading to recombination of photogenerated charges. The charge collection efficiency (defined as the fraction of charges collected at the electrodes) as a function of the applied voltage V and the mixed layer thickness d_m is[13]

$$\eta_{CC}(V) = \frac{L_c(V)}{d_m}\left\{1 - \exp\left[-\frac{d_m}{L_c(V)}\right]\right\}, \quad (2)$$

where $L_c(V)=L_{c0}(V_{bi}-V)/V$ is the charge collection length,[13] L_{c0} is a constant, and V_{bi} is the built-in potential. Given $J_i = J_i(V_i)$ (i=1,2) the J–V characteristics of the tandem cell are obtained from the requirement that $J=J_1=J_2$ and $V=V_1+V_2$, from which the PV cell performance parameters (V_{OC}, short-circuit current density J_{SC} fill factor FF, and η_P) are obtained.

Cell A (see Table I) has optimized mixed layer thicknesses leading to η_P=5.2% under 1 sun AM1.5G solar illumination. A full optimization of all photoactive layer thicknesses leads to a higher efficiency of η_P=5.9% (cell B). The PTCBI layer in the double HJ front cell may also contribute to the photocurrent when the front-cell homogeneous C_{60} layer is removed, as CuPc molecules in the mixed layer form an exciton dissociation interface with PTCBI. This leads to a higher J_{SC} and a maximum η_P=6.5% in the optimized cell C, as the PTCBI absorption[1] peak at λ=550 nm fills the gap between the absorption regions of CuPc and C_{60}.

Figure 1(b) shows the calculated optical field intensity profile in cell B. The intensity at λ=450 nm peaks at approximately 400 Å from the reflecting Ag cathode, or 300 Å closer than for λ=650 nm. Hence, making the front cell rich in longer-wavelength absorbing material(s) and the back cell rich in shorter-wavelength absorbing material(s) leads to increased absorption of the broad solar spectrum. In cell B, the back cell has a significantly thicker homogeneous C_{60} layer than the front cell, leading to a higher external quantum efficiency in the C_{60} absorption region (λ < 550 nm), as shown in Fig. 1(c). As the light intensity at $\lambda \approx 650$ nm is primarily located in the front cell, the quantum efficiency at 550 nm < λ < 750 nm is higher in the front cell although the

Downloaded 12 Jan 2008 to 141.213.8.105. Redistribution subject to AIP license or copyright; see http://apl.aip.org/apl/copyright.jsp

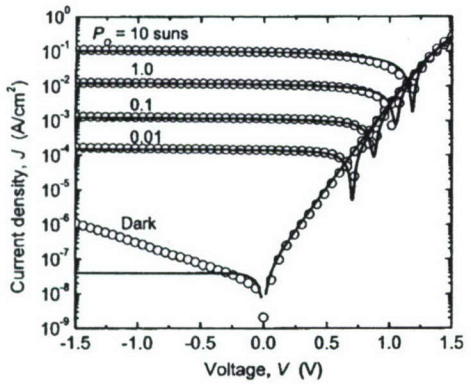

FIG. 2. *J–V* characteristics of the asymmetric organic tandem cell A, in the dark and under various intensities of simulated AM1.5G solar illumination. The open symbols are experimental data, whereas the solid lines are model calculations.

thicknesses of the homogeneous CuPc and the mixed layers are approximately the same in both subcells.

The experimental *J–V* characteristics of tandem cell A in the dark and under various intensities of simulated AM1.5G solar illumination are shown in Fig. 2 (open symbols). The open-circuit voltage is $V_{OC}=1.04$ *V* under 1 sun illumination, and approaches 1.2 V under 10 suns, approximately twice of that of a single CuPc/C_{60} hybrid PM-HJ cell.[13] The solid lines are calculated *J–V* characteristics, which agree with the experimental data except for the reverse-bias dark current, in which case generation–recombination or thermally assisted tunneling may significantly contribute to J_d.

The power conversion efficiency of tandem cell A, derived from the experimental *J–V* characteristics in Fig. 2, reaches a maximum of $\eta_P=(5.4\pm0.3)\%$ at $P_O=0.34$ suns, as shown in Fig. 3 (filled squares). Under higher intensity illumination, *FF* decreases (inset, Fig. 3) due to the relatively thick and resistive mixed layers. With thinner mixed layers, tandem cell B (open circles) exhibits $FF=0.56$ even at 11 suns. This leads to $\eta_P=(5.7\pm0.3)\%$ at $P_O\geqslant 1$ sun, in agreement with the model (see Table I). However, tandem cell C (filled triangles) has a lower efficiency than the model prediction (6.5%), mainly due to a low $FF\approx 0.51$. This suggests that a small energy barrier at the C_{60}/PTCBI interface impedes electron transport toward the charge recombination zone. Nevertheless, the efficiencies of tandem cells A and B are higher than 5% for the single CuPc/C_{60} hybrid PM-HJ cell (open inverted triangles in Fig. 3),[13] demonstrating the effectiveness of stacking cells.

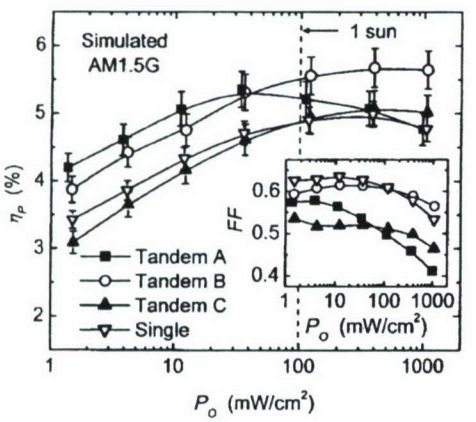

FIG. 3. Illumination intensity (P_O) dependence of the power conversion efficiencies (η_P) of asymmetric organic tandem cells (A, filled squares; B, open circles; C, filled triangles) under simulated AM1.5G solar illumination, compared with that of the single element CuPc/C_{60} hybrid PM-HJ cell (open inverted triangles). Inset: The fill factor (*FF*) of the tandem and single hybrid PM-HJ cells (see Ref. 13).

In conclusion, we demonstrate that the power conversion efficiency of a tandem organic PV cell with hybrid PM-HJs has the potential for reaching that of *a*-Si cells, currently in production at 4% to 6%.[17] By applying antireflection coatings to the glass substrates, an additional 10% improvement to efficiencies are possible, suggesting that the tandem cell structure can attain efficiencies in excess of 7%. However, the ultimate advantage of the asymmetric tandem cell structure lies in the ability to incorporate different D–A material combinations in the individual subcells to cover a broader solar spectral region than the current CuPc/C_{60} system. Indeed, full solar spectral coverage may be optimally achieved employing a three-subcell device, with two subcells absorbing across the blue to red, and a third primarily absorbing in the near infrared following the design principles outlined here. Provided that high production yields and long operational lifetimes are possible in properly packaged organic solar cell modules, the asymmetric hybrid PM-HJ tandem cell has considerable potential for use in generating inexpensive, abundant electrical power from the clean and renewable energy generated by the sun.

The authors acknowledge the support of National Renewable Energy Laboratory, Air Force Office of Scientific Research, and Global Photonic Energy Corporation.

[1]P. Peumans, A. Yakimov, and S. R. Forrest, J. Appl. Phys. **93**, 3693 (2003).
[2]C. J. Brabec, N. S. Sariciftci, and J. C. Hummelen, Adv. Funct. Mater. **11**, 15 (2001).
[3]C. W. Tang, Appl. Phys. Lett. **48**, 183 (1986).
[4]J. J. M. Halls, C. A. Walsh, N. C. Greenham, E. A. Marseglia, R. H. Friend, S. C. Moratti, and A. B. Holmes, Nature (London) **376**, 498 (1995).
[5]G. Yu, J. Gao, J. C. Hummelen, F. Wudl, and A. J. Heeger, Science **270**, 1789 (1995).
[6]P. Peumans and S. R. Forrest, Appl. Phys. Lett. **79**, 126 (2001).
[7]S. E. Shaheen, C. J. Brabec, N. S. Sariciftci, F. Padinger, T. Fromherz, and J. C. Hummelen, Appl. Phys. Lett. **78**, 841 (2001).
[8]A. Yakimov and S. R. Forrest, Appl. Phys. Lett. **80**, 1667 (2002).
[9]F. Padinger, R. S. Rittberger, and N. S. Sariciftci, Adv. Funct. Mater. **13**, 85 (2003).
[10]J. Xue, S. Uchida, B. P. Rand, and S. R. Forrest, Appl. Phys. Lett. **84**, 3013 (2004).
[11]S. Uchida, J. Xue, B. P. Rand, and S. R. Forrest, Appl. Phys. Lett. **84**, 4218 (2004).
[12]B. Maenning, J. Drechsel, D. Gebeyehu, P. Simon, F. Kozlowski, A. Werner, F. Li, S. Grundmann, S. Sonntag, M. Koch, K. Leo, M. Pfeiffer, H. Hoppe, D. Meissner, N. S. Sariciftci, I. Riedel, V. Dyakonov, and J. Parisi, Appl. Phys. A: Mater. Sci. Process. **79**, 1 (2004).
[13]J. Xue, B. P. Rand, S. Uchida, and S. R. Forrest, Adv. Mater. (in press).
[14]M. Hiramoto, M. Suezaki, and M. Yokoyama, Chem. Lett. **1990**, 327 (1990).
[15]P. Peumans, V. Bulovic, and S. R. Forrest, Appl. Phys. Lett. **76**, 2650 (2000).
[16]L. A. A. Pettersson, L. S. Roman, and O. Inganäs, J. Appl. Phys. **86**, 487 (1999).
[17]A. V. Shah, H. Schade, M. Vanecek, J. Meier, E. Vallat-Sauvain, N. Wyrsch, U. Kroll, C. Droz, and J. Bailat, Prog. Photovoltaics **12**, 113 (2004).

Downloaded 12 Jan 2008 to 141.213.8.105. Redistribution subject to AIP license or copyright; see http://apl.aip.org/apl/copyright.jsp

Controlled growth of a molecular bulk heterojunction photovoltaic cell

FAN YANG[1], MAX SHTEIN[2] AND STEPHEN R. FORREST[1]*

[1]Department of Electrical Engineering, [2]Department of Chemical Engineering, Princeton Institute for the Science and Technology of Materials (PRISM),Princeton University, Princeton, New Jersey 08544, USA

*e-mail: forrest@princeton.edu

Published online: xx xxxx xxxx; doi:10.1038/nmat1285

The power conversion efficiency of organic photovoltaic cells has increased with the introduction of the donor–acceptor heterojunction that serves to dissociate strongly bound photogenerated excitons[1]. Further efficiency increases have been achieved in both polymer[2,3] and small-molecular-mass[4] organic photovoltaic cells through the use of the bulk heterojunction (BHJ), where the distance an exciton must diffuse from its generation to its dissociation site is reduced in an interpenetrating network of the donor and acceptor materials. However, the random distribution of donor and acceptor materials in such structures can lead to charge trapping at bottlenecks and cul-de-sacs in the conducting pathways to the electrodes. Here, we present a method for growing crystalline organic films into a controlled bulk heterojunction; that is, the positions and orientations of donor and acceptor materials are determined during growth by organic vapour-phase deposition (OVPD[5]), eliminating contorted and resistive conducting pathways while maximizing the interface area. This results in a substantial increase in power conversion efficiency compared with the best values obtained by 'random' small-molecular-weight BHJ solar cells formed by high-temperature annealing, or planar double heterojunction photovoltaic cells using the same archetypal materials systems.

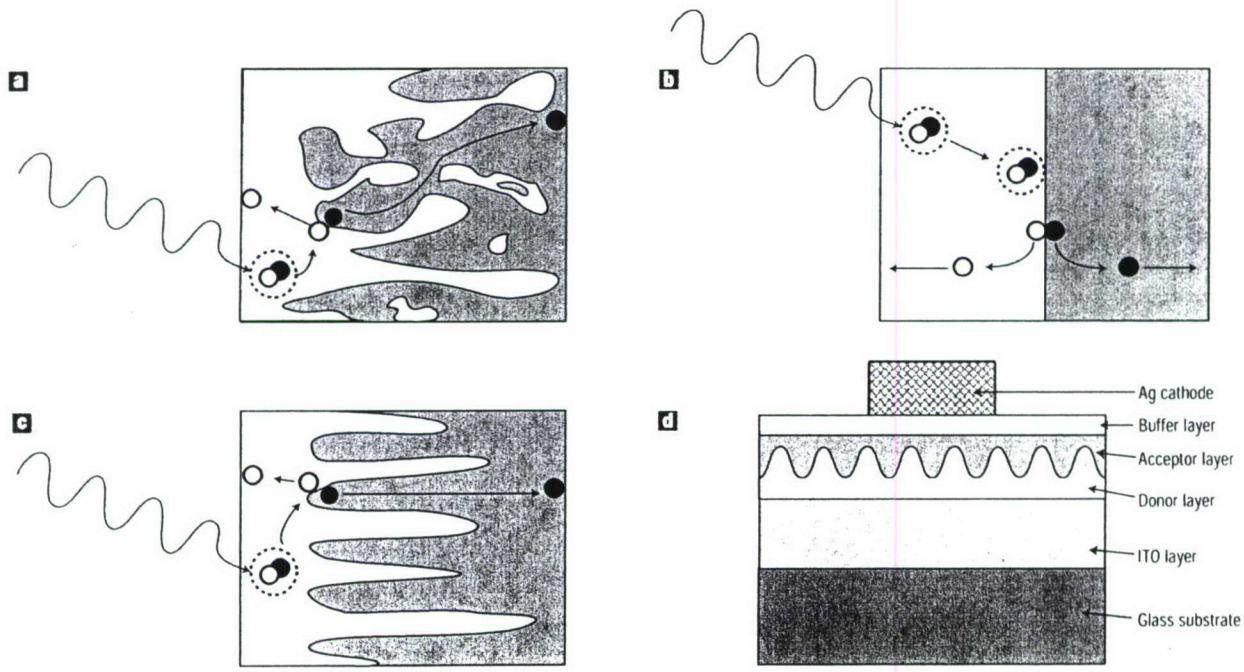

Figure 1 Schematic diagram of the types of organic donor–acceptor heterojunctions and the structure of the controlled bulk heterojunction (BHJ) device. **a**, Thermodynamically driven BHJ formed by phase segregation. The carrier-conducting pathways contain bottlenecks and cul-de-sacs. **b**, Planar heterojunction. **c**, BHJ with a large donor–acceptor interface area and continuous carrier-conducting pathways to the opposing electrodes formed by controlled growth. **d**, Schematic diagram of a controlled BHJ photovoltaic device structure grown on top of indium tin oxide (ITO)-coated glass. The donor material is CuPc and the acceptor is PTCBI. The buffer layer is BCP. Electrons are indicated by closed circles, holes by open circles, and excitons by pairs enclosed in dashed circles.

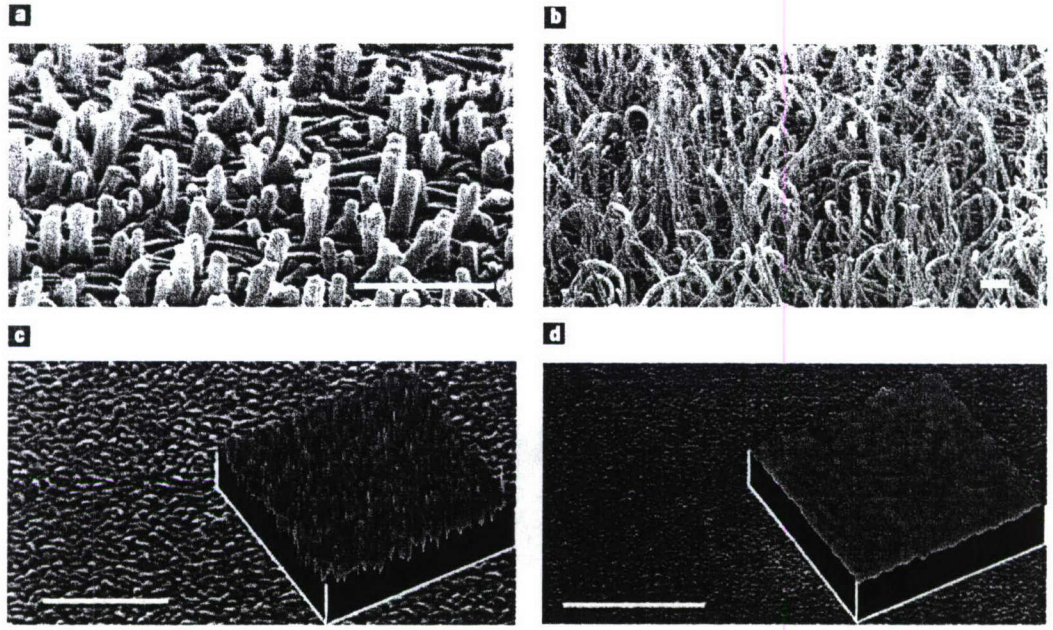

Figure 2 SEM and atomic force microscope (AFM) images of CuPc films. a, Surface of a CuPc film with a continuous wetting layer plus short needle-like crystals grown on a silicon wafer surface by organic vapour phase deposition (OVPD). During a 10-min growth duration, the source evaporation temperature and substrate temperature are fixed at (440 ± 5) °C and (100 ± 5) °C, respectively. The nitrogen carrier gas flow rate is (30.0 ± 0.1) s.c.c.m., and the chamber pressure is (0.45 ± 0.01) torr. **b**, Surface of a CuPc film grown on ITO-coated glass substrate under the same growth conditions as the film in **a**. **c**, Surface of CuPc film grown on top of ITO-coated glass by OVPD. This structure containing a very high density of the protrusions is suitable as the bottom layer of a bulk heterojunction. The source evaporation and substrate temperatures are fixed at (425 ± 5) °C and (100 ± 5) °C, respectively. The nitrogen carrier-gas flow rate increases linearly from 14 s.c.c.m. to 200 s.c.c.m. during the 6.5-min growth duration, and chamber pressure rises from 0.18 torr to 0.70 torr. Inset: AFM image of the same sample. The average peak-to-valley height is 35 nm. **d**, Surface of a 500-Å-thick CuPc film deposited on ITO glass by VTE. Inset: AFM image of the sample with an average peak-to-valley height of 3 nm. Scale bars: all 500 nm.

Bulk heterojunction devices are characterized by an interpenetrating network of donor and acceptor materials, providing a large interface area where photoinduced charge transfer by excitons into separated electrons and holes can efficiently occur (Fig. 1a). In this case, excitons are always generated within a diffusion length (~3–10 nm) of a donor–acceptor interface, potentially leading to a higher cell efficiency than a planar heterojunction (Fig. 1b). Two methods have been reported to make BHJs in organic photovoltaic cells: phase separation during spin-coating of polymers[2,3], and phase segregation from a donor–acceptor mixture induced by high-temperature annealing of small-molecular-weight organic layers[4]. Both of these 'thermodynamically driven' methods have resulted in increased power conversion efficiencies (η_P). For example, in photovoltaic cells based on copper phthalocyanine (CuPc) as the donor and 3,4,9,10-perylenetetracarboxylic bis-benzimidazole (PTCBI) as the acceptor, η_P increases from 1% in a planar heterojunction[1] to 1.4% in devices with a BHJ formed by annealing-induced phase segregation of a homogeneous mixture phase of the two materials[4]. Because of space charge effects in the confines of the BHJ structure, the fill factor (FF) is usually lower than for a planar heterojunction under standard 1-sun illumination (100 mW cm^{-2}) conditions[2,4]. Hence, although the high surface-area characteristic of the BHJ is desirable, the disordered structure is ultimately limited by a high series resistance. In this work, we show that OVPD can be used in the controlled growth of an ordered BHJ (Fig. 1c), largely free of the conductive bottlenecks and cul-de-sacs that are characteristic of thermodynamically driven systems where the interdigitation between the donor and acceptor layers is randomly structured owing to the entropy of the interface formation process.

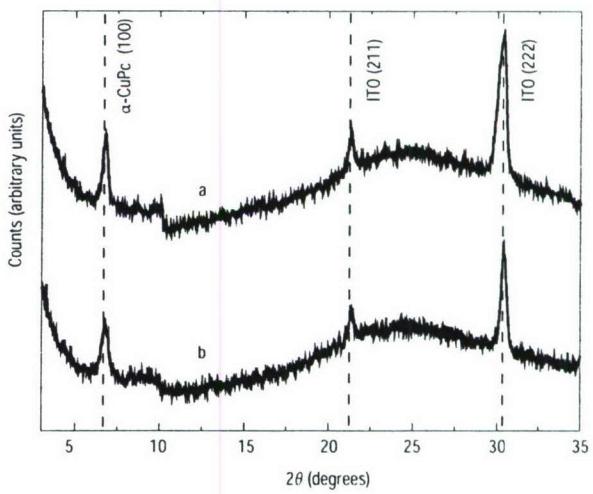

Figure 3 Bragg–Brentano X-ray diffractograms of CuPc films grown on ITO using the Cu-Kα line. a, Diffraction from a CuPc film with a highly folded surface as shown in Fig. 2c. The average film thickness is ~450 Å. **b**, Diffraction from a 500-Å-thick, planar CuPc film grown by VTE, as shown in Fig. 2d. CuPc and ITO crystal indices are noted.

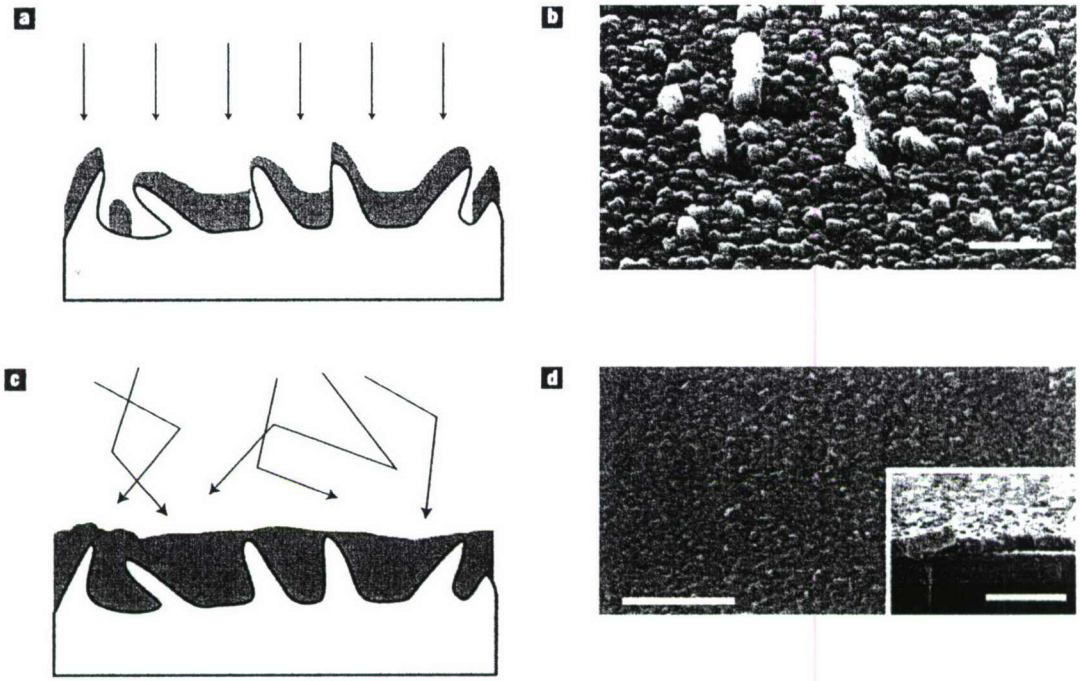

Figure 4 Morphology of films grown on top of a highly folded underlying CuPc layer by VTE and OVPD. a, Schematic diagram of the conformal surface and shadowing effects resulting from the ballistic trajectories followed by the incident molecules in VTE. **b**, SEM image of the surface of a PTCBI/BCP/Ag film grown by VTE on top of CuPc needle arrays. Voids form at the bases of the protruding needles because of shadowing. Note the striations clearly apparent on the sides of the needles, suggesting their crystalline nature. **c**, Schematic diagram of the planar surface and gap-filling characteristic of the top film grown by OVPD that results from increased surface diffusion and random arrival directions of molecules. **d**, SEM images of the planarized surface of a PTCBI layer (500 ± 25) Å thick grown on top of CuPc needles, shown in Fig. 2c. Inset: cross-section of the completed photovoltaic device. From bottom to top, the layers are: glass, ITO (thickness: ~1,500 Å); CuPc/PTCBI/BCP (100 Å); Ag (1,000 Å). Scale bars: all 500 nm.

A schematic of the controlled bulk heterojunction photovoltaic cell is shown in Fig. 1d. The cell is grown on a pre-cleaned, glass substrate coated with 15 Ω/sq.**[Author: Please clarify, is this 'per square of'?]** indium tin oxide (ITO), followed by the donor (CuPc) and acceptor (PTCBI) layers, an exciton blocking and electron-conducting layer of bathocuproine (BCP), and finally an Ag cathode. The use of the exciton blocking layer forms a second heterojunction that significantly increases efficiency in thin photovoltaic cells[6]. To form the BHJ, the top surface of the donor layer needs to be highly folded, whereas the acceptor layer should fill the gaps and recesses of the underlying, rough donor film. In addition, the top surface of the acceptor layer should be flat to prevent the formation of shorts or pinholes between the opposing electrodes.

Organic thin-film crystal size and morphology is controllable in OVPD by adjusting the substrate temperature, carrier-gas flow rate and chamber pressure[5,7]. Hence, this technique can prove useful when applied to the growth of both the planar and highly folded layers, as required in a BHJ solar cell. Furthermore, as will be discussed below, a unique and critical feature of OVPD compared with vacuum thermal evaporation (VTE) is the large molecular surface diffusivity and the non-ballistic trajectories followed by the molecules in their arrival at the substrate surface[8]. Hence, OVPD growth is particularly effective in generating planar layers that fill preexisting voids and other surface non-uniformities on the substrate.

In our devices, CuPc and PTCBI are deposited in a quartz reactor that is similar to the glass reactor previously described for the growth of organic thin-film transistors and light emitting devices[7,9]. In contrast to those earlier device demonstrations, however, materials used in photovoltaic cells have considerably higher evaporation temperatures (~450 °C versus ~250 °C for pentacene transistors, for example), requiring modification of the deposition system to prevent material re-evaporation after physisorption on the substrate. With the source evaporation temperature at (440 ± 5) °C, a substrate temperature at (100 ± 5) °C, a nitrogen carrier-gas flow rate of (30.0 ± 0.1) standard cubic centimetres per minute (sccm), and a chamber pressure of (0.45 ± 0.01) torr, a 10-min OVPD strained-layer deposition of CuPc onto a silicon substrate results in a Stranski-Krastonov island-plus-layer growth mode[10], generating the combination of a thin but continuous wetting layer plus short needles, as shown by the scanning electron microscope (SEM) image in Fig. 2a.

Under the same growth conditions, crystalline CuPc needles as long as a few micrometres are grown on ITO-coated glass (Fig. 2b), apparently because of the larger strain between the film and the ITO crystallites, in contrast to the relatively low strain introduced by the thin amorphous oxide layer on the silicon wafer surface. In this case, however, the needle length is ~100 times that required in an efficient photovoltaic cell (about 50 nm).

For high-efficiency charge transfer, the donor–acceptor interface should lie within a diffusion length (~10–50 nm for CuPc) of the exciton generation site. Because a colder substrate favours a higher nucleation density, the substrate temperature is reduced to (16 ± 2) °C, whereas the source material temperature is (425 ± 5) °C. Furthermore, the N_2 flow rate is increased linearly from 14 sccm to

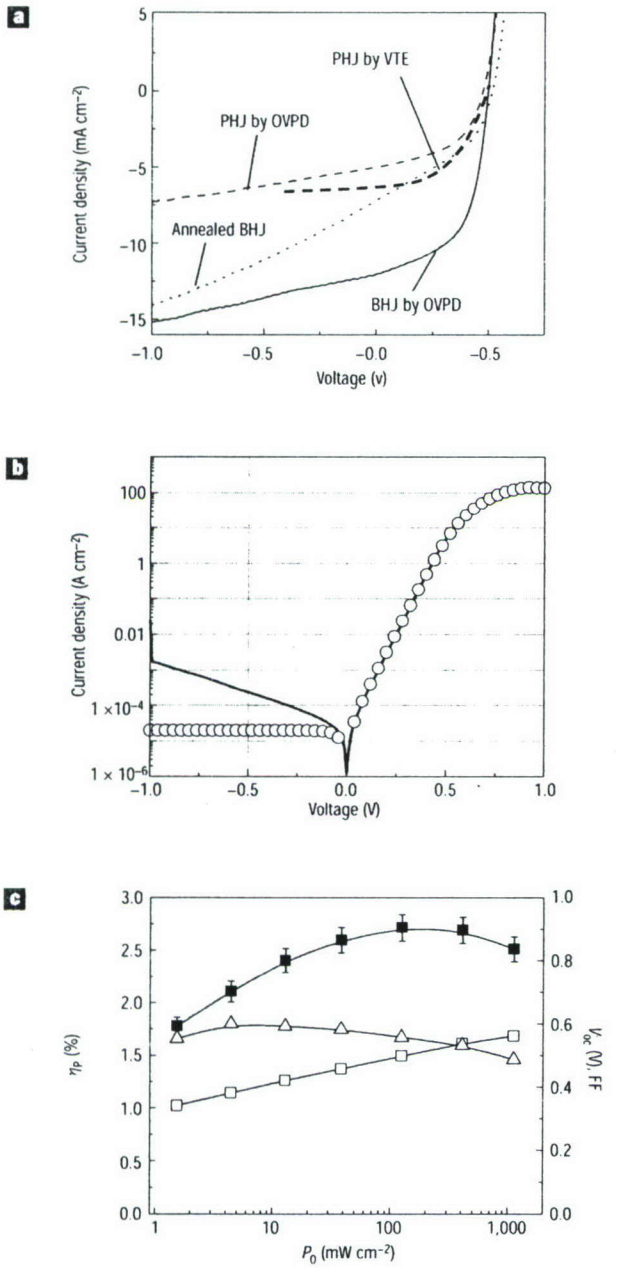

Figure 5 Performance of an OVPD-grown, controlled CuPc/ PTCBI BHJ photovoltaic cell. a, Typical current–voltage characteristics of the BHJ device in comparison with a planar heterojunction (PHJ) produced by OVPD, PHJ by VTE, and BHJ by annealing[4] at incident power level of 1 sun using AM1.5G simulated solar irradiation. The open-circuit voltages are similar for all CuPc/PTCBI cells, and the maximum photocurrent density is achieved in the BHJ device by OVPD. The comparison of device characteristics is listed in Table 1. **b**, Fit of the dark *J–V* characteristics of the OVPD BHJ device, where the solid line is the experimental data, and the circles are a fit according to the modified ideal diode equation. Under reverse bias, the dark current is higher than predicted by this simple analysis owing to the presence of current sources other than diffusion (for example, generation–recombination and shunt currents may also be present). **c**, The power conversion efficiency, η_P (closed squares), open-circuit voltage, V_{OC} (open squares), and fill factor, FF (triangles), as functions of the incident optical power intensity P_0 for the OVPD-grown, controlled CuPc/PTCBI BHJ photovoltaic device. A maximum power efficiency at 1 sun (100 mW cm^{-2}) intensity of $\eta_P = (2.7 \pm 0.1)\%$ is obtained, a value significantly higher than is achieved for planar or 'random' BHJ structures previously reported for this archetypal materials system for photovoltaic cells.

200 sccm during the 6.5-min growth duration, resulting in a rise in chamber pressure from 0.18 to 0.70 torr. In this case, the densely distributed short needles have an average diameter of 30 nm and peak-to-valley height of 35 nm, corresponding to 70% of the mean thickness of the CuPc film (Fig. 2c). In contrast, the average peak-to-valley height of a vacuum-deposited CuPc film of the same thickness is only 3 nm (Fig. 2d).

The X-ray diffraction spectrum of the OVPD CuPc film is shown in Fig. 3a, and is similar to that of a 500-Å-thick CuPc film grown by vacuum thermal evaporation (Fig. 3b). The diffraction peak at $2\theta = 6.7°$ confirms the existence of the α-CuPc phase. The domain size is calculated to be (20 ± 5) nm from the full width at half maximum of the diffraction peak[11], from which we infer that each small protrusion in Fig. 2c is a single CuPc microcrystalline domain. Because the charge mobility is higher in crystalline than in amorphous materials[12,13], the existence of crystalline structures is important for ensuring a low cell series resistance.

Growth of CuPc is followed by that of a PTCBI layer (500 ± 25) Å thick without exposing the interface to atmosphere. To ensure a flat surface, the source material is heated to (462 ± 3) °C, while the substrate is maintained at (16 ± 5) °C. The N_2 flow rate is fixed at (150 ± 1) sccm for 10.4 min, resulting in a chamber pressure of (0.58 ± 0.01) torr. A 100-Å-thick BCP exciton-blocking and electron-conducting layer and a 1,000-Å-thick silver circular cathode contact (1 mm^2) deposited through a shadow mask are grown by conventional vacuum thermal evaporation to complete the photovoltaic cell.

In VTE, the deposited film typically has a morphology that conforms to the underlying surface, resulting in some shadowed areas (see Fig. 4a), owing to the long mean free paths and ballistic trajectories followed by the incident molecules. Hence, the PTCBI surface follows that of the CuPc protrusions, also resulting in a second, highly folded top surface. In that case, voids will develop where the protrusions shadow the underlying surface of the film from the PTCBI source cell (Fig. 4b). Although these problems can be reduced (but not eliminated) by using substrate rotation, this can increase the processing cost and also prohibit adaptation for continuous roll processing, which is more easily accomplished by the conformal character of OVPD. The diagonal striations on the edges of the needles give a further suggestion of their crystalline nature. In contrast, in OVPD growth, surface diffusion coupled to the random arrival directions as the molecules traverse the boundary layer at the substrate surface[8] results in a flattened top film surface with complete filling of the spaces beneath the needles in the underlying CuPc, as shown in Fig. 4c and d.

For comparison to the bulk heterojunction photovoltaic cell, we also grew a planar heterojunction ITO/450 Å CuPc/500 Å PTCBI/100 Å BCP/1,000 Å Ag. The planar CuPc layer was deposited for 3 min with a source temperature of (445 ± 3) °C, a substrate temperature of (3 ± 5) °C, and a N_2 flow rate of (100 ± 1) sccm. The PTCBI is deposited under the same conditions as used for the BHJ device.

The current density–voltage characteristics of the BHJ and other double heterojunction CuPc/PTCBI photovoltaic cells are combined in Fig. 5a, whose performances are compared in Table 1. The short-circuit current density (J_{SC}) for the controlled BHJ is about twice that obtained for a vacuum-deposited[6] or OVPD-grown planar heterojunction photovoltaic cell. Furthermore it is about 20% higher than for a previously reported 'thermodynamically driven' BHJ demonstrated by annealing a mixed CuPc/PTCBI layer[4]. More significantly, the dependence of the photocurrent on reverse bias of the grown BHJ is considerably reduced from that observed for the annealed device. We fitted the dark-current density characteristics using the ideal diode equation including series resistance that has been previously shown to apply to molecular organic photovoltaic

Table 1 Comparison of performance of several ITO/CuPc/PTCBI/BCP/Ag photovoltaic cell structures*

	J_s (mA cm^{-2})	V_{oc} (V)	FF	η_p (%)	R_{SA} (Ω cm^2)	Ref.
Planar VTE heterojunction	6	0.49	0.49	1.1 ± 0.1	30 ± 10	6
Annealed bulk heterojunction	9	0.50	0.40	1.4 ± 0.1	60 ± 10	4
Planar OVPD heterojunction	5	0.48	0.47	1.1 ± 0.1	18.2 ± 0.5	This work
Controlled bulk OVPD heterojunction	11	0.49	0.58	2.7 ± 0.1	2.2 ± 0.1	This work

Here, J_s is the short-circuit current density, V_{oc} is the open-circuit voltage, FF is the fill factor, η_p is the external power efficiency and R_{SA} is the specific series resistance.

*The illumination intensity is 1 sun (100 mW cm^{-2}) simulated AM1.5G for all four devices.

devices[6,14,15]. From Fig. 5b, showing the fit (circles) to the data (solid line), we infer a specific series resistance of $R_{SA} = (2.2 \pm 0.1)\ \Omega\ cm^2$, which is smaller than the value obtained from a random BHJ device[4] where $R_{SA} = (60 \pm 10)\ \Omega\ cm^2$. This suggests that series resistance due to the amorphous growth, or to bottlenecks to carrier collection has been reduced in the OVPD-grown BHJ cell.

The dependence of the performance characteristics under illumination is shown in Fig. 5c. For control, we obtain a 1% power-conversion efficiency for a conventional CuPc/PTCBI bilayer cell[1] under AM1.5G illumination using a calibrated solar simulator[6], which is consistent with efficiencies reported elsewhere[16,17]. In the case of the BHJ cell, using 1-sun-intensity, AM1.5G simulated radiation, we obtain an open-circuit voltage of $V_{OC} = (0.50 \pm 0.03)$ V at 1 sun intensity (100 mW cm^{-2}), characteristic of the CuPc/PTCBI heterojunction system. The fill factor of the OVPD-grown, controlled BHJ device is FF > 0.5 for illumination over the range of 0.01–10 suns (1–1000 mW cm^{-2}). The combination of high photocurrent density and fill factor results in a high external power conversion efficiency (η_P), with a maximum of $\eta_P = (2.7 \pm 0.1)\%$ at 100 mW cm^{-2}. Referring to Table 1, η_P is about 2.5 times as high as was achieved using a comparable planar heterojunction photovoltaic cell, and 1.9 times as high as an annealed, thermodynamically driven BHJ, suggesting that the controlled growth of the CuPc/PTCBI BHJ results in the desired increase in junction surface area without introducing an increased cell series resistance. Because the CuPc crystal sizes deduced from X-ray diffraction are the same (~20 nm) for the OVPD-grown BHJ and the previously reported annealed BHJ[1], we infer that the increase in efficiency is mainly due to the larger carrier-transport efficiency in a highly ordered bulk heterointerface. In addition, we have observed that the power efficiency of an OVPD-grown CuPc/C_{60} BHJ device is the same as a VTE-grown CuPc/C_{60} mixed layer heterojunction[18], from which we can also infer that the large interface area plays a significant role.

This work opens several new avenues for controlling the thin-film morphology of organic heterojunction devices, and has already resulted in a striking increase in efficiency for an organic BHJ solar cell. We expect that further understanding and control of the unique growth properties characteristic of OVPD will produce further improvements in the performance of organic photovoltaic and other optoelectronic devices.

Received 16 July 2004; accepted 18 October 2004; published xx xxxx 2004.

References

1. Tang, C. W. Two-layer organic photovoltaic cell. *Appl. Phys. Lett.* **48**, 183–185 (1986).
2. Yu, G., Gao, J., Hummelen, J. C., Wudl, F. & Heeger, A. J. Polymer photovoltaic cells: enhanced efficiencies via a network of internal donor-acceptor heterojunctions. *Science* **270**, 1789–1791 (1995).
3. Halls, J. J. M. *et al.* Efficient photodiodes from interpenetrating polymer networks. *Nature* **376**, 498–500 (1995).
4. Peumans, P., Uchida, S. & Forrest, S. R. Efficient bulk heterojunction photovoltaic cells using small-molecular-weight organic thin films. *Nature* **425**, 158–162 (2003).
5. Baldo, M. *et al.* Organic vapor phase deposition. *Adv. Mater.* **10**, 1505–1514 (1998).
6. Peumans, P., Bulović, V. & Forrest, S. R. Efficient photon harvesting at high optical intensities in ultrathin organic double-heterostructure photovoltaic diodes. *Appl. Phys. Lett.* **76**, 2650–2652 (2000).
7. Shtein, M., Mapel, J., Benziger, J. B. & Forrest, S. R. Effects of film morphology and gate dielectric surface preparation on the electrical characteristics of organic-vapor-phase-deposited pentacene thin-film transistors. *Appl. Phys. Lett.* **81**, 268–270 (2002).
8. Shtein, M., Peumans, P., Benziger, J. B. & Forrest, S. R. Micropatterning of small molecular weight organic semiconductor thin films using organic vapor phase deposition. *J. Appl. Phys.* **93**, 4005–4016 (2003).
9. Shtein, M., Gossenberger, H. F., Benziger, J. B. & Forrest, S. R. Material transport regimes and mechanisms for growth of molecular organic thin films using low-pressure organic vapor phase deposition. *J. Appl. Phys.* **89**, 1470–1476 (2001).
10. Venables, J. A., Spiller, G. D. T. & Hanbucken, M. Nucleation and growth of thin films. *Rep. Prog. Phys.* **47**, 399–459 (1984).
11. Klug, H. P. & Alexander, L. E. *X-ray Diffraction Procedures* (Wiley, New York, 1974).
12. Forrest, S. R. Ultrathin organic films grown by organic molecular beam deposition and related techniques. *Chem. Rev.* **97**, 1793–1896 (1997).
13. Makinen, A. J., Melnyk, A. R., Schoemann, S., Headrick, R. L. & Gao, Y. Effect of crystalline domain size on the photophysical properties of thin organic molecular films. *Phys. Rev. B* **60**, 14683–14687 (1999).
14. Xue, J., Uchida, S., Rand, B. P. & Forrest, S. 4.2% efficient organic photovoltaic cells with low series resistances. *Appl. Phys. Lett.* **84**, 3013–3015 (2004).
15. Hoppe, H. & Sariciftci, N. S. Organic solar cells: an overview. *J. Mater. Res.* **19**, 1924–1945 (2004).
16. Rostalski, J. & Meissner, D. Photocurrent spectroscopy for the investigation of charge carrier generation and transport mechanisms in organic p/n-junction solar cells. *Solar Energy Mater. Solar Cells* **63**, 37–47 (2000).
17. Sharma, G. D. & Saxena, D. Characterization of ITO/ZnPc/CHR/In p-n junction photovoltaic device using *J-V*, *C-V* and photoaction measurements. *J. Mater. Sci.* **10**, 539–544 (1999).
18. Uchida, S., Xue, J., Rand, B. P. & Forrest, S. Organic small molecule solar cells with a homogeneously mixed copper phthalocyanine: C_{60} active layer. *Appl. Phys. Lett.* **84**, 4218–4220 (2004).

Acknowledgements

We thank J. Xue, S. Uchida, R. Holmes, B. Rand and P. Peumans for discussions. We also thank the US Air Force Office of Scientific Research, the National Renewable Energy Laboratory and Global Photonic Energy Corporation for financial support.

Correspondence and requests for materials should be addressed to S.R.F.

Competing financial interests

The authors declare that they have no competing financial interests.

Experimental

The foaming solutions were prepared by mixing a cationic surfactant (tetradecyltrimethylamonium bromide, TTAB) or an anionic surfactant (sodium dodecylsulfate, SDS), with water, titanium ethoxide, and HCl. Typically, titanium ethoxide was added to an aqueous solution of TTAB (35 wt.-%) or SDS (15 wt.-%) in order to reach a proportion of 10 wt.-%. Then, the pH of the solution was adjusted to pH = 1 by adding HCl (37 %). The mixture was subjected to strong stirring for 30 min to homogenize the solution and to evaporate ethanol produced by the hydrolysis of titanium alkoxide. A particulate sol could be obtained by aging for 20 h. Foam was obtained by bubbling nitrogen through a porous glass disk into perfluorohexane in a 2.5 cm-diameter, 60 cm-high Plexiglas column. Different porosity glass disks (100–160 μm, 40–100 μm, 16–40 μm, or 10–16 μm) could be used to introduce nitrogen into the foaming solution. The reaction took place inside the Plexiglas column. During the reaction, the foam was wetted from above with the foaming solution. Imposing a sol flux Q at the top of the foam allowed the imposition of a constant and homogeneous liquid fraction to the entire sample. Varying the sol flux Q at the top of the foam varied the liquid fraction, and thus tuned the morphology of the foam. Metastable foams were recovered at the top of the column with a spatula and stored in a beaker. Then, the foam was immediately treated with an aqueous ammonia solution (20 wt.-%) with a pipette in order to promote titanium dioxide condensation. The quantity of ammonia used during the process depended upon the foam-liquid fraction. Typically, we used 0.5 mL of ammonia solution for 100 mL of foam and a sol flux of 0.024 $g\,s^{-1}$, so the ratio was 2 mL/100 mL for a sol flux of 0.160 $g\,s^{-1}$. The final foams were then frozen overnight and lyophilized for 5 h. The resulting hybrid organic–inorganic monolith-type materials were then thermally treated at 500 °C in order to obtain the anatase structure of TiO_2, or at 900 °C to obtain the rutile structure. The heating rate was 2 °C min^{-1}, with a first Plateau at 200 °C for 2 h. The cooling process was uncontrolled and depended upon oven cooling. The final inorganic scaffolds were then analyzed.

Transmission electron microscopy (TEM) experiments were performed with a Jeol 2000 FX microscope (acceleration voltage of 200 kV). The samples were prepared as follows: TiO_2 scaffolds in a powder state were deposited on a copper grid coated with a Formvar/carbon membrane. Scanning electron microscopy (SEM) observations were performed with a Jeol JSM-840A SEM operating at 10 kV. The specimens were gold-coated or carbon-coated prior to examination. Mesoscale surface areas and pore characteristics were obtained with a Micromeritics ASAP 2010 instrument, employing the Brunauer–Emmett–Teller (BET) method. Prior to performing the nitrogen adsorption–desorption measurements, the macrocellular-foam monoliths were reduced to a powder state. Small-angle X-ray experiments were carried on with an 18 kW rotating-anode X-ray source (Rigaku-200) using a Ge (111) crystal as the monochromator. The scattered radiation was collected on a two-dimensional detector (Imaging Plate system from Mar Research, Hamburg). The sample–detector distance was 500 mm.

Received: July 6, 2004
Final version: October 11, 2004

[1] a) C. T. Kresge, M. E. Leonowicz, W. J. Roth, J. C. Vartuli, J. S. Beck, *Nature* **1992**, *359*, 710. b) J. S. Beck, J. C. Vartuli, W. J. Roth, M. E. Leonowicz, C. T. Kresge, K. D. Schmitt, C. T.-W. Chu, D. H. Olson, E. W. Sheppard, S. B. McCullen, J. B. Higgins, J. L. Schlenker, *J. Am. Chem. Soc.* **1992**, *114*, 10834.

[2] a) S. Mann, *Nature* **1988**, *332*, 119. b) D. D. Archibald, S. Mann, *Nature* **1993**, *364*, 430. c) P. Feng, X. Bu, G. D. Stucky, D. J. Pine, *J. Am. Chem. Soc.* **2000**, *5*, 994. d) H. Yang, A. Kuperman, N. Coombs, S. Mamiche-Afara, G. A. Ozin, *Nature* **1996**, *379*, 703.

[3] a) A. Imhof, D. J. Pine, *Nature* **1997**, *389*, 948. b) S. Schacht, Q. Huo, I. G. Voigt-Martin, G. D. Stucky, F. Schüth, *Science* **1996**, *273*, 768. c) F. Carn, A. Colin, M.-F. Achard, E. Sellier, M. Birot, H. Deleuze, R. Backov, *J. Mater. Chem.* **2004**, *14*, 1370.

[4] G. Fornasieri, S. Badaire, R. Backov, O. Mondain-Monval, C. Zakri, P. Poulin, *Adv. Mater.* **2004**, *16*, 1094.

[5] J. H. Jung, Y. Yoshiyuki, S. Shinkai, *Angew. Chem. Int. Ed.* **2000**, *39*, 1862.

[6] S. R. Hall, H. Bolger, S. Mann, *Chem. Commun.* **2003**, 2784.

[7] D. Wang, R. A. Caruso, F. Caruso, *Chem. Mater.* **2001**, *13*, 364.

[8] a) S. M. Yang, I. Sokolov, N. Coombs, C. T. Kresge, G. A. Ozin, *Adv. Mater.* **1999**, *11*, 1427. b) G. A. Ozin, *Chem. Commun.* **2000**, 419. c) S. Mann, G. A. Ozin, *Nature* **1996**, *382*, 313.

[9] F. Carn, A. Colin, M.-F. Achard, H. Deleuze, R. Backov, *Adv. Mater.* **2004**, *16*, 140.

[10] a) A. Fujishima, K. Hashimoto, T. Watanabe, *TiO_2 Photocatalysis: Fundamentals and Applications*, BKC, Tokyo, Japan **1999**. b) M. Alfonso, D. Bahnemann, A. E. Cassano, R. Dilert, R. Goslich, *Catal. Today* **2000**, *58*, 199.

[11] E. L. Crepaldi, G. J. A. A. Soler-Illia, D. Grosso, F. Cagnol, F. Ribot, C. Sanchez, *J. Am. Chem. Soc.* **2003**, *125*, 9770.

[12] I. M. Ioannis, P. Falars, *Nano Lett.* **2003**, *3*, 249.

[13] S. Kobayashi, K. Hanabusa, N. Hamasaki, M. Kimura, H. Shirai, S. Shinkai, *Chem. Mater.* **2000**, *12*, 1523.

[14] Z. R. Tian, J. A. Voigt, J. Liu, B. McKenzie, H. Xu, *J. Am. Chem. Soc.* **2003**, *125*, 12384.

[15] J. H. Jung, H. Kobayashi, K. J. C. van Bommel, S. Shinkai, T. Shimizu, *Chem. Mater.* **2002**, 14, 1445.

[16] T. Nakashima, N. Kimizuka, *J. Am. Chem. Soc.* **2003**, *125*, 6386.

[17] R. Phelan, D. Weare, E. A. J. F. Peters, G. Verbist, *J. Phys.: Condens. Matter* **1996**, *8*, 475.

[18] Z. Schwartz, C. H. Lohmann, J. Oefinger, L. F. Bonewald, D. D. Dean, B. D. Boyan, *Adv. Dent. Res.* **1999**, *13*, 510.

[19] A. Rezania, K. Healy, *Biotechnol. Prog.* **1999**, *15*, 755.

[20] A. Norbert, B. Brun, C. Dara, *Bull. Soc. Fr. Mineral. Cristallogr.* **1975**, *98*, 111.

[21] *Natl. Bur. Stand. (U.S.) Monogr.* **1969**, *25*, 82.

[22] *Natl. Bur. Stand. (U.S.) Monogr.* **1969**, *25*, 83.

A Hybrid Planar–Mixed Molecular Heterojunction Photovoltaic Cell**

By *Jiangeng Xue*, *Barry P. Rand*, *Soichi Uchida*, and *Stephen R. Forrest**

The interest in photovoltaic (PV) devices has long been motivated by the need to replace depleting, polluting fossil fuels with the clean and renewable alternative of solar energy.[1] Organic materials, both small molecules and conjugated polymers, have the potential to offer low-cost solar energy conversion due to their light weight, low cost, and compatibil-

[*] Prof. S. R. Forrest, Dr. J. Xue, B. P. Rand, Dr. S. Uchida[+]
Department of Electrical Engineering and Princeton Institute for the Science and Technology of Materials (PRISM)
Princeton University
Princeton, NJ 08544 (USA)
E-mail: forrest@princeton.edu

[+] Present address: Central Technical Research Laboratory, Nippon Oil Corporation, 8 Chidori-cho, Naka-ku, Yokohama, 230-0815, Japan.

[**] We gratefully acknowledge the National Renewable Energy Laboratory, the Air Force Office of Scientific Research, and Global Photonic Energy Corporation for partial support of this work.

 © 2005 WILEY-VCH Verlag GmbH & Co. KGaA, Weinheim DOI: 10.1002/adma.200400617

ity with flexible substrates. Over the past decade, the power conversion efficiency (η_P) of organic PV cells has steadily improved,[2–6] reaching 4.2 % under intense simulated AM1.5G (AM: air mass, G: global) solar illumination,[7] although further improvements in efficiency and stability are necessary for commercial application.[3,6]

In organic materials, light absorption leads to the formation of excitons, or bound electron–hole pairs, rather than the free electron–hole pairs produced in inorganic semiconductors.[8] Efficient exciton dissociation occurs under strong electric fields, or at donor–acceptor (D–A) heterointerfaces, where the differences in the electron affinities and the ionization potentials between the contacting materials are sufficiently large to overcome the exciton binding energy.[3] The latter mechanism has been employed to create an organic D–A planar heterojunction (HJ) PV cell with $\eta_P \sim 1$ %,[2] which was limited because the exciton diffusion length ($L_D \leq 100$ Å)[3] is much shorter than the optical absorption length ($L_A \sim 1000$ Å). The use of C_{60} ($L_D \sim 400$ Å)[3] as the acceptor material in a double HJ cell leads to a considerably improved power conversion efficiency of $\eta_P \leq 4.2$ %.[7,9]

One way to improve the fraction of photogenerated excitons that diffuse to the D–A interface (i.e., the exciton diffusion efficiency) is to create an interpenetrating network of the donor and acceptor materials, resulting in a spatially distributed D–A interface that lies within a distance, L_D, of every exciton generation site. This so-called bulk HJ, formed by using blends of donor and acceptor polymers[10,11] or mixtures of co-deposited small molecules,[12–15] has been used to achieve internal quantum efficiencies up to 85 % and $\eta_P \leq 3.5$ %.[13,16,17] The collection efficiency of photogenerated carriers at the respective electrodes in a bulk HJ cell, however, is critically dependent on the transport properties of the interpenetrating network of the donor and acceptor materials.

Here, we demonstrate a hybrid planar–mixed molecular heterojunction (PM–HJ) photovoltaic cell consisting of a mixed layer of donor and acceptor molecules sandwiched between homogeneous layers of the donor and acceptor materials. Because each homogeneous layer has a thickness of approximately L_D, excitons generated across the entire heterojunction structure have a high probability of diffusing to a nearby D–A interface. Efficient exciton dissociation occurs throughout the mixed layer as well as at the interfaces between the mixed layer and the adjacent homogeneous layers. While the thicknesses of the homogeneously composed layers were determined by L_D, we found that the mixed-layer thickness must be less than a characteristic parameter referred to as the carrier collection length, L_c, in order to alleviate the charge-collection bottleneck in the resistive mixed layer. Hence, the hybrid PM–HJ structure has both the high exciton-diffusion efficiency of a bulk HJ structure, and the low resistance to charge transport of a planar HJ. We fabricated a PM–HJ photovoltaic cell consisting of the donor, copper phthalocyanine (CuPc), and the acceptor, C_{60}, and obtained a power conversion efficiency of $\eta_P = (5.0 \pm 0.3)$ % under 1 to 4 suns of simulated AM1.5G solar illumination (1 sun = 100 mW cm^{-2}).

The structure of the hybrid PM–HJ cell is indium tin oxide (ITO)/CuPc/CuPc:C_{60}(1:1 by weight)/C_{60}/bathocuproine (BCP)/1000 Å Ag. Similar three-layered structures have been reported previously,[18,19] however, the advantage of the hybrid PM–HJ structure was not fully realized due to the use of excessively thick mixed layers (400 Å, which exceeded L_c) and a different material system in those earlier works. Figure 1 shows the dark-current density versus voltage (J–V) characteristics for a planar HJ and a hybrid PM–HJ cell whose

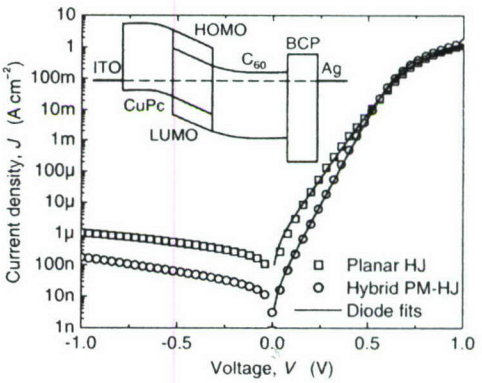

Figure 1. Dark-current density versus voltage (J–V) characteristics for a planar HJ (open squares) and a hybrid PM–HJ (open circles) organic photovoltaic cell. The device structures are ITO/CuPc(200 Å)/C_{60}(400 Å)/BCP(100 Å)/Ag(1000 Å) and ITO/CuPc(100 Å)/CuPc:C_{60}(200 Å; 1:1 by weight)/C_{60}(300 Å)/BCP(100 Å)/Ag(1000 Å), respectively. The solid lines are fits to the J–V characteristics based on the modified diode equation (see text). Inset: schematic energy level diagram of the hybrid PM–HJ cell.

schematic energy level diagram is shown in the inset. The planar HJ cell had a donor layer thickness $d_D = 200$ Å and an acceptor layer thickness $d_A = 400$ Å. For the hybrid PM–HJ cell, $d_D = 100$ Å, $d_A = 300$ Å, and the thickness of the mixed layer was $d_m = 200$ Å. Both cells exhibited rectification ratios $> 10^6$ at ±1 V, and shunt resistances > 1 MΩ cm^2. The forward-bias characteristics can be fit (solid lines) using the modified diode equation:[20]

$$J = J_s \left\{ \exp\left[\frac{q(V - JR_S)}{nkT}\right] - 1 \right\} \quad (1)$$

where J_s is the reverse-bias saturation current density, n is the ideality factor, R_S is the series resistance, q is the electron charge, k is Boltzmann's constant, and T is the temperature. While R_S (~0.25 Ω cm^2) is approximately the same for both cells, n is reduced from 1.94 ± 0.08 for the planar HJ cell, to 1.48 ± 0.05 for the hybrid PM–HJ cell, and J_s is also reduced from $(5 \pm 1) \times 10^{-7}$ A cm^{-2} (planar HJ) to $(1.0 \pm 0.3) \times 10^{-8}$ A cm^{-2} (hybrid PM–HJ).

The lower n and J_s for the hybrid PM–HJ cell are attributed to the reduction in the recombination current in the depletion region of this structure. The large highest occupied molecular orbital (HOMO) and lowest unoccupied molecular orbital (LUMO) offsets (~1 eV)[9] at the CuPc/C_{60} interface lead to a

 © 2005 WILEY-VCH Verlag GmbH & Co. KGaA, Weinheim

negligible diffusion-emission current in the planar HJ cell.[21] Hence, the dark current is dominated by recombination in the depletion region, leading to $n \approx 2$.[20] According to the Shockley–Hall–Read model, J_s for the recombination current is expressed as:[20]

$$J_{s,rec} = \frac{qn_i W}{2\tau} = \frac{1}{2} qn_i W N_t \sigma v_{th} \quad (2)$$

where n_i is the intrinsic electron or hole concentration, W is the depletion width, $\tau = 1/(N_t \sigma v_{th})$ is the effective carrier lifetime, N_t is the total density of recombination centers, σ is the electron- or hole-capture cross-section, and v_{th} is the carrier thermal velocity. It has been shown[22] that v_{th} is approximately proportional to the carrier mobility μ in disordered semiconductors, where carrier transport occurs via hopping. As the mean distance between neighboring molecules of the same species in a D–A mixture is larger than that in a homogeneous layer, the hopping mobilities for holes in the donor and for electrons in the acceptor materials are reduced upon molecular intermixing, thereby resulting in a reduction of J_s. Consequently, the contribution of diffusion to the dark current becomes appreciable, leading to $n \sim 1.5$ in the hybrid PM–HJ cell. Moreover, by comparing J_s for the planar HJ and hybrid PM–HJ cells, we infer that the hole mobility in CuPc and the electron mobility in C_{60} are reduced by approximately one and a half orders of magnitude by intermixing CuPc and C_{60} at a ratio of 1:1 by weight.

Because of the reduced mobility in the mixed D–A layer, the carrier drift length, l, in an electric field, E, ($l = \mu\tau E$) before recombination, may be comparable to or less than the mixed-layer thickness, leading to incomplete collection of photogenerated charges at the electrodes. Charge transport in the homogeneous layers is considered to be lossless as photogenerated holes and electrons are spatially separated,[3] except when the applied voltage approaches the built-in potential (corresponding to significantly reduced carrier drift lengths).[7] Hence, following the treatment by Crandall used for p–i–n amorphous-silicon (a-Si) solar cells,[23] we obtained the charge-collection efficiency, η_{CC}, (i.e., the percentage of photogenerated charges collected at the electrodes) for an organic PV cell with a mixed D–A layer as follows:

$$\eta_{CC} = \frac{L_c}{d_m}\left[1 - \exp\left(-\frac{d_m}{L_c}\right)\right] \quad (3)$$

where the collection length, L_c, is the sum of the hole and electron drift lengths.[23] From Equation 3, it is clear that $\eta_{CC} \approx 1$ for $d_m \ll L_c$, and $\eta_{CC} \approx L_c/d_m$ for $d_m \gg L_c$, suggesting that the mixed layer should be thinner than the corresponding collection length to obtain a high charge-collection efficiency. Furthermore, η_{CC} is a function of the applied voltage through the field dependence of L_c:

$$L_c = \left(\tau_p \mu_p + \tau_n \mu_n\right)(V_{bi} - V)/W \approx L_{c0}(V_{bi} - V)/V_{bi} \quad (4)$$

where τ_p (τ_n) is the hole (electron) lifetime, μ_p (μ_n) is the hole (electron) mobility, V_{bi} is the built-in potential, and $L_{c0} = (\tau_p \mu_p + \tau_n \mu_n) V_{bi}/W = L_c(V = 0)$. Hence, η_{CC} decreases with the applied voltage, more significantly so for a cell with a thicker mixed layer, corresponding to a lower fill factor (FF) for the PV cell. It is therefore important to have high carrier mobilities in the mixed layer such that L_c is comparable to the optical absorption length, to take full advantage of the high exciton-diffusion efficiency of the mixed molecular HJ structure.

With the dark-current density, J_d, described by Equation 1, and the photocurrent density, J_{Ph}, given by $J_{Ph}(V) = P_O R_0 \eta_{CC}(V)$, where P_O is the incident optical power density and R_0 is the responsivity corresponding to $\eta_{CC} = 1$, we now obtain the total current density under illumination as $J(V) = J_d(V) + J_{Ph}(V)$. As shown in Figure 2, our model (solid lines) reproduced the experimental J–V characteristics of both the hybrid PM–HJ cell in Figure 1 (open squares, $d_m = 200$ Å)

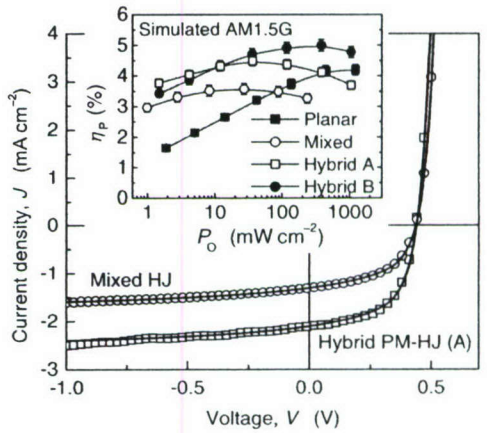

Figure 2. Comparison of predicted (solid lines) and experimental current density vs. voltage (J–V) characteristics of the hybrid PM–HJ cell in Figure 1 (A, open squares, $d_m = 200$ Å) and a mixed HJ cell [13] (open circles, $d_m = 330$ Å) under simulated AM1.5G solar illumination. Refer to Table 1 for relevant parameters. Inset: comparison of the power conversion efficiencies (η_P) of organic photovoltaic cells with a planar HJ [7] (filled squares), a mixed HJ [13] (open circles), and a hybrid PMHJ (Hybrid A: open squares, Hybrid B: filled circles), as a function of the incident optical power density P_O (simulated AM1.5G). The lines are guides to the eye. A maximum value of η_P of (5.0 ± 0.3) % under 1 to 4 suns solar illumination is achieved in the hybrid PM–HJ cell B, which has the structure ITO/CuPc(150 Å)/CuPc:C_{60}(100 Å;1:1)/C_{60}(350 Å)/BCP(100 Å)/Ag(1000 Å).

and a mixed HJ cell[13] (open circles, $d_m = 330$ Å) under simulated AM1.5G solar illumination, and lead to fill factors (FF) that were in agreement with the experimental data (summarized in Table 1). The carrier collection length in the 1:1 mixed CuPc:C_{60} was $L_{c0} = (450 \pm 50)$ Å, corresponding to $\eta_{CC} \approx 0.8$ at short-circuit for the hybrid PM–HJ cell, and $\eta_{CC} \approx 0.7$ for the mixed HJ cell.

The illumination-intensity dependence of η_P under simulated AM1.5G solar illumination for the hybrid PM–HJ cell is shown in the inset (Hybrid A, open squares), as compared with those of a planar HJ cell[7] (filled squares) and the mixed

 © 2005 WILEY-VCH Verlag GmbH & Co. KGaA, Weinheim

Table 1. Parameters used in fitting the J–V characteristics under illumination for the hybrid PM–HJ cell in Figure 1 and a mixed HJ cell, used from a previous work [13]. See text for parameter definitions.

Cell	d_m [Å]	n	J_s [cm^2]	R_S [Ω cm^2]	P_O [mW cm^{-2}]	L_{c0} [Å]	R_0 [A W^{-1}]	V_{bi} [V]	FF Fitting	FF Exp.
Hybrid PM-HJ	200	1.5	10	0.25	12	450	0.21	0.60	0.567	0.573
Mixed HJ	330	1.6	20	0.22	8.3	480	0.20	0.60	0.511	0.512

HJ cell[13] (open circles). A maximum $\eta_P \approx (4.5 \pm 0.3)$ % at $P_O = 0.4$ suns is achieved for Hybrid A. Optimizing the thicknesses of the photoactive layers in the hybrid PM–HJ structure lead to a higher η_P ((5.0 ± 0.3) %) under 1 to 4 suns illumination in a cell with the following thicknesses: $d_0 = 150$ Å, $d_m = 100$ Å, and $d_A = 350$ Å (Hybrid B, filled circles). Table 2 summarizes the performance parameters of these cells under approximately 1 sun illumination.

The short-circuit current density for either hybrid PM–HJ cell was significantly higher than that of the planar HJ cell, and furthermore, was higher in Hybrid A, which had a thicker mixed layer. This is attributed to the improved exciton-diffusion efficiency in the mixed layers over that in the planar layers. The thinner photoactive region in the mixed HJ cell, however, was responsible for its lower short-circuit current density, J_{SC}, than that of Hybrid A. Using a mixed layer with $d_m > 330$ Å in the mixed HJ cell[13] or $d_m > 200$ Å in the hybrid PM–HJ cell leads to a reduction in J_{SC} due to the significantly reduced η_{CC} (see Eq. 3). This also explains the lower efficiencies in similar CuPc:C_{60} cells[24,25] since the excessively thick mixed layer ($d_m \geq 500$ Å) leads to a very low η_{CC}, although material purity has also been pointed out to be an important factor.[13]

Both PM–HJ cells have a higher FF than the mixed-layer cell, again due to the thinner mixed layers used in the former structures. With $d_m = 100$ Å $\ll L_{c0}$, Hybrid B has an FF as high as that of the planar HJ cell under 1 sun illumination that is only slightly reduced under higher illumination intensities. However, the FF for Hybrid A decreased from 0.57 at $P_O = 0.12$ suns (Table 1) to 0.50 at $P_O = 1.2$ suns (Table 2), suggesting that charge collection is less efficient in a thicker mixed layer under higher illumination intensities due to its inherently higher series resistance.

The different dependencies of J_{SC} and FF on d_m not only lead to the higher η_P in Hybrid B than in Hybrid A at 1 sun, but lead to the peaking of η_P at different illumination intensities. With J_{SC} nearly proportional to P_O, and with V_{OC} increasing logarithmically with P_O,[7,20] η_P reached a maximum at $P_O = 0.4$ suns for Hybrid A as the FF decreased with P_O, whereas η_P peaked under 1 to 4 suns for Hybrid B due to its high and relatively intensity-independent FF. The slight difference in V_{OC} between these cells was attributed to their differences in n and J_s, which affect the logarithmic dependence of V_{OC} on P_O.[7,20] Overall, both hybrid PM–HJ cells A and B exhibited higher η_P than the other HJ architectures. In particular, $\eta_P = (5.0 \pm 0.3)$ % under 1 to 4 suns is achieved in the PM–HJ cell Hybrid B, which is approximately 40 % higher than for a single planar or mixed HJ. Details on the performance of these hybrid PM–HJ cells will be published elsewhere.

We used X-ray diffraction (XRD) to examine the morphology of the pure and mixed CuPc and C_{60} films. As shown in Figure 3, the XRD pattern for the pure CuPc film exhibited a prominent peak at $2\theta = (6.85 \pm 0.05)°$, corresponding to an interplanar spacing of $d = (12.9 \pm 0.1)$ Å, or the (100) Bragg reflection of the α-CuPc phase,[26] whereas the broad peak centered at $2\theta = 21°$ is due to diffraction from the glass substrate. The pure C_{60} film showed no apparent diffraction peak, indicating that the film is amorphous. The CuPc (100) reflection is not present in the 1:1 mixed CuPc:C_{60} film, suggesting that no significant phase separation occurred. This is consistent with previous optical absorption studies of mixed CuPc:C_{60} films, where it was found that CuPc molecules showed a reduced tendency to aggregate with increasing C_{60} content.[13]

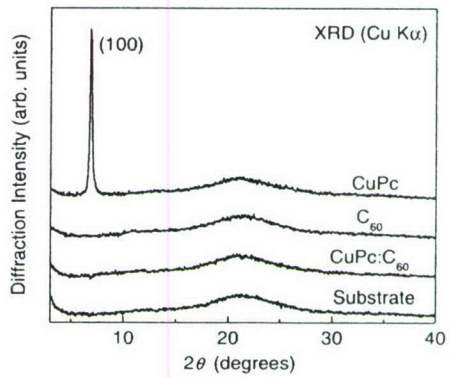

Figure 3. XRD patterns for a CuPc film, a C_{60} film, a mixed CuPc:C_{60} (1:1) film, and the glass substrate taken in the θ–2θ geometry using Cu Kα radiation. All organic films were 1000 Å thick.

Table 2. Performance comparison of organic photovoltaic cells incorporating a planar HJ, a mixed HJ, and a hybrid PM–HJ as the photoactive region, under approximately 1 sun simulated AM1.5G illumination. See text for parameter definitions.

Cell	d_D [Å]	d_m [Å]	d_A [Å]	P_O [suns]	J_{SC}/P_O [mA W^{-1}]	FF	V_{OC} [V]	η_P [%]	Reference
Planar HJ	200	–	400	1.3	11.8±0.5	0.61	0.51	3.7±0.2	[7]
Mixed HJ	–	330	100	0.9	15.4±0.7	0.46	0.50	3.5±0.2	[13]
Hybrid PM-HJ (A)	100	200	300	1.2	17.1±0.9	0.50	0.51	4.4±0.2	This work
Hybrid PM-HJ (B)	150	100	350	1.2	15.0±0.6	0.61	0.54	5.0±0.3	This work

© 2005 WILEY-VCH Verlag GmbH & Co. KGaA, Weinheim

Figure 4a schematically shows an idealized bulk HJ structure, where donor and acceptor molecules (or polymers) segregate to form an interdigitated structure with lateral feature sizes no larger than the exciton diffusion lengths. In some archetypal D–A molecular systems such as CuPc and 3,4,9,10-perylenetetracarboxylic bis-benzimidazole (PTCBI), the as-grown, homogeneously mixed D–A layer shows very poor transport of photogenerated carriers,[15,19] indicating a transport picture such as that in Figure 4b, where percolating paths across the entire mixed layer do not exist. However, as illustrated in Figure 4c, the relatively long charge-transport length in the CuPc:C_{60} (1:1) layer suggests that small, disordered CuPc and C_{60} domains may form, which provide percolating paths for hole and electron transport, as well as a nanostructured, spatially distributed D–A interface for efficient exciton diffusion (and dissociation). Hence, these pathways result in replicating the idealized structure in Figure 4a, with each path only one or a few molecules wide, thereby meeting the condition that exciton dissociation occurs within L_D of a D–A junction. The difference between the scenarios in Figures 4b and 4c is attributed to the spherical shapes of the C_{60} molecules that allow close packing, which is hindered by the planar CuPc and PTCBI molecules.

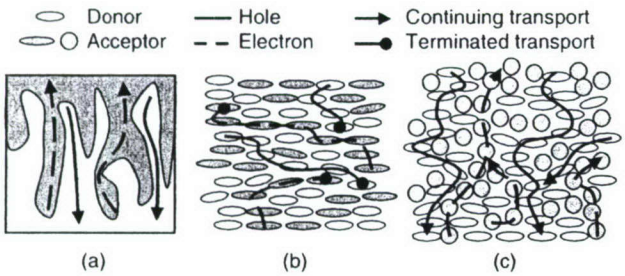

Figure 4. Illustrations of different transport scenarios in a donor–acceptor mixture. a) An idealized bulk HJ structure in which segregation of the donor and acceptor molecules leads to an interdigitated structure with lateral-feature sizes no larger than the exciton diffusion lengths. b) No percolating paths across the entire film exist, leading to trapping of the charges (and ultimately, recombination). c) Percolating paths are formed across the film, although the carrier mobility in the mixture is reduced compared to its value in pure films. The nanostructured, spatially distributed donor–acceptor interface is responsible for efficient exciton diffusion in the mixture.

In conclusion, we have demonstrated that a hybrid donor–acceptor molecular HJ structure, i.e., a mixed layer of donor and acceptor materials sandwiched between homogeneous donor and acceptor layers, can significantly improve the performance of organic photovoltaic cells over those that use a planar D–A HJ or a mixed HJ with a thick, mixed D–A layer. A maximum power conversion efficiency of $\eta_P = (5.0 \pm 0.3)$ % was achieved under 1 to 4 suns simulated AM1.5G solar illumination in a hybrid PM–HJ cell with a 100 Å thick, mixed layer. The current–voltage characteristics of the hybrid PM–HJ cell were accurately described using an analysis based on a field-dependent carrier collection length in the D–A mixture. The mixed CuPc:C_{60} film showed no significant phase separation between the donor and acceptor molecules, although percolating paths for efficient charge transport were inferred to exist in the mixture.

Experimental

The organic hybrid PM–HJ photovoltaic cells were fabricated on glass substrates pre-coated [27] with a ~1500 Å thick, transparent, conducting ITO anode with a sheet resistance per square of 15 Ω. The substrates were cleaned [28] in solvent followed by UV–ozone treatment for 5 min [29]. The organic layers and a metal cathode were deposited via thermal evaporation in a high-vacuum chamber with a base pressure of $\sim 2 \times 10^{-7}$ torr (1 torr ≈ 133.3 Pa). A CuPc layer with a thickness of $d_D \sim 50$–200 Å, a co-deposited layer of CuPc:C_{60} (1:1 by weight) with a thickness of $d_m \sim 0$–300 Å, and a C_{60} layer with a thickness of $d_A \sim 250$–400 Å, were sequentially deposited onto the ITO anode, followed by a 100 Å thick exciton-blocking layer [30] of BCP. Finally, a 1000 Å thick Ag cathode was evaporated through a shadow mask with 1 mm diameter openings.

Current–voltage characteristics of the PV cells at 25 °C in the dark and under simulated AM1.5G solar illumination from a 150 W xenon arc lamp (Oriel Instruments) were measured using an HP 4155B semiconductor parameter analyzer. The illumination intensity was varied using neutral density filters and measured with a calibrated broadband optical power meter (Oriel Instruments). The XRD patterns of a 1000 Å thick 1:1 mixed (by weight) CuPc:C_{60} film deposited on a glass substrate as well as those of pure CuPc and C_{60} films were taken with a Rigaku diffractometer in the θ–2θ geometry using Cu Kα radiation.

Received: April 25, 2004
Final version: September 13, 2004
Published online: November 25, 2004

[1] A. Goetzberger, C. Hebling, H.-W. Schock, *Mater. Sci. Eng., R* **2003**, *40*, 1.
[2] C. W. Tang, *Appl. Phys. Lett.* **1986**, *48*, 183.
[3] P. Peumans, A. Yakimov, S. R. Forrest, *J. Appl. Phys.* **2003**, *93*, 3693.
[4] B. A. Gregg, *J. Phys. Chem. B* **2003**, *107*, 4688.
[5] C. J. Brabec, N. S. Sariciftci, J. C. Hummelen, *Adv. Funct. Mater.* **2001**, *11*, 15.
[6] J. Nelson, *Curr. Opin. Solid State Mater. Sci.* **2002**, *6*, 87.
[7] J. Xue, S. Uchida, B. P. Rand, S. R. Forrest, *Appl. Phys. Lett.* **2004**, *84*, 3013.
[8] M. Pope, C. E. Swenberg, *Electronic Processes in Organic Crystals and Polymers*, 2nd ed., Oxford University Press, New York **1999**.
[9] P. Peumans, S. R. Forrest, *Appl. Phys. Lett.* **2001**, *79*, 126.
[10] J. J. M. Halls, C. A. Walsh, N. C. Greenham, E. A. Marseglia, R. H. Friend, S. C. Moratti, A. B. Holmes, *Nature* **1995**, *376*, 498.
[11] G. Yu, J. Gao, J. C. Hummelen, F. Wudl, A. J. Heeger, *Science* **1995**, *270*, 1789.
[12] T. Tsuzuki, Y. Shirota, J. Rostalski, D. Meissner, *Sol. Energy Mater. Sol. Cells* **2000**, *61*, 1.
[13] S. Uchida, J. Xue, B. P. Rand, S. R. Forrest, *Appl. Phys. Lett.* **2004**, *84*, 4218.
[14] G. Gebeyehu, B. Maennig, J. Drechsel, K. Leo, M. Pfeiffer, *Sol. Energy Mater. Sol. Cells* **2003**, *79*, 81.
[15] P. Peumans, S. Uchida, S. R. Forrest, *Nature* **2003**, *425*, 158.
[16] S. E. Shaheen, C. J. Brabec, N. S. Sariciftci, F. Padinger, T. Fromherz, J. C. Hummelen, *Appl. Phys. Lett.* **2001**, *78*, 841.
[17] F. Padinger, R. S. Rittberger, N. S. Sariciftci, *Adv. Funct. Mater.* **2003**, *13*, 85.

 © 2005 WILEY-VCH Verlag GmbH & Co. KGaA, Weinheim

[18] M. Hiramoto, H. Fujiwara, M. Yokoyama, *Appl. Phys. Lett.* **1991**, *58*, 1062.
[19] M. Hiramoto, H. Fujiwara, M. Yokoyama, *J. Appl. Phys.* **1992**, *72*, 3781.
[20] S. M. Sze, *Physics of Semiconductor Devices*, 2nd ed., Wiley, New York **1981**.
[21] B. L. Sharma, R. K. Purohit, *Semiconductor Heterojunctions*, Pergamon Press, New York **1974**.
[22] G. Paasch, T. Lindner, S. Scheinert, *Synth. Met.* **2002**, *132*, 97.
[23] R. S. Crandall, *J. Appl. Phys.* **1983**, *54*, 7176.
[24] P. Sullivan, S. Heutz, S. M. Schultes, T. S. Jones, *Appl. Phys. Lett.* **2004**, *84*, 1210.
[25] S. Heutz, P. Sullivan, B. M. Sanderson, S. M. Schultes, T. S. Jones, *Sol. Energy Mater. Sol. Cells* **2004**, *83*, 229.
[26] R. Prabakaran, R. Kesavamoorthy, G. L. N. Reddy, F. P. Xavier, *Phys. Status Solidi B* **2002**, *229*, 1175.
[27] S. R. Marder, J. W. Perry, C. P. Yakymyshyn, *Chem. Mater.* **1994**, *6*, 1137.
[28] P. E. Burrows, Z. Shen, V. Bulovic, D. M. McCarty, S. R. Forrest, J. A. Cronin, M. E. Thompson, *J. Appl. Phys.* **1996**, *79*, 7991.
[29] J. Xue, S. R. Forrest, *J. Appl. Phys.* **2004**, *95*, 1869.
[30] P. Peumans, V. Bulovic, S. R. Forrest, *Appl. Phys. Lett.* **2000**, *76*, 2650.

Template Synthesis of Sc@C_{82}(I) Nanowires and Nanotubes at Room Temperature**

By *Cong-Ju Li, Yu-Guo Guo, Bing-Shi Li, Chun-Ru Wang,* Li-Jun Wan,** and *Chun-Li Bai**

Endohedral metallofullerenes are constructed by enclosing one or several metal atoms inside fullerene cages, and their electronic properties are determined by both the caged metal atoms and the parent fullerenes. Because of their unique structure and many novel electronic properties, metallofullerenes are expected to be widely used in chemistry, physics, medicine, materials science, and many other fields.[1–3] Here we report the fabrication of Sc@C_{82} metallofullerene nanowires and nanotubes by a template method[4] together with an electrochemical deposition strategy. This method, which has been used successfully to prepare a variety of metal nanowires,[5,6] metal nanotubes,[7] metal/metal composite nanowires,[8] and C_{60} nanowires,[9] was also found to produce metallofullerene nanostructures such as nanowires and nanotubes in a controllable way.

Sc@C_{82} has two structural isomers reported so far.[10] The current study was performed on Sc@C_{82}(I) (see Fig. 1a), whose structure and electronic properties have been studied

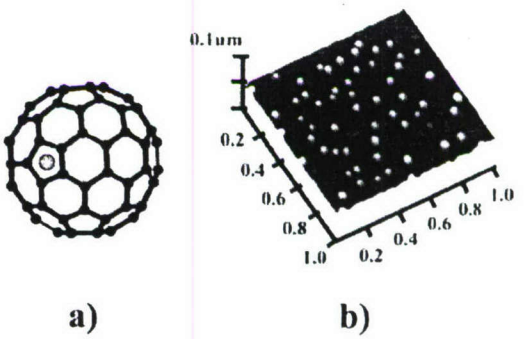

Figure 1. a) The geometrical structure of Sc@C_{82}. b) Typical AFM image of Sc@C_{82} clusters prepared in acetonitrile/toluene.

in detail previously.[10,11] The sample was generated by arc-discharging scandium/graphite composite rods in helium atmosphere and isolated by the recycling high-performance liquid chromatography (HPLC) method. Around 3 mg Sc@C_{82} was prepared and the sample's high purity (99 %) was confirmed by both positive and negative time-of-flight (TOF) mass spectrometry.

It has been found that fullerenes and metallofullerenes are soluble in some organic solvents, such as benzene, toluene, and carbon disulfide, but not in some other solvents, such as ethanol, acetone, and acetonitrile, at room temperature.[12] If fullerenes and metallofullerenes are put in a mixture of the above two types of solvents, for example toluene/acetonitrile, they usually form optically transparent nanoclusters,[13,14] and these nanoclusters are easily charged under direct current (DC). Therefore, with the nanoclusters, one- or two-dimensional (1D or 2D) fullerene nanostructures may be constructed by an electrochemical method.[9,15] Figure 1b shows a typical atomic force microscopy (AFM) image of metallofullerene clusters. The size of the Sc@C_{82} clusters was distributed between 15 and 35 nm, which is somewhat larger than the uniform C_{60} clusters[4] (ca. 13 nm) formed in similar experimental conditions. Details on the fabrication of nanowires and nanotubes using templates can be found in the Experimental section.

The morphology of Sc@C_{82} nanostructures was characterized by scanning electron microscopy (SEM) and transmission electron microscopy (TEM). As shown in Figure 2, it was found that the morphology of Sc@C_{82} nanostructures (nano-

[*] Prof. C.-R. Wang, Prof. L.-J. Wan, Prof. C.-L. Bai, Dr. C.-J. Li,[+]
Dr. Y.-G. Guo, Dr. B.-S. Li
Institute of Chemistry, Chinese Academy of Sciences
Beijing 100080 (P. R. China)
E-mail: crwang@iccas.ac.cn; wanlijun@iccas.ac.cn; clbai@iccas.ac.cn
Dr. C.-J. Li[+]
Graduate School
Chinese Academy of Sciences,
Beijing 100080 (P. R. China)
[+] Current address: Beijing Key Laboratory of Clothing Material, R&D and Assessment, Beijing Institute of Clothing Technology, Beijing 100029, P. R. China.

[**] Financial support from the National Natural Science Foundation of China (grant nos. 50225206, 90206045, 20025308, and 20177025), National 863 Project (2002AA302201), National Key Project on Basic Research (Grant G2000077501), and the Chinese Academy of Sciences is gratefully acknowledged. We also thank Prof. P. V. Kamat at the University of Notre Dame for useful suggestions.

 DOI: 10.1002/adma.200400155 © 2005 WILEY-VCH Verlag GmbH & Co. KGaA, Weinheim

Organic solar cells with sensitivity extending into the near infrared

Barry P. Rand, Jiangeng Xue,[a] Fan Yang, and Stephen R. Forrest[b]
Department of Electrical Engineering and Princeton Institute for the Science and Technology of Materials (PRISM), Princeton University, Princeton, New Jersey 08544

(Received 21 July 2005; accepted 11 October 2005; published online 2 December 2005)

We describe an organic photovoltaic cell based on a tin(II) phthalocyanine (SnPc)/C_{60} donor/acceptor heterojunction with sensitivity at wavelengths of $\lambda > 900$ nm. We find that the low hole mobility in polycrystalline thin films of SnPc, $\mu_h = (2 \pm 1) \times 10^{-10}$ cm^2/V s, prevents the use of thick layers, leading to low fill factors and therefore low-power conversion efficiencies. However, owing to its large absorption coefficient, a 50-Å-thick layer of SnPC yields solar cell external quantum efficiencies of up to 21% at $\lambda = 750$ nm. With the double heterostructure of indium-tin oxide/100 Å copper phthalocyanine/50 Å SnPc/540 Å C_{60}/75 Å bathocuproine/Ag, we obtain a power conversion efficiency of (1.0±0.1)% under 1 sun standard AM1.5G solar illumination and efficiencies of (1.3±0.1)% under intense (10 suns) standard AM1.5G solar illumination. © *2005 American Institute of Physics*. [DOI: 10.1063/1.2140075]

Photodetectors and photovoltaic (PV) cells using small molecular weight organic thin films deposited on plastic substrates have the potential advantages of being low-cost and lightweight.[1] Recently, the power conversion efficiency of molecular organic PV cells has steadily improved due to the use of new materials and device architectures.[2,3] One limitation of organic PV energy conversion, however, is the limited overlap between the active layer absorption with the solar spectrum. Indeed, over 60% of the total solar photon flux is at wavelengths $\lambda > 600$ nm with approximately 50% in the red and near-infrared (NIR) spectrum at $600 < \lambda < 1000$ nm. Therefore, new materials need to be developed and investigated that can absorb NIR radiation, and efficiently convert absorbed photons into current. Recently, a polymer-based solar cell sensitive to NIR radiation up to $\lambda = 1000$ nm achieved a power conversion efficiency of 0.7% under 1 sun illumination.[4,5]

The photogeneration process in organic materials starts with the absorption of a photon that creates an exciton, or bound electron-hole pair. In efficient organic photovoltaic devices, the exciton is then dissociated at a donor-acceptor (DA) interface into free charge carriers, which are subsequently collected at their respective electrodes. Here, we investigate the properties of a tin(II) phthalocyanine (SnPc) layer used as the electron donor in double heterostructure small molecular weight organic solar cells. We demonstrate that the SnPc layer efficiently converts incident NIR (with an onset at $\lambda = 1000$ nm) light to photocurrent, and that power conversion efficiencies of $\eta_P = (1.0 \pm 0.1)\%$ under 1 sun standard AM1.5G (air mass 1.5 global) solar illumination are possible. The high efficiency results since the fill factor is FF=0.5 for ultrathin SnPc layers, whereas previously demonstrated devices[4] had FF=0.32. This high FF is achieved through control of SnPc layer thickness such that its low hole mobility does not negatively impact device performance.

All devices were fabricated on 1500-Å-thick layers of indium-tin oxide (ITO) commercially precoated onto glass substrates with a sheet resistance of 15 Ω/sq. The solvent cleaned[6] ITO surface was treated in ultraviolet/O_3 for 5 min immediately before loading the substrates into a high-vacuum chamber (base pressure $\sim 3 \times 10^{-7}$ Torr), where organic layers and a 1000-Å-thick Ag cathode were deposited via thermal evaporation. Prior to deposition, the organic materials were purified in three cycles using vacuum thermal gradient sublimation.[7] The Ag cathode was evaporated through a shadow mask with 1 mm diameter openings to define the device area. The current density versus voltage (J-V) characteristics were measured in the dark and under simulated AM1.5G solar illumination (Oriel Instruments) using an HP4155B semiconductor parameter analyzer. Illumination intensity and quantum efficiency measurements were conducted using standard methods employing a National Renewable Energy Laboratory traceable calibrated Si detector.[8] Differences between the simulated and actual (i.e., standard) solar spectra were corrected in our final efficiency determination. Absorption spectra were measured on quartz substrates using a Perkin–Elmer Lambda 800 ultraviolet/visible spectrometer referenced to clean quartz substrates to cancel out absorption losses in the quartz. The SnPc hole conductivity was measured for devices consisting of a 1000-Å-thick layer sandwiched between ITO and Au contacts.

In Fig. 1, we show the J-V characteristics of a device with the structure ITO/CuPc (100 Å)/SnPc (50 Å)/C_{60} (540 Å)/BCP (75 Å)/Ag (here CuPc denotes copper phthalocyanine, and BCP is bathocuproine) in the dark and under various illumination intensities (P_0) of AM1.5G standard solar illumination. The DA heterojunction is defined at the SnPc/C_{60} interface and BCP serves as an exciton blocking layer.[9] Fitting the dark current to classical p-n junction diode theory[10] yields a series resistance of $R_S = 0.17\ \Omega\ \text{cm}^2$ and an ideality factor of $n = 1.96 \pm 0.05$. A proposed energy level scheme is shown in the inset to Fig. 1, where the highest occupied molecular orbital energy levels are measured by ultraviolet photoelectron spectroscopy. The lowest unoccupied molecular orbital energies are estimated using the optical energy gap of each material.

Figure 2 shows the various PV cell performance parameters for the same device as a function of P_0. Here, FF

[a]Also with: Global Photonic Energy Corporation, 375 Phillips Boulevard, Ewing, New Jersey 08618; current address: Department of Materials Science and Engineering, University of Florida, Gainesville, Florida 32611.
[b]Electronic mail: forrest@princeton.edu

 © 2005 American Institute of Physics
Downloaded 12 Jan 2008 to 141.213.8.105. Redistribution subject to AIP license or copyright; see http://apl.aip.org/apl/copyright.jsp

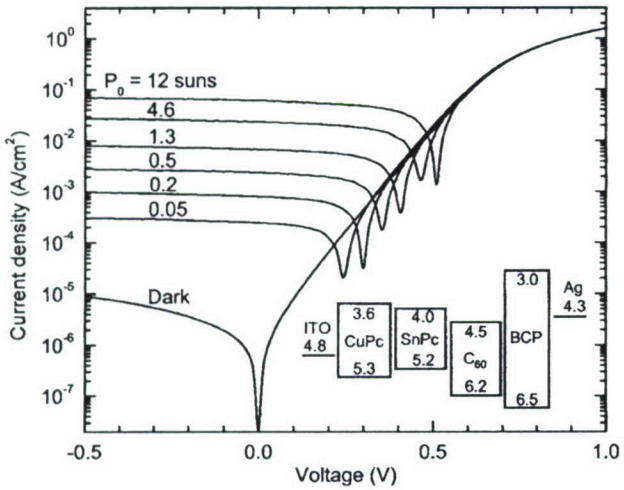

FIG. 1. Current density vs voltage characteristics in the dark and under various intensities (P_0) of AM1.5G standard solar illumination with the following device structure: ITO/CuPc (100 Å)/SnPc (50 Å)/C_{60} (540 Å)/BCP (75 Å)/Ag (1000 Å). Inset: Schematic energy diagram of the device structure.

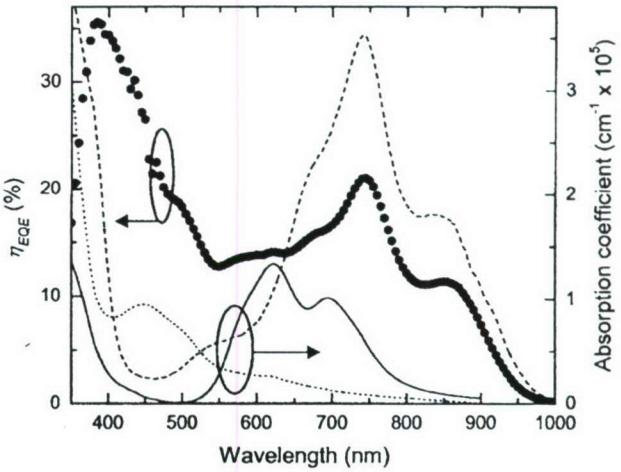

FIG. 3. Measured external quantum efficiency (η_{EQE}) spectrum (filled circles) for the device of Fig. 1. The absorption coefficients of CuPc (solid line), a 50-Å-thick film on SnPc (dashed line), and C_{60} (dotted line) are also shown.

~ 0.5 throughout the measured range of intensities, while the open-circuit voltage (V_{OC}) increases logarithmically with P_0, having a value of 0.4 V at 1 sun (100 mW/cm^2) and up to 0.51 V at 12 suns intensity. The responsivity (equal to J_{SC}/P_0, where J_{SC} is the short-circuit current density) remains relatively constant with $P_0=(0.05\pm0.02)$ A/W. As a result of these trends in device parameters, η_P increases along with V_{OC} to (1.0 ± 0.1)% under 1 sun standard AM1.5G solar illumination, reaching (1.3 ± 0.1)% under 12 suns. The fact that both FF and J_{SC}/P_0 are constant with P_0 from 1 to 12 suns indicates that carrier collection in the device is efficient, and that carrier recombination does not increase significantly with intensity.

The external quantum efficiency, η_{EQE}, and the absorption coefficients, α, of the active layers of the device are shown in Fig. 3 as functions of wavelength. The low-energy Q band of SnPc (dashed line) exhibits considerably stronger absorption than that of CuPc (solid line), reaching peak values of $\alpha=3.5\times10^5$ cm^{-1} at $\lambda=740$ nm, as opposed to 1.3 $\times10^5$ cm^{-1} at $\lambda=620$ nm, respectively. Also, α for SnPc extends into the NIR, with significant absorption up to $\lambda=1000$ nm. The absorption coefficient was calculated from a 50-Å-thick film of SnPc; the same as that used in the device. Increasing the thickness of the film leads to a change in spectral shape, in that the peak at $\lambda=860$ nm increases with respect to the peak at 740 nm (data not shown), possibly a result of molecular aggregates forming SnPc dimers. That is, if we assume that the very thinnest SnPc layers do not provide uniform coverage of the surface, some regions will contain SnPc clusters with a high density of dimers, whereas other regions will have either monolayer or no coverage completely absent of dimers. In this case, the long-wavelength aggregate peak intensity will also be reduced. Aggregation has been studied by absorption for solutions of substituted lead phthalocyanines, another nonplanar phthalocyanine, where a similar redshifted peak in the Q-band was assigned to dimer aggregate formation.[11] The η_{EQE} of the PV cell in Fig. 1 (filled circles, Fig. 3) follows the absorption of the constituent materials, with the photocurrent contribution from C_{60} generated between $350<\lambda<550$ nm, peaking at $\eta_{EQE}=36$%, while the SnPc layer contributes from $600<\lambda<1000$ nm, peaking at 21%.

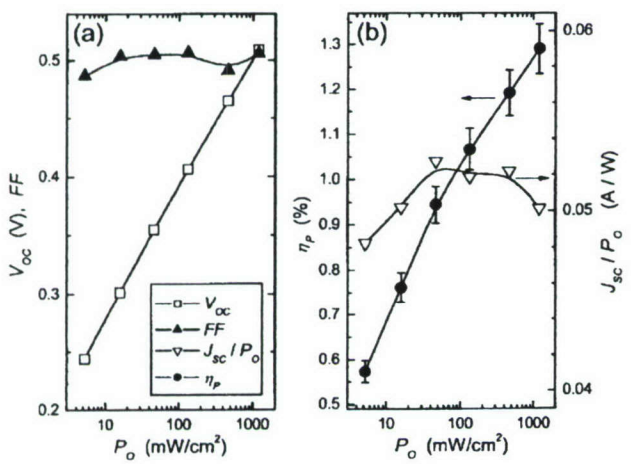

FIG. 2. (a) Fill factor (FF), open-circuit voltage (V_{OC}), (b) responsivity (J_{SC}/P_0), and power conversion efficiency (η_P) of devices with the same structure as Fig. 1 under various AM1.5G standard solar illumination intensities, P_0. The solid lines serve as guides for the eyes.

Optical modeling using transfer matrices[12] suggests that the SnPc region contributes to an internal quantum efficiency of $\sim$40%. There are additional small response peaks in η_{EQE} at $\lambda=575$ and 620 nm, corresponding to a contribution from the underlying CuPc layer. This latter response arises since the 50-Å-thick SnPc layer is discontinuous, allowing for local direct contact between the CuPc and C_{60} that form efficient charge separating regions, further supporting our assumption of nonuniform layer coverage for the thinnest films.[10]

The central Sn atom lies 1.13 Å out of the molecular plane, causing SnPc to crystallize in the triclinic phase.[13,14] The powder x-ray diffraction of the purified source material is shown in Fig. 4(a), and the peaks are identified using the known molecular crystal structure. A 1000-Å-thick film of SnPc deposited on ITO is shown in Fig. 4(a) to have a single peak at $2\theta=(12.60\pm0.05)°$, corresponding to a lattice plane spacing of $d_{(\bar{1}01)}=(7.03\pm0.02)$ Å. This indicates that the

Downloaded 12 Jan 2008 to 141.213.8.105. Redistribution subject to AIP license or copyright; see http://apl.aip.org/apl/copyright.jsp

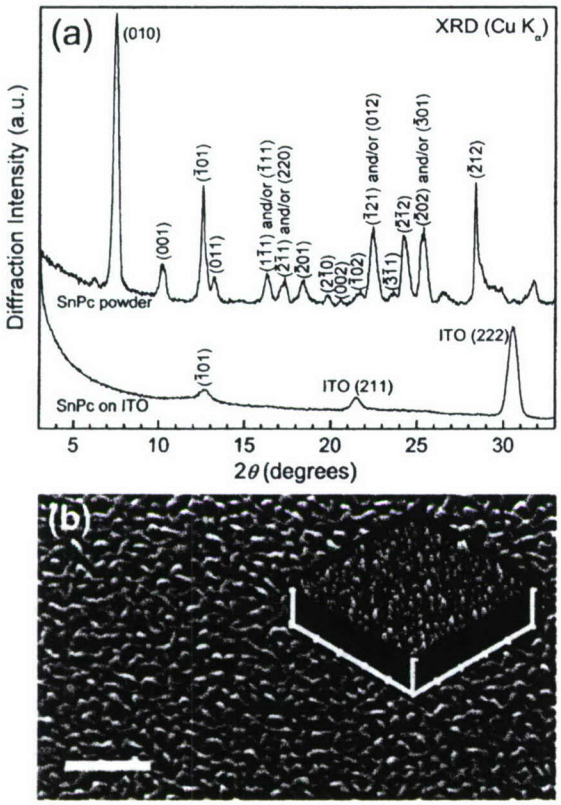

FIG. 4. (a) X-ray diffraction patterns for SnPc powder and a 1000-Å-thick film of SnPc deposited on ITO, taken in the $\theta-2\theta$ geometry using Cu $K\alpha$ radiation. (b) Scanning electron microscope (SEM) and tapping mode atomic force microscope (AFM) images of a 250-Å-thick SnPc film deposited on quartz. The scale bar in the SEM image is 200 nm, and the scan size in the AFM image is 1 μm × 1 μm, with a height increment of 50 nm.

SnPc film is polycrystalline with molecules preferentially lying flat on the ITO surface, in agreement with past studies.[15,16] Figure 4(b) shows the surface morphology of a 250-Å-thick SnPc film on quartz. The scanning electron micrograph shows a rough, corrugated surface, indicative of a polycrystalline film, while the atomic force micrograph [Fig. 4(b), inset] yields a root mean square roughness of 47 Å.

The hole mobility in SnPc films was measured by fitting the current of a ITO/SnPc (1000 Å)/Au device to a field dependent space-charge-limited mobility model,[17,18] assuming a relative dielectric constant of 3 for the organic. This analysis yields a hole mobility of $\mu_h=(2\pm1)\times10^{-10}$ cm^2/V s, as compared with CuPc[18] which has $\mu_h=(7\pm1)\times10^{-4}$ cm^2/V s. It is possible that the polycrystalline film of the nonplanar SnPc molecule has less molecular orbital overlap as compared with CuPc due to a larger intermolecular spacing. Indeed, the spacing between the planes formed by the four coordinating N atoms in SnPc alternates within a unit cell between 3.56 Å and 2.87 Å,[13] whereas it is 3.34 Å in the case of CuPc.[19] It is the larger of the two spacings in the SnPc lattice that determines the hole mobility, which may explain the significant differences in μ_h observed between these materials. The low mobility of SnPc results in increased series resistance, and hence a low FF in PV cells as the layer thickness is increased. That is, FF=0.5 for a 50-Å-thick SnPc layer [c.f. Fig. 2(a)], falling to 0.31 for a 200-Å-thick SnPc donor layer at 1 sun intensity. Depositing a 100-Å-thick CuPc wetting layer on the ITO surface prior to the SnPc deposition prevents the subsequent C_{60} acceptor layer from directly contacting the ITO through discontinuities in the thin donor layer.

In summary, we have demonstrated an organic solar cell with sensitivity extending into the NIR, using SnPc as an electron donor layer. Cell external quantum efficiency is significant for wavelengths between $350<\lambda<1000$ nm, remaining over 10% in the range of $350<\lambda<875$ nm. By optimizing layer thicknesses to retain good charge transport, and by placing the donor/acceptor interface in the region of highest incident light intensity, we achieve power conversion efficiencies of (1.0±0.1)% under 1 sun standard AM1.5G solar illumination, and up to (1.3±0.1)% under intense illumination. These results highlight the ability for the SnPc/C_{60} junction to find use in tandem organic solar cells[3,20] to extend the responsivity of organic photovoltaic cells into the infrared.

The authors thank the National Renewable Energy Laboratory, the Air Force Office of Scientific Research, and Global Photonic Energy Corporation for partial support of this work.

[1]S. R. Forrest, Nature (London) **428**, 911 (2004).
[2]S. R. Forrest, Mater. Res. Bull. **30**, 28 (2005).
[3]J. Xue, S. Uchida, B. P. Rand, and S. R. Forrest, Appl. Phys. Lett. **85**, 5757 (2004).
[4]X. J. Wang, E. Perzon, J. L. Delgado, P. de la Cruz, F. L. Zhang, F. Langa, M. Andersson, and O. Inganas, Appl. Phys. Lett. **85**, 5081 (2004).
[5]X. Wang, E. Perzon, F. Oswald, F. Langa, S. Admassie, M. R. Andersson, and O. Inganas, Adv. Funct. Mater. **15**, 1665 (2005).
[6]J. Xue and S. R. Forrest, J. Appl. Phys. **95**, 1869 (2004).
[7]R. A. Laudise, C. Kloc, P. G. Simpkins, and T. Siegrist, J. Cryst. Growth **187**, 449 (1998).
[8]ASTM Standards E1021, E948, and E973 (American Society for Testing and Materials, W. Conshohocken, PA).
[9]P. Peumans, V. Bulovic, and S. R. Forrest, Appl. Phys. Lett. **76**, 2650 (2000).
[10]J. Xue, S. Uchida, B. P. Rand, and S. R. Forrest, Appl. Phys. Lett. **84**, 3013 (2004).
[11]E. M. Maya, A. W. Snow, J. S. Shirk, R. G. S. Pong, S. R. Flom, and G. L. Roberts, J. Mater. Chem. **13**, 1603 (2003).
[12]L. A. A. Pettersson, L. S. Roman, and O. Inganas, J. Appl. Phys. **86**, 487 (1999).
[13]M. K. Friedel, B. F. Hoskins, R. L. Martin, and S. A. Mason, Chem. Commun. 400 (1970).
[14]R. Kubiak and J. Janczak, J. Alloys Compd. **189**, 107 (1992).
[15]K. Walzer and M. Hietschold, Surf. Sci. **471**, 1 (2001).
[16]L. B. Chen, A. Wagiki, T. Anzawa, M. Yamashita, and T. Tako, Acta Phys. Sin. **45**, 146 (1996).
[17]M. Pope and C. E. Swenberg, *Electronic Processes in Organic Crystals and Polymers*, 2nd ed. (Oxford University Press, New York, 1999).
[18]B. P. Rand, J. Xue, S. Uchida, and S. R. Forrest (unpublished).
[19]C. J. Brown, J. Chem. Soc. A 2488 (1968).
[20]B. P. Rand, P. Peumans, and S. R. Forrest, J. Appl. Phys. **96**, 7519 (2004).

Downloaded 12 Jan 2008 to 141.213.8.105. Redistribution subject to AIP license or copyright; see http://apl.aip.org/apl/copyright.jsp

Semitransparent organic photovoltaic cells

Rhonda F. Bailey-Salzman and Barry P. Rand
Department of Electrical Engineering, Princeton University, Princeton, New Jersey 08544

Stephen R. Forrest[a)]
Department of Electrical Engineering and Computer Science, University of Michigan, Ann Arbor, Michigan 48109; Department of Physics, University of Michigan, Ann Arbor, Michigan 48109; and Department of Materials Science and Engineering, University of Michigan, Ann Arbor, Michigan 48109

(Received 25 February 2006; accepted 8 May 2006; published online 5 June 2006)

We demonstrate semitransparent, small molecular weight organic solar cells employing a thin silver/indium tin oxide compound cathode with a maximum transmission of (60±6)% averaged over the visible spectral range and with a power conversion efficiency, $\eta_p=(0.28\pm0.03)\%$ under simulated, AM1.5G, 1 sun illumination. By increasing the Ag thickness, an average transmission of (26±3)% is achieved with $\eta_p=(0.62\pm0.06)\%$, a value approximately half of that obtained for the same structure employing a conventional, reflective, and thick Ag cathode. A semitransparent tandem organic solar cell with $\eta_p=(0.48\pm0.02)\%$ and an average transmission of (44±4)% is also demonstrated. Semitransparent organic photovoltaic cells have potential uses as tinted and power-generating thin-film coatings on architectural surfaces, such as windows and walls. The use of a transparent top electrode also significantly simplifies the design of tandem cells, relaxing requirements for the placement of different absorbing materials at the maxima of optical fields introduced by reflective cathodes. © *2006 American Institute of Physics*. [DOI: 10.1063/1.2209176]

Small molecular weight bilayer heterojunction organic photovoltaic (OPV) cells are recognized for their possible uses in large-area, flexible, and low-cost power generation applications. The thicknesses of the OPV active layers are limited by the relatively short exciton diffusion lengths that are on the order of a few tens of nanometers.[1] This leads to comparatively thin organic layers that can have a high optical transmissivity over the visible spectral range. Here, we demonstrate both single junction and tandem OPV cells that have a maximum average transmission of up to (60±6)% over the wavelength range from $\lambda=450$ to 750 nm, coupled with a relatively high power conversion efficiency. These cells have the potential for use as power-generating tinted thin-film coatings on windows and other architectural surfaces. For example, they can be used to replace current, passive tinted window coatings with a large power-generating surface with nearly identical optical properties. Indeed, semitransparent windows using dye-sensitized TiO_2 have already been demonstrated.[2] Previous work in inorganic photovoltaics has achieved semitransparent solar cells by introducing small holes in crystalline[3,4] and amorphous[5] Si cells, and by the use of two transparent conducting oxide electrodes in $Cu(InGa)Se_2$ cells.[6] Furthermore, ultrathin film organic solar cells have significant constraints on the placement of the absorbing layers with respect to the reflective metal cathode at the peak of the incident optical field. The use of transparent electrodes eliminates this constraint, thereby considerably simplifying the design of both single heterojunction and multijunction (tandem) cells.

The cells employ the archetype donor-acceptor (D-A) bilayer system[7] comprised of copper phthalocyanine (CuPc) and 3,4,9,10-perylenetetracarboxylic bis-benzimidazole (PTCBI). Purified organic source materials[8] were loaded into a high vacuum thermal evaporation chamber with a base pressure of 5×10^{-7} Torr. The materials were deposited at a growth pressure of 1×10^{-6} Torr, at a rate of 2 Å/s. When not under high vacuum, the sources were stored under a nitrogen atmosphere, with water and oxygen levels ≤1 ppm. Glass substrates coated with a 1500 Å thick indium tin oxide (ITO) anode having a sheet resistance of 15 Ω/□ were cleaned as described elsewhere,[8] followed by 5 min exposure to an ultraviolet-ozone surface treatment. The double heterojunction solar cell consisted of a 200 Å thick CuPc donor layer, a 250 Å thick PTCBI acceptor, and a 100 Å thick bathocuproine (BCP) exciton blocking layer,[9] while the two-cell tandem structure consisted of two, 200 Å thick CuPc by 200 Å thick PTCBI layer pairs forming heterojunctions separated by a sheet of ~0.5 nm diameter Ag nanoparticles,[10] followed by a 100 Å thick BCP layer. Layers of Ag, ranging in thickness from 0 to 100 Å, were thermally deposited through a shadow mask with an array of 1 mm diameter holes, followed by a 350 Å thick layer of ITO sputter deposited at 10 W and 13.56 MHz, resulting in a deposition rate of 5 Å/min. A vacuum break and exposure to air between organic film and cathode deposition were necessary prior to attachment of the shadow mask, which was done in a nitrogen ambient. Solar cell performance was characterized in the dark and under simulated AM1.5G solar illumination (uncorrected for solar spectral mismatch) using a 150 W xenon arc lamp.[11] Transmission measurements were obtained using a Perkin-Elmer spectrometer on unpatterned films grown simultaneously alongside of the photovoltaic structures.

Figure 1(a) shows a photograph of a metal-free organic thin-film photovoltaic cell with a patterned stripe of sputter-deposited ITO placed over a background image to demonstrate their transparent appearance. The stripe of ITO is not clearly discernible because of the similar transmissivity with

a)Electronic mail: stevefor@umich.edu

 © 2006 American Institute of Physics
Downloaded 12 Jan 2008 to 141.213.8.105. Redistribution subject to AIP license or copyright; see http://apl.aip.org/apl/copyright.jsp

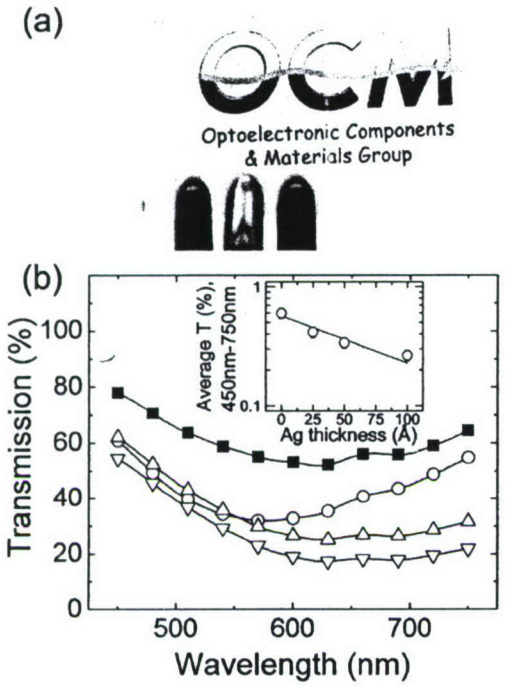

FIG. 1. (Color) (a) Image of a photovoltaic double heterojunction structure consisting of 200 Å copper phthalocyanine/250 Å 3,4,9,10-perylenetetracarboxylic bis-benzimidazole/100 Å bathocuproine on glass substrate precoated with an indium tin oxide (ITO) anode layer. The sample has a 350 Å sputter-deposited vertical stripe ITO cathode, which is not discernible due to the similar transmissivity with and without the ITO cathode. (b) Transmission spectra for photovoltaic structures as in (a), with 0 Å (filled squares), 25 Å (open circles), 50 Å (open triangles), and 100 Å (open upside-down triangles) thick Ag cathode layers. The curve shapes reflect the absorption spectrum of copper phthalocyanine. The inset shows optical transmission averaged over wavelengths of 450–750 nm vs thickness of the Ag layer. The line represents a fit to the data.

[(60±6)% averaged over the overlap between the thin-film absorbance and the solar spectrum] and without [(59±6)%] the ITO cathode. The transmission spectra of four semitransparent PV cells on glass, with the Ag in the compound ITO/Ag cathode ranging in thickness from 0 to 100 Å, are shown in Fig. 1(b). For the metal-free structure, the transmission T varies from approximately 60% at wavelengths between $\lambda=450$ and 700 nm, with a minimum at $\lambda=625$ nm corresponding to the absorption maximum of CuPc.[1] At a Ag thickness of 25 Å, the spectrum takes a slightly different shape, with enhanced absorption occurring in the blue. We attribute this effect to the discontinuity of thin Ag layers, leading to surface-plasmon enhancement of the optical field in the PTCBI layer.[10] The trend of decreasing T with increasing Ag layer thickness is shown in the inset of Fig. 1(b). The best fit to $T=T_o e^{(-x/\delta)}$ (where T_o is the average transmission of the metal-free device, x is the Ag thickness, and δ is the average optical skin depth), plotted as a solid line in Fig. 1(b), gives $\delta=(110\pm20)$ Å. This is similar to previous calculations of δ for thin Mg–Ag layers used as electron-injecting contacts in transparent organic light-emitting devices.[12]

The power conversion efficiency, η_p, and the responsivity, J_{sc}/P_o, are plotted versus Ag layer thickness in Fig. 2. Here, J_{sc} is the short circuit current density and P_o is the incident optical power density. The dashed lines represent the values obtained for conventional (i.e., nontransparent)

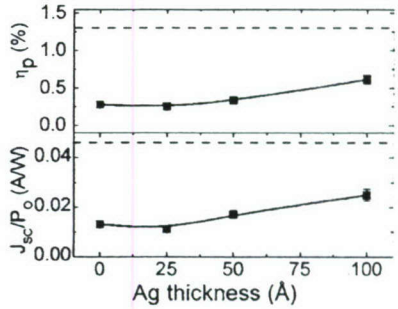

FIG. 2. Power conversion efficiency, η_p, and responsivity, J_{sc}/P_o, under simulated AM1.5G solar illumination vs cathode Ag layer thickness. The solid lines serve as guides to the eye, while the dashed lines represent values for conventional devices.

devices and the solid lines connecting data points are a guide for the eye. Conventional devices with the same organic layer thicknesses employing a thick Ag cathode were grown alongside the semitransparent devices as experimental controls. The conventional devices exhibited $\eta_p=(1.3\pm0.1)\%$, whereas the Ag-free structure has $\eta_p=(0.28\pm0.03)\%$. Increasing the Ag layer thickness from 25 to 100 Å results in $\eta_p=(0.25\pm0.03)\%$ to $(0.62\pm0.06)\%$, respectively.

Comparisons of the semitransparent cell efficiencies with that of the control must account for reflections that occur in the latter cell, contributing to the photocurrent via optical interference effects.[1] The increase in power conversion efficiency with Ag thickness is primarily due to the increasing responsivities of the cells with increasing cathode reflectivity. Thus, the corresponding responsivities are (0.013 ± 0.001) A/W (for a Ag thickness of $x=0$ Å), (0.011 ± 0.001) A/W ($x=25$ Å), (0.017 ± 0.002) A/W ($x=50$ Å), (0.025 ± 0.002) A/W ($x=100$ Å), and (0.046 ± 0.003) A/W for the conventional, thick Ag cathode cell. Simulations of the optical field within the metal-free structure predict that J_{sc} should be only 28% of that obtained for a conventional Ag cathode cell, which is in agreement with the experimentally determined ratio of 0.28 ± 0.04.

The small difference in the open circuit voltages of $V_{oc}=(0.40\pm0.02)$ V for the semitransparent cells, and (0.45 ± 0.02) V for the control, is expected due to the lower responsivity of the semitransparent cells. The open circuit voltage can be calculated using $V_{oc}\approx(nkT/q)\ln(J_{sc}/J_s+1)$, where n is the ideality factor, q is the electron charge, kT is the thermal energy at temperature T, and J_s is the reverse saturation current density.[13] Using typical values for our conventional cells ($n=1.64$, $J_s=10^{-4}$ A/cm^2), we calculate $V_{oc}=0.46$ V at $T=300$ K, and 0.40 V for the lowest responsivity transparent cell, values in agreement with the experimental results. All semitransparent cells have a fill factor of $FF=0.55\pm0.09$, which is somewhat less than for the control (where $FF=0.62\pm0.05$), possibly due to resistance of the compound cathode, and reduced J_{sc} and V_{oc}.

External quantum efficiency (EQE) data are shown in Fig. 3 for both conventional and semitransparent cells, with the latter having having $x=0$, 25, 50, and 100 Å Ag(x)/ITO cathodes. The curves all have similar shapes, with a peak EQE near $\lambda=625$ nm of $(17\pm1)\%$ for the conventional device, and $(5\pm1)\%$, $(4\pm1)\%$, $(6\pm1)\%$, and $(10\pm1)\%$ for the transparent cells, respectively. These data are consistent with

Downloaded 12 Jan 2008 to 141.213.8.105. Redistribution subject to AIP license or copyright; see http://apl.aip.org/apl/copyright.jsp

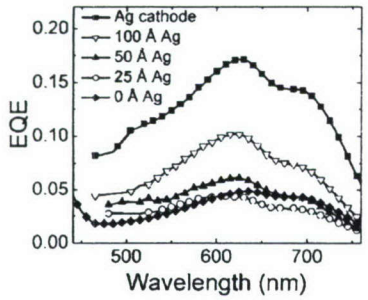

FIG. 3. External quantum efficiency (EQE) for a conventional, opaque cell (filled squares), a semitransparent cell with a 100 Å thick Ag/ITO compound cathode (open upside-down triangles), a semitransparent cell with a 50 Å thick Ag/ITO compound cathode (filled triangles), a semitransparent cell with a 25 Å thick Ag/ITO compound cathode (open circles), and a semitransparent cell with an ITO-only cathode (filled diamonds).

the expectations developed by analyzing the behavior of responsivity with increasing Ag thickness.

One possible advantage of the semitransparent structure is the possibility of stacking many cells to achieve even higher efficiency. We note that optical interference effects constrain the design of tandem cells when the top metal cathode is highly reflective. That is, because there is little reflection at the cathode in the semitransparent cells, optical interference effects between the incident and reflected optical fields are reduced, yielding a more uniform intensity distribution throughout the active layer structure. This relaxes the conditions restricting the placement of absorbing layers at a particular distance from the reflecting surface to maximize cell responsivity.

Current-voltage characteristics under AM1.5G, 1 sun intensity simulated illumination of a single, metal-free cell and a metal-free tandem cell are shown in Fig. 4. The single cell has $T=(60\pm6)\%$, $\eta_p=(0.28\pm0.02)\%$, $V_{oc}=0.38$ V, FF=0.54, and $J_{sc}/P_o=0.014$ A/W, while the tandem cell has $T=(44\pm4)\%$, $\eta_p=(0.48\pm0.02)\%$, $V_{oc}=0.75$ V, FF=0.49,

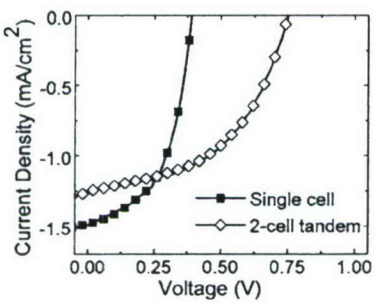

FIG. 4. Current-voltage characteristics for a single metal-free heterojunction cell (filled squares), and a two-cell tandem stack (open diamonds).

and $J_{sc}/P_o=0.013$ A/W. This represents an expected doubling in V_{oc} and a near doubling in η_p for the tandem cell. This tandem structure has not been fully optimized and we anticipate that even higher efficiencies can be achieved and a larger number of stacks implemented using this concept.

In conclusion, we have demonstrated a semitransparent small molecular weight organic photovoltaic cell with a peak average transmission over the visible spectrum of $(60\pm6)\%$, and a power conversion efficiency of $\eta_p=(0.28\pm0.03)\%$ under simulated AM1.5G, 1 sun illumination. Our results indicate that the exciton separation and charge extraction efficiencies of transparent devices are equivalent to those obtained for a conventional organic photovoltaic cell employing the same materials combinations, once the different optical characteristics of the two cell structures are taken into consideration. In addition, we have demonstrated a semitransparent tandem photovoltaic cell with nearly double the power conversion efficiency and open circuit voltage of a similar, single element cell. These results suggest that semitransparent organic photovoltaic cells have application to tinted power-generating and light attenuating coatings for windows and other architectural surfaces. Furthermore, the elimination of the reflective cathode considerably simplifies the design of single and multiple junction OPV cells.

This work was supported in part by funds from the Air Force Office of Scientific Research, the National Renewable Energy Laboratory (NREL), and Global Photonic Energy Corp., Ewing, NJ.

[1]P. Peumans, A. Yakimov, and S. R. Forrest, Appl. Phys. Rev. **93**, 3693 (2003).
[2]M. G. Kang, N. Park, Y. J. Park, K. S. Ryu, and S. H. Chang, Sol. Energy Mater. Sol. Cells **75**, 475 (2003).
[3]R. Kühn, A. Boueke, A. Kress, P. Fath, G. P. Willeke, and E. Bucher, IEEE Trans. Electron Devices **46**, 2013 (1999).
[4]P. Fath, H. Nussbaumer, and R. Burkhardt, Sol. Energy Mater. Sol. Cells **74**, 127 (2002).
[5]A. Takeoka, S. Kouzuma, H. Tanaka, H. Inoue, K. Murata, M. Morizane, N. Nakamura, H. Nishiwaki, M. Ohnishi, S. Nakano, and Y. Kuwano, Sol. Energy Mater. Sol. Cells **29**, 243 (1993).
[6]T. Nakada, Y. Hirabayashi, T. Tokado, D. Ohmori, and T. Mise, Sol. Energy **77**, 739 (2004).
[7]C. W. Tang, Appl. Phys. Lett. **48**, 183 (1986).
[8]R. F. Salzman, J. Xue, B. P. Rand, A. Alexander, M. E. Thompson, and S. R. Forrest, Org. Electron. **6**, 242 (2005).
[9]P. Peumans, V. Bulovic, and S. R. Forrest, Appl. Phys. Lett. **76**, 2650 (2000).
[10]B. P. Rand, P. Peumans, and S. R. Forrest, J. Appl. Phys. **96**, 7519 (2004).
[11]Oriel Instruments, 150 Long Beach Blvd., Stratford, CT 06615.
[12]V. Bulovic, G. Gu, P. E. Burrows, S. R. Forrest, and M. E. Thompson, Nature (London) **380**, 29 (1996).
[13]J. Xue, S. Uchida, B. P. Rand, and S. R. Forrest, Appl. Phys. Lett. **84**, 3013 (2004).

Downloaded 12 Jan 2008 to 141.213.8.105. Redistribution subject to AIP license or copyright; see http://apl.aip.org/apl/copyright.jsp

J|A|C|S
COMMUNICATIONS

Published on Web 06/02/2006

Enhanced Open-Circuit Voltage in Subphthalocyanine/C_{60} Organic Photovoltaic Cells

Kristin L. Mutolo,[†] Elizabeth I. Mayo,[†] Barry P. Rand,[‡] Stephen R. Forrest,[‡,§] and Mark E. Thompson*[,†]

Department of Chemistry, University of Southern California, Los Angeles, California 90089, Department of Electrical Engineering and Princeton Institute for the Science and Technology of Materials (PRISM), Princeton University, Princeton, New Jersey 08544, and Departments of Electrical Engineering and Computer Science, Physics and Materials Science and Engineering, University of Michigan, Ann Arbor, Michigan 48109

Received March 9, 2006; E-mail: met@usc.edu

Organic photovoltaic (PV) cells have attracted attention due to their ease of fabrication and potential for low-cost production.[1-4] Since Tang reported the first thin-film organic PV cell based on a single donor−acceptor (D−A) heterojunction,[4] research has been focused on enhancing the efficiency of these cells through use of new materials and device structures. PV cells employing polymer−fullerene heterojunctions have been shown to have power conversion efficiencies (η_P) approaching 5%,[5] obtained through variations in the processing techniques. Recently, Xue et al. reported efficiencies as high as 4% under 4 suns simulated AM1.5G illumination in a double-heterostructure copper phthalocyanine (CuPc)/C_{60} thin-film cell with Ag as the metal cathode.[6] PV cells such as these can be further enhanced by stacking two cells in series, yielding efficiencies exceeding 5.5%.[7]

Efficiency is dependent on the open circuit voltage (V_{oc}), the short-circuit current density (J_{sc}), and the fill factor (FF) via[3]

$$\eta_P = (J_{sc}\, V_{oc}\, FF)/P_o \qquad (1)$$

where P_o is the incident optical power. Here, FF depends on the series resistance and is typically between 0.5 and 0.65 for small-molecular-weight organic photovoltaics. J_{sc} is controlled by the overlap between the absorption of the organics and the solar spectrum, as well as the magnitudes of the extinction coefficients and thicknesses of the absorbing layers. However, enhanced spectral overlap must be accomplished without a significant loss in exciton diffusion length or in the charge transport properties of the materials. The typical $V_{oc} \cong 500$ mV at 1 sun for conventional CuPc donor-based PV cells is significantly less than the energy of the absorbed photon (~2 eV). Clearly, an increase in V_{oc} offers a significant opportunity for substantial improvement in η_P. However, it has proven difficult to achieve large increases in the V_{oc} without an accompanying decrease in J_{sc} or FF.[8]

The origin of V_{oc} in organic solar cells is not well understood.[9,10] It has been suggested that this quantity depends on the energy difference between the lowest unoccupied molecular orbital (LUMO) of the acceptor-like material and the highest occupied molecular orbital (HOMO) of the donor-like material at the heterointerface in a bilayer cell (referred to as the interface gap, I_g, Figure 1, inset).[11] In this paper, we report on a double-heterostructure boron subphthalocyanine chloride (SubPc)/C_{60} thin-film cell with $I_g = 1.9$ eV, compared to a CuPc/C_{60} cell with $I_g = 1.5$ eV, resulting in an increase in V_{oc} of approximately the same magnitude, suggesting that V_{oc} is indeed a function of I_g.

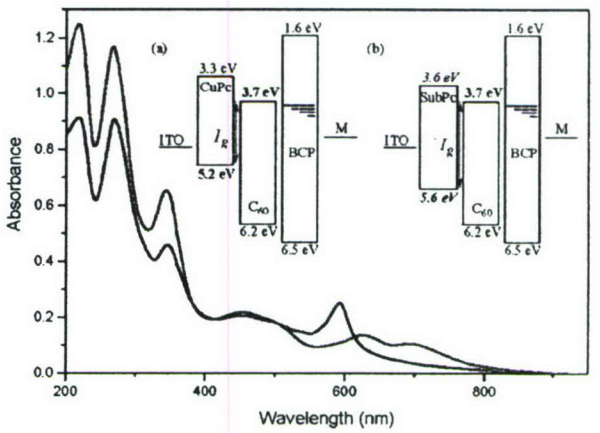

Figure 1. Absorbance spectra (on quartz) of stacked CuPc (200 Å)/C_{60} (400 Å)/BCP (100 Å) (red) and of SubPc (130 Å)/C_{60} (325 Å)/BCP (100 Å) (blue). Inset: Schematic energy level diagram for devices with (a) CuPc or (b) SubPc as the donor layer. HOMO energies are from UPS, and the LUMO energies are from IPES measurements, except for SubPc, where the LUMO[12] and HOMO[13] energies are determined from electrochemistry.

While CuPc is a planar compound with an 18 π-electron phthalocyanine macrocycle, SubPc is composed of three N-fused diiminoisoindole rings centered around a boron core. This 14 π-electron aromatic macrocycle has a nonplanar cone-shaped structure with the tetrahedral boron center out of plane with the aromatic ligand and can pack in different orientations, depending on the deposition conditions.[14,15] With strong absorption in the visible and extinction coefficients similar to CuPc (Figure 1), SubPc is a candidate as an electron donor material. The first oxidation and reduction potentials are 0.69 and −1.40 V vs a ferrocene (Fc/Fc^+) reference.[16] C_{60}, with oxidation and reduction potentials of 1.26 and −1.06 V vs Fc/Fc^+,[17] should therefore be suitable as the acceptor material in a PV cell based on SubPc.[3]

A range of efficiencies have been reported for CuPc/C_{60} device architectures.[3,18-21] To eliminate performance variance due to fabrication conditions, control devices were fabricated simultaneously with the SubPc cells. Conventional PV cell structures fabricated as controls were ITO/CuPc (200 Å)/C_{60} (400 Å)/BCP (100 Å) with a Ag (CuPc1) or Al cathode (CuPc2). The SubPc cells consisted of ITO/SubPc (200 Å)/C_{60} (400 Å)/BCP (100 Å) and a Ag (SubPc1) or Al (SubPc2) cathode.

The current density vs voltage ($J-V$) characteristics were measured in the dark and under 1−5 suns AM1.5G simulated illumination, uncorrected for solar mismatch. $J-V$ characteristics at 1 sun are provided in Table 1. The V_{oc} of SubPc1 and SubPc2 is 150 mV higher than for CuPc cells, although both J_{sc} and FF are

[†] University of Southern California.
[‡] Princeton University.
[§] University of Michigan.

10.1021/ja061655o CCC: $33.50 © 2006 American Chemical Society

Table 1. Structure and Photovoltaic Data for Devices Illuminated under 1 Sun AM1.5G Simulated Solar Illumination

cell	D/C_{60} (A)	M[c]	J_{sc} (mA cm^{-2})	V_{oc} (V)	FF	η
CuPc1	200[a]/400	Ag	4.13	0.43	0.61	1.2
CuPc2	200[a]/400	Al	3.07	0.42	0.58	0.9
SubPc1	200[b]/400	Ag	2.05	0.57	0.33	0.4
SubPc2	200[b]/400	Al	1.83	0.58	0.36	0.4
SubPc3	130[b]/325	Ag	3.61	0.98	0.41	1.7
SubPc4	130[b]/325	Al	3.36	0.97	0.57	2.1

[a] D = CuPc. [b] D = SubPc. [c] M is the cathode material.

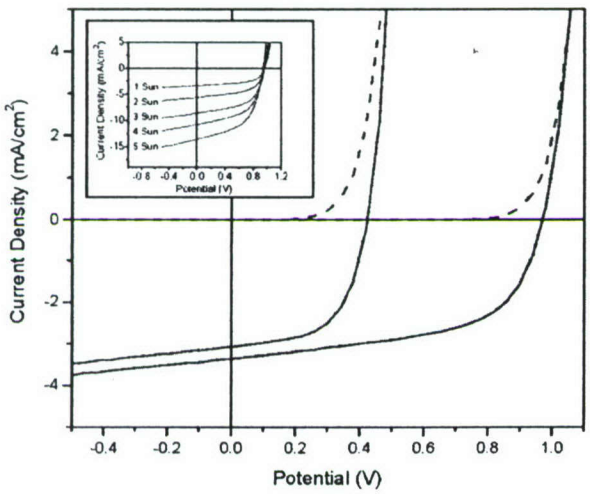

Figure 2. $J-V$ characteristics of CuPc2 (red) and SubPc4 (blue) under 1 sun AM 1.5G simulated illumination (solid) and in the dark (dashed). Inset: Intensity dependence of the SubPc4 device at 1−5 suns.

reduced, resulting in a reduced power efficiency. This is likely due to a high series resistance, which suggests that thinner donor layers are necessary for optimal device performance. Since SubPc absorbs at shorter wavelengths than CuPc, an optimal cell structure requires a corresponding decrease in C_{60} thickness to ensure that the SubPc/C_{60} interface is located in a region where the short-wavelength light intensity is highest.[22] Following this criterion, a device with the following structure was fabricated: ITO/SubPc (130 Å)/C_{60} (325 Å)/BCP (100 Å) with a Ag (SubPc3) or Al (SubPc4) cathode.

The $J-V$ characteristics of SubPc4 and CuPc2 are shown in Figure 2. In this case, V_{oc} of SubPc4 is more than double that of CuPc2, accompanied by a nearly 10% increase in J_{sc}. Although the SubPc absorption is blue-shifted relative to that of CuPc with a decreased absorbance at $\lambda = 700$ nm (Figure 1), this is compensated by the increased absorbance at $\lambda = 590$ nm, which is in a higher intensity region of the solar spectrum. V_{oc} and FF of SubPc4 are nearly independent of light intensity between 1 and 5 suns (Figure 2, inset), while the power conversion efficiency achieves a maximum value of $\eta_P = 2.1 \pm 0.2\%$ at 1 sun.

A proposed energy level diagram for the CuPc and SubPc devices is shown in the Figure 1 inset. The SubPc/C_{60} device has an I_g that is 400 meV greater than that for the CuPc/C_{60} device, correlating to an increase of V_{oc} of approximately the same magnitude (550 mV). We attribute the significant increase in V_{oc} to the smaller HOMO energy of SubPc and the subsequent increase in I_g, supporting the hypothesis that V_{oc} is dependent on I_g. V_{oc} can be increased by series resistance, which may, in turn, depend on the presence of impurities or crystalline disorder (an effect which will be discussed elsewhere). Note that the increase in V_{oc} is approximately 20% higher than that in I_g, suggesting that resistance may be affecting V_{oc}; however, the high FF's indicate that resistance alone cannot account for the increased V_{oc}.

It has been shown that varying the metal cathode has a minimal effect on V_{oc}.[4,11] However, CuPc1 with a Ag cathode shows an increased J_{sc} and FF relative to the analogous device with Al (CuPc2). It is unclear why such an effect on J_{sc} and FF is observed, whereas V_{oc} is the same for both devices. Alternatively for SubPc, FF decreases for the Ag device (SubPc3) compared to the Al device (SubPc4).

In summary, SubPc/C_{60}-based PV cells have more than twice the V_{oc} as compared to conventional devices based on CuPc/C_{60} cells, resulting in a more than doubling of the cell power conversion efficiency. By using a strongly absorbing donor material with a deep HOMO, I_g and, consequently, V_{oc} are increased without a concomitant reduction in J_{sc}. This work supports the hypothesis that I_g is a dominant factor in determining V_{oc} in organic heterojunction cells.

Acknowledgment. This work was supported by Global Photonic Energy Corp., the Air Force Office of Scientific Research, and the National Renewable Energy Laboratory.

Supporting Information Available: Experimental conditions for device fabrication, CuPc and SubPc structures (Figure S1), and $J-V$ characteristics for 1−5 suns for SubPc4 (Table S1 and Figure S2). This material is available free of charge via the Internet at http://pubs.acs.org.

References

(1) Granstrom, M.; Petritsch, K.; Arias, A. C.; Lux, A.; Andersson, M. R.; Friend, R. H. *Nature* **1998**, *395*, 257−260.
(2) Halls, J. J. M.; Walsh, C. A.; Greenham, N. C.; Marseglia, E. A.; Friend, R. H.; Moratti, S. C.; Holmes, A. B. *Nature* **1995**, *376*, 498−500.
(3) Peumans, P.; Yakimov, A.; Forrest, S. R. *J. Appl. Phys.* **2004**, *95*, 2938−2938.
(4) Tang, C. W. *Appl. Phys. Lett.* **1986**, *48*, 183−185.
(5) Ma, W. L.; Yang, C. Y.; Gong, X.; Lee, K.; Heeger, A. J. *Adv. Funct. Mater.* **2005**, *15*, 1617−1622.
(6) Xue, J. G.; Uchida, S.; Rand, B. P.; Forrest, S. R. *Appl. Phys. Lett.* **2004**, *84*, 3013−3015.
(7) Xue, J. G.; Uchida, S.; Rand, B. P.; Forrest, S. R. *Appl. Phys. Lett.* **2004**, *85*, 5757−5759.
(8) Singh, V. P.; Singh, R. S.; Parthasarathy, B.; Aguilera, A.; Anthony, J.; Payne, M. *Appl. Phys. Lett.* **2005**, *86*, 0821061−0821063.
(9) Brabec, C. J.; Cravino, A.; Meissner, D.; Sariciftci, N. S.; Fromherz, T.; Rispens, M. T.; Sanchez, L.; Hummelen, J. C. *Adv. Funct. Mater.* **2001**, *11*, 374−380.
(10) Gledhill, S. E.; Scott, B.; Gregg, B. A. *J. Mater. Res.* **2005**, *20*, 3167−3179.
(11) Gadisa, A.; Svensson, M.; Andersson, M. R.; Inganas, O. *Appl. Phys. Lett.* **2004**, *84*, 1609−1611.
(12) Bredas, J. L.; Silbey, R.; Boudreaux, D. S.; Chance, R. R. *J. Am. Chem. Soc.* **1983**, *105*, 6555−6559.
(13) D'Andrade, B. W.; Datta, S.; Forrest, S. R.; Djurovich, P.; Polikarpov, E.; Thompson, M. E. *Org. Electron.* **2005**, *6*, 11−20.
(14) Claessens, C. G.; Gonzalez-Rodriguez, D.; Torres, T. *Chem. Rev.* **2002**, *102*, 835−853.
(15) Mattheus, C. C.; Michaelis, W.; Kelting, C.; Durfee, W. S.; Wohrle, D.; Schlettwein, D. *Synth. Met.* **2004**, *146*, 335−339.
(16) del Rey, B.; Keller, U.; Torres, T.; Rojo, G.; Agullo-Lopez, F.; Nonell, S.; Marti, C.; Brasselet, S.; Ledoux, I.; Zyss, J. *J. Am. Chem. Soc.* **1998**, *120*, 12808−12817.
(17) Webster, R. D.; Heath, G. A. *Phys. Chem. Chem. Phys.* **2001**, *3*, 2588−2594.
(18) Schultes, S. M.; Sullivan, P.; Heutz, S.; Sanderson, B. M.; Jones, T. S. *Mater. Sci. Eng. C: Biomimetic Supramol. Syst.* **2005**, *25*, 858−865.
(19) Salzman, R. F.; Xue, J. G.; Rand, B. P.; Alexander, A.; Thompson, M. E.; Forrest, S. R. *Org. Electron.* **2005**, *6*, 242−246.
(20) Peumans, P.; Forrest, S. R. *Appl. Phys. Lett.* **2002**, *80*, 338−338.
(21) Khodabakhsh, S.; Sanderson, B. M.; Nelson, J.; Jones, T. S. *Adv. Funct. Mater.* **2006**, *16*, 95−100.
(22) Pettersson, L. A. A.; Roman, L. S.; Inganas, O. *J. Appl. Phys.* **1999**, *86*, 487−496.

JA061655O

Offset energies at organic semiconductor heterojunctions and their influence on the open-circuit voltage of thin-film solar cells

Barry P. Rand and Diana P. Burk
Department of Electrical Engineering and Princeton Institute for the Science and Technology of Materials (PRISM), Princeton University, Princeton, New Jersey 08544, USA

Stephen R. Forrest*
Departments of Electrical Engineering and Computer Science, Physics, and Materials Science and Engineering, University of Michigan, Ann Arbor, Michigan 48109, USA

(Received 2 October 2006; revised manuscript received 17 January 2007; published 27 March 2007)

Organic semiconductor heterojunction (HJ) energy level offsets are modeled using a combination of Marcus theory for electron transfer, and generalized Shockley theory of the dark current density vs voltage (J-V) characteristics. This model is used to fit the J-V characteristics of several donor-acceptor combinations commonly used in thin film organic photovoltaic cells. In combination with measurements of the energetics of donor-acceptor junctions, the model predicts tradeoffs between the junction open-circuit voltage (V_{OC}) and short-circuit current density (J_{SC}). The V_{OC} is found to increase with light intensity and inversely with temperature for 14 donor-acceptor HJ materials pairs. In particular, we find that V_{OC} reaches a maximum at low temperature ($\sim$175 K) for many of the heterojunctions studied. The maximum value of V_{OC} is a function of the difference between the donor ionization potential and acceptor electron affinity, minus the binding energy of the dissociated, geminate electron-hole pair: a general relationship that has implications on the charge transfer mechanism at organic heterojunctions. The fundamental understanding provided by this model leads us to infer that the maximum power conversion efficiency of double heterostructure organic photovoltaic cells can be as high as 12%. When combined with mixed layers to increase photocurrent and stacked cells to increase V_{OC}, efficiencies approaching 16% are within reach.

DOI: 10.1103/PhysRevB.75.115327 PACS number(s): 73.40.Lq, 72.80.Le, 71.35.−y

I. INTRODUCTION

Semiconductor heterojunctions (HJ) are an ubiquitous feature of almost all photonic device structures, as they are useful in locally confining or controlling both charge and photons.[1] One of the most important issues facing the study of heterojunctions in new materials systems is the magnitude and the origin of the heterobarrier between dissimilar, contacting semiconductors. In contrast to inorganic heterojunctions, organic HJs generally do not have a significant amount of free charge that redistribute when materials are brought into contact.[2] Furthermore, their energetics are rarely influenced by the crystalline morphology at the interface since most of these van der Waals bonded materials do not require lattice matching to form ordered structures.[3] Both of these factors lead to a considerable simplification in our ability to quantitatively determine the source of the heterobarrier, and to grow organic heterojunctions to test these theories over an exceptionally wide range of materials properties. Hence, they present an opportunity to understand many of the factors governing the nature of charge transport and energetics of this most fundamental semiconductor property.

Among the class of organic HJs that are important to investigate, donor-acceptor (DA) junctions used in organic photovoltaic (PV) cells are key to cell efficiency, as they are the site for photogenerated exciton dissociation and charge transfer into the contacting materials forming this active junction. For this reason, the PV cell represents an ideal vehicle for studying HJ properties. Indeed, organic PV cells based on small-molecular weight materials and conjugated polymers have recently attracted interest as a potential approach to realizing low cost solar energy conversion.[4–6] Despite gains in power conversion efficiency (η_P) to approximately 5% for both small-molecule and polymer-based structures,[7,8] further improvements are necessary to realize practical devices. To fully optimize these PV cells, there needs to be a more complete understanding of the physics governing their operation, and in particular, the physics of photoinduced charge transfer at the DA HJ.

One issue of considerable focus in DA HJs has been the HJ open-circuit voltage (V_{OC}), typically in the range of 0.5 V to 1 V,[9] whereas the peak absorption of the solar spectrum of the constituent organic materials is at photon energies $>$2.5 eV. In principle, if qV_{OC} (where q is the electron charge) approaches the photon energy, organic solar cells would be 2 to 5 times more efficient than currently obtained. The experimental effort to determine the origin of the low V_{OC} has primarily consisted of understanding observed correlations between V_{OC} and the difference between the highest occupied molecular orbital (HOMO) of the donor material and lowest unoccupied molecular orbital (LUMO) of the acceptor.[9–14] This correlation is consistent with the fact that V_{OC} is a property of the DA energy levels and their offsets at the contacting heterointerface rather than due to the work function differences between the metal electrodes, as has also been proposed.[10]

To understand the fundamental physics governing V_{OC} and its relationship with the offset energies at DA HJs, in this work we measure the *maximum* V_{OC} attainable in organic PV cells based on a variety of combinations of donor and accep-

 ©2007 The American Physical Society

tor materials. To determine this maximum value, either temperature is reduced or light intensity increased until V_{OC} reaches saturation. The maximum value of V_{OC} is found to be related to the donor HOMO and acceptor LUMO energies, as well as the binding energy of the dissociated, geminate electron-hole pair created as a result of electron transfer.

To explore the dependence of V_{OC} on the energetic properties of the contacting materials, we present a comprehensive model for organic *DA* HJs based on molecular materials commonly employed in PV cells. The dark currents of various HJs are modeled using a generalized Shockley equation for *p-n* junctions.[15] By adapting a model for electron transfer based on nonadiabatic Marcus theory[16] to determine the photocurrent as a function of voltage, we fit the response of different *DA* HJ PV cells as functions of temperature and illumination intensity to extract the electron transfer rates. These rates are shown to follow the predictions of Marcus theory of electron transfer,[17] including an inverted region at a large *DA* offset energy. Applying this theory reveals that η_P approaching 12% is feasible for a single *DA* HJ, and possibly up to 16% by incorporating other more complex architectures,[7,18,19] demonstrating that practical efficiencies are within reach.

This paper is organized as follows: In Sec. II, we describe the principles of photocurrent generation at a *DA* HJ. This includes a presentation of quantitative models for the photocurrent and dark current, and the maximum, or saturated value of V_{OC} based on Marcus theory as applied to a heterointerface in combination with Shockley's theory for *p-n* junctions. Experimental details are described in Sec. III. The dependence of the dark current and PV operating parameters on temperature and HJ composition are provided in Sec. IV. Section V presents a discussion of the key findings as well as model predictions for the maximum η_P in *DA* HJ solar cells consisting of materials and structures analogous to those studied here. We provide conclusions in Sec. VI. A detailed derivation of the current model is given in the Appendix.

II. THEORY

A. Photocurrent at a donor-acceptor heterojunction

A schematic energy diagram for an organic HJ based on a contact between a donor and acceptor material is shown in Fig. 1. The difference between the ionization potential (IP) and electron affinity (EA) is known as the transport gap, E_{tran}. The optical energy gap of each material, E_{opt}, is defined as the position of the low-energy absorption edge. The exciton binding energy is $E_B = \mathrm{IP} - \mathrm{EA} - E_{opt}$, which typically ranges from 0.2 eV to 1 eV for organic semiconductors.[20,21]

The external quantum efficiency, η_{EQE}, determines the number of electrons collected per incident photon. For the organic HJ, η_{EQE} is[22]

$$\eta_{EQE}(\lambda, V) = \eta_A(\lambda)\,\eta_{ED}\,\eta_{CT}(V)\,\eta_{CC}(V). \quad (1)$$

Here, η_A is the absorption efficiency of the incident photons in the photoactive region resulting in the formation of excitons, η_{ED} is the efficiency of photogenerated excitons that diffuse to the *DA* interface, η_{CT} is the charge transfer efficiency for excitons to dissociate into holes in the donor and electrons in the acceptor layers at the HJ, and η_{CC} is the charge collection efficiency, equal to the fraction of photogenerated charge carriers collected at the electrodes. The wavelength of the incident light is λ, and V is the applied voltage.

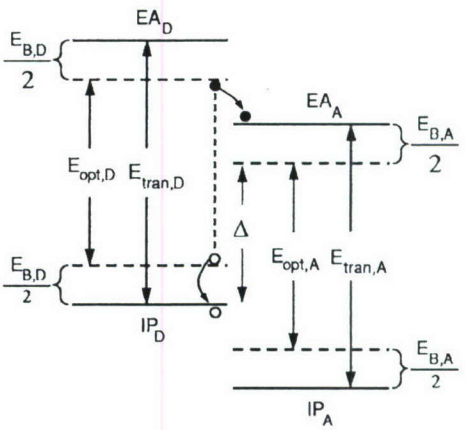

FIG. 1. Proposed energy level diagram of an organic heterojunction between a donor (D) and an acceptor (A) layer. Here IP and EA are the ionization potential and electron affinity, respectively. The exciton binding energy (E_B) of each material is equal to the difference between the transport gap (E_t) and optical gap (E_{opt}). Also, Δ is the interface energy gap. The process of charge transfer of an exciton from $D \rightarrow A$ is also illustrated.

To determine η_A, the dielectric constants, thicknesses, and optical field intensities within the active layers are required. The exciton diffusion length, L_D, determines η_{ED}, where L_D is from 5 nm to 30 nm for most photoactive molecular organic materials used in PV cells.[22] When the energy level offsets for the HOMO or LUMO between the donor and acceptor layers (ΔE_{HOMO} or ΔE_{LUMO}, respectively) are greater than E_B, charge transfer at the *DA* interface is energetically favorable, as shown in Fig. 1.

Both η_{CT} and η_{CC} are functions of V, as implied by Eq. (1). To evaluate these efficiencies, we adapt nonadiabatic Marcus theory to molecular organic HJs, as described by Nelson *et al.*[16] A representation of the model is shown in Fig. 2, where unshaded arrows correspond to the contribution to the donor photocurrent (J_D), while shaded arrows represent contributions to the acceptor photocurrent (J_A). The excited electron may be transferred from the donor LUMO, E_{cD} to the acceptor LUMO, E_{cA}. Similarly, the hole is transferred from the acceptor HOMO, E_{vA} to the donor HOMO, E_{vD}. The quasi-Fermi levels, μ (dotted lines in Fig. 2), determine the occupation probabilities of the various energy levels at voltage, V, (i.e., $f_i = \{1 + \exp[(E_i - \mu_i)/k_B T]\}^{-1}$, where f is the occupation probability, k_B is Boltzmann's constant, and T is the temperature). Here, we outline the steps used to calculate J_D, where the calculation of J_A follows an analogous procedure.

The method for calculating the current density generated by light absorption, G_{vcD}, is provided in the Appendix [cf. Eq. (A1)]. Here, the first two lower-case subscripts refer to a transition from the valence level, v, or HOMO, to the conduction level, c, or LUMO. The third subscript corresponds to either donor, D, or acceptor, A, as in Fig. 2. Thus, G_{vcD} is

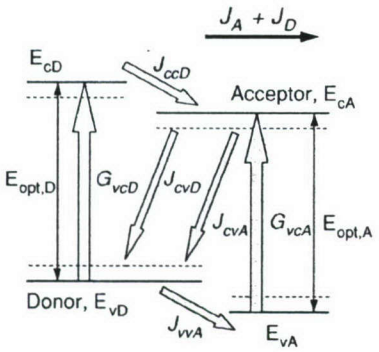

FIG. 2. Schematic of the various contributions to the current generated at a donor-acceptor heterojunction. Unshaded arrows correspond to the donor photocurrent while shaded arrows represent contributions to the acceptor photocurrent. Dotted lines show the Fermi energy levels. The subscripts v, c, A, and D refer to the valance and conduction energy levels in the acceptor and donor layers, respectively. For example, J_{cvD} is the current from the conduction level of the acceptor flowing to the valance level of the donor. Also, opt refers to energy gaps measured by optical means.

the source current for electron transfer, from which the efficiencies, η_{CT} and η_{CC}, are calculated. The forward and reverse current densities, J_{ccD} and J_{cvD}, respectively, are calculated using[16]

$$J_{if} = qk_{if}[f_i(1-f_f) - \exp(-E_{if}/k_BT)f_f(1-f_i)]. \quad (2)$$

Here, i and f represent initial and final energy levels that correspond to the first two subscripts of the currents given in Fig. 2. The Boltzmann factor is due to the junction energy barrier to reverse current flow. The free energy difference between i and f is $E_{if}=E_i-E_f$, and k_{if} is the electron transfer rate, given by nonadiabatic Marcus theory[17] as

$$k_{if} = \left(\frac{4\pi^3}{h^2\lambda_{if}k_BT}\right)^{1/2} V_{if}^2 \exp\left(-\frac{(E_{if}+\lambda_{if})^2}{4\lambda_{if}k_BT}\right). \quad (3)$$

Here, V_{if} is the electronic coupling matrix element, assumed to be equal for a given DA pair, h is Planck's constant, and λ_{if} is the molecular reorganization energy. In the case of forward electron transfer (k_{ccD}), E_B is added to E_{if}, thereby reducing the electron transfer rate (for exothermic transfer, $E_{if}<0$).

To determine $\eta_{CT}(V)$ and $\eta_{CC}(V)$, J_D is calculated as a function of the difference in quasi-Fermi energies in the D and A materials. The Fermi level is $\mu_0=E_v+E_{tran}/2$ at equilibrium. Then, $J_D=J_{ccD}-J_{cvD}$ and $G_{vcD}=J_{ccD}+J_{cvD}$, while $qV=\mu_a-\mu_d=2(\mu_a-\mu_0)$, where μ_a (μ_d) is the quasi-Fermi level of the acceptor (donor) layer. A solution is found using a set of parametric equations (see Appendix) to calculate the possible occupation probabilities (and therefore V). From the resulting J_D-V characteristic, we calculate the collection function, $H(V)$, for the donor photocurrent contribution, *viz.*,

$$H_D(V) = \eta_{CT}(V)\eta_{CC}(V) = \left(\frac{k_{ccD}}{k_{ccD}+k_{cvD}}\right)\frac{J_D}{q\phi_s}, \quad (4)$$

where ϕ_s is the optical absorption rate (see Appendix), and the total $H(V)=H_D(V)+H_A(V)$.

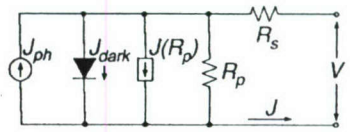

FIG. 3. Equivalent circuit for an organic heterojunction used to understand the current density versus voltage (J-V) model. The specific series and parallel resistances are R_s and R_p, respectively, $J(R_p)$ is the current density due to R_p, and J_{dark} and J_{ph} the dark and photocurrent densities, respectively.

B. Current-voltage characteristics of the donor-acceptor heterojunction

The equivalent circuit of an organic PV cell is shown in Fig. 3, and forms for basis for our current model. The photocurrent source, J_{ph}, opposes the dark current, J_{dark}, which is limited by the series and parallel resistances, R_s and R_p, respectively. Here, $J(R_p)$ is the current flowing through R_p. The J-V characteristics of an organic PV cell can then be expressed by the generalized Shockley equation[15]

$$J = \frac{R_p}{R_s+R_p}\left\{J_S\left[\exp\left(\frac{q(V-JR_s)}{nk_BT}\right)-1\right]+\frac{V}{R_p}\right\} - J_{ph}(V) \quad (5)$$

where n is the diode ideality factor, and J_S is the reverse saturation current, *viz.*,[23]

$$J_S = J_{S0}\exp\left(-\frac{E_g}{2nk_BT}\right). \quad (6)$$

Here, E_g is the HJ activation energy barrier, equal to $E_g=IP_D-EA_A$, and J_{S0} is a temperature independent prefactor. The photocurrent density in Eq. (5) is

$$J_{ph}(V) = \int \frac{q\lambda}{hc}\eta_{EQE}(\lambda,V)S(\lambda)d\lambda, \quad (7)$$

where $S(\lambda)$ is the spectral irradiance of the incident light, and c is the speed of light. By inserting Eqs. (1) and (4) into Eq. (7),

$$J_{ph}(V) = P_0R_0H(V). \quad (8)$$

Here, $P_0=\int S(\lambda)d\lambda$ is the incident optical power density, and $R_0=\int\frac{q\lambda}{hc}\eta_A(\lambda)\eta_{ED}d\lambda$ is the responsivity for $\eta_{CT}=\eta_{CC}=1$, calculated using the transfer-matrix approach to determine the optical field intensity, and L_D in the D and A layers.[24]

The dark current density, J_{dark}, is also given by Eq. (5) when $J_{ph}=0$. From the $J-V$ characteristics, the short-circuit current density, J_{SC}, V_{OC}, the fill factor [FF $=\max(JV)/J_{SC}V_{OC}$], and the power conversion efficiency, $\eta_P=J_{SC}V_{OC}FF/P_0$, are calculated.

C. Maximum open-circuit voltage

To understand how V_{OC} changes with P_0 and T, we solve Eq. (5) at $J=0$ for $V=V_{OC}$.

TABLE I. Donor and acceptor materials and their corresponding ionization potentials (IP), electron affinities (EA), and optical energy gaps (E_{opt}).

Label[a]	Material[b]	IP[c] (eV)	EA (eV)[d]	E_{opt} (eV)	Reference
1	CuPc	5.2(7)	3.2(7)	1.7	43
2	Pentacene	5.1(9)	3	1.8(8)	43
3	NPD	5.5	1.7	3.1	43
4	SubPc	5.6		2.0	38
5	$Ru(acac)_3$	4.9		2.1	25
A	C_{60}	6.2(4)	3.6	1.8	44
B	C_{70}	6.4(1)	4.3	1.7(3)	44
C	PTCBI	6.2	3.6	1.7	43
D	PTCDA	6.8	4.6	2.2	43

[a]Numbers represent donor materials while letters represent acceptor materials.
[b]CuPc, copper phthalocyanine; NPD, *N*,*N*′-di-1-naphthyl-*N*,*N*′-diphenyl-1,1′-biphenyl-4,4′diamine; SubPc, boron subphthalocyaninechloride; $Ru(acac)_3$, ruthenium (III) trisacetylacetonato; PTCBI, 3,4,9,10-perylenetetracarboxylic bisbenzimidazole, and PTCDA, perylene-3,4,9,10-tetracarboxylic-3,4,9,10-dianhydride.
[c]Measured with ultraviolet photoemission spectroscopy with an error of ±0.1 eV.
[d]Measured with inverse photoemission spectroscopy with an error of ±0.5 eV.

$$V_{OC} = \frac{nk_BT}{q} \ln\left(\frac{J_{ph}(V_{OC})}{J_S} + 1 - \frac{V_{OC}}{J_S R_p}\right). \quad (9)$$

Equations (8) and (9) show that as P_0 increases, $V_{OC} \propto \ln(P_0)$ assuming that n and $H(V_{OC})$ are constant, and the product $J_S R_p \gg V_{OC}$. This is true at P_0 less than a few suns intensity (1 sun=100 mW/cm^2), but for larger P_0, $R_p \propto P_0^{-1}$ (see Sec. IV A) and $H(V_{OC})$ decreases. As P_0 is increased further, V_{OC} saturates at a maximum, V_{OC}^{max}. Similarly, as T is reduced, $V_{OC} \propto T^{-1}$ owing to the rapid reduction of $J_S(T)$ [see Eq. (6)]. Ultimately, however, as $H(V_{OC})$ decreases with T, V_{OC} again saturates at the same V_{OC}^{max} (see Sec. IV B).

Now, V_{OC}^{max} is achieved when the quasi-Fermi levels of the donor and acceptor layers become pinned at high currents. Examining the energy level diagram in Fig. 1, and taking into account exciton bonding, the *intrinsic* open circuit voltage, which corresponds to V_{OC}^{max}, can be written as

$$qV_{OC}^{max} = IP_D - EA_A - \frac{q^2}{4\pi\varepsilon_0\varepsilon_r r}, \quad (10)$$

where ε_0 is the vacuum permittivity, ε_r is the relative dielectric constant of the bulk organic material, and r_{DA} is the initial separation distance of the optically generated hole and electron pair in the donor and acceptor layers, respectively, immediately following charge transfer. The third term on the right-hand side of Eq. (10) corresponds to the binding energy, E_B, of the bound electron-hole geminate pair following charge transfer.

III. EXPERIMENT

Organic HJs were grown on glass substrates precoated with a 1500 Å thick, transparent conducting indium tin oxide (ITO) anode with a sheet resistance of 15 Ω/□. Prior to organic deposition, the substrates were cleaned in acetone, isopropanol, and trichloroethylene followed by exposure to UV ozone for 5 min. The organic films and a metal cathode were deposited via high vacuum thermal evaporation in a chamber with a base pressure of 2×10^{-7} Torr. The organic source materials were purified by three gradient sublimation cycles prior to use.[3] In all cases, the structure is ITO/donor/acceptor/exciton blocking layer (EBL)/cathode. The various donors and acceptors and their energy levels used in this work are listed in Table I. The values of IP were obtained from ultraviolet photoemission spectroscopy, whereas EA was taken from inverse photoemission spectroscopy measurements at the low energy edge of the LUMO signal. The donor (acceptor) layers were each at least 150 (250) Å thick. The exciton blocking layer (EBL) was composed of a 100 Å thick layer of bathocuproine (BCP).[25] A 1000 Å thick Ag, Al, or Au cathode was evaporated through a shadow mask with 0.8 mm^2 circular openings defining the device active area.

Current-voltage characteristics in the dark and under simulated air mass global (AM1.5G) solar illumination from a 1000 W Xe-arc lamp were measured using an HP 4155B semiconductor parameter analyzer. The samples were placed in an open cycle liquid He cryostat. Temperature was measured using a Si diode sensor placed on the sample surface. The illumination intensity was varied using neutral density filters, and measured with a calibrated Si detector coupled to a broadband optical power meter.

IV. RESULTS

A. Device current in the dark and under illumination

Figure 4(a) shows the dark *J*-*V* characteristics in 20 K steps over the temperature range 120 K$\leq T\leq$ 300 K for the structure: ITO/200 Å copper phthalocyanine (CuPc)/400 Å C_{60}/BCP/Al. The data are shown by open circles, while the lines are fits to the data using Eq. (5), with

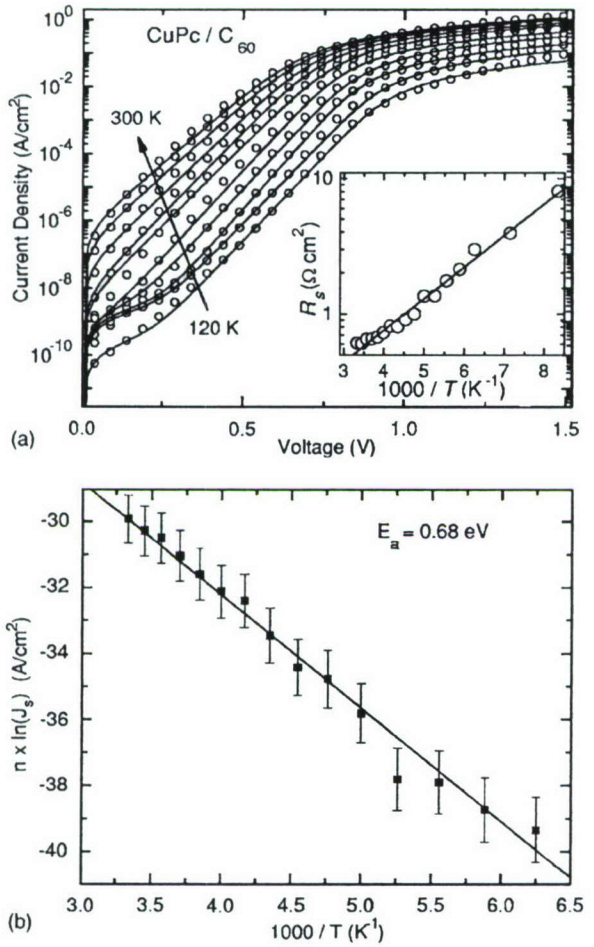

FIG. 4. (a) Dark current density versus voltage (J_{dark}-V) characteristics (open circles) over the temperature range 120 K $\leq T \leq$ 300 K at 20 K intervals for the heterojunction structure: ITO/CuPc(200 Å)/C_{60}(400 Å)/BCP(100 Å)/Al(1000 Å). The solid lines are fits to the J-V characteristics based on Eq. (5) in text. Inset: The specific series resistance, R_s vs T^{-1} for the same structure extracted from the fits. (b) The parameter $n \ln(J_S)$ (J_S the reverse saturation current density) vs T^{-1} for the device of (a). The solid line is a linear fit to $n \ln(J_S)$, satisfying Eq. (6) in text with an activation energy 0.68 eV.

$J_{ph}(V)=0$. The values of $n \ln(J_S)$ extracted from the data in Fig. 4(a) are shown in Fig. 4(b) versus $1000/T$. Over this temperature range, n decreases from $n=2$ at 300 K, to 1.6 at 150 K. The dependence of the specific series resistance, $R_s(T)$, is plotted in the inset of Fig. 4(a).

The J-V characteristics of the device in Fig. 4 in the dark (squares) and under AM1.5G illumination of 1.5 suns intensity (circles) are replotted on a linear current scale in Fig. 5. To simulate the device under illumination, we use Eq. (8) to define $J_{ph}(V)$, and let $R_p=R_p(P_0)$, to represent the light-intensity-dependent specific parallel resistance.[26,27] The fits are shown in Fig. 5, with both theory and experiment yielding $V_{OC}=(0.5\pm0.02)$ V and FF=0.58±0.01. The inset of Fig. 5 shows R_p versus P_0, where R_p decreases from $3 \times 10^5\ \Omega\,\mathrm{cm}^2$ at 0.15 mW/cm², to $R_p=320\ \Omega\,\mathrm{cm}^2$ at

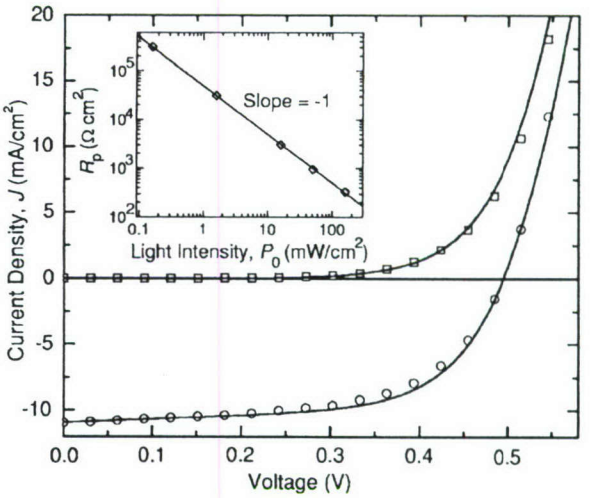

FIG. 5. Linear current density versus voltage (J-V) characteristics for the device of Fig. 4 at 300 K in the dark (open squares) and under an incident optical intensity (P_0) of 150 mW/cm² (open circles). The solid lines are fits to the data as described in the text. Inset: The specific parallel resistance under illumination, R_p versus P_0. The solid line is a linear best fit to the data.

150 mW/cm², following $R_p=(45\pm5\ \Omega\,\mathrm{W})/P_0$ over more than three orders of magnitude in incident power.

B. Temperature dependence

Figures 6(a) and 6(b) show V_{OC} and FF, respectively, for the device in Figs. 4 and 5 as functions of T. Here, V_{OC} increases inversely with T until approximately 175 K, at which point V_{OC} saturates for a given P_0. The value of V_{OC} at a constant T also increases with P_0, consistent with Eq. (9). The FF of the device reaches a peak of 0.65 at 225 K, and decreases rapidly at $T<200$ K.

Figure 7 shows the dependence of V_{OC} on T under illumination for several DA pairs and cathode (Ag, Al, Au) combinations. For the CuPc/C_{60} structure in Fig. 3, V_{OC} saturates for both Al (open circles) and Au (filled squares) at approxi-

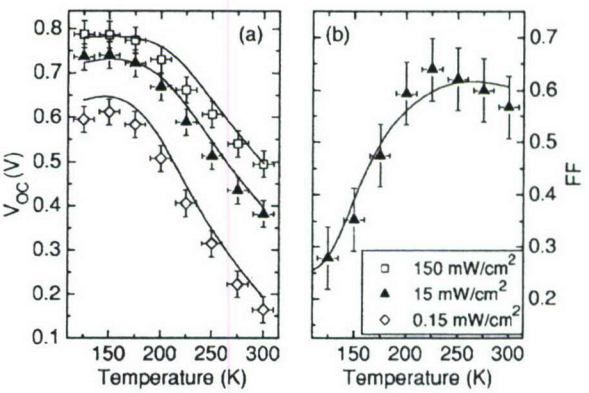

FIG. 6. Temperature dependencies of (a) the open-circuit voltage (V_{OC}) at various incident optical light intensities, and (b) fill factor (FF), for the CuPc/C_{60} heterostructure of Fig. 4. The solid lines are fits to the data as described in the text.

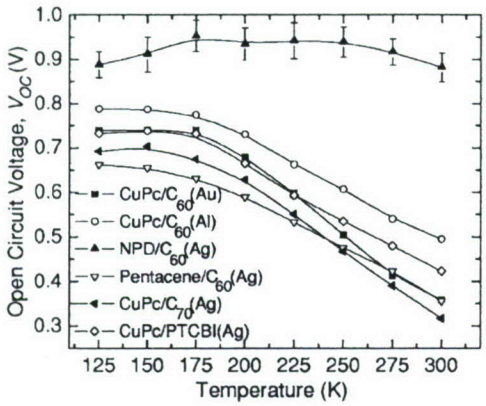

FIG. 7. Open-circuit voltage (V_{OC}) versus T for various donor-acceptor heterojunctions. The metal in parentheses in the legend indicates the cathode material for that device. The error bars displayed for the NPD/C_{60} (Ag) device are typical for all of the heterojunctions.

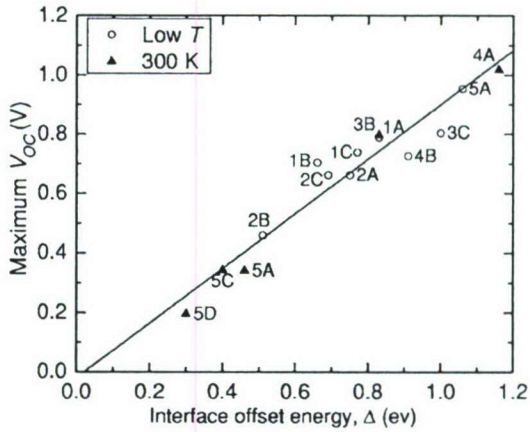

FIG. 8. The maximum value of the open-circuit voltage (V_{OC}^{max}) for different donor-acceptor photovoltaic cells versus the interface energy Δ as defined in text. The closed triangles correspond to heterojunction devices for which the maximum open circuit voltage, V_{OC}^{max}, was measured at 300 K, whereas open circles are V_{OC}^{max} collected at $T<300$ K. The solid line shows a linear best fit to the data (slope=0.92 and intercept=−0.02). The various letters and numbers for each point refer to materials listed in Table I.

mately 175 K, with $V_{OC}^{max}=(0.79\pm0.03)$ V for Al, and (0.76 ± 0.02) V for Au. In contrast, $V_{OC}(T)$ for the N,N'-di-1-naphthyl-N,N'-diphenyl-1,1′-biphenyl-4,4′ diamine (NPD)/C_{60} HJ is relatively temperature independent. This HJ reaches saturation at 300 K for $P_0>1$ sun, similar to previously reported polymer blend junctions.[28]

Figure 8 shows V_{OC}^{max} for 14 *DA* pairs plotted vs the interface offset energy, $\Delta=IP_D-EA_{opt,A}$ (see Fig. 1). Here, $EA_{opt,A}$ is the electron affinity of the acceptor as determined from its optical energy gap. Open circles correspond to V_{OC}^{max} taken at low T, whereas filled triangles represent V_{OC}^{max} at 300 K at high P_0. The labels for each point correspond to the molecules listed in Table I. The line corresponds to a linear best fit through the data with slope=(0.92 ± 0.02), and intercept=$-(0.02\pm0.03)$ V.

V. DISCUSSION

A. Heterojunction current

The *J-V* characteristic fit to the generalized Shockley theory [Eq. (5)] suggests that the heterojunction at the *DA* interface is well defined and planar. Also, $n=2$ at 300 K implies that the *DA* junction dark current is dominated by recombination. Further evidence is provided in Fig. 4(b), where the fit of $n\ln(J_S)$ to $1/T$ corresponding to Eq. (6) (solid line) indicates that this quantity is thermally activated with energy $E_g/2=(0.68\pm0.06)$ eV. This is consistent with the[23] CuPc/C_{60} HJ, where $E_g=IP_D-EA_A=(1.6\pm0.6)$ eV. The discrepancy of ~0.2 eV is due to errors associated with the inverse photoelectron spectroscopic measurement of EA_A (see Table I). Hence, the *DA* HJ is the dominant factor in determining the dark *J-V* characteristics. The value of J_S, in particular, affects V_{OC} [cf. Eq. (9)] and, in turn, FF, as described below. The other extracted dark current fit parameters (listed in Table II) reveal that R_p is not strongly temperature dependent, while the inset to Fig. 4(a) suggests that $R_s \propto \exp(-E_a/k_BT)$, with a small activation energy of $E_a=5$ meV, most likely due to an increase in the bulk hole and electron mobilities with decreasing T.

TABLE II. Parameters from Eq. (5) in text for various donor/acceptor heterojunction combinations at 300 K in the dark.

Donor-Acceptor interface[a]	J_S (A/cm^2)	n	R_s (Ω cm^2)	R_p (Ω cm^2)
Pentacene/C_{70}	3.3×10^{-5}	2.1	3.4	3.5×10^{4}
CuPc/C_{70}	1.0×10^{-5}	2.0	0.7	7.9×10^{4}
Pentacene/C_{60}	2.7×10^{-6}	2.0	0.1	8.1×10^{4}
Pentacene/PTCBI	2.5×10^{-7}	1.6	0.7	5.0×10^{5}
CuPc/C_{60}	1.0×10^{-6}	2.0	0.1	1.1×10^{6}
CuPc/PTCBI	5.5×10^{-7}	1.7	0.2	9.1×10^{5}
NPD/C_{60}	7.1×10^{-10}	2.6	28.4	2.2×10^{6}
SubPc/C_{60}	5.8×10^{-9}	1.6	0.9	1.2×10^{5}

[a]See Table I for chemical name.

TABLE III. Parameters for Eq. (3) in text for various donor-acceptor interfaces.

Donor-Acceptor interface[a]	Donor to Acceptor		Acceptor to Donor		
	k_{ccD} (s^{-1})	λ_{ccD} (eV)[b]	k_{vvA} (s^{-1})	λ_{vvA} (eV)[b]	λ_{cv} (eV)[b]
Pentacene/C_{60}	$(8\pm2)\times10^{11}$	0.9	$(3\pm1)\times10^{11}$	1.1	0.8
CuPc/C_{60}	$(2\pm0.7)\times10^{10}$	1.0	$(2\pm0.9)\times10^{11}$	0.6	0.7
CuPc/PTCBI	$(4\pm1)\times10^{8}$	0.8	$(1\pm0.8)\times10^{9}$	0.6	0.7
NPD/C_{60}	$(1\pm0.8)\times10^{7}$	1.3	$(4\pm1)\times10^{7}$	0.4	0.9
CuPc/C_{70}	$(2\pm0.9)\times10^{11}$	0.7	$(3\pm1)\times10^{11}$	0.7	0.7
Pentacene/C_{70}	$(4\pm1)\times10^{10}$	0.9	$(3\pm2)\times10^{11}$	0.7	0.5

[a]See Table I for chemical name.
[b]Fit parameter with an error of ±0.1 eV.

Resistance also plays a role in the fill factor,[15]

$$\mathrm{FF}(R_s,R_p)\approx \mathrm{FF}(0,\infty)\left(1-\frac{J_{SC}R_s}{V_{OC}}-\frac{V_{OC}}{J_{SC}R_p}\right). \quad (11)$$

Equation (11) indicates that FF is reduced below its maximum in junctions with high R_s and low R_p. The thermally activated R_s provides the dominant resistive contribution to the decrease in FF with T (see Fig. 6), although this is small in comparison with the FF dependence of $V_{OC}(T)$.

In contrast, there is an inverse dependence of R_p on light intensity (Fig. 5, inset). This has also been reported for pentacene/C_{60} cells[26] as well as for bulk HJ polymer/fullerene devices.[27,29] This suggests that photoconductivity in the separate D and A layers contributes to free electron and hole generation, in addition to charge transfer at the DA heterointerface. Photoconductivity in homogeneous organic semiconductors has been widely observed, and is often attributed to exciton dissociation in the bulk of the D and A layers due to their interaction with trapped charges, impurities, defects, and other material imperfections.[30,31] For example, an exciton can undergo annihilation on collision with a trapped charge, resulting in free carrier emission to the LUMO. This process is expected to produce charge carriers with a linear dependence on exciton density, which in turn is linearly dependent on P_0, consistent with Fig. 5. The photoconductive quantum efficiency can be estimated using $\eta_{PC}=L^2V_{ph}/(R_pP_0\tau_{rec}\mu)$, where $V_{ph}\sim2$ eV is the photon voltage, $L=50$ nm is the D or A layer thickness, $\tau_{rec}\sim5$ ns is the carrier recombination time, and $\mu\sim10^{-2}$ cm^2/V s is the charge mobility within its respective transport layer. The data in Fig. 5 suggest $\eta_{PC}\approx2\%$ for the CuPc/C_{60} HJ (compared to ~50% due to exciton dissociation at the HJ itself). This process, and its reduction of R_p with increasing P_0 represents a property that is intrinsic to organic HJs, and ultimately reduces FF and η_P at high light intensities in PV cells.

B. Open-circuit voltage of donor-acceptor heterojunctions

To probe the origin of V_{OC}, we compare V_{OC}^{max} for the set of DA HJ materials combinations in Table III. This is in contrast with previous studies that have sought to correlate V_{OC} with material energy levels, where V_{OC} was measured at $T=300$ K, and typically at $P_0=1$ sun.[9–14] As shown in Fig. 7, V_{OC}^{max} for CuPc/C_{60} HJs with either Al or Au cathodes (with work functions of $\phi_{mc}=4.3$ eV and 5.1 eV, respectively) differ by only 0.03 V, which is within the experimental error. This suggests that it is the DA pair energy levels that determine V_{OC}^{max}, and not the cathode material work function.[32] We note that previous studies have often shown a weak dependence[10] of V_{OC} on ϕ_{mc}, possibly due to measuring V_{OC} below V_{OC}^{max}.

Charge transfer at a DA interface results in a Coulombically bound electron-hole pair.[33] An estimate of the pair binding energy immediately following a nearest-neighbor charge transfer reaction gives $E_B\sim0.5$ eV $\gg k_BT$, assuming $\varepsilon_r=3$ and $r_{DA}=10$ Å [cf. Eq. (10)]. This is approximately equal to E_B for many small-molecular weight organic semiconductors.[20,21] Hence, in Fig. 8 we plot V_{OC}^{max} vs $\Delta=IP_D-EA_{opt,A}$, where the best fit line to the data is consistent with a unity slope and an intercept at the origin. From this linear relationship, we conclude that the geminate polaron-pair[33,34] or exciplex[35,36] state is rapidly dissociated into free charge carriers, thereby contributing to the photocurrent. To fully dissociate, the exciplex must overcome the Coulombic attraction between the hole on a donor molecule and electron on a neighboring, interfacial acceptor molecule. Consequently, the largest potential developed across the HJ, V_{OC}^{max}, must account for this energy loss as expressed in Eq. (10).

We note that the relationship, $\Delta=IP_D-EA_{opt,A}$, is only approximate. According to Fig. 1, the interface gap is equal to $\Delta=IP_D-IP_A+E_{opt,A}+E_{B,A}$, while the total energy that results from exciton dissociation should be simply IP_D-EA_A. However, on relaxation following charge transfer, the hole polarization results in a loss of $E_{B,D}/2$ and likewise, the electron loses $E_{B,A}/2$ as it relaxes from the LUMO. For most of the high mobility donors and acceptors considered here, the polarization energies for both holes and electrons in the D and A layers, respectively, are approximately equal. In this case, the resulting energy of the geminate pair is therefore approximately equal to $\Delta\cong IP_D-EA_A-E_B$, as expressed by Eq. (10) and in Fig. 1, and as observed. Note that the precise distribution of the energy loss between electron and hole is unimportant, as it is the total energy loss that determines the ultimate value of V_{OC}^{max}.

Note that V_{OC}^{max} is not attainable for all DA HJs under standard operating conditions of $T=300$ K and $P_0=1$ sun

intensity, due to large values of J_S. Nevertheless, V_{OC}^{max} is obtained under normal operating conditions for NPD/C_{60} and boron subphthalocyaninechloride (SubPc)/C_{60} HJs.[37,38] The maximum potential difference observed for these two HJs is $V_{OC} \approx 1$ V, in contrast to, for example, the CuPc/C_{60} HJ, where $V_{OC} \approx 0.5$ V at 300 K and 1 sun versus $V_{OC}^{max} \approx 0.8$ V.

C. Electron transfer rate

As V_{OC} increases, the potential drop at the HJ decreases, thereby resulting in a concomitant decrease in J_{SC}. Hence, the maximum power conversion efficiency, $\eta_P = J_{SC} V_{OC} FF / P_0$, is obtained for the optimal combination of V_{OC} and J_{SC}. To estimate the effect of V_{OC} on J_{SC}, we must first determine the charge transfer rate at the HJ for a given *DA* pair. We begin by fitting $J_{ph}(V)$ characteristics of the *DA* HJ using nonadiabatic Marcus theory. This model describes intermolecular charge transfer at the *DA* interface, and the probability for separation of the geminate state immediately following this process. Once fully separated, the electrons and holes are collected at their respective contacts following transport through the homogeneous *A* and *D* layers.

The solid lines in Fig. 6 correspond to calculations based on Eqs. (5)–(9). The dark current is described by J_S, R_s, R_p, and n for each HJ pair (see Table II). To fit the photocurrent characteristics, J_S, R_s, and n determined in the dark are kept constant with P_0, and R_p and n independent of T. Also, J_S and R_s vary with T as discussed above. Parameters V_{if}, λ_{ccD}, λ_{vvA}, λ_{cv} are then used to fit the *J-V* characteristics vs P_0 and T. Here, V_{if} and λ_{cv} are assumed to be identical for both donor-to-acceptor ($D \rightarrow A$) and $A \rightarrow D$ transitions. The fitting procedure is repeated for each P_0 to obtain an average final value and error (shown in Fig. 9) for the electron transfer rate, k_{ET}.

Figure 9 is a plot of k_{ET} for $D \rightarrow A$ and $A \rightarrow D$ transfer for several *DA* HJs in Table I as a function of ΔE_{LUMO} and ΔE_{HOMO}, respectively. Here, k_{ET} increases with offset energy, eventually reaching a plateau, and then decreases once again at high energies, corresponding to highly exothermic electron transfer reactions. The region of energy that corresponds to increasing k_{ET} is the "normal" region, and decreasing k_{ET} occurs in the Marcus "inverted" region.[17] This behavior has previously been observed for electron transfer reactions in fullerenes.[39]

The $D \rightarrow A$ transition of the CuPc/C_{60} HJ yields $k_{ET} = (2.0 \pm 0.7) \times 10^{10}$ s^{-1}, comparable to $k_{ET} = 8 \times 10^{10}$ s^{-1} reported for a oligo(*p*-phenylene vinylene) fullerene dyad.[40] Furthermore, the various rates for the CuPc/C_{60} *DA* interface suggest that $H(0\text{ V}) \approx 0.9$; i.e., 90% of excitons that reach a *DA* interface contribute to photocurrent. This is consistent with the high values of η_{EQE} that have been reported for the CuPc/C_{60} HJ.[41] The other HJs have $H(0\text{ V})$ varying from 0.6 to 0.95. This is comparable to the prediction of Mihailetchi *et al.*,[42] where a model based upon Onsager's theory of geminate recombination suggests $H(0\text{ V}) = 0.6$ for a polymer-fullerene bulk heterojunction device. Now, k_{ET} decreases with T [cf. Eq. (9)], resulting in a similar reduction in both $H(\text{V})$ and J_{SC}. Indeed, J_{SC} exponentially decreases with T,

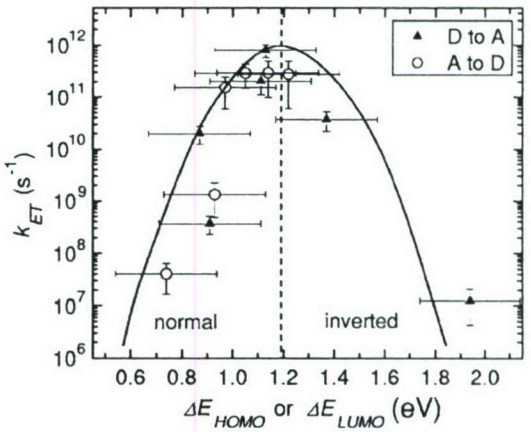

FIG. 9. The electron transfer rate, k_{ET}, for donor-to-acceptor transfer ($D \rightarrow A$, filled triangles) and acceptor-to-donor transfer ($A \rightarrow D$, open circles), versus the difference between the lowest unoccupied molecular orbitals (ΔE_{LUMO}) in the case of $D-A$, and the difference between highest occupied molecular orbitals (ΔE_{HOMO}) in the case of $A \rightarrow D$. The line serves as a guide to the eye. The vertical dashed line delineates the so-called Marcus normal and inverted regions for charge transfer.

similar to the behavior for polymer-fullerene bulk HJ devices,[27] and consistent with the model.

D. Efficiency limits to organic DA heterojunction cells

These findings have important consequences in the design of *DA* junctions used in organic PV cells. From the energy diagram of Fig. 1, a high V_{OC} is obtained by increasing Δ, since that results in a reduced J_S. To simulate an optimized structure that maximizes the product, $V_{OC} \cdot J_{SC}$, we used a genetic algorithm for a double heterostructure device with the following structure: ITO/*D*/*A*/EBL/Ag. The real part of the index of refraction is assumed to be 1.9 for both the *D* and *A* layers, and 1.7 for the EBL—values close to those of materials used in conventional cells.[22] The imaginary part of the index of refraction is taken equal to 1 for incident photon energies larger than the optical gap of the *D* and *A* layers, while it is 0 for the EBL. The diffusion length for both *D* and *A* is $L_D = 20$ nm. The algorithm then optimizes the thicknesses of the organic layers using a transfer-matrix approach that includes optical interference effects.[24]

We select $E_{opt,A} = 1.8$ eV, similar to that of C_{60}, as shown in the inset of Fig. 10(a). For the simulations at 1 sun AM1.5G solar illumination and $T = 300$ K, we use R_s, R_p, n, E_B, k_{ET}, and λ typical of archetype CuPc/C_{60} junctions given in Tables I and II. The results are shown in Fig. 10 for J_{SC} [Fig. 10(a)] with a maximum at $E_{opt,D} = 1.4$ eV. This is expected since a smaller optical gap material can harvest a larger percentage of the solar spectrum that extends well into the infrared. However, as the offset energy is increased to >1 eV, J_{SC} drops rapidly due to a decreasing ΔE_{LUMO} and ΔE_{HOMO}, which inhibit efficient exciton dissociation. The FF remains approximately constant at 0.7, since it is primarily controlled by both series and parallel resistance [cf. Eq. (11)].

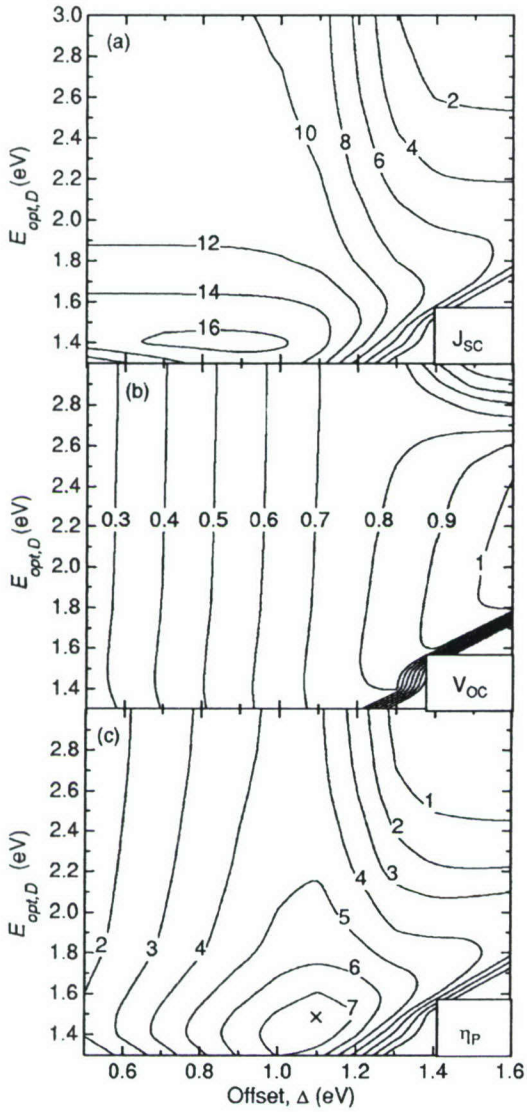

FIG. 10. Calculated contour plots of (a) short-circuit current density (J_{SC}[mA/cm^2]), (b) open-circuit voltage (V_{OC} [V]), and (c) power conversion efficiency (η_P [%]) for optimized device structures as functions of the donor (D) optical gap ($E_{opt,D}$) and offset energy, $\Delta = IP_D - EA_{opt,A}$ (see Fig. 1), where IP is the ionization potential, EA is the electron affinity, A is the acceptor material, and $EA_{opt,A} = E_{opt,A} - IP_A = 1.8$ eV. The general device structure is ITO/D/A/exciton blocking layer/Ag. The "×" in (c) shows the location of the maximum η_P.

Now, V_{OC} [Fig. 10(b)] increases monotonically with offset energy, with an approximately 0.3 V difference between V_{OC} and the offset, Δ. This difference arises from the operating conditions of $P_0 = 1$ sun and $T = 300$ K corresponding to $V_{OC} < V_{OC}^{max}$, and is close to that reported for polymer-fullerene bulk HJs.[9] These device parameters result in a maximum $\eta_P = 7.9\%$ [corresponding to point "×" in Fig. 10(c)] for an optimized double heterostructure device, with $E_{opt,D} = 1.5$ eV and $\Delta = 1.1$ eV.

Using the optimized values of $E_{opt,A} = 1.8$ eV, $E_{opt,D} = 1.5$ eV, and $\Delta = 1.1$ eV, we next simultaneously vary the diffusion lengths, L_D, in the D and A layers. Figure 11 shows

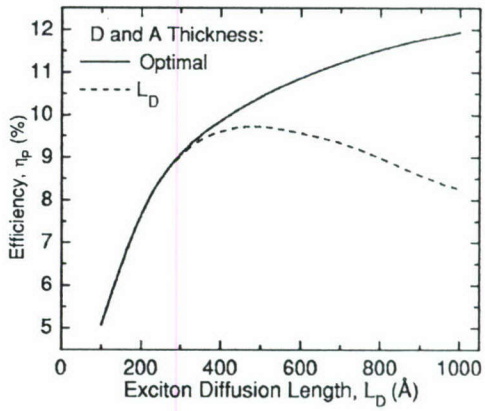

FIG. 11. Calculated power conversion efficiency (η_P) as a function of donor (A) and acceptor (A) exciton diffusion length, L_D, for the device structure: ITO/D/A/exciton blocking layer (EBL)/Ag as defined in text. The solid line shows the case of optimal D, A, and EBL layer thickness, while the dashed line shows the case where D and A thickness equals L_D.

the results of this simulation, where η_P increases monotonically until $L_D \approx 400$ Å. For $L_D \geq 400$ Å, η_P decreases due to a saturation of η_A, resulting in decreased absorption in the acceptor layer (dashed line). By choosing optimized D and A thicknesses (solid line), this decrease can be avoided, leading to $\eta_P \approx 12\%$ for $L_D = 1000$ Å. To further increase efficiency, a DA mixed layer can be inserted between the D and A layers[19] to achieve an approximately 25% increase in J_{SC}, yielding $\eta_P \approx 15\%$. Also, by stacking two such devices in a tandem geometry using materials that span a broader range of the solar spectrum than the CuPc/C_{60} system,[7] the efficiency can be increased to $\eta_P > 16\%$.

VI. CONCLUSIONS

We have presented a comprehensive device model that clarifies the interrelationships between the energetic characteristics of the donor and acceptor materials that comprise an organic heterojunction, and the limitations those characteristics impose when such a junction is employed in a photovoltaic cell. The model is based on the generalized Shockley equation for p-n junctions that describes the dark current characteristics of organic heterostructure barriers. The voltage dependent photocurrent is understood in the context of the Marcus theory of electron transfer, providing basic insights into the factors that govern the magnitude of the energy level offset between two contacting organic semiconductor materials. The electron transfer rates are shown to follow the predictions of Marcus theory, increasing with HOMO-HOMO and LUMO-LUMO offsets until reaching the inverted region, after which the rate decreases. Also, the HJ parallel resistance is found to be a linearly decreasing function of illumination intensity due to photoconductive charge generation. This effect may ultimately limit device efficiency.

The maximum open-circuit voltage for each donor-acceptor pair was measured, and was found to be a function of the difference between the donor ionization potential, ac-

ceptor electron affinity, and the exciplex binding energy. Based upon the fundamental understanding of the factors governing the offset energies at organic heterointerfaces in the absence of a high density of background charge, we find that power conversion efficiencies approaching 12% are possible for a single HJ cell, increasing to more than 16% by incorporating tandem solar cell structures. Ultimately, our models of charge transfer at organic heterointerfaces suggests that there exists an intrinsic compromise between increasing J_{SC} by tuning the HOMO-HOMO and LUMO-LUMO offsets and optical gaps, and increasing V_{OC} by increasing the difference between the donor HOMO and acceptor LUMO. This compromise forms the ultimate limitation to the power conversion efficiency obtainable by an organic *DA* HJ cell structure.

ACKNOWLEDGMENTS

The authors gratefully acknowledge the National Renewable Energy Laboratory, the Air Force Office of Scientific Research, and Global Photonic Energy Corporation for partial support of this work.

APPENDIX

To determine the donor current density vs voltage characteristic, J_D vs V, G_{vcD} is found following Ref. 16. That is

$$G_{vcD} = q\left(\phi_s + \phi_a - \frac{k_g}{x_c^2 - 1}\right)\left(\frac{x_c - 1}{x_c + 1}\right), \tag{A1}$$

where $x_c = 1/f_c - 1$, k_g is the recombination rate given as $k_g = f_{osc}(2\pi E_{opt}^2/h^3c^2)$, and ϕ_s and ϕ_a are the solar and ambient spectral photon flux densities, respectively. Thus[16]

$$\phi_s = \frac{2\pi F_s f_{osc}}{c^2 h^3} \frac{E_{opt}^2}{\exp(E_{opt}/k_B T_s) - 1} \tag{A2}$$

and

$$\phi_a = \frac{2\pi(1 - F_s) f_{osc}}{c^2 h^3} \frac{E_{opt}^2}{\exp(E_{opt}/k_B T) - 1}. \tag{A3}$$

The oscillator strength, $f_{osc} = 1 \times 10^{-21}$ eV m^2, $F_s = 2.16 \times 10^{-5}$ is the relative angular range of the sun, and $T_s = 5760$ K is the black-body temperature of the sun.

Now,

$$qV = 2(\mathrm{IP}_D - \mathrm{EA}_A) - E_{\mathrm{tran},D} - 2k_B T \ln x_a - k_B T \ln x_c, \tag{A4}$$

where $x_a = 1/f_a - 1$, and

$$f_a = \frac{k_{ccD} - k_{cvD}\delta_{cvD}(1 - f_c) - G_{vcD}/q}{(k_{ccD} - k_{cvD})f_c + (k_{ccD}\delta_{ccD} - k_{cvD}\delta_{cvD})(1 - f_c)}, \tag{A5}$$

where $\delta_{if} = \exp[-(E_i - E_f)/k_B T]$. The limits on x_c are found by solving the quadratic equations that result from setting the probability, f_a, equal to 0 and 1. Then, from a known set of x_c, J_{ccD}, and J_{cvD}, then J_D, and V are calculated. The same procedure also is also used to find the acceptor J_A-V. This model for charge transfer using nonadiabatic Marcus theory differs from that described previously[16] in that it is applicable to both symmetric and asymmetric donor-acceptor heterojunctions.

*Electronic address: stevefor@umich.edu

[1] S. M. Sze, *Physics of Semiconductor Devices*, 2nd ed. (Wiley, New York, 1981).
[2] I. G. Hill, D. Milliron, J. Schwartz, and A. Kahn, Appl. Surf. Sci. **166**, 354 (2000).
[3] S. R. Forrest, Chem. Rev. (Washington, D.C.) **97**, 1793 (1997).
[4] S. R. Forrest, MRS Bull. **30**, 28 (2005).
[5] G. Dennler and N. S. Sariciftci, Proc. IEEE **93**, 1429 (2005).
[6] S. E. Gledhill, B. Scott, and B. A. Gregg, J. Mater. Res. **20**, 3167 (2005).
[7] J. Xue, S. Uchida, B. P. Rand, and S. R. Forrest, Appl. Phys. Lett. **85**, 5757 (2004).
[8] G. Li, V. Shrotriya, J. S. Huang, Y. Yao, T. Moriarty, K. Emery, and Y. Yang, Nat. Mater. **4**, 864 (2005).
[9] M. C. Scharber, D. Wuhlbacher, M. Koppe, P. Denk, C. Waldauf, A. J. Heeger, and C. J. Brabec, Adv. Mater. (Weinheim, Ger.) **18**, 789 (2006).
[10] C. J. Brabec, A. Cravino, D. Meissner, N. S. Sariciftci, T. Fromherz, M. T. Rispens, L. Sanchez, and J. C. Hummelen, Adv. Funct. Mater. **11**, 374 (2001).
[11] C. J. Brabec, A. Cravino, D. Meissner, N. S. Sariciftci, M. T. Rispens, L. Sanchez, J. C. Hummelen, and T. Fromherz, Thin Solid Films **403**, 368 (2002).
[12] X. Y. Deng, L. P. Zheng, C. H. Yang, Y. F. Li, G. Yu, and Y. Cao, J. Phys. Chem. B **108**, 3451 (2004).
[13] A. Gadisa, M. Svensson, M. R. Andersson, and O. Inganas, Appl. Phys. Lett. **84**, 1609 (2004).
[14] T. Kietzke, D. A. M. Egbe, H. H. Horhold, and D. Neher, Macromolecules **39**, 4018 (2006).
[15] R. H. Bube and A. L. Fahrenbruch, *Advances in Electronics and Electron Physics* (Academic, New York, 1981), p. 163.
[16] J. Nelson, J. Kirkpatrick, and P. Ravirajan, Phys. Rev. B **69**, 035337 (2004).
[17] R. A. Marcus and N. Sutin, Biochim. Biophys. Acta **811**, 265 (1985).
[18] B. P. Rand, P. Peumans, and S. R. Forrest, J. Appl. Phys. **96**, 7519 (2004).
[19] J. Xue, B. P. Rand, S. Uchida, and S. R. Forrest, Adv. Mater. (Weinheim, Ger.) **17**, 66 (2005).
[20] M. Knupfer, Appl. Phys. A: Mater. Sci. Process. **77**, 623 (2003).
[21] I. G. Hill, A. Kahn, Z. G. Soos, and R. A. Pascal, Chem. Phys. Lett. **327**, 181 (2000).
[22] P. Peumans, A. Yakimov, and S. R. Forrest, J. Appl. Phys. **93**, 3693 (2003).
[23] A. L. Fahrenbruch and J. Aranovich, *Solar Energy Conversion* (Springer-Verlag, New York, 1979), p. 257.

[24] L. A. A. Pettersson, L. S. Roman, and O. Inganas, J. Appl. Phys. **86**, 487 (1999).
[25] B. P. Rand, J. Li, J. Xue, R. J. Holmes, M. E. Thompson, and S. R. Forrest, Adv. Mater. (Weinheim, Ger.) **17**, 2714 (2005).
[26] S. Yoo, B. Domercq, and B. Kippelen, J. Appl. Phys. **97**, 103706 (2005).
[27] I. Riedel, J. Parisi, V. Dyakonov, L. Lutsen, D. Vanderzande, and J. C. Hummelen, Adv. Funct. Mater. **14**, 38 (2004).
[28] J. A. Barker, C. M. Ramsdale, and N. C. Greenham, Phys. Rev. B **67**, 075205 (2003).
[29] C. Waldauf, M. C. Scharber, P. Schilinsky, J. A. Hauch, and C. J. Brabec, J. Appl. Phys. **99**, 104503 (2006).
[30] M. Pope and C. E. Swenberg, *Electronic Processes in Organic Crystals and Polymers*, 2nd ed. (Oxford University Press, New York, 1999).
[31] J. Reynaert, V. I. Arkhipov, P. Heremans, and J. Poortmans, Adv. Funct. Mater. **16**, 784 (2006).
[32] B. A. Gregg and M. C. Hanna, J. Appl. Phys. **93**, 3605 (2003).
[33] T. Offermans, S. C. J. Meskers, and R. A. J. Janssen, Chem. Phys. **308**, 125 (2005).
[34] P. Peumans and S. R. Forrest, Chem. Phys. Lett. **398**, 27 (2004).
[35] A. C. Morteani, P. Sreearunothai, L. M. Herz, R. H. Friend, and C. Silva, Phys. Rev. Lett. **92**, 247402 (2004).
[36] T. Offermans, P. A. van Hal, S. C. J. Meskers, M. M. Koetse, and R. A. J. Janssen, Phys. Rev. B **72**, 045213 (2005).
[37] G. P. Kushto, W. H. Kim, and Z. H. Kafafi, Appl. Phys. Lett. **86**, 093502 (2005).
[38] K. L. Mutolo, E. I. Mayo, B. P. Rand, S. R. Forrest, and M. E. Thompson, J. Am. Chem. Soc. **128**, 8108 (2006).
[39] S. Fukuzumi, K. Ohkubo, H. Imahori, and D. M. Guldi, Chem.-Eur. J. **9**, 1585 (2003).
[40] P. A. van Hal, R. A. J. Janssen, G. Lanzani, G. Cerullo, M. Zavelani-Rossi, and S. De Silvestri, Phys. Rev. B **64**, 075206 (2001).
[41] J. Xue, B. P. Rand, S. Uchida, and S. R. Forrest, J. Appl. Phys. **98**, 124903 (2005).
[42] V. D. Mihailetchi, L. J. A. Koster, J. C. Hummelen, and P. W. M. Blom, Phys. Rev. Lett. **93**, 216601 (2004).
[43] A. Kahn, N. Koch, and W. Y. Gao, J. Polym. Sci., Part B: Polym. Phys. **41**, 2529 (2003).
[44] P. J. Benning, D. M. Poirier, T. R. Ohno, Y. Chen, M. B. Jost, F. Stepniak, G. H. Kroll, J. H. Weaver, J. Fure, and R. E. Smalley, Phys. Rev. B **45**, 6899 (1992).

ADVANCED MATERIALS

DOI: 10.1002/adma.200700837

Efficient Solar Cells Using All-Organic Nanocrystalline Networks**

By *Fan Yang*, *Kai Sun*, and *Stephen R. Forrest**

The power conversion efficiencies of organic photovoltaic (PV) cells have steadily increased since the introduction of the donor/acceptor (DA) heterojunction.[1] Further improvements have been reported in entangled or "bulk-heterojunction" (BHJ) structures, where the DA interface is within an exciton diffusion length (~10 nm) of the site for photon absorption.[2] However, the high series resistance[3,4] of these amorphous blends limits the active layer thickness, leading to low fill factor and reduced light absorption, and hence a low solar energy conversion efficiency.[5] One means to circumvent the low mobility of charge in disordered organic films has been the use of inorganic semiconductor "quantum dots".[6] These nanocrystals serve as charge generation sites that, when loaded into a polymer film at high density, can form a high conductivity percolating path to extract photogenerated charge from the device active region. Unfortunately, the mismatch in optical and excitonic properties between the quantum dots and the polymer matrix has limited PV cell efficiencies of photovoltaic cells based on these materials. In this work, we demonstrate that controlled crystallization of organic molecules results in a PV cell in which the active layer comprises a nanocrystalline organic region that forms high conductivity networks for charge extraction. This cell shares many of the benefits of organic/inorganic quantum dot cells as well as all-organic bulk heterojunctions without many of their disadvantages. Structural analysis confirms the existence of crystalline phases of the constituent donor molecule, copper phthalocyanine (CuPc), and the acceptor, C_{60}. The new device architecture results in a three-fold increase of power conversion efficiency over that of an efficient planar HJ solar cell control.

To reduce cell series resistance in the organic BHJ it is necessary to create morphological order that leads to a low resistance to charge conduction, lacking bottlenecks or islands that impede carrier extraction. Indeed, spatial ordering induced by vertical phase separation led to increased charge collection in organic/inorganic quantum dot hybrid cells from 1.7 %[6] for a disordered cell to 2.8 %.[7] For this reason, we recently reported organic solar cells with an ordered, interdigitated DA interface formed by crystalline donor protrusions and a planarizing acceptor layer, grown by the process of organic vapor phase deposition (OVPD). Control of organic film crystallization and morphology resulted in a low resistance, ordered, interdigitated interface that, when employed in solar cell structures, led to significantly improved efficiency over otherwise identical planar HJs.[8] Such an interface, however, does not increase efficiency for the materials with large exciton diffusion lengths, e.g., C_{60}, where the finite protrusion size and density do not lead to increased exciton dissociation.[9] In the current work, we have expanded the DA crystalline interface concept into an extended bulk, highly interconnected and entangled interpenetrating network. This concept employing a thicker DA region significantly increases the HJ interface area while maintaining crystalline regions that effectively conduct charges to the opposing electrodes of the cells. This architecture opens up a range of possibilities for attaining high efficiency organic PV cells, including the mixing of three or more organic constituents in a single active region to provide full coverage of the solar spectrum.

The nanocrystalline network relies on the growth of ultrathin, alternating layers of the D and A molecules such that any given layer does not fully cover the layer that lies below. Incomplete coverage results from a combination of lack of surface wetting, and control of film morphology and crystalline texture using OVPD (see Experimental).

The growth of nanocrystalline DA networks was simulated by including gas phase molecular transport, surface diffusion, and re-evaporation back into gas phase,[10] with results shown in Figure 1a. Periodic boundary conditions apply in both in-plane directions. Organic molecules randomly originate far from the substrate in the gas phase, and diffuse toward the substrate. Upon reaching a solid surface, the admolecule diffuses on the solid film surface, where the jumping rate be-

[*] Prof. S. R. Forrest, F. Yang
Department of Electrical Engineering & Computer Science
University of Michigan, Ann Arbor, MI 48109 (USA)
E-mail: stevefor@umich.edu
S. R. Forrest, K. Sun
Department of Materials Science & Engineering, University of Michigan
Ann Arbor, MI 48109 (USA)
S. R. Forrest
Department of Physics, University of Michigan
Ann Arbor, MI 48109 (USA)
F. Yang
Department of Electrical Engineering, Princeton University
Princeton, NJ 08544 (USA)
K. Sun
Electron Microbeam Analysis Laboratory, University of Michigan
Ann Arbor, MI 48109 (USA)

[**] The authors gratefully acknowledge Barry P. Rand and Jay B. Benziger for helpful discussions, and Guodan Wei for absorption measurements. We also thank the US Air Force Office of Scientific Research and Global Photonic Energy Corporation for financial support.

© 2007 WILEY-VCH Verlag GmbH & Co. KGaA, Weinheim

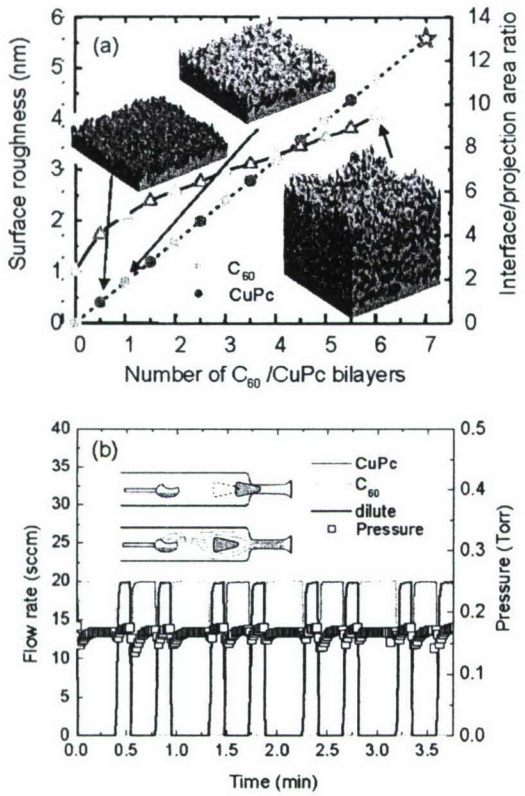

Figure 1. Simulation and growth methods of $[C_{60}(3\text{ nm})/CuPc(3\text{ nm})]_n$ nanocrystalline donor/acceptor (DA) networks. a) Simulation of the growth progression of a six period network. The plot shows, the root mean square (rms) surface roughness (open triangles) and the interface area relative to a planar DA junction (filled circles) as functions of number of bilayers. The star shows the final area ratio after the 6-period network is covered by a continous C_{60} planarizing layer. The three inset pictures show the evolution of the film structure and surface morphology of the C_{60} (magenta)/CuPc (cyan) nanocrystals at different growth stages in the progression, as well as the CuPc network formed after the sixth C_{60}/CuPc cycle, where 3-D interconnected networks can be clearly seen. b) Mass flow rates and pressure change recorded during the organic vapor phase deposition of the C_{60}/CuPc structure. Top inset: Barrel valve in the off position, preventing organics from diffusing out of the barrel. Bottom inset: Carrier gas conveying organic molecules out of the barrel when the valve is in the on position.

tween two sites, i and j, is determined by the site energy E_i and E_j as[10]

$$K_{1\to j} = \nu f(E_i, E_j) \tag{1}$$

Here ν is the lattice vibration factor and

$$f(E_i, E_j) = \begin{cases} \exp\left(\dfrac{-E_j - E_i}{k_B T}\right) & \text{if } E_j > E_i \\ 1 & \text{if } E_j > E_i \end{cases} \tag{2}$$

The site energy, E_i, is the sum of van der Waals interactions between the admolecule and all proximal neighboring molecules. The interaction energies between nearest neighbors are taken as 0.867 eV (CuPc – CuPc),[11] 1.5 eV (C_{60} – C_{60}),[12,13] and 0.044 eV (CuPc – C_{60}).[14] respectively. Since the interaction between like molecules is much larger than the interaction between unlike molecular pairs, similar molecules tend to aggregate. The simulated growth of the network begins on a continuous layer of CuPc on a transparent conductive substrate, e.g., indium-tin-oxide (ITO). Then a thin layer of C_{60} is deposited on top of the underlying, continuous CuPc layer. The aggregates in the C_{60} layer do not provide a full coverage of the underlayer, leaving part of the CuPc exposed. A second, thin CuPc layer is then deposited, partially covering the C_{60} layer with portions of the second CuPc layer directly contacting the first, continuous CuPc layer. By continuously alternating the deposition of C_{60} and CuPc, 3D interpenetrating nanocrystalline networks of C_{60} and CuPc are formed. The growth simulation indicates a monotonic increase of the interface area as the number of alternating DA bilayers is increased. As shown in Figure 1a, the final interface area in a nanocrystalline cell with 6 C_{60}/CuPc pairs is 11 times that of a planar interface. The root mean square (rms) surface roughness of the nanocrystlline films also increases, and reaches a maximum of approximately 4 nm. The final step is the growth of a continuous C_{60} layer on top of the network, planarizing the film surface to prevent shorts.[8]

We used OVPD to grow the crystalline network PV cells. Large nitrogen gas flow rates (150 sccm for CuPc and 100 for C_{60}) and low substrate temperatures ($T_{sub} = 4 \pm 1\,^{\circ}C$) were used for the bottom and top continuous layers, resulting in a flat surface. Smaller nitrogen flow rates (20 sccm for both CuPc and C_{60}) and higher T_{sub} ($15 \pm 1\,^{\circ}C$) were used to promote crystallization during the discontinuous layer growth.[15] The crystalline film texture of an OVPD-grown multilayer (grown by the process illustrated in Figure 1b, and described in the Experimental) is confirmed by transmission electron microscopy (TEM). X-ray diffraction (XRD) and atomic force microscopy (AFM), as shown in Figure 2. A cross-sectional TEM image of $[CuPc(6.1\text{ nm})/C_{60}(6.1\text{ nm})]_{10}$ is shown in Figure 2a. (Here, the notation $[D(x\text{ nm})/A(y\text{ nm})]_n$ refers to the thicknesses x, y of the D and A layers, respectively, and n is the number of DA pairs.) The CuPc and C_{60} phases are similar to those observed in a crystalline bilayer film.[16] The C_{60} phase has clearly ordered, close packed molecular planes, while the monoclinic CuPc lattice appears less ordered since the image is not taken along the projection of a single, crystallographic plane.[17] Both electron and X-ray diffraction confirm the existence of crystalline domains of CuPc and C_{60}. Crystalline domain sizes range from 5 nm to 10 nm, similar to those found in homogeneous films of C_{60} but smaller than ZnPc crystals obtained by thermal evaporation[18,19]. We obtained similar TEM images of $[CuPc(3.1\text{ nm})/C_{60}(3.1\text{ nm})]_{17}$, where the crystallites are similar in shape but have slightly smaller sizes, as expected. High-angle annular dark-field images confirm the presence of CuPc aggregates, with sizes comparable to the domain sizes observed in Figure 2a.

© 2007 WILEY-VCH Verlag GmbH & Co. KGaA, Weinheim

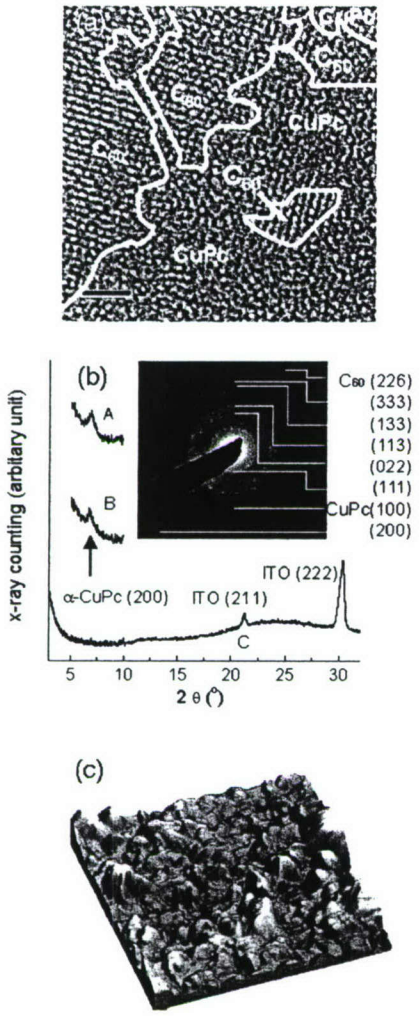

Figure 2. Structural characterization of a C_{60}/CuPc nanocrystalline film grown on an indium-tin-oxide (ITO) substrate. a) Cross sectional high-resolution TEM image of a $[CuPc(6.1\ nm)/C_{60}(6.1\ nm)]_{10}$ film, showing nanocrystalline domains indicated by white curves that approximately locate the domain boundaries. The scale bar corresponds to 5 nm. b) Bragg-Brentano x-ray diffraction pattern of an OVPD grown A. $[C_{60}(3.5\ nm)/CuPc(3.5\ nm)]_5$ film, and B. a $[C_{60}(1.9\ nm)/CuPc(1.9\ nm)]_{10}$ film. C. A 100-nm thick C_{60}:CuPc = 1:1 mixed film grown by vacuum thermal coevaporation. The CuPc (200) and ITO (211), (222) indices are indicated. The lack of a CuPc peak in C. indicates the absence of crystalline domains. Inset: Plan-view selective area diffraction pattern taken for the film in a. The diffraction indicies of α-CuPc and C_{60} are marked. Well defined diffraction spots indicating a high degree of crystalline order. c) Atomic force micrscopic surface morphology of the same film in a, showing an rms roughness of 12.7 nm in the 100 × 100 nm^2 area.

A selected-area electron diffraction (SAED) image of the same $[CuPc(6.1\ nm)/C_{60}(6.1\ nm)]_{10}$ film in plan-view (Fig. 2b, inset) shows diffraction spots corresponding to ordered domains of α-CuPc[20] and face-centered cubic (fcc) C_{60}.[21] The crystallites have a similar size and distribution as those seen in cross-sectional view. The well defined diffraction spots indicate a high degree of crystalline order and orientation within the region of the probe beam. In addition, the XRD patterns of $[CuPc(3.5\ nm)/C_{60}(3.5\ nm)]_5$ and $[CuPc(1.9\ nm)/C_{60}(1.9\ nm)]_{10}$ shown in Figure 2b, confirm the existence of α-CuPc in the two samples. No C_{60} diffraction peaks can be identified in the scanning range owing to its large lattice constant (a = 14.16 Å).[21] These structural studies show that crystalline phases are obtained by alternating the growth of the D and A materials using OVPD, as opposed to amorphous CuPc:C_{60} mixed films grown by co-evaporation[4] (bottom scan, Fig. 2b), where the crystalline phase separation is limited.[4,5,18,19,22] As shown in Figure 2c, the surface morphology of the same $[CuPc(6.1\ nm)/C_{60}(6.1\ nm)]_{10}$ film observed by AFM shows the crystalline texture with an rms roughness of 12.7 nm, reflecting the roughing effect (c.f. Fig. 1a) caused by the crystallite growth over the ITO substrate whose rms roughness < 3 nm.

The absorption spectra of the nanocrystalline films are fit to the linear sum of the neat CuPc and C_{60} absorption spectra (α_{CuPc} and α_{C60}, respectively). Figure 3a shows the absorption coefficient of $[CuPc(3.1\ nm)/C_{60}(3.1\ nm)]_{17}$ grown on a fused quartz substrate, fit using $\alpha_{NC} = 0.48\ \alpha_{C60} + 0.23\ \alpha_{CuPc}$. Films with different DA cycle thicknesses are fit using similar expres-

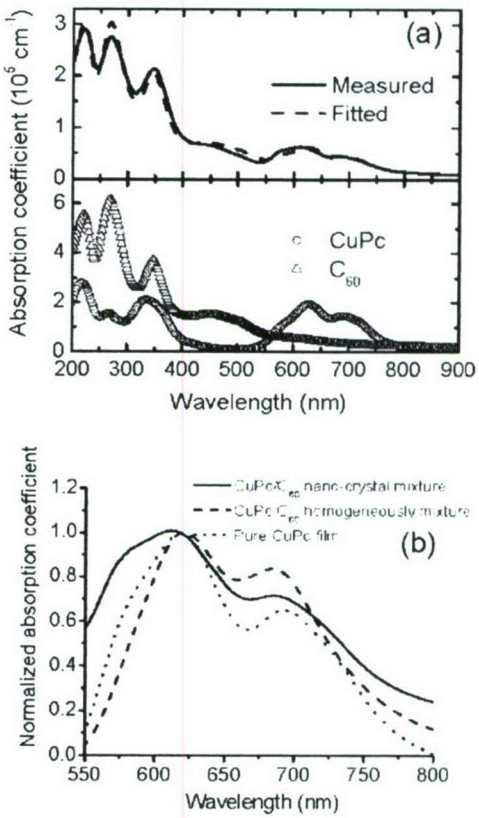

Figure 3. Absorption coefficients (α) of CuPc and C_{60} films on fused silica substrates. a) Absorption of a nanocrystalline $[C_{60}(3.1\ nm)/CuPc(3.1\ nm)]_{17}$ film, and a fit by $\alpha_{NC} = 0.48\ \alpha_{C60} + 0.23\ \alpha_{CuPc}$. The absorption of the pure films are shown in the lower part of the figure. b) Normalized absorption spectra in the low-energy Q-band of CuPc.

© 2007 WILEY-VCH Verlag GmbH & Co. KGaA, Weinheim

sions. Pure CuPc films have two peaks centered at wavelengths of λ = 620 and 695 nm, corresponding to dimer and monomer absorption, respectively.[20] For amorphous CuPc:C_{60} mixtures, the absorption at λ = 695 nm is enhanced due to an increased intermolecular distance.[4,22,23] By comparison, the nanocrystalline layer peak at λ = 695 nm is less pronounced than in the mixed film, implying the presence of a high density of CuPc crystallites (Fig. 3b).[22] The asymmetry in the CuPc and C_{60} absorption obtained in our fits may be an effect of differing crystal sizes for these two molecular constituents.

We note that these crystalline structures are in a stable, rather than metastable, structures, as observed in annealed mixtures of CuPc and 3,4,9,10-perylenetetracarboxylic bisbenzimidazole (PTCBI).[24] Furthermore, compared to phase-separated polymer cells prepared by annealing at 110–150 °C,[3,15] the small molecular weight films in our PV cells have high glass transition temperatures (> 400 °C). Further phase separation of these cells is, therefore, not expected to occur under normal operating conditions and required operational lifetimes (10–20 years) of such devices.

A series of CuPc(14.5 ± 0.2 nm)/[C_{60}(3.2 ± 0.2 nm)/CuPc(3.2 ± 0.2 nm)]$_n$/C_{60}(40.0 ± 0.5 nm)/BCP(10 nm)/Ag (BCP = bathocuproine) double heterojunction PV cells[25] were fabricated, where n ranged from 0 to 12. Here, BCP was used as an exciton blocking layer. The nominal thicknesses of the C_{60}(3.2 nm)/CuPc(3.2 nm) multilayers were varied between 6.4 and 76.8 nm, keeping C_{60}:CuPc = 1 for all samples. Hence, for n = 12, the total organic active film thickness was t = 141 nm, which exceeds t = 100 nm, typical of that of a conventional, bilayer small molecular weight cell. This in turn increases the optical absorption because of its exponential dependence on thickness (i.e., cell responsivity follows (1–exp[–αt])), where α is the absorption coefficient of the organic material. Furthermore, the top C_{60} layer is thicker than used in the optimized bilayer device,[25,26] as necessary to planarize the rough film surface[8] (c.f. Fig. 2c).

The dark current density-voltage (J–V) characteristics of all cells have rectification ratios > 10^4 at ± 1 V, as shown in Figure 4a. Fitting the forward J–V curves using the ideal diode equation[8,26] yields the specific series resistance, R_{SA}, as a function of the number of alternating DA pairs (and hence total active layer thickness) in Figure 4b. The bilayer (n = 0) cell has R_{SA} = 0.5 Ω·cm^2, gradually increasing to 3.0 Ω·cm^2 for n = 12. That R_{SA} increases by a factor of ~6 for a cell only twice as thick indicates that the nanocrystalline region is not completely free of bottlenecks to charge conduction. However, multilayers with fewer periods show only a 2 to 3 times increase in R_{SA}, suggesting that disorder increases significantly only for the deepest stacks.

The photoresponse of the same cells as in Figure 4 measured under simulated 100 ± 4 mW cm^{-2} AM 1.5G solar irradiation are shown in Figure 5a. The short circuit current (J_{SC}), open circuit voltage (V_{OC}), and fill factor (FF) are plotted in Figure 5b. With n increasing from 2 to 6, J_{SC} significantly increases by nearly a factor of 3, from 5.6 ± 0.1 mA cm^{-2} in the bilayer cell to 17.0 ± 0.2 mA cm^{-2}, and then drops as n is increased further, owing to the high series resistance of the thickest cells with large and entangled crystalline networks. In the same figure, V_{OC} increases from 0.44 ± 0.01 V in the bilayer cell (n = 0), and gradually increasing to 0.50 ± 0.01 V at n = 12. Finally, FF decreases slightly from 0.57 ± 0.01 at n = 0 to 0.56 at n = 6, and drops to 0.44 ± 0.01 at n = 12, once more reflecting the increase of resistance in the deepest stacks, as shown in Figure 4b.

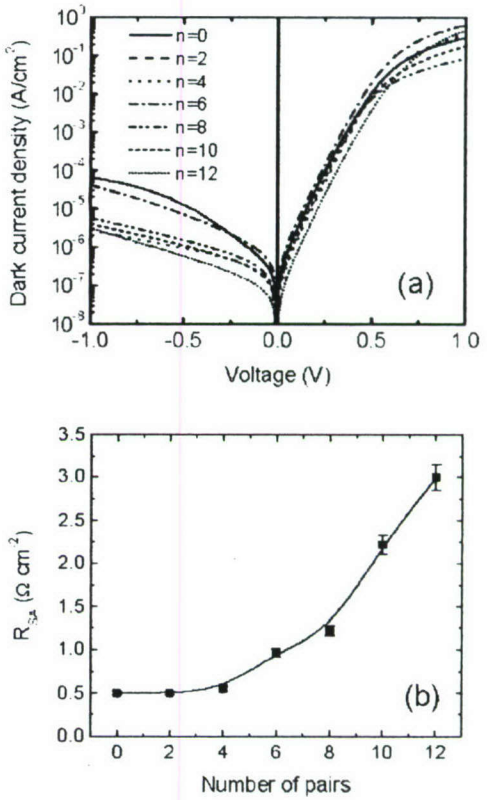

Figure 4. The performance of CuPc(14.5 ± 0.2 nm)/[C_{60}(3.2 ± 0.2 nm)/CuPc(3.2 ± 0.2 nm)]$_n$/C_{60}(50.0 ± 0.5 nm)/BCP (10 nm)/Ag solar cells, with n varying from 0 to 12, and the total thickness of the active layers varying from 54.5 to 141 nm.. a. Dark current density–applied voltage (J–V) characteristics b. Specific resistance (R_{sa}) as a function of n and C_{60}/CuPc nanocrystalline layer thickness, calculated by fitting the dark J–V characteristics using the ideal diode equation..

The external quantum efficiency (EQE) as a function of wavelength[27] is shown in Figure 5c. The EQE peak, centered between λ = 430 and 470 nm, results from C_{60} absorption,[28] whereas the peaks at λ = 620 and 695 nm are due to CuPc absorption[4] (c.f. Fig. 3a). As the number of C_{60}/CuPc pairs increases from n = 0 to n = 6, the EQE increases rapidly, i.e., the λ = 620 nm peak increases from 25 % to 76 %, and the peak at λ = 450 nm increases from 22 % to 64 %, both showing a 3-fold increase with n. In fact, in a previously reported photodetector composed of *continuous* ultrathin (≥ 0.5 nm) CuPc/PTCBI multilayer stacks grown in vacuum, an EQE of up to 75 % was achieved at a reverse bias of –10 V.[29] In contrast to that device, the nanocrystalline solar cell with its en-

© 2007 WILEY-VCH Verlag GmbH & Co. KGaA, Weinheim

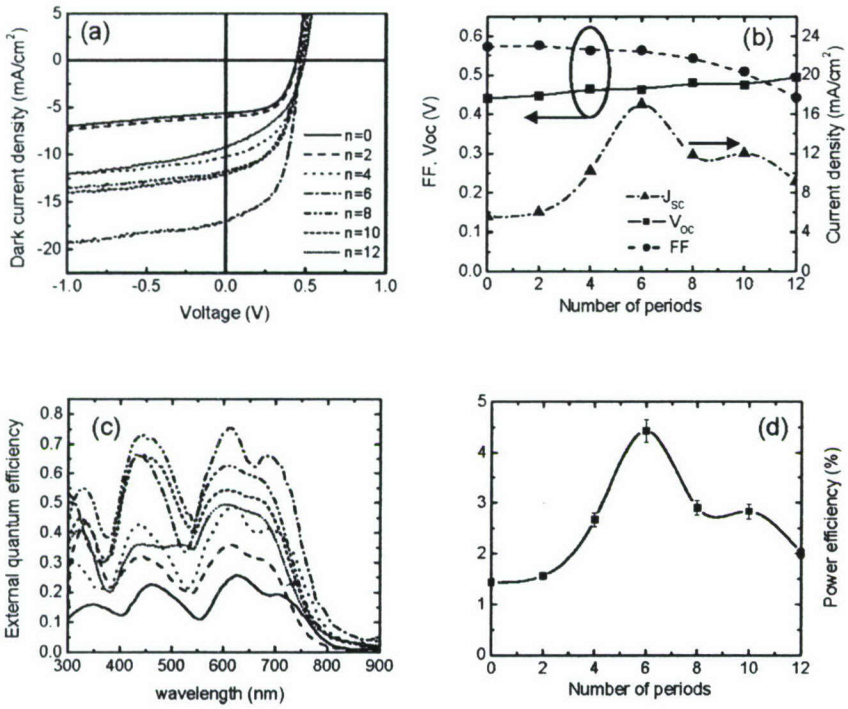

Figure 5. Parameters affecting room-temperature power-conversion efficiency of the solar cells in Figure 4. a) *J–V* characteristics at simulated AM 1.5 global 105 ± 5 mW cm^{-2} solar illumination. b) Short circuit current density (J_{sc}), open circuit voltage (V_{OC}) and fill factor (*FF*) as functions of the number of C_{60}/CuPc growth cycles, *n*. c) External quantum efficiency (η_{EQE}) spectra of devices with different *n*. d) Power conversion efficiency (η_P) as a function of *n* and C_{60}/CuPc nanocrystalline layer thickness.

tangled heterointerface shows the same large EQE at zero bias, implying success in achieving continous conductive pathways. The EQE decreases at larger *n* owing to a lower carrier collection efficiency resulting from increased resistance, possibly indicating that the percolating conducting paths formed by the network of nanocrystallites are interrupted by bottlenecks or islands. Note that the broad peak corresponding to C_{60} absorption shifts to shorter wavelength as *n* increases, as a result of the optical field changes with the thickness.

Previously, it was shown that the growth of an organized interdigitated DA interface results in a 2.7 times increase in efficiency in a CuPc/PTCBI solar cell[8] over its planar analog, but that architecture showed no improvement when the CuPc/C_{60} system was used.[9] This lack of improvement was attributed to the long (~40 nm) exciton diffusion length[2] in C_{60}, which exceeded the interdigitated feature width. The CuPc/PTCBI cell characteristic diffusion lengths were < 10 nm, or half of the feature size, hence leading to the efficiency improvement observed. In contrast, the photoresponse of CuPc and C_{60} in the nanocrystalline cells both increase by more than 3 times, suggesting that the high carrier mobility in the extended, percolating networks is primarily responsible for their improvement in efficiency.

The power conversion efficiency, η_P, is plotted as a function of *n* in Figure 5d. The photocurrent and power efficiencies of unpackaged devices were measured in air referenced to an NREL-calibrated Si detector. Here, $\eta_P = 1.4 \pm 0.1$ % in the bilayer device ($n = 0$) increases by a factor of 3, to a maximum of 4.4 ± 0.2 % at $n = 6$, corresponding to a total thickness of the nanocrystalline region of 38 nm, which is almost double the optimum thickness of a mixed CuPc:C_{60} solar cell active region.[5] The efficiency rolls off to 2.1 ± 0.1 % at $n = 12$. The power efficiency of the unoptimized CuPc/C_{60} bilayer control cell is consistent with that reported by other groups,[30,31] although it is not as high as the best reported for planar cells using the same materials system grown by vacuum thermal evaporation.[26] The solar cell efficiency showed minor (~ 5 %) degradation when exposed to ambient for 24 hours.

By controlling the organic molecule crystallization conditions, we used OVPD to deposit an organic solar cell architecture incorporating an all-organic nanocrystalline network which has both a large DA HJ interface area favorable for exciton dissociation, and a large thickness for light absorption.[32] The crystalline order introduces only a small series resistance with increasing thickness, and our demonstration has resulted in a three-fold increase of efficiency over planar HJ controls in a one-to-one comparison. The solar cell active region thicknesses are > 100 nm, eliminating shorts commonly observed in thinner cells, while also increasing the active region thickness, leading to an exponential increase in light absorption. Furthermore, changing the nanocrystalline size,[8,9] varying the DA ratio,[22] incorporating more than two molecular components to obtain broader coverage of the solar spectrum, and employing multiple cells in a tandem structure[18] may lead to even higher efficiencies. We emphasize that the devices reported here do not represent a practical demonstration, which would only be possible with large solar cell modules with long operational lifetimes. Rather, our work demonstrates that control of the fully organic nanostructure morphology leads to highly interconnected nanocrystalline networks that significantly improve both exciton dissociation and charge collection that have potential application to a new generation of solar energy conversion devices.

Experimental

The organic source material: CuPc, C_{60}, and BCP were purified by gradient sublimation prior to use. The films were deposited on a 300 nm thick ITO-coated glass substrate (Nippon Sheet Glass Co.).

© 2007 WILEY-VCH Verlag GmbH & Co. KGaA, Weinheim

precleaned with organic solvents and exposed to ultraviolet/ozone before loading into the OVPD chamber [8,9] with a base pressure < 0.09 Torr. OVPD employed a continuous flow of purified N_2 through the organic source barrels regulated with mass flow controllers and a throttle valve. The substrate temperature T_{sub} was kept constant at 15 ± 0.5 °C for all growth. The conditions for the growth of the first CuPc continuous layer were: source temperature, T_{CuPc} = 446 ± 1 °C; N_2 flow rate = 150 sccm; reactor pressure P = 0.587 ± 0.001 Torr; and growth time t_g = 1 min. The conditions for the last C_{60} planarizing layer were: T_{C60} = 471 ± 2 °C, N_2 flow rate = 100 sccm, P = 0.421 ± 0.001 Torr, and t_g = 7 min. For the discontinuous CuPc and C_{60} nano-crystallite growth the source temperatures were: T_{CuPc} = 420 ± 1 °C, T_{C60} = 463 ± 2 °C, respectively. The thickness of each layer grown by OVPD is limited by quickly switching the carrier gas flow on and off through the two molecular source barrels (Fig. 1b, inset). Constant N_2 flow at 20 sccm through the CuPc or C_{60} molecular source barrels was used during deposition, with the same N_2 flow used for 9 s between the switching of C_{60} and CuPc to minimize material mixing of the D and A molecules in the chamber prior to deposition.. The constant flow results in a stable pressure of 0.166 ± 0.007 Torr during the growth (see Fig. 1b). In each C_{60}/CuPc cycle, C_{60} was deposited at a rate of 0.14 ± 0.01 nm s^{-1} and CuPc was deposited at a rate of 0.25 ± 0.01 nm s^{-1}, calibrated from previous growth runs where the product film thicknesses were measured using ellipsometry. Cone-shape stoppers were used at the barrel nozzle exit ports to prevent organics from diffusing into the chamber when the source flow is off. After CuPc/C_{60} growth, the samples were transferred through a N_2 glove-box into a vacuum chamber where a 10 nm thick BCP layer, and the 100 nm thick Ag cathode were deposited using thermal evaporation at a pressure less than 4×10^{-7} Torr through a shadow mask with an array of 1 mm diameter circular openings.

For the cross-sectional TEM, a 100 nm thick Au layer was deposited on top of the organic films to protect the organic during the thinning process. Two such pieces were glued together face-to-face. The sample was then ground, polished, and thinned to less than 100 nm by ion milling. A 200 kV JEOL JEM2010F STEM/TEM was used for high-resolution electron microscopy and high-angle annular dark-field imaging. SAED was used for plan-view organic films pealed off from the substrates. The SAED diffraction was calibrated to Au sample and the calculated lattice constants matches literature values with errors < 5 % for α-CuPc [33] and < 2.5 % for C_{60} [21]. The absorption spectra were measured using a Perkin–Elmer Lambda 800 UV/vis spectrometer for samples grown on fused quartz substrates.

Solar cell performance was tested in ambient conditions in air without encapsulation. To measure the EQE, a monochromatic beam of light from a Xe-lamp was chopped at 400 Hz and focused to a spot on the 1 mm diameter device. The light intensity was measured using a NREL-standard calibrated Si solar cell, and photocurrent spectra were measured using a lock-in amplifier referenced to the chopper frequency [27]. The J–V characteristics and power-conversion efficiencies of the devices were measured using an Oriel 150 W solar simulator equipped with AM1.5G filters (Newport). We also checked the solar spectral mismatch factor, M, using AM 1.5G spectra, the simulation illumination spectra and the photoresponsivity of reference cell, yielding $M \sim 1$. The difference between measured and spectrally corrected J_{SC} are within the errors of our measurements.

Received: April 8, 2007
Revised: August 3, 2007
Published online: ■

[1] C. W. Tang, *Appl. Phys. Lett.* **1986**, *48*, 183.
[2] P. Peumans, A. Yakimov, S. R. Forrest, *J. Appl. Phys.* **2003**, *93*, 3693.
[3] W. Ma, C. Yang, X. Gong, K. Lee, A. J. Heeger, *Adv. Funct. Mater.* **2005**, *15*, 1617.
[4] B. P. Rand, J. Xue, S. Uchida, S. R. Forrest, *J. Appl. Phys.* **2005**, *98*, 124902.
[5] J. Xue, B. P. Rand, S. Uchida, S. R. Forrest, *Adv. Mater.* **2005**, *17*, 66.
[6] W. U. Huynh, J. J. Dittmer, A. P. Alivisatos, *Science* **2002**, *295*, 2425.
[7] B. Sun, H. J. Snaith, A. S. Dhoot, S. Westenhoff, N. C. Greenham, *J. Appl. Phys.* **2004**, *97*, 014914.
[8] F. Yang, M. Shtein, S. R. Forrest, *Nat. Mater.* **2005**, *4*, 37.
[9] F. Yang, M. Shtein, S. R. Forrest, *J. Appl. Phys.* **2005**, *98*, 014906.
[10] R.-F. Xiao, J. I. D. Alexander, F. Rosenberger, *Phys. Rev. A* **1991**, *43*, 2977.
[11] D.-J. Liu, R. L. B. Selinger, J. D. Weeks, *J. Chem. Phys.* **1996**, *105*, 4751.
[12] V. P. Antropov, O. Gunnarsson, O. Jepsen, *Phys. Rev. B* **1992**, *46*, 13647.
[13] R. W. Lof, M. A. van Veenendaal, B. Koopmans, H. T. Jonkman, G. A. Sawatzky, *Phys. Rev. Lett.* **1992**, *68*, 3924.
[14] M. Fendrich, T. Wagner, M. Stohr, R. Moller, *Phys. Rev. B* **2006**, *73*, 115433.
[15] G. Li, V. Shrotriya, J. Huang, Y. Yao, T. Moriarty, K. Emery, Y. Yang, *Nat. Mater.* **2005**, *4*, 864.
[16] V. Bhosle, J. T. Prater, F. Yang, D. Burk, S. R. Forrest, J. Narayan, *J. Appl. Phys.* **2007**, *102*, 023501.
[17] J. R. Fryer, *J. Electron Microsc. Tech.* **1989**, *11*, 310.
[18] B. Maennig, J. Drechsel, D. Gebeyehu, P. Simon, F. Kozlowski, A. Werner, F. Li, S. Grundmann, S. Sonntag, M. Koch, K. Leo, M. Pfeiffer, H. Hoppe, D. Meissner, N. S. Sariciftci, I. Riedel, V. Dyakonov, J. Parisi, *Appl. Phys. A* **2004**, *79*, 1.
[19] P. Simon, B. Maennig, H. Lichte, *Adv. Funct. Mater.* **2004**, *14*, 669.
[20] C. C. Leznoff, A. B. P. Lever, *Phthalocyanines: Properties and Applications*, VCH, New York **1989**.
[21] P. A. Heiney, J. E. Fischer, A. R. McGhie, W. J. Romanow, A. M. Denenstein, J. P. McCauley Jr., A. B. Smith, D. E. Cox, *Phys. Rev. Lett.* **1991**, *66*, 2911.
[22] P. Sullivan, S. Heutz, S. M. Schultes, T. S. Jones, *Appl. Phys. Lett.* **2004**, *84*, 1210.
[23] S. Heutz, P. Sullivan, B. M. Sanderson, S. M. Schultes, T. S. Jones, *Sol. Energy Mater. Sol. Cells* **2004**, *83*, 229.
[24] P. Peumans, S. Uchida, S. R. Forrest, *Nature* **2003**, *425*, 158.
[25] P. Peumans, S. R. Forrest, *Appl. Phys. Lett.* **2001**, *79*, 126.
[26] J. Xue, S. Uchida, B. P. Rand, S. Forrest, *Appl. Phys. Lett.* **2004**, *84*, 3013.
[27] Standard ASTM E1021–95, Standard Test Methods for Measuring Spectral Response of Photovoltaic Cell, American Society for Testing and Materials, West Conshohocken, PA, USA **2001**.
[28] S. Mochizuki, M. Sasaki, R. Ruppin, *J. Phys. Condens. Matter* **1998**, *10*, 2347.
[29] P. Peumans, V. Bulovic, S. R. Forrest, *Appl. Phys. Lett.* **2000**, *76*, 3855.
[30] K. Fostiropoulos, M. Vogel, B. Mertesacker, A. Weidinger, *Proc. SPIE-Int. Soc. Opt. Eng.* **2003**, *4801*, 1.
[31] Z. R. Hong, C. J. Liang, X. Y. Sun, X. T. Zeng, *J. Appl. Phys.* **2006**, *100*, 93711.
[32] Note added in review: Analogous but not identical structures utilizing ultrathin organic layers grown by vacuum evaporation also show a modest improvement of power conversion efficiency: Z. R. Hong, B. Maennig, R. Lessmann, M. Pfeiffer, K. Leo, P. Simon, *Appl. Phys. Lett.* **2007**, *90*, 203505.
[33] P. Erk, H. Hengelsberg, in *Applications of Phthalocyanines*, Vol. 19 (Eds: K. M. Kadish, K. M. Smith, R. Guilard), Elsevier, New York **2003**, p. 105.

© 2007 WILEY-VCH Verlag GmbH & Co. KGaA, Weinheim

Solar Cells

F. Yang, K. Sun, S. R. Forrest* ..... ■ – ■

Efficient Solar Cells Using All-Organic Nanocrystalline Networks

A full-organic donor/acceptor (DA) network formed by crystalline molecules is introduced to organic solar cells. Structural analysis shows that the network is composed of donor and acceptor nanocrystals. The increased DA interface area increases photo current generation and the interconnected networks form conductive pathways for charge extraction. The solar cell using nanocrystalline DA network shows a three-fold improvement on photocurrent over that of a bilayer cell using the same DA combination.

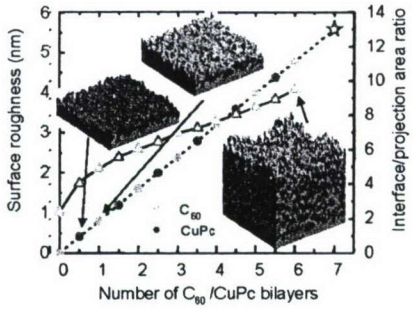

© 2007 WILEY-VCH Verlag GmbH & Co. KGaA, Weinheim

Strong Exciton-Photon Coupling and Exciton Hybridization in a Thermally Evaporated Polycrystalline Film of an Organic Small Molecule

R. J. Holmes and S. R. Forrest

Princeton Institute for the Science and Technology of Materials (PRISM), Department of Electrical Engineering, Princeton University, Princeton, New Jersey 08544, USA

(Received 1 April 2004; published 28 October 2004)

We demonstrate strong exciton-photon coupling in an optical microcavity containing a thermally evaporated polycrystalline organic thin film. Microcavity polaritons result from coupling between the 0-0 excitonic transition of 3,4,7,8 napthalenetetracarboxylic dianhydride and a cavity photon. For thicker films, the 0-1 transition also couples to the cavity mode, as vibronic relaxation is overcome by the short Rabi period for strong coupling. To our knowledge, this is the first report of strong coupling between a cavity photon and multiple vibronic transitions in a single material, made possible by the pronounced vibronic absorption features characteristic of crystalline organic materials.

DOI: 10.1103/PhysRevLett.93.186404 PACS numbers: 71.36.+c, 42.70.Jk, 72.80.Le

Since the first demonstration of strong exciton-photon coupling in an optical microcavity (OMC) [1], there has been significant interest in the study of microcavity polaritons. In this work, OMCs containing the thermally evaporated polycrystalline organic 3,4,7,8 napthalenetetracarboxylic dianhydride (NTCDA) [2] exhibit strong coupling and the hybridization of excitons arising from separate vibronic transitions characteristic of this molecular species. Indeed, organic films deposited by thermal evaporation offer a unique means for exploring the strongly coupled state: namely, the ability to examine polaritonic processes as a function of film morphology and hence phonon coupling strength in a single material.

For strong coupling to be observed, narrow absorption features are required, implying long exciton lifetimes during which coupling to the cavity photon can occur. Hence, observation of strong coupling in thermally evaporated polycrystalline thin films was thought to be difficult or even impossible due to their characteristically broad and featureless transition linewidths that arise from strong intermolecular interactions [2]. For this reason, the study of microcavity polaritons in organic semiconductors has, until now, been confined to materials that have been spun cast to form a thin film [3–7]. Doping organic materials at low concentrations into a polymer matrix decreases the interaction between guest molecules, often resulting in a reduction of the transition linewidth. To our knowledge, this is the first report of strong coupling in a thermally evaporated, crystalline organic thin film, and of coupling between separate, multiple vibronic transitions in a single material, made possible by their narrow and intense spectral lines. This work opens up new avenues for the understanding and application of strongly coupled states in this important class of semiconductor materials.

To observe large optical gain in strongly coupled media [8,9], we require efficient scattering from large wave vector to zero wave vector states. This process is often inhibited by the polariton relaxation bottleneck [10]. In organic materials, an additional relaxation pathway to the zero wave vector state is available: namely, phonon assisted relaxation. The use of a thermally evaporated organic film allows for a range of active medium morphologies, from amorphous to polycrystalline, and, consequently, allows for a range of phonon coupling strengths. Hence, crystalline or polycrystalline active media may enhance the strength of the phonon assisted relaxation in the lower polariton branch, thus allowing for a more efficient population of the zero wave vector state.

Distributed Bragg reflectors (DBR) consisting of eight pairs of quarter wavelength thick SiO_2 and SiN_x layers were deposited on quartz substrates using plasma enhanced chemical vapor deposition, yielding a peak reflectivity of 95%. A polycrystalline film [11] of NTCDA was deposited onto the DBR mirror by sublimation at 10^{-7} Torr, forming a cavity between the DBR and a 200 nm Al cap deposited onto the NTCDA surface by thermal evaporation. The closely spaced and pronounced 0-0 and 0-1 absorptive vibronic transitions of NTCDA allow them both to be accessed within a single DBR cavity mode. The dispersion relation of each OMC was determined by using angularly resolved reflection spectroscopy, measuring sample reflectivity as a function of excitation wavelength and angle [12]. Angular reflectivity spectra were collected under illumination through the quartz substrate with *p*-polarized, monochromated white light using a spectroscopic ellipsometer at room temperature.

The inset of Fig. 1 depicts the room temperature absorbance and photoluminescence emission spectrum of an NTCDA film. The full-width at half-maximum linewidths of the 0-0 (3.19 ± 0.05 eV) and 0-1 (3.39 ± 0.05 eV) transitions are (145 ± 5) meV and ($138 \pm$

 © 2004 The American Physical Society

5) meV, respectively, while the Stokes shift between the 0-0 absorption and emission lines is approximately 30 meV. The 0-0 and 0-1 transitions arise from absorption from the S_0 ground state vibronic level to either the lowest or the first vibronic level of the S_1 excited state.

Reflectivity spectra from an OMC containing a 20 nm thick film of NTCDA exhibit two clearly defined features, with anticrossing at an angle of $\theta = 28°$ (Fig. 1). Reflectivity peak energies were extracted using Gaussian fits to the multiple absorption features. Both branches of the peak dispersion in Fig. 1 were fit by a conventional two-level interaction Hamiltonian [13], yielding the energy eigenvalues:

$$\varepsilon = \frac{(E_p + E_{ex})}{2} \pm \frac{1}{2}\sqrt{(E_p - E_{ex})^2 + 4V^2}. \quad (1)$$

The potential, V, includes the interaction of the exciton and the cavity photon. Here the uncoupled exciton dispersion (E_{ex}) is independent of angle, with the cavity photon energy, E_p, following [14]:

$$E_p = E_0\left(1 - \frac{\sin^2\theta}{n^2}\right)^{-1/2}, \quad (2)$$

where the cutoff energy is E_0, and n is the effective index of refraction of the uncoupled and nonabsorbing cavity. The fits in Fig. 1 were obtained following Eqs. (1) and (2) using the parameters listed in Table I, yielding $V = (78 \pm 2)$ meV. Since V is related to the normal mode Rabi splitting (i.e., $V = \Omega/2$) [13], then $\Omega = (156 \pm 4)$ meV.

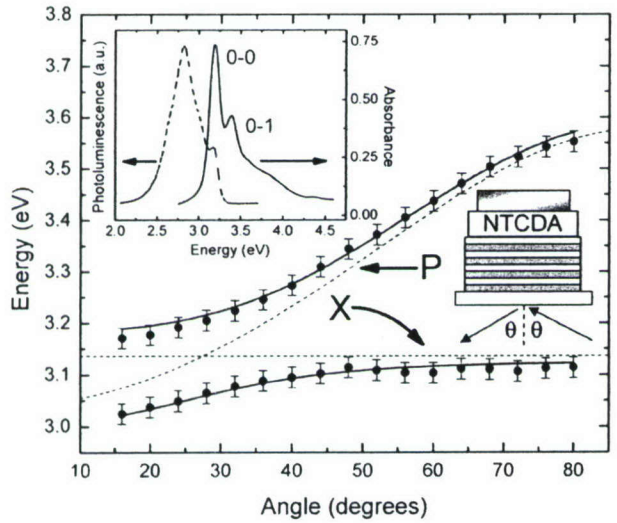

FIG. 1. Dispersion relation for an organic microcavity with a 20 nm thick NTCDA active layer. The broken curves are the uncoupled photon (P) and exciton (X) dispersion relations as determined by the fitting parameters of Table I and Eq. (2). Inset: Room temperature photoluminescence and absorbance spectra for a 50 nm thick film of NTCDA. Absorption peaks at 3.19 and 3.39 eV are designated as the 0-0 and 0-1 transitions.

Microcavities with 40 and 60 nm thick active layers were also fabricated. In general, Ω varies as $(\alpha L)^{1/2}$, where α and L are the absorption coefficient and thickness of the NTCDA layer, respectively [1]. Reflectivity spectra collected at selected angles for these microcavities are depicted in Fig. 2. Aside from the features arising from coupling between the cavity mode and the 0-0 transition of NTCDA, a third feature is also observed at higher energy, consistent with coupling to the 0-1 transition of NTCDA, yielding the dispersion relations in Fig. 3. Anticrossing between branches is observed, and both the middle and the upper branches asymptotically approach their respective uncoupled exciton energies at low angle. The middle branch of the dispersion relation for both thicknesses becomes clearly visible at $\theta > 20°$, whereas the top branch is observed at $\theta > 35°$, where this branch acquires significant photon character (Fig. 4).

The coupled mode formalism can be extended to include a third excitonic oscillator via [15–17]

$$\begin{bmatrix} E_p & V_1 & V_2 \\ V_1 & E_{ex1} & 0 \\ V_2 & 0 & E_{ex2} \end{bmatrix}\begin{bmatrix} \alpha \\ \beta \\ \gamma \end{bmatrix} = \varepsilon\begin{bmatrix} \alpha \\ \beta \\ \gamma \end{bmatrix}, \quad (3)$$

where α, β, and γ are the mixing coefficients of the new eigenvectors of the strongly coupled system. Here, two interaction potentials (V_1, V_2) are included in the Hamiltonian as well as two separate uncoupled exciton energy states (E_{ex1}, E_{ex2}). The energy eigenvalues can be determined numerically to model the dispersion relations of Fig. 3 (solid lines), yielding the parameters in Table I. Here, E_{ex1} is fixed to the value obtained from the 20 nm film, and E_{ex2} is held constant for both the 40 and 60 nm films. Branch splittings of $\Omega_{0\text{-}0} = (280 \pm 20)$ meV and $\Omega_{0\text{-}1} = (100 \pm 20)$ meV for the 40 nm film and $\Omega_{0\text{-}0} = (360 \pm 20)$ meV and $\Omega_{0\text{-}1} = (120 \pm 20)$ meV for the 60 nm film scale with thickness following $(60\ \text{nm}/40\ \text{nm})^{1/2} = 1.22$, as expected.

In Fig. 4, the mixing coefficients $|\alpha|^2$, $|\beta|^2$, and $|\gamma|^2$ [from Eq. (3)] are plotted versus angle for each branch of the dispersion relation for the 40 nm thick film. The lower branch (Fig. 4, top) has symmetrically varying amounts of cavity photon and Ex_1 (0-0 transition) character, with no Ex_2 (0-1 transition) mixing. At the point of strongest

TABLE I. Model parameters for 20, 40, and 60 nm films.[a]

Thickness (nm)	E_0 (eV)	n	V_1 (meV)[b]	V_2 (meV)
20	3.04 ± 0.05	1.90 ± 0.05	78 ± 2	
40	2.88 ± 0.05	1.80 ± 0.05	140 ± 10	50 ± 10
60	2.70 ± 0.05	1.60 ± 0.05	180 ± 10	60 ± 10

[a]Best fits were obtained with uncoupled exciton energies fixed at $E_{ex1} = 3.14$ eV and $E_{ex2} = 3.35$ eV for all thicknesses.
[b]Rabi splittings are equal to twice the interaction potentials V_1 and V_2.

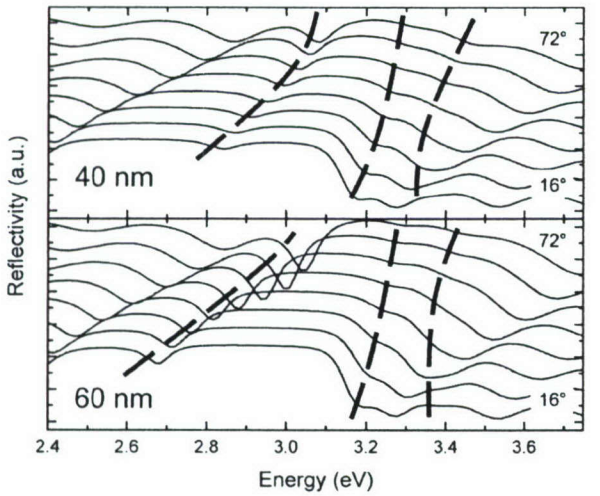

FIG. 2. Reflectivity spectra versus angle of incidence, θ, for devices consisting of 40 nm (top) and 60 nm (bottom) thick NTCDA films. Broken lines indicate a third, high energy feature in the dispersion relation consistent with strong coupling to the 0-1 transition of NTCDA.

coupling ($\theta \sim 50°$), there is significant mixing between the cavity photon and both excitons for the middle branch. Equal coupling is never achieved, although sufficient mixing is present to identify the excitonic states as hybridized. Finally, mixing is observed between the cavity photon and Ex_2 in the upper branch (bottom, Fig. 4). As the branches extend to large angles, some mixing of the Ex_1 state also becomes apparent, likely a result of the strong coupling between the cavity and Ex_1.

Strong coupling in a polycrystalline organic material such as NTCDA tests the conventional application of the coupled mode formalism of Eq. (3). In NTCDA, since the cavity photon and exciton modes cannot be separated, it is impossible to define an "empty-cavity" regime between the mirrors. The index of refraction, n, used in Eq. (2) is that found in the absence of the absorber, a decoupled scheme that is not experimentally realizable in NTCDA. Hence, since the excitation is near the dispersion edge of NTCDA, the best fits to the data require that n be decreased slightly with increased film thickness as a result of the lower cavity photon energies intrinsic to thicker cavities.

Equation (3) assumes that no coupling between the 0-0 and 0-1 excitonic states exists in the absence of the cavity mode. The large splittings between the middle and upper branches ($\sim$100 meV) reinforce this notion since coupling would not be observed due to competition with energy transfer between the excitonic states. Observation of exciton hybridization between neighboring vibronic transitions offers a new means to study the rate of vibronic relaxation in organic materials. For 40 and 60 nm thick films, the rate of strong coupling dominates the rate of vibronic relaxation from the first excited vibronic state, for 20 nm thick films, coupling to the 0-1 transition is overcome by vibronic relaxation to the ground vibronic state. The Rabi period for a 40 nm thick film gives a lower limit estimate of the lifetime of the first excited vibronic state. More accurate estimates can be made by measuring the Rabi period as a function of film thickness or concentration in a transparent host (and hence coupling strength); the Rabi period prior to strong coupling being overcome by vibronic relaxation provides an estimate of

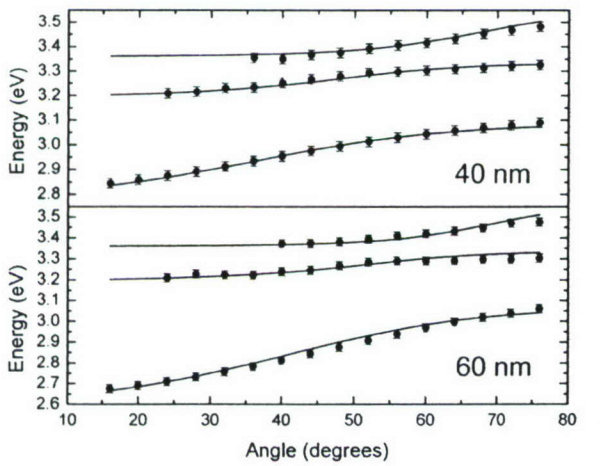

FIG. 3. Dispersion relations extracted from the reflectivity spectra in Fig. 2 for 40 and 60 nm thick films. The coupled oscillator model yields splittings of $\Omega_{0\text{-}0} = (280 \pm 20)$ meV and $\Omega_{0\text{-}1} = (100 \pm 20)$ meV for the 40 nm thick film and of $\Omega_{0\text{-}0} = (360 \pm 20)$ meV and $\Omega_{0\text{-}1} = (120 \pm 20)$ meV for the 60 nm thick film.

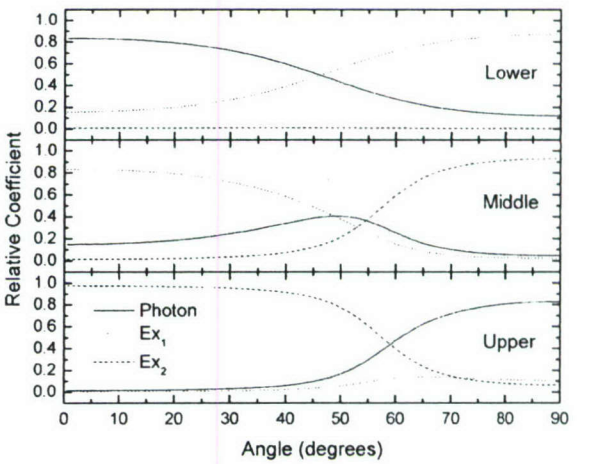

FIG. 4. Mixing coefficients $|\alpha|^2$, $|\beta|^2$, and $|\gamma|^2$ extracted from fits to the 40 nm thick film of Fig. 3. The middle branch has significant mixing between both excitons and the cavity photon at $\theta \sim 50°$. The lower and upper branches of the dispersion relation show contributions from the cavity photon and Ex_1 for the lower branch and Ex_2 for the upper branch.

the lifetime of the first excited vibronic state. This technique should also permit the estimation of the rate of intersystem crossing (ISC) from the singlet to triplet excitonic manifolds for phosphorescent organic molecules, by gradually reducing the strength of coupling to the singlet until the coupling is overcome by ISC to the triplet state.

In strongly coupled organic microcavities, only a fraction of the photogenerated states are thought to be coherent [18]. For example, in J aggregates, it has been suggested that there exists a cutoff wave vector for the lower (upper) branch of the dispersion relation above (below) which states are localized and incoherent [18]. These incoherent states are the result of the broad dispersionless character of electronic transitions in organic semiconductors within an OMC. The incoherent state can be excited nonresonantly, and then radiatively transfer energy to resonantly pump coherent states of the lower branch. This avoids the polariton bottleneck that exists in inorganic materials where exciton-phonon coupling is much weaker, and the uncoupled exciton state is itself coherent. In NTCDA, the exciton linewidth (Fig. 1) is large compared with the Rabi splitting, and hence the majority of the excited states at room temperature are incoherent.

We have demonstrated strong exciton-photon coupling in organic microcavities consisting of a neat, thermally evaporated, polycrystalline small molecule active layer of NTCDA. Large Rabi splittings are observed, and exciton hybridization between a single cavity mode and two neighboring vibronic transitions of NTCDA is understood using a three-body coupled oscillator framework. In addition to exhibiting large Rabi splittings, thermally evaporated polycrystalline films provide a means for understanding effects of morphology and long range order on the strongly coupled state. The observation of strong coupling in polycrystalline materials may allow for increased phonon assisted relaxation to the zero wave vector state as a result of enhanced phonon coupling in the film. This potential for efficient population of the zero wave vector state without the need for stimulated scattering can serve to elucidate the fundamental differences between the strongly coupled state in organic and inorganic semiconductors.

The authors acknowledge many helpful discussions with Professor V. M. Agranovich. This work was partially supported by the Air Force Office of Scientific Research (Charles Lee) and Universal Display Corporation.

[1] C. Weisbuch, M. Nishioka, A. Ishikawa, and Y. Arakawa, Phys. Rev. Lett. **69**, 3314 (1992).
[2] S. R. Forrest, Chem. Rev. **97**, 1793 (1997).
[3] T. Fujita, Y. Sato, T. Kuitani, and T. Ishihara, Phys. Rev. B **57**, 12 428 (1998).
[4] D. G. Lidzey, D. D. C. Bradley, M. S. Skolnick, T. Virgili, S. Walker, and D. M. Whittaker, Nature (London) **395**, 53 (1998).
[5] D. G. Lidzey, D. D. C. Bradley, T. Virgili, A. Armitage, M. S. Skolnick, and S. Walker, Phys. Rev. Lett. **82**, 3316 (1999).
[6] P. Schouwink, H. V. Berlepsch, L. Dahne, and R. F. Mahrt, Chem. Phys. Lett. **344**, 352 (2001).
[7] N. Takada, T. Kamata, and D. D. C. Bradley, Appl. Phys. Lett. **82**, 1812 (2003).
[8] M. Saba, C. Ciuti, J. Bloch, V. Thierry-Mieg, R. Andre, L. S. Dang, S. Kundermann, A. Mura, G. Bongiovanni, J. L. Staehli, and B. Deveaud, Nature (London) **414**, 731 (2001).
[9] P. G. Savvidis, J. J. Baumberg, R. M. Stevenson, M. S. Skolnick, D. M. Whittaker, and J. S. Roberts, Phys. Rev. Lett. **84**, 1547 (2000).
[10] A. I. Tartakovskii, M. Emam-Ismail, R. M. Stevenson, M. S. Skolnick, V. N. Astratov, D. M. Whittaker, J. J. Baumberg, and J. S. Roberts, Phys. Rev. B **62**, R2283 (2000).
[11] S. R. Forrest, M. L. Kaplan, and P. H. Schmidt, J. Appl. Phys. **56**, 543 (1984).
[12] R. Houdre, C. Weisbuch, R. P. Stanley, U. Oesterle, P. Pellandini, and M. Ilegems, Phys. Rev. Lett. **73**, 2043 (1994).
[13] M. S. Skolnick, T. A. Fisher, and D. M. Whittaker, Semicond. Sci. Technol. **13**, 645 (1998).
[14] A. Yariv, *Optical Electronics in Modern Communications* (Oxford University Press, New York, 1997), 5th ed.
[15] J. Wainstain, C. Delalande, G. Gendt, M. Voos, J. Bloch, V. Thierry-Mieg, and V. Planel, Phys. Rev. B **58**, 7269 (1998).
[16] D. G. Lidzey, D. D. C. Bradley, A. Armitage, S. Walker, and M. S. Skolnick, Science **288**, 1620 (2000).
[17] A. Armitage, M. S. Skolnick, A. Kavokin, D. M. Whittaker, V. N. Astratov, G. A. Gehring, and J. S. Roberts, Phys. Rev. B **58**, 15 367 (1998).
[18] V. M. Agranovich, M. Litinskaia, and D. G. Lidzey, Phys. Rev. B **67**, 085311 (2003).

Exciton-photon coupling in organic materials with large intersystem crossing rates and strong excited-state molecular relaxation

R. J. Holmes and S. R. Forrest
Princeton Institute for the Science and Technology of Materials (PRISM), Department of Electrical Engineering, Princeton University, Princeton, New Jersey 08544, USA
(Received 21 December 2004; published 10 June 2005)

We examine the influence of singlet-triplet intersystem crossing (ISC) and excited-state molecular relaxation on strong exciton-photon coupling in optical microcavities filled with small-molecular-weight organic materials. The effect of ISC is considered by comparing coupling effects in the phosphorescent organic platinum(II) octaethylporphyrin to those in the fluorescent free-base porphyrin tetraphenylporphyrin (TPP). The influence of excited-state molecular relaxation is studied by examining coupling to the Soret band of TPP. Both ISC and excited-state molecular relaxation prevent the population of polariton states under nonresonant optical excitation. The interplay between strong coupling and relaxation processes offers a unique opportunity to directly probe fundamental ultrafast excitonic phenomena. The competition between coupling in microcavities and these processes allows for estimation of their relative transition rates.

DOI: 10.1103/PhysRevB.71.235203 PACS number(s): 71.35.−y, 72.80.Le, 71.36.+c

I. INTRODUCTION

Organic semiconductor optical microcavities have recently been studied for their large exciton binding energies (~1 eV) and oscillator strengths, leading to the demonstration of room temperature Rabi splittings (Ω) exceeding 100 meV.[1–5] However, little attention has been paid to other properties of organic materials as they relate to strong optical coupling in microcavities, specifically singlet-triplet exciton intersystem crossing (ISC) and excited-state molecular relaxation processes.[6] These phenomena influence coupling by depopulating the excited state and competing with polariton formation, thereby reducing the potential for coupling between the exciton population and the cavity. When the rate of excitonic depopulation by ISC or molecular relaxation exceeds the Rabi frequency, strong coupling vanishes and only the relaxation is observed. This competition allows for the use of optical microcavities to elucidate the relaxation pathway for a particular excited state. Given that the rate of coupling at the point of quenching is known, the characteristic rate of relaxation can be estimated by a means exclusively available to coupled organic microcavities.

To support strong coupling, the molecular excited state and the cavity photon must simultaneously exist over a time scale longer than the Rabi period (equal to h/Ω).[7] While photon lifetimes can be enhanced using microcavities, excited-state lifetimes are not easily controlled. In an organic material, there exist a number of radiative and nonradiative pathways by which a state may decay. Indeed, a nonresonantly pumped excitonic state that can efficiently relax via a nonradiative route may not populate a coupled state. If, however, the state is resonantly populated at a lower energy than can access a nonradiative pathway, coupling should be observable. This situation arises in the presence of either ISC or other rapid molecular relaxation processes.

Here, we examine the effects of ISC and molecular relaxation on coupling in organic optical microcavities (OMCs) using small-molecular-weight vacuum-deposited porphyrins: the phosphor platinum(II) octaethylporphyrin (PtOEP), and the fluorophor tetraphenylporphyrin (TPP). The molecular structure as well as thin-film absorbance and photoluminescence (PL) spectra for both molecules are shown in Figs. 1 and 2, respectively. Porphyrins are well suited for studying strong-coupling phenomena due to their narrow and intense spectral emission and absorption lines.[8]

In particular, PtOEP was selected as a representative of a class of phosphorescent molecules with large ISC rates. In the absorbance spectrum of Fig. 1, the Q bands[8] of PtOEP each consist of two closely spaced transitions. This structure is the result of an aggregate state, and the double-peaked Q band collapses to a single transition at 2.30 eV in a dilute

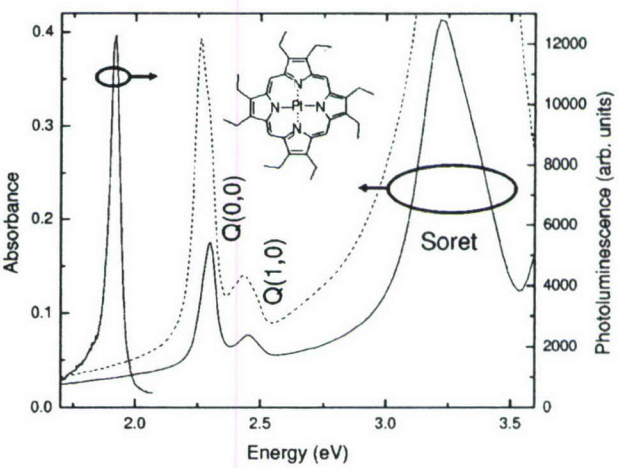

FIG. 1. The molecular structure, absorbance, and phosphorescence spectra of a neat film of PtOEP (broken line, 52±5 nm thick), and doped at 50 wt % in mCP (solid lines, E_{exc}=2.30 eV, 62±5 nm thick). The Q and Soret bands arise from S_0-S_1 and S_0-S_2 absorption, respectively. $Q(b,a)$ corresponds to the transition from the ath vibronic level of S_0 to the bth vibronic level of S_1 (see Ref. 8). Note the doublet, apparent in the narrow low-energy peak of the $Q(0,0)$ transition for the neat film.

 ©2005 The American Physical Society

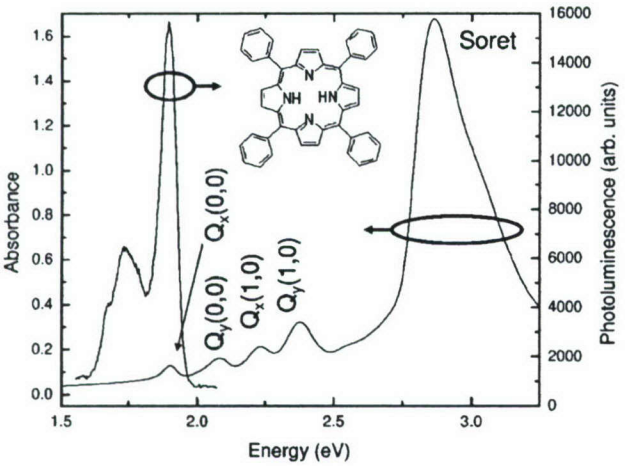

FIG. 2. The molecular structure, absorbance, and fluorescence (E_{exc}=2.82 eV) spectra of a (60±5)-nm-thick neat film of TPP. The lack of a central heavy metal atom splits each of the Q-band transitions into two additional transitions.

doped film (Fig. 1).[9] The PL of PtOEP has been ascribed to exciton recombination from the triplet (T_1) state,[10] resulting in a large energetic shift between singlet absorbance and triplet emission. In contrast, fluorescent TPP molecules have negligible ISC due to the absence of a heavy metal atom. Luminescence originates from the lowest-energy singlet state with an almost zero Franck-Condon shift (FCS) between the absorption and luminescence spectra (Fig. 2).[8]

Similarities in molecular structure between PtOEP and TPP allow for the effects of ISC on coupling to be isolated when examining the lowest-energy absorption features of both materials. The use of TPP also serves as a probe of the Soret band, which undergoes rapid molecular relaxation to the Q band prior to emission. By coupling to the Soret feature, the influence of excited-state molecular relaxation can also be studied.

This work employs spectrally and angularly resolved cavity reflectance and PL to study strong coupling in the presence of both ISC and excited-state molecular relaxation. Examining coupling in neat and doped films demonstrates that both ISC and molecular relaxation compete as nonradiative pathways for excitons that can potentially couple to a cavity mode. Quenching of strong coupling by these processes then permits estimates of their rates.

This paper is organized as follows. In Sec. II, the experimental details of microcavity fabrication and various characterization methods are described. The theoretical basis for understanding our experimental findings is provided in Sec. III, while experimental results are presented in Sec. IV. This is followed by a discussion of the results in Sec. V. Conclusions and implications of this work are provided in Sec. VI.

II. EXPERIMENT

Both PtOEP and TPP were used as neat films and also as dilute guests doped into transparent organic hosts. Platinum(II) octaethylporphyrin has a low PL efficiency in neat film as a result of concentration quenching and nonradiative triplet-triplet annihilation.[11] To reduce these effects, PtOEP was coevaporated at 50 wt % into an N,N'-dicarbazolyl-3,5-benzene (mCP) host.[12] For TPP, the Q band is luminescent in the neat film; however, to observe strong coupling to its high-energy Soret band, the molecule is codeposited at 20 wt % into the transparent host p-bis(triphenylsilyly)benzene (UGH2).[13] The lumophores were obtained from commercial sources,[14,15] while the host materials were prepared using literature procedures, and were purified using thermal gradient sublimation.[16,17]

Organic microcavities consisted of the optically active organic film deposited in vacuum at 10^{-7} Torr by thermal sublimation onto distributed Bragg reflectors (DBRs). Substrates consisted of either eight (for the PtOEP Q band, Sec. IV A, and the TPP Soret band, Sec. IV C) or 12 (for the TPP Q band, Sec. IV B) pairs of SiN_x (refractive index $n\sim2.00$) and SiO_2 ($n\sim1.46$) deposited using plasma-enhanced chemical vapor deposition onto a quartz substrate. Prior to film deposition, the quartz substrates were cleaned by rinsing in detergent and deionized water, followed by sonication in acetone and immersion in boiling trichloroethylene and 2-propanol. A 100-nm-thick film of Al deposited by thermal evaporation at 10^{-7} Torr onto the organic film serves as the top mirror, completing the microcavity.

The structures were examined using reflectivity and PL experiments. Angularly resolved reflectivity measurements were carried out using a spectroscopic ellipsometer under p-polarized monochromated white light.[18] The PL data were collected at various, independently adjustable angles of incidence and detection. For PtOEP, an InGaN laser diode[19] with wavelength λ=408 nm was used as an excitation source, while for TPP a solid-state laser with wavelength λ=475 nm was used as the optical pump.[20] Photoluminescence signals were detected using a fiber coupled spectrometer and streak camera.[21,22] The pump laser was modulated using an optical chopper (1 kHz), and the streak camera was triggered by the chopper.

Optical constants for all materials were extracted using a Cauchy model[23] to fit ellipsometric data collected for neat films deposited on Si substrates. Using films grown on quartz substrates, absorbance spectra were obtained using a Perkin-Elmer Lambda 800 uv-visible spectrometer,[24] while neat film PL was collected using a Photon Technology International fluorescence spectrometer.[25]

III. THEORY

The dispersion relation for strong coupling between a single excitonic transition and a cavity photon can be modeled by a two-level interaction Hamiltonian,[26] yielding the following eigenvalues:

$$\varepsilon = \frac{(E_p + E_{ex})}{2} \pm \frac{1}{2}\sqrt{(E_p - E_{ex})^2 + 4V^2}. \quad (1)$$

The potential V includes the interaction between the exciton and the cavity photon. The uncoupled exciton dispersion (E_{ex}) is taken as independent of wavevector, and thus also of the angle of incidence measured normal to the substrate

plane, while the cavity photon energy E_p follows:[27]

$$E_p = E_0\left(1 - \frac{\sin^2\theta}{n^2}\right)^{-1/2}. \quad (2)$$

Here, the cutoff energy is E_0, and n is the effective index of refraction of the uncoupled nonabsorbing cavity. This analysis is typically applied to structures in which an active material (e.g., quantum well, organic dye) is embedded into an inactive, transparent medium (e.g., bulk inorganic semiconductor, transparent polymer). In such cases, the index of refraction of the cavity is approximately equal to that of the transparent material. For neat film OMCs, n should be roughly equal to the index of refraction far from the excitonic resonance.

Generally, the Rabi splitting in an OMC can be expressed as[28]

$$\Omega = \left(\frac{\alpha d F \delta_{ex}\delta_{cav}}{\pi} - \frac{(\delta_{ex} - \delta_{cav})^2}{4}\right)^{1/2}, \quad (3)$$

where α and d are the absorption coefficient and thickness of the active region, δ_{ex} and δ_{cav} are the uncoupled exciton and cavity transition full widths at half maxima (FWHMs) respectively, and F is the cavity finesse. For a guest molecule doped into a transparent host matrix at guest concentration fraction f, Eq. (3) becomes

$$\Omega = \left(\frac{fd}{d_0}\frac{4k_0 d_0 F \delta_{ex}\delta_{cav}}{\lambda} - \frac{(\delta_{ex} - \delta_{cav})^2}{4}\right)^{1/2}, \quad (4)$$

where the absorbance of the doped film is simply the product of f and the neat film absorption coefficient α_0, and where the material extinction coefficient is k_0 at the center transition wavelength λ ($\alpha_0 = 4\pi k_0/\lambda$). To include small sample-to-sample variations in thickness, the doped layer thickness d is divided by the normalizing thickness d_0.

Equation (4) can be used to calculate the finesse of a given OMC provided that the dependence of the Rabi splitting on the guest fraction (f or fd/d_0) is known, along with the uncoupled physical properties of the exciton and cavity mode:

$$F = \frac{1}{fd/d_0}\frac{\lambda}{4k_0 d_0 \delta_{ex}\delta_{cav}}\left(\Omega^2 + \frac{(\delta_{ex} - \delta_{cav})^2}{4}\right). \quad (5)$$

This result can be compared to a calculation of the finesse based on mirror reflectivities (R_{DBR} and R_{Al} for the DBR and Al mirrors, respectively):[27]

$$F = \frac{\pi\sqrt{R_{DBR}R_{Al}}}{1 - R_{DBR}R_{Al}}, \quad (6)$$

providing a consistency check to Eq. (4).

IV. RESULTS

A. Strong coupling in a phosphorescent organic small molecule: PtOEP

1. Reflectivity of neat PtOEP microcavities

In Fig. 1, we show the room-temperature absorbance and PL spectra of a (52±5)-nm-thick film of PtOEP. The Gaussian FWHMs for the Q-band transitions at 2.26±0.02 and 2.30±0.02 eV are 47±5 and 39±4 meV, respectively. The phosphorescence spectrum of PtOEP also has two peaks, centered at 1.91±0.02 and 1.94±0.02 eV. The shift between the lowest-energy singlet absorption and highest-energy triplet emission is 320±30 meV.

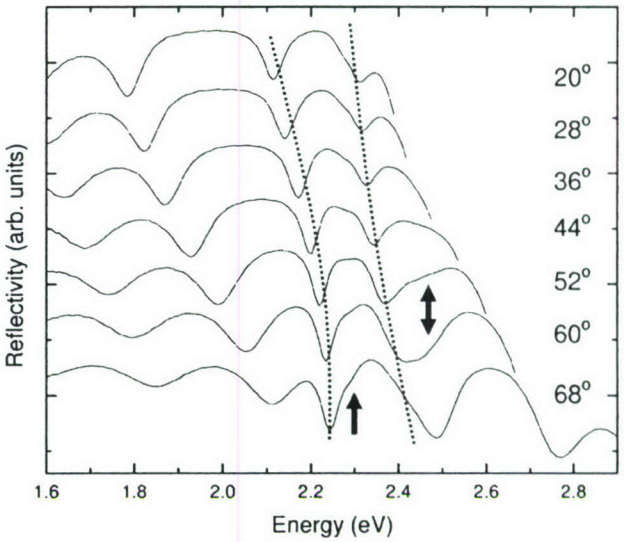

FIG. 3. Angularly resolved reflectivity spectra for an optical microcavity containing a (58±5)-nm-thick PtOEP film. The broken lines are guides indicating the strongly coupled features. The bold arrows denote the 2.26 and 2.43 eV excitonic transitions (see Fig. 1). The angular dependencies of these peaks are obscured by the two polaritonic transitions.

In Fig. 3, the reflectivity spectra for an OMC containing a (58±5)-nm-thick film of PtOEP exhibit two strongly coupled features, with additional uncoupled excitonic peaks at 2.26 and 2.43 eV (arrows, Fig. 3). Strong coupling occurs between the cavity and the Q-band transition at 2.30 eV. The peaks at 2.26 and 2.43 eV are attributed to uncoupled excitonic transitions; however, their angular dependence is masked by the intense spectral features, making a clear assignment problematic.

In Fig. 4, the dispersion relation for the PtOEP-filled OMC of Fig. 3 is plotted versus angle, where the angle of reflection is related to the photon in-plane wave vector by $\sin\theta$.[26] The fits to the dispersion relation of Fig. 4 are obtained using Eq. (1) with the parameters listed in Table I.

2. Reflectivity and photoluminescence of doped mCP:PtOEP microcavities

Figure 1 also shows the absorbance and PL spectra of a (62±5)-nm-thick film of 50 wt% PtOEP in mCP. The Q-band absorbance of the mixed film is roughly half that of the neat sample of similar thickness as expected, and an additional peak associated with mCP appears at energies >4 eV (not shown). Another difference between the neat and doped film absorbance is that the doublet of the $Q(0,0)$ transition in the neat film merges into a single peak centered at 2.30 eV.

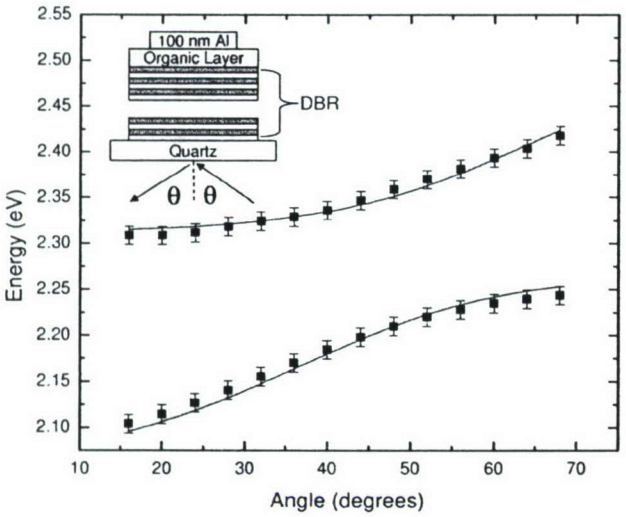

FIG. 4. Dispersion relation extracted from the spectra of Fig. 3 and fit to Eq. (1) to yield a Rabi splitting of $\Omega = 140 \pm 10$ meV.

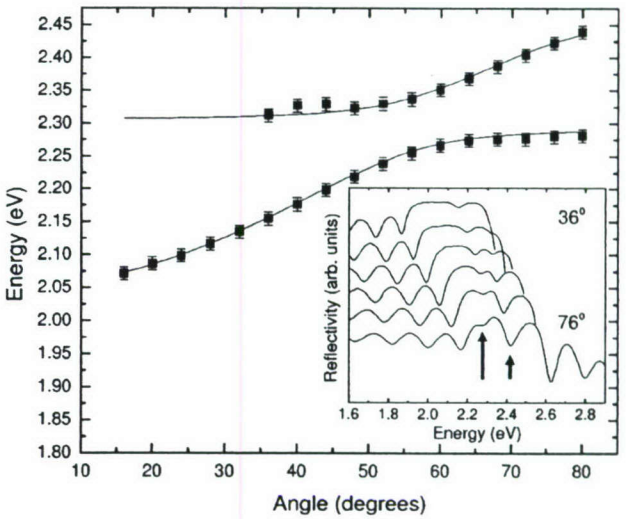

FIG. 5. Dispersion relation for an optical microcavity containing a (62 ± 5)-nm-thick film of PtOEP doped at 50 wt % into mCP determined from reflectivity measurements. Fit to Eq. (1) yields a Rabi splitting of $\Omega = 82 \pm 10$ meV. Inset: Reflectivity spectra for the same OMC at angles of 36°–76°; arrows mark the positions of the strongly coupled features.

The inset of Fig. 5 shows the reflectivity spectra for a cavity containing a (62 ± 5)-nm-thick active layer of a PtOEP-doped film, yielding the dispersion curves in Fig. 5. Multiple OMCs were fabricated, keeping the active layer thickness constant while reducing the PtOEP concentration in mCP. Figure 6 shows the dependence of the Rabi splitting on the normalized PtOEP fraction, with a fit to the data (solid line) using Eq. (4). The dependence of the extinction coefficient of the $Q(0,0)$ band of PtOEP on concentration in mCP is plotted in the inset of Fig. 6.

In previous work on OMCs, angularly resolved PL has been found to track the dispersion curve extracted from reflectivity spectra.[4,29] Figure 7 shows the PL from the mCP:PtOEP OMC of Fig. 5 under excitation at $\lambda = 408$ nm (3.04 eV). Photoluminescence is observed only from the PtOEP triplet, and not from the strongly coupled state. This observation is discussed further in Sec. V.

B. Strong coupling to the Q band of a fluorescent organic small molecule: TPP

The absorbance of TPP in Fig. 2 has four well-defined Q-band transitions from 1.50 to 2.50 eV.[8] The $Q_x(0,0)$ is centered at 1.90 eV with FWHM of 53 ± 5 meV. There is no apparent FCS between the $Q_x(0,0)$ absorption and the highest-energy PL emission (Fig. 2) centered at 1.89 eV. Reflectivity spectra for an OMC consisting of a (65 ± 5)-nm-thick layer of TPP are shown in the inset of Fig. 8. Two pronounced features (arrows, Fig. 8) are observed as a result of coupling between the cavity photon and the $Q_x(0,0)$ band. For large angles, a third feature at 2.08 eV is observed, possibly as a result of coupling to the $Q_y(0,0)$ transition (Fig. 2). Figure 8 shows the dispersion relation for the TPP-filled OMC; coupling is observed with the strongest mixing at $\theta \cong 52°$. The dispersion curves were fitted (solid lines) using Eq. (1).

Contrary to the case of PtOEP, ISC in TPP is negligible. Figure 9(a) shows PL spectra obtained from the TPP OMC of Fig. 8 under excitation at $\lambda = 475$ nm (2.61 eV). Emission from both branches of the dispersion curve is clearly visible. Figure 9(b) shows the agreement between PL and reflectivity spectra at a detection angle of $55° \pm 2°$. We observe that the PL dispersion curve (Fig. 10) is nearly identical to that obtained from reflectivity experiments (Fig. 8), as expected for a material with no ISC or molecular relaxation processes present.

TABLE I. Fit parameters for dispersion curves of Figs. 4, 5, 8, and 11.

Material	Thickness (nm)	E_0 (eV)	E_{ex} (eV)	n	Ω (meV)
PtOEP	58 ± 5	2.10 ± 0.01	2.29	1.95 ± 0.04	140 ± 10
mCP:PtOEP[a]	62 ± 5	2.06 ± 0.01	2.30	1.86 ± 0.04	82 ± 10
TPP	65 ± 5	1.73 ± 0.02	1.90	1.85 ± 0.04	42 ± 10
UGH2:TPP[b]	50 ± 5	2.68 ± 0.02	2.95	1.93 ± 0.04	285 ± 20

[a]PtOEP was coevaporated with mCP at 50 wt %.
[b]TPP was coevaporated with UGH2 at 20 wt %.

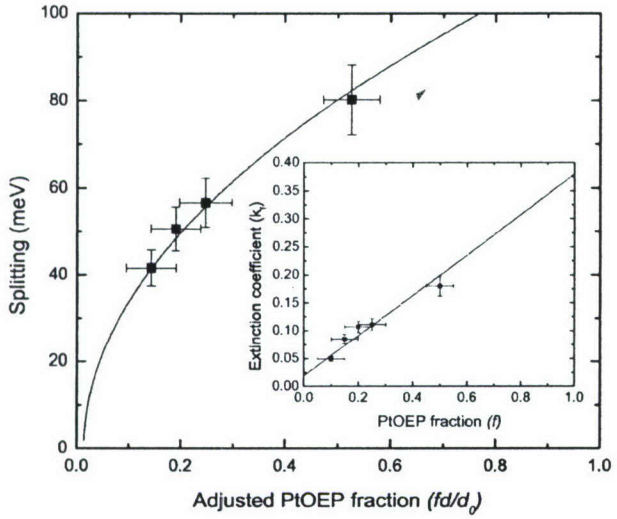

FIG. 6. Variation of the Rabi splitting with the concentration of PtOEP in mCP in optical microcavities. The fit is obtained using Eq. (4) and a thickness $d_0=60$ nm, with the cavity finesse as a free parameter. Inset: The dependence of the doped film extinction coefficient k_f on the concentration of PtOEP in mCP. The linear fit yields an average neat film extinction coefficient [$Q(0,0)$ band] of 0.36 ± 0.04.

C. Strong coupling to the Soret band of TPP

Microcavities tuned to the Soret band of TPP were fabricated to quantify the effect of excited-state molecular relaxation on strong coupling. In a neat film, the Soret band consists of two peaks centered at 2.86 ± 0.02 and 2.99 ± 0.02 eV, with FWHMs of 132 ± 13 and 270 ± 27 meV, respectively (Fig. 2). Coupling to the Soret band of a porphyrin molecule has been previously observed in a guest-host polymer system;[2] however, no study of the effect of molecular relaxation on the PL of the OMC was presented.

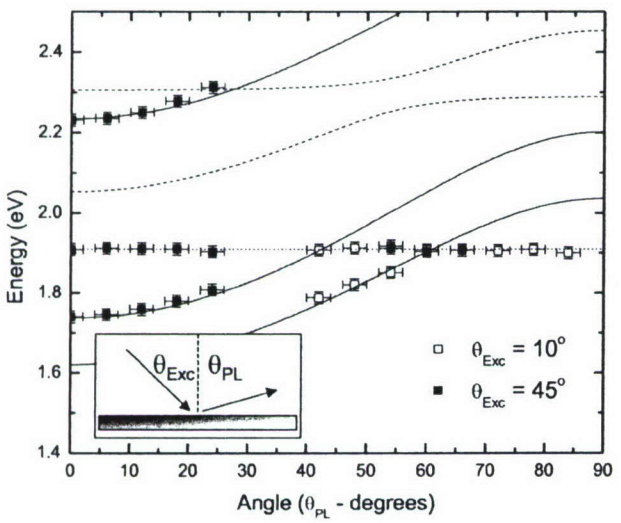

FIG. 7. Angularly resolved photoluminescence ($E_{exc}=3.04$ eV) of the mCP:PtOEP optical microcavity of Fig. 5. Photoluminescence is observed from the uncoupled triplet state as a result of ISC from S_2 to excited triplet levels that prevents the population of the strongly coupled state. Dashed and solid lines are reflectivity features reproduced from Fig. 5, where solid lines are the dispersion of the low-reflectivity DBR sidebands. For small angles, some photoluminescence leaks through the low-reflectivity sidebands that lie below the energy of the uncoupled T_1 state. Various excitation angles (θ_{exc}) are employed to trace the full dispersion of the cavity.

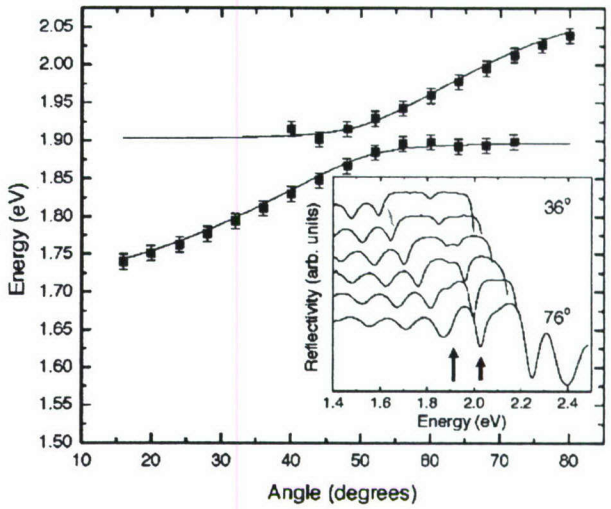

FIG. 8. Dispersion relation for an optical microcavity containing a (65 ± 5)-nm-thick film of TPP. Fitting using Eq. (1) yields $\Omega=42\pm10$ meV. Inset: Reflectivity spectra for the optical microcavity at reflection angles of 36°–76°; arrows denote the positions of the strongly coupled features.

Organic microcavities tuned to the TPP Soret band were constructed by doping 20 wt % TPP in a (50 ± 5)-nm-thick film of UGH2. Figures 11(a) and 11(b) show reflectivity spectra and the dispersion relation measured for this OMC. In this film, the Soret band consists of two transitions at 2.92 ± 0.04 and 3.06 ± 0.04 eV, with FWHMs of 143 ± 14 and 105 ± 10 meV, respectively. The PL observed under nonresonant excitation at $\lambda=408$ nm (3.04 eV) behaves similarly to that of PtOEP, with luminescence only observed from the $Q_x(0,0)$ band. A typical photoluminescence spectrum for this case is shown in the inset of Fig. 11(b).

V. DISCUSSION

A. Reflectivity of PtOEP-based microcavities

The dispersion curves of Figs. 4 and 5 were both fitted to Eq. (1) using the parameters in Table I. In the case of neat PtOEP microcavities, the Rabi splitting is large, $\Omega=140\pm10$ meV, consistent with the large absorbance of the $Q(0,0)$ band of PtOEP. In comparison, the fits obtained for OMCs based on an active layer of 50 wt % PtOEP in mCP show a reduced Rabi splitting of $\Omega=82\pm10$ meV, consistent with the reduction of the absorbance of PtOEP accompanying this dilution.

Adjusting the concentration of the active material in a transparent host matrix allows for a reduction in the Rabi splitting. Figure 6 shows the dependence of the Rabi splitting on the normalized PtOEP fraction (fd/d_0) following the square root dependence of Eq. (4). The data were fitted using

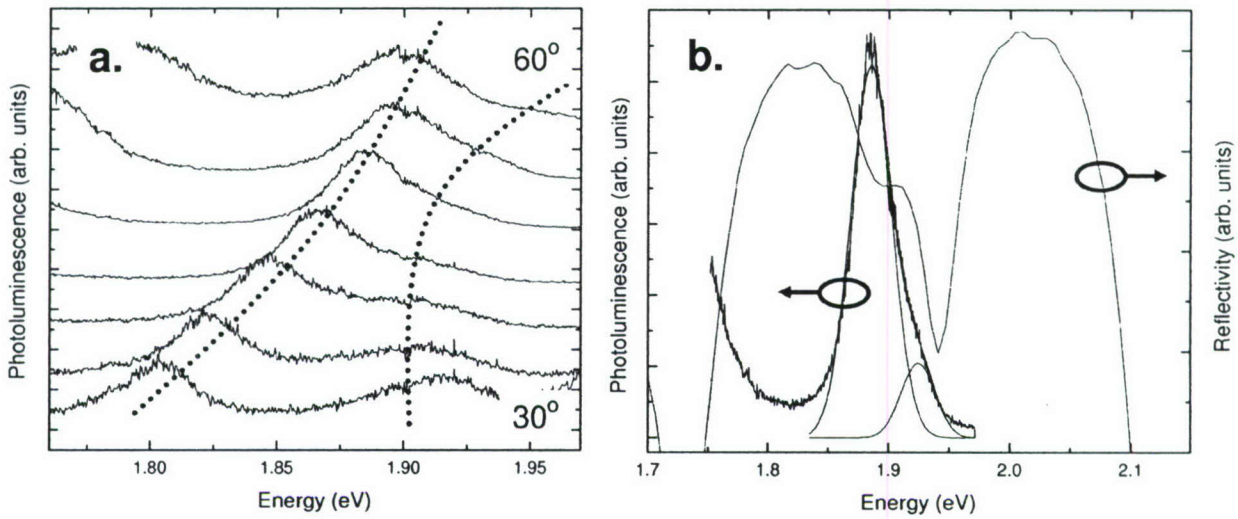

FIG. 9. (a) Photoluminescence spectra for the TPP optical microcavity of Fig. 8 for $E_{exc}=2.61$ eV excitation at normal incidence and detection angles ranging from 30° to 60°. Both branches are clearly visible (dotted lines), with the lower branch being significantly more intense. (b) Comparison of the reflectivity and photoluminescence spectra obtained for the TPP OMC at a detection angle of $55°\pm2°$. Multipeak fitting allows photoluminescence from both branches to be resolved, and agreement is obtained with the reflectivity spectrum for the same OMC at the same excitation angle.

Eq. (4) with the cavity finesse as the adjustable parameter. The $Q(0,0)$-band extinction coefficient was measured as a function of concentration for PtOEP in mCP to determine k_0, in Fig. 6, inset. Since we expect $k_f=f^*k_0$, where k_f is the extinction coefficient of the doped film, we obtain a neat film $Q(0,0)$-band extinction coefficient of $k_0=0.36\pm0.04$ from the fit (solid line).

The FWHM of the exciton transition was determined by fitting a Gaussian to the extinction coefficient feature centered at 2.30 eV and averaging values obtained for different concentrations. This leads to a mean exciton linewidth of $\delta_{cx}=55\pm5$ meV, which differs from the neat film where $\delta_{cx}=39\pm4$ meV (Fig. 1). This difference is due to the aggregate peak, observed only in the neat film.

The uncoupled cavity mode linewidth was determined from the reflectivity of an OMC containing a (58 ± 5)-nm-thick mCP film. A fit to a Gaussian at a low angle of excitation (16°) gives a cavity mode linewidth of $\delta_{cav}=82\pm10$ meV. With these parameters, Eq. (4) is used to determine the cavity finesse $F=18.4\pm0.6$. This is compared to a calculation of the finesse based on the mirror reflectivities of $R_{DBR}=0.95\pm0.01$ and $R_{Al}=0.92\pm0.01$,[30] from which we infer $F=23.3\pm0.4$. The discrepancy between the two values reflects the uncertainty in the determination of the cavity mode linewidth. Even off resonance, the presence of PtOEP in mCP will affect the cavity mode FWHM as is apparent in Fig. 3, where the FWHM of the lower polariton branch at low angle (16°) is ~51 meV, yielding a finesse of ~28. At this angle, the polariton is photonlike, and hence should closely resemble the cavity mode in both energy and shape.

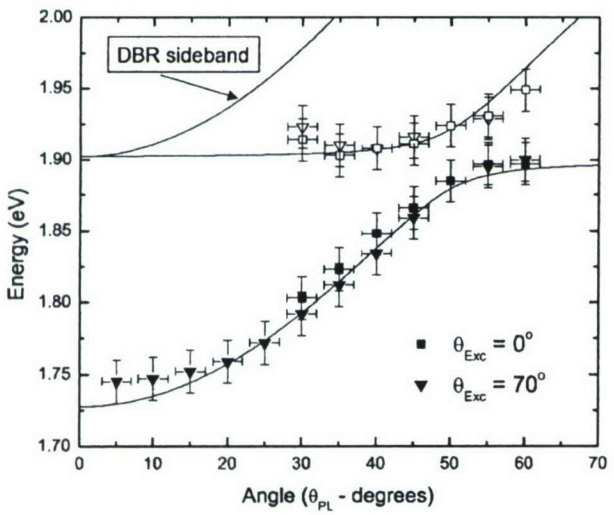

FIG. 10. The nonresonantly excited photoluminescence (symbols, $E_{exc}=2.61$ eV) and reflectivity (solid lines) from a (65 ± 5)-nm-thick TPP optical microcavity. Photoluminescence is observed from both the upper (open symbols) and lower (closed symbols) polariton branches near the point of strongest coupling. Excitation at both zero and 70° allows for the resolution of the full OMC dispersion in photoluminescence. The (DBR) sideband prevents the detection of upper-branch photoluminescence at small angles.

B. Photoluminescence of mCP:PtOEP microcavities

While originating from the coupled state, relaxation between branches often results in PL only being visible from the lower polariton branch.[4,29] In the presence of ISC, however, the situation is different. Figure 7 shows the PL from the PtOEP OMC of Fig. 5 under excitation at $\lambda=408$ nm (3.04 eV). The excitons relax via phonon emission through the S_2 manifold, and then subsequently relax from the vibronic ground state of S_2 to S_1 by internal conversion at a slower rate. If the molecule relaxes into the lowest vibronic level of S_1, it couples to the cavity photon, exhibiting PL from the coupled state. In PtOEP, this relaxation is hindered by the rapid ISC of the S_2 exciton into an excited triplet state,

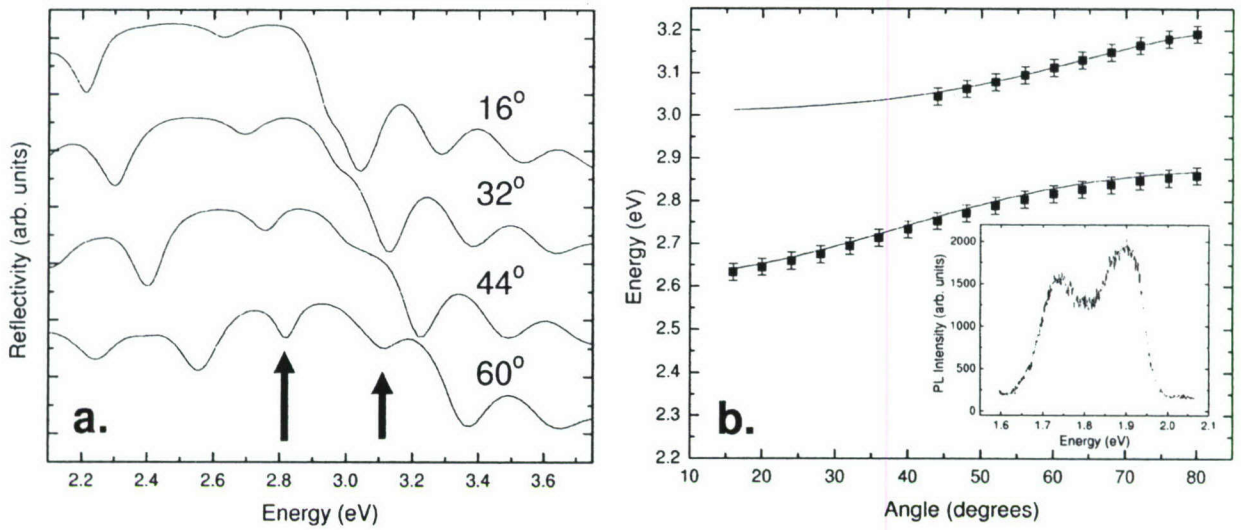

FIG. 11. (a) Reflectivity spectra for an optical microcavity consisting of a (50±5)-nm-thick film of TPP doped at 20 wt % into UGH2. Arrows indicate the positions of the strongly coupled features; the upper polariton is obscured by the sideband of the distributed Bragg reflector at low angles. (b) Dispersion relation extracted from the reflectivity spectra of (a) showing strong coupling between the cavity photon and the Soret-band excitonic transition. The dispersion relation is fitted using Eq. (1) with a Rabi splitting of $\Omega=280\pm20$ meV. Inset: Photoluminescence observed from a 20 wt % TPP in UGH2 OMC at an excitation angle of $\theta_{exc}=10°$ and energy $E_{exc}=3.04$ eV, and detected at $\theta_{PL}=45°$.

making the observation of strongly coupled PL problematic. Given rapid ISC or sufficiently nonresonant excitation, only uncoupled triplet emission can be observed. This behavior is illustrated in Fig. 7 for PtOEP OMCs. Photoluminescence is observed for the uncoupled $T_1 \rightarrow S_0$ transition with additional luminescence channeled through the low-reflectivity sidebands of the DBR. Figure 12(a) shows the energy level structure of PtOEP. Under excitation into the Soret band, excitons undergo ISC directly into an excited triplet level. The triplet exciton relaxes by phonon emission and internal conversion to the vibronic ground state of T_1, and then subsequently undergoes radiative recombination.

Previous work has shown that the quenching of strong coupling by nonradiative processes such as ISC or molecular

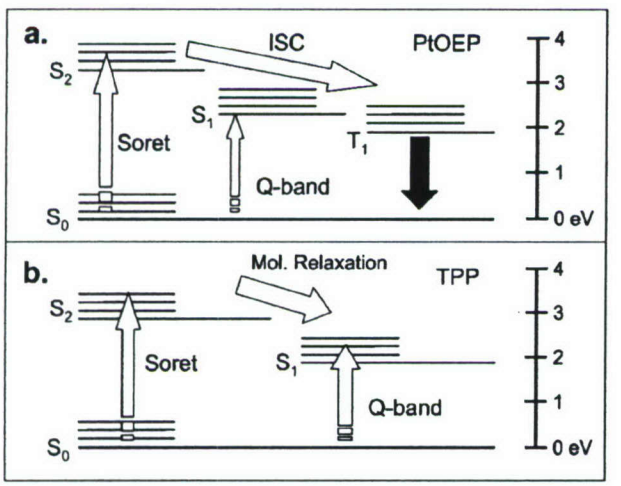

FIG. 12. Energy level diagrams for (a) PtOEP and (b) TPP extracted from absorption measurements (vibronic level splittings not to scale).

relaxation permits estimates of their transition rates.[1] In Fig. 6, the concentration of PtOEP in mCP is reduced to increase the Rabi period of the system above τ_{ISC} [cf. Eq. (4)], so that coupling vanishes and ISC becomes the dominant relaxation pathway (i.e., $\tau_{ISC} < \tau_{Rabi} = h/\Omega$). For PtOEP, ISC is observed to compete with strong coupling when the Rabi splitting is on the order of δ_{cx} and δ_{cav}; thus resolving the Rabi splitting becomes difficult when ISC dominates. If the splitting were resolvable at lower concentrations, or if the rate of ISC was larger, it would be possible to accurately estimate τ_{ISC}. In a guest-host system such as PtOEP doped into mCP, a crossover concentration (f_x) is defined as the guest concentration for which strong coupling is overcome by relaxation, and hence is no longer observed. An estimate to τ_{ISC} can be made by calculating the Rabi splitting at the crossover point f_x giving simply:

$$\tau_{ISC} = \frac{h}{\Omega_x}, \tag{7}$$

where Ω_x is the Rabi splitting calculated at the concentration f_x using Eq. (4) and Fig. 6. Since this point is not clearly resolved in data for PtOEP, we estimate a lower limit for the ISC transfer time of $\tau_{ISC} \geq 100$ fs (corresponding to $f=0.15$).

The resolution of this measurement of τ_{ISC} can be improved by observing the low-temperature reflectance (or absorbance), thus narrowing coupled features to better resolve the splitting at lower concentrations. Additionally, a phosphor with a shorter τ_{ISC} than PtOEP would result in the loss of strong coupling for larger values of the Rabi splitting, making the competition with ISC easier to resolve. The challenge with using materials with very short τ_{ISC} (e.g., Ir-based phosphors[31,32]) is that their absorbance spectra consist of several broad and overlapping transitions.

C. Reflectivity and photoluminescence of TPP microcavities

1. Q-band transition of TPP

The dispersion relation of Fig. 8 was fitted using Eq. (1), with the parameters listed in Table I, including a Rabi splitting of $\Omega = 42 \pm 10$ meV. The Rabi splitting for coupling to the $Q_x(0,0)$ band of TPP is significantly smaller than that observed for coupling to the $Q(0,0)$ band of neat PtOEP due to the larger absorbance associated with the latter molecule (Figs. 1 and 2).

In Fig. 9(a), PL spectra for the TPP OMC of Fig. 8 are shown. Luminescence from both the upper and lower branches is clearly resolved. For angles much larger than the anticrossing point, it is difficult to determine whether the upper branch is present, since the lower-branch PL intensity masks the weak nearby transitions. Figure 9(b) demonstrates the agreement between PL and reflectivity spectra collected for the same OMC at the same detection angle of $55° \pm 2°$. The consistently low intensity of the upper branch is likely the result of branch-to-branch relaxation. In Fig. 10, the dispersion relation extracted from the PL spectra of Fig. 9(a) agrees with the dispersion relation acquired from reflectivity measurements. From the observation of PL from the coupled state in TPP OMCs, we infer that the lack of strongly coupled PL from mCP:PtOEP OMCs is the result of ISC in the phosphor.

2. Soret-band transition of TPP

Microcavities consisting of 20 wt % TPP in UGH2 exhibit large Rabi splittings of $\Omega = 280 \pm 20$ meV. The dispersion curves in Fig. 11(b) were fitted using Eq. (1), with parameters given in Table I. From the reflectivity spectra of Fig. 11(a), it is apparent that the upper branch is present at small angles of excitation; however, the exact position of the upper branch at these angles cannot be accurately extracted due to interference from the DBR sideband.

Under optical excitation at $\lambda = 408$ nm (3.04 eV), 20 wt % TPP in UGH2 exhibited PL from the uncoupled Q-band transition, but not from the strongly coupled state [Fig. 11(b), inset]. This confirms that molecular relaxation leads to nonradiative exciton decay prior to reaching the lowest vibronic level in the Soret band. In solution, relaxation from the TPP Soret band to the $Q_y(1,0)$ band occurs in less than 50 fs without populating the lowest Soret vibronic as an intermediate step.[33] The energy diagram for TPP is shown in Fig. 12(b). Excitation into the Soret band leads to rapid molecular relaxation directly from an excited vibronic level of S_2 to the S_1 manifold. This is consistent with the observation of uncoupled Q-band (S_1) PL from Soret band OMCs.

VI. CONCLUSION

We have demonstrated strong exciton-photon coupling in phosphorescent materials with dominant ISC and excited-state molecular relaxation pathways. Under resonant excitation, coupling is sufficiently intense to overcome dissipative losses of the radiative state. For the case of nonresonant excitation, ISC and excited-state molecular relaxation compete with strong coupling. In the phosphor PtOEP, relaxation to the coupled state is circumvented by ISC from S_2 to an excited triplet manifold. In contrast, for the fluorophor TPP, the dispersion relations obtained from PL and reflectivity data are similar since there is no ISC to disrupt relaxation into the $Q(0,0)$ band. Coupling is defeated for nonresonant excitation of the TPP Soret band since relaxation from an excited vibronic level of the Soret band to the $Q_y(1,0)$ band occurs without passing through the ground state.

The quenching of strong coupling by ISC and excited-state molecular relaxation offers a means to study ultrafast relaxation phenomena. Further, strong-coupling quenching allows for estimates of the relative transition rates of these relaxation processes. In this work, $\tau_{ISC} > 100$ fs is found for PtOEP; however, the rate of ISC for PtOEP is too slow to allow for an upper limit to be determined using analysis of the OMC spectral response data. Phosphors with even shorter ISC relaxation times, which are challenging to measure using conventional means, should be well suited for measurements based on strong-coupling phenomena.

ACKNOWLEDGMENTS

This work was partially supported by the Air Force Office of Scientific Research and Universal Display Corporation.

[1] R. J. Holmes and S. R. Forrest, Phys. Rev. Lett. **93**, 186404 (2004).
[2] D. G. Lidzey, D. D. C. Bradley, M. S. Skolnick, T. Virgili, S. Walker, and D. M. Whittaker, Nature (London) **395**, 53 (1998).
[3] P. Schouwink, H. V. Berlepsch, L. Dahne, and R. F. Mahrt, Chem. Phys. Lett. **344**, 352 (2001).
[4] N. Takada, T. Kamata, and D. D. C. Bradley, Appl. Phys. Lett. **82**, 1812 (2003).
[5] P. A. Hobson, W. L. Barnes, D. G. Lidzey, G. A. Gehring, D. M. Whittaker, M. S. Skolnick, and S. Walker, Appl. Phys. Lett. **81**, 3519 (2002).
[6] N. J. Turro, *Modern Molecular Photochemistry* (University Science Books, Sausalito, CA, 1991).
[7] C. Weisbuch, M. Nishioka, A. Ishikawa, and Y. Arakawa, Phys. Rev. Lett. **69**, 3314 (1992).
[8] M. Gouterman, in *The Porphyrins*, edited by D. Dolphin (Academic, New York, 1978), Vol. 3, p. 1.
[9] R. N. Gillanders, M. C. Tedford, P. J. Crilly, and R. T. Bailey, Anal. Chim. Acta **502**, 1 (2004).
[10] D. Eastwood and M. Gouterman, J. Mol. Spectrosc. **35**, 359 (1970).
[11] M. A. Baldo, C. Adachi, and S. R. Forrest, Phys. Rev. B **62**, 10967 (2000).
[12] R. J. Holmes, S. R. Forrest, Y.-J. Tung, R. C. Kwong, J. J. Brown, S. Garon, and M. E. Thompson, Appl. Phys. Lett. **82**, 2422 (2003).

[13] R. J. Holmes, B. W. D'Andrade, S. R. Forrest, X. Ren, J. Li, and M. E. Thompson, Appl. Phys. Lett. **83**, 3818 (2003).
[14] Frontier Scientific, Logan, UT 84323.
[15] Acros Organics USA, Morris Plains, NJ 07950.
[16] V. Adamovich, J. Brooks, A. Tamayo, A. M. Alexander, P. Djurovich, B. W. D'Andrade, C. Adachi, S. R. Forrest, and M. E. Thompson, New J. Chem. **26**, 1171 (2002).
[17] H. Gilman and G. D. Lichtenwalte, J. Am. Chem. Soc. **80**, 608 (1958).
[18] J. A. Woollam Co., Inc., Lincoln, NE 68508.
[19] V-Series Blue/Violet Laser Diode, Coherent Inc., Santa Clara, CA 95054.
[20] Model NT55-873 Solid State Laser, Edmund Optics Inc., Barrington, NJ 08007-1380.
[21] Model 250i Chromex Spectrometer, Bruker Optics Inc., Billerica, MA 01821-3991.
[22] Model C4334 Streak Scope, Hamamatsu Photonics, Hamamatsu City, Japan.
[23] F. L. Pedrotti and L. S. Pedrotti, *Introduction to Optics*, 2nd ed. (Prentice-Hall, Englewood Cliffs, NJ, 1993).
[24] PerkinElmer Inc., Wellesley, MA 02481-4078.
[25] Photon Technology International Inc., Lawrenceville, NJ 08648.
[26] M. S. Skolnick, T. A. Fisher, and D. M. Whittaker, Semicond. Sci. Technol. **13**, 645 (1998).
[27] A. Yariv, *Optical Electronics in Modern Communications*, 5th ed. (Oxford University Press, New York, 1997).
[28] Y. Zhu, D. J. Gauthier, S. E. Morin, Q. Wu, H. J. Carmichael, and T. W. Mossberg, Phys. Rev. Lett. **64**, 2499 (1990).
[29] D. G. Lidzey, D. D. C. Bradley, T. Virgili, A. Armitage, M. S. Skolnick, and S. Walker, Phys. Rev. Lett. **82**, 3316 (1999).
[30] *CRC Handbook of Chemistry and Physics*, 84th ed., edited by D. R. Lide (CRC Press, Boca Raton, FL, 2003).
[31] S. Lamansky, P. Djurovich, D. Murphy, F. Abdel-Razzaq, R. C. Kwong, I. Tsyba, M. Bortz, B. Mui, R. Bau, and M. E. Thompson, Inorg. Chem. **40**, 1704 (2001).
[32] S. Lamansky, P. Djurovich, D. Murphy, F. Abdel-Razzaq, H.-E. Lee, C. Adachi, P. E. Burrows, S. R. Forrest, and M. E. Thompson, J. Am. Chem. Soc. **123**, 4304 (2001).
[33] J. S. Baskin, H.-Z. Yu, and A. H. Zewail, J. Phys. Chem. A **106**, 9837 (2002).

Accumulation of electric-field-stabilized geminate polaron pairs in an organic semiconductor to attain high excitation density under low intensity pumping

N. C. Giebink
Princeton Institute for the Science and Technology of Materials (PRISM), Princeton University, Princeton, New Jersey 08544 and Department of Electrical Engineering, Princeton University, Princeton, New Jersey 08544

S. R. Forrest[a)]
Department of Electrical Engineering and Computer Science, University of Michigan, Ann Arbor, Michigan 48109; Department of Physics, University of Michigan, Ann Arbor, Michigan 48109; and Department of Materials Science and Engineering, University of Michigan, Ann Arbor, Michigan 48109

(Received 1 September 2006; accepted 26 September 2006; published online 8 November 2006)

The recombination dynamics of geminate polaron pair (PP) states are investigated by monitoring electric-field-induced delayed fluorescence in thin films consisting of the green laser dye, Coumarin-6 (C6) doped at 1 wt % into 4,4′-bis(*N*-carbazolyl)biphenyl. We find that the PP decay follows τ^{-m} (with $m \sim 0.1$), where τ is the time that the PPs are held in the field. This sublinear decay suggests the possibility for accumulation of PPs over time that can then be reconverted into excitons upon field removal. We demonstrate the generation of short (~50 ns full width at half maximum) bursts of C6 fluorescence with peak intensities >20 times the steady-state fluorescence intensity (corresponding to a C6 singlet exciton density $N_S > 4 \times 10^{15}$ cm^3) when pumped continuously by a low intensity (<1 W/cm^2) laser in the presence of a pulsed electric field. © *2006 American Institute of Physics*. [DOI: 10.1063/1.2385840]

The past several years have witnessed substantial progress[1,2] in the development of optically pumped organic semiconductor lasers (OSLs), with the ultimate goal of achieving electrically pumped lasing. Efforts to create an electrically pumped OSL are driven by the broad wavelength tunability and high temperature stability of their emission characteristics that have been demonstrated in optically pumped devices.[3] Several factors have prevented the realization of an electrically pumped OSL, including singlet-triplet and singlet-polaron annihilation,[4] increased cavity loss resulting from polaron and excited state absorption,[5] and high waveguide loss due to incorporation of injecting electrodes into the cavity.[1]

In contrast to optical excitation, electrical injection introduces polarons in addition to forming three triplet excitons for every singlet.[6,7] Both singlet-triplet and singlet-polaron annihilation reactions[8,9] can dramatically quench the radiative singlet density under high electrical injection.[4] Quenching by these species is worsened under electrical excitation since triplet and polaron densities are ~1000 times higher than the singlet density due to their comparatively longer lifetimes (≥ 10 μs). Attaining high singlet density in the absence of triplets and polarons, as in the case of optically pumped OSLs, is crucial to reaching the lasing threshold.[4]

Here, we investigate the recombination dynamics of metastable geminate polaron-pair (PP) states by monitoring the electric-field-induced delayed fluorescence produced by the guest/host system of Coumarin-6 (C6) doped into 4,4′-bis(*N*-carbazolyl)biphenyl (CBP). We use low intensity, continuous-wave (cw) optical pumping in the presence of a pulsed electric field to accumulate a high density of metastable PP states over time, that are then rapidly reconverted into excitons upon removal of the electric field, leading to peak singlet densities of $\sim 4 \times 10^{15}$ cm^{-3}. This suggests a method to reach laser threshold excitation densities[3] ($\sim 10^{17}$ cm^{-3}) by continuously pumping with a low intensity (<1 W/cm^2) optical source. In comparison with direct electrical injection, free polaron densities should be reduced by this process, and triplet exciton formation is expected to be minimal based on previous work concerning the spin-conserving nature of geminate pair recombination.[8,10]

Field-induced delayed fluorescence has been observed previously in ladder-type poly(para-phenylene) polymers.[10,11] In those studies, samples were excited by a laser pulse in the presence of an electric field, and at times long after the natural photoluminescent (PL) decay, a burst of luminescence was observed upon removal of the field. It was concluded that a portion of the initially generated singlet excitons forms interchain PPs that can be stabilized against geminate recombination by the external electric field, which acts to screen the PP Coulomb potential. When the field is removed, rapid reformation into singlet excitons occurs, which then radiatively decay in a fluorescence burst. Here, we study this phenomenon in the small molecule guest/host system consisting of 1 wt % C6 doped into the host material CBP.

Devices consisted of a symmetric organic insulator (50 nm)/organic semiconductor active layer (100 nm)/organic insulator (50 nm) stack sandwiched between two electrodes to form a capacitor. Commercially available Teflon AF was used for the insulating layers due to its high thin-film dielectric breakdown strength (>2 MV/cm) (Ref. 12) and optical transparency in the ultraviolet. The organic layers were thermally evaporated in sequence onto a precleaned[13] indium tin oxide (ITO) coated glass substrate under a vacuum of 10^{-7} Torr. The active layer

a)Electronic mail: stevefor@umich.edu

 © 2006 American Institute of Physics
Downloaded 12 Jan 2008 to 141.213.8.105. Redistribution subject to AIP license or copyright; see http://apl.aip.org/apl/copyright.jsp

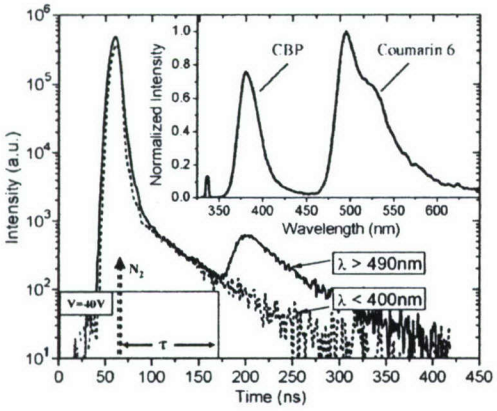

FIG. 1. Luminescence transients for CBP ($\lambda < 400$ nm, dashed line) and C6 ($\lambda > 490$ nm, solid line) measured in the vicinity of voltage turnoff. The timing relationship between excitation and voltage pulse is shown at lower left. Inset: Spectrum of the prompt photoluminescence.

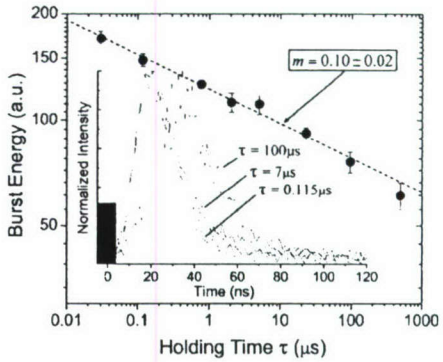

FIG. 2. Decay of the time-integrated burst intensity vs holding electric field time τ. The decay is fitted with a power law τ^{-m}, where $m=0.10\pm0.02$. Inset: Fluorescent burst transients for $\tau=0.115$, 7, and 100 μs.

consists of CBP coevaporated with C6 at a 100:1 weight ratio. The devices were completed by depositing a 100 nm thick Al cathode through a shadow mask with an array of 1 mm diameter openings. For testing, samples were loaded into an electrically and optically accessible cryostat evacuated to 50 mTorr. Luminescent transients were collected by focusing light from each device into a Hamamatsu C4334 streak camera. Electrical pulses were provided at a rate of 17 Hz by an HP4114A pulse generator, connected in parallel to the 50 Ω termination of an oscilloscope to monitor the voltage transient. Device capacitances were measured to be $\sim$260 pF at 1 MHz, resulting in a RC time constant of $\sim$13 ns.

Approximately 1 μs after the application of a $V=40$ V pulse, a $\lambda=337$ nm wavelength N_2 laser pulse (600 ps duration, 6.8 μJ energy, focused to a 1 mm diameter spot) was incident on the device through the ITO contact. This wavelength is strongly absorbed in CBP ($\alpha=2\times10^5$ cm^{-1} at 337 nm), but not in C6 ($\lambda_p=450$ nm). Accounting for the dielectric constants of the organic layers ($\varepsilon_{\text{Teflon}}=1.9$, $\varepsilon_{\text{org}}=3.0$), this applied voltage translates into a uniform field of 1.6 MV/cm across the active layer. The streak camera detection window was synchronized to observe the point of voltage turnoff, occurring at a time τ following laser excitation.

As shown in Fig. 1 for $\tau=115$ ns, a burst of only C6 luminescence appears (rise time $\sim$20 ns) upon field removal, independent of bias polarity. The large fraction of CBP luminescence in the prompt spectrum (Fig. 1, inset) arises from incomplete CBP$\rightarrow$C6 Förster transfer that results from donor/acceptor spectral mismatch. Note that the long lifetime component of the CBP transient is likely the result of repopulation of the CBP singlet from triplet-triplet annihilation.[14] The C6 transient also contains this component as a result of the CBP$\rightarrow$C6 transfer.

After background subtracting the long-time component from the C6 transient, we find that the burst decay is monoexponential with lifetime $\tau_F=13\pm2$ ns. This is significantly longer than the natural lifetime of C6, $\tau_{C6}=2.1\pm0.1$ ns, measured in these devices. However, it corresponds well with the calculated RC time constant. Thus, for short holding times ($\tau<10$ μs), the burst dynamics are likely limited by the discharge of the electric field across the device.[11]

Figure 2 shows the energy of the C6 burst as a function of τ. The burst energy declines over four orders of magnitude in time according to τ^{-m}, where $m\sim0.1$. This is qualitatively similar to the behavior found in polymers;[11,15–17] however, the exponent in that case was $m\sim0.5$. The slow power law decay and the low degree of dispersion in burst transients with variation in τ are reflective of the stability of the PPs against dissociation. Indeed, energetic disorder is crucial to the burst phenomenon since PPs that relax into the tail of the density of states have their motion restricted, increasing the likelihood that they will remain correlated while in the electric field.

The field-delayed burst was not observed in neat CBP films. Nor does it occur in CBP-C6 devices if the excitation wavelength is below the optical gap of CBP, where only C6 molecules are excited. Thus, the use of a guest/host system is critical to generate the stable PP states that create the fluorescence burst. Here, the energetic difference in the highest occupied molecular orbital (HOMO) levels of C6 and CBP (5.4 and 6.3 eV, respectively[18,19]) provides a driving force to break the strongly bound [$E_B\sim1$ eV (Ref. 20)] CBP Frenkel excitons. The hole is then localized on the C6 HOMO in the potential well created by the surrounding CBP molecules. This further stabilizes the PP against complete dissociation, since only the low mobility electron is capable of hopping out of the mutual Coulomb potential.

Due to the sublinear decay in density, PPs can *accumulate* at a rate of roughly τ^{1-m} by continuous optical pumping. To accomplish this, we use the $\lambda=325$ nm line of a cw HeCd laser, focused to a 1 mm diameter spot (0.9 W/cm^2) on the same devices as in the N_2 pumped experiments. Voltage pulses of 45 V were superimposed upon a -5 V dc bias. The interpulse reverse bias offset removes free charges resulting from fully dissociated PPs generated during the pulses by aiding their recombination. For detection, sample luminescence is filtered (long pass cutoff at $\lambda>450$ nm) to isolate the C6 emission. The PL is focused onto a Hamamatsu C5460 Si avalanche photodiode (APD)/preamplifier module ($f_c=10$ MHz).

Figure 3(a) shows the APD output for $\tau=10$, 20, 40, and 80 μs. A postpulse burst of luminescence that grows in proportion to τ is observed. A magnified view of the increase in burst intensity is shown in the inset; the burst transients are limited by the APD frequency response.

We quantify the intensity of the burst through the enhancement factor M, equal to the ratio of the burst intensity, I_{burst}, to the steady-state luminescence intensity, I_{SS}. Figure

Downloaded 12 Jan 2008 to 141.213.8.105. Redistribution subject to AIP license or copyright; see http://apl.aip.org/apl/copyright.jsp

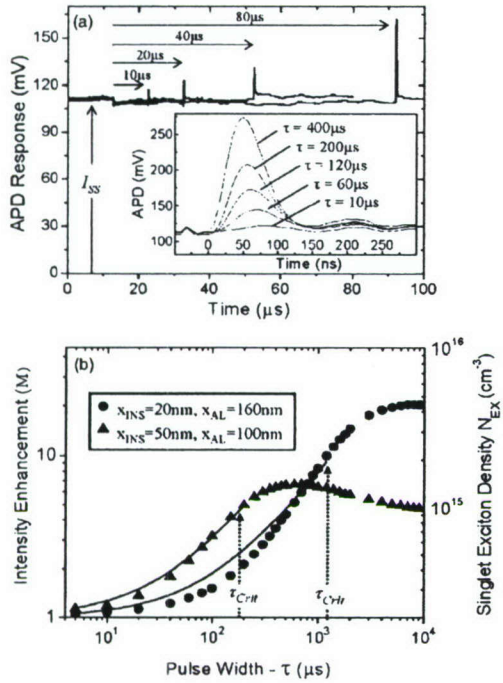

FIG. 3. (a) Measured APD output showing the growth in burst intensity for τ=10, 20, 40, and 80 μs. Inset: Burst transients shown at increased time resolution. (b) Plot of M, for two devices with different insulating barrier thicknesses x_{ins}. The solid lines show fits to Eq. (2) with m=0.1 and N_{PP0}/N_{SS}=0.014±0.002 and 0.033±0.003 for x_{ins}=20 nm and x_{ins}=50 nm, respectively.

3(b) shows M plotted versus pulse width τ for two devices of differing insulating barrier thickness, x_{ins}, but with identical total device thicknesses. Here, the excited state density of the burst, N_{ex}, shown on the right-hand scale, is calculated by estimating the steady-state C6 singlet density N_{SS} as

$$N_{SS} = \frac{I_0(\lambda/hc)[0.86]\phi_{C6}\tau_{C6}}{2L_{abs}} \quad (1)$$

and scaling as $N_{ex}=MN_{SS}$. In Eq. (1), I_0 is the incident laser intensity ($W/$ cm^2) and h is Planck's constant. Since the active layer thickness, x_{al}=100 nm, is double the CBP absorption length, L_{abs}=50 nm at λ=325 nm, roughly $(1-\exp(-x_{al}/L_{abs})=0.86)$ of the incident pump is absorbed in a single pass through the active layer, making cathode reflection and other microcavity effects negligible. The fraction, ϕ_{C6}=78%, of CBP excitations is transferred to C6 molecules, as estimated from the relative magnitudes of CBP and C6 emission in the PL spectrum (see Fig. 1, inset).

The early τ portions of each curve are fitted using the PP decay power law with m=0.1. That is,

$$M = \frac{N_{SS} + N_{PP0}\tau^{1-m}}{N_{SS}} = 1 + (N_{PP0}/N_{SS})\tau^{1-m}, \quad (2)$$

where N_{PP0} is the number of initially generated singlets that can undergo the singlet→PP→singlet chain of conversions. The roll-off onset in M occurring at τ_{crit} [see Fig. 3(b)] results from a buildup of space charge over time due to those PPs that completely dissociate. The resulting space charge creates an opposing internal field that cancels the applied field, reducing M. Thinning the insulating barriers to x_{ins}=20 nm [Fig. 3(b)] allows some of the accumulated space charge to tunnel out of the device. The result is an improvement of τ_{crit} by a factor of 6, and an increase in the peak enhancement to M=22, corresponding to a C6 singlet density of $N_{ex}=4\times10^{15}$ cm^{-3}. Electrical generation of comparable singlet density would require a current density $J>30$ A/cm^2, where it has been shown that both pump-induced absorption[5] and annihilation losses are already significant.[4]

In summary, we have investigated the decay dynamics of external-field-stabilized geminate polaron pairs in the C6/CBP guest/host system by monitoring the field-induced delayed fluorescence bursts following voltage turnoff. The PP density decays sublinearly according to τ^{-m} (with $m\sim0.1$). We show that geminate PPs can be accumulated under continuous optical pumping, and then rapidly (<10 ns) reconverted into singlet excitons. The cancellation of the external field by an internal space-charge field arising from fully dissociated PPs currently limits the maximum attainable PP density. A peak singlet exciton density of $N_{ex}=4\times10^{15}$ cm^{-3} is obtained under low intensity optical pumping (0.9 W/cm^2), with expectations for future improvement toward the ultimate goal of reaching laser threshold when integrated within an optical microcavity.

The authors thank the Air Force Office of Scientific Research (AFOSR) and Universal Display Corp. for support of this work. In addition, they thank R. J. Holmes and B. P. Rand for helpful discussions.

[1]V. G. Kozlov, G. Parthasarathy, P. E. Burrows, V. B. Khalfin, J. Wang, S. Y. Chou, and S. R. Forrest, IEEE J. Quantum Electron. **36**, 18 (2000).
[2]N. Tessler, G. J. Denton, and R. H. Friend, Nature (London) **382**, 695 (1996).
[3]V. G. Kozlov, V. Bulovic, P. E. Burrows, M. Baldo, V. B. Khalfin, G. Parthasarathy, S. R. Forrest, Y. You, and M. E. Thompson, J. Appl. Phys. **84**, 4096 (1998).
[4]M. A. Baldo, R. J. Holmes, and S. R. Forrest, Phys. Rev. B **66**, 035321 (2002).
[5]V. G. Kozlov, P. E. Burrows, G. Parthasarathy, and S. R. Forrest, Appl. Phys. Lett. **74**, 1057 (1999).
[6]M. A. Baldo, D. F. O'Brien, M. E. Thompson, and S. R. Forrest, Phys. Rev. B **60**, 14422 (1999).
[7]M. Segal, M. A. Baldo, R. J. Holmes, S. R. Forrest, and Z. G. Soos, Phys. Rev. B **68**, 075211 (2003).
[8]E. J. W. List, C. H. Kim, A. K. Naik, U. Scherf, G. Leising, W. Graupner, and J. Shinar, Phys. Rev. B **6415**, 155204 (2001).
[9]E. J. W. List, U. Scherf, K. Mullen, W. Graupner, C. H. Kim, and J. Shinar, Phys. Rev. B **66**, 235203 (2002).
[10]M. Reufer, M. J. Walter, P. G. Lagoudakis, B. Hummel, J. S. Kolb, H. G. Roskos, U. Scherf, and J. M. Lupton, Nat. Mater. **4**, 340 (2005).
[11]B. Schweitzer, V. I. Arkhipov, and H. Bassler, Chem. Phys. Lett. **304**, 365 (1999).
[12]P. P. Budenstein, P. J. Hayes, J. L. Smith, and W. B. Smith, J. Vac. Sci. Technol. **6**, 289 (1969).
[13]P. E. Burrows, Z. Shen, V. Bulovic, D. M. McCarty, S. R. Forrest, J. A. Cronin, and M. E. Thompson, J. Appl. Phys. **79**, 7991 (1996).
[14]M. Pope and C. Swenberg, *Electronic Processes in Organic Crystals and Polymers* (Oxford University Press, New York, NY, 1999), Chap. 1.
[15]A. F. Nogueira, I. Montanari, J. Nelson, J. R. Durrant, C. Winder, and N. S. Sariciftci, J. Phys. Chem. B **107**, 1567 (2003).
[16]I. Montanari, A. F. Nogueira, J. Nelson, J. R. Durrant, C. Winder, M. A. Loi, N. S. Sariciftci, and C. Brabec, Appl. Phys. Lett. **81**, 3001 (2002).
[17]T. Offermans, S. C. J. Meskers, and R. A. J. Janssen, J. Chem. Phys. **119**, 10924 (2003).
[18]H. Suzuki and S. Hoshino, J. Appl. Phys. **79**, 858 (1996).
[19]M. A. Baldo, S. Lamansky, P. E. Burrows, M. E. Thompson, and S. R. Forrest, Appl. Phys. Lett. **75**, 4 (1999).
[20]I. G. Hill, A. Kahn, Z. G. Soos, and R. A. Pascal, Chem. Phys. Lett. **327**, 181 (2000).

Downloaded 12 Jan 2008 to 141.213.8.105. Redistribution subject to AIP license or copyright; see http://apl.aip.org/apl/copyright.jsp

Strong coupling and hybridization of Frenkel and Wannier-Mott excitons in an organic-inorganic optical microcavity

R. J. Holmes,[1,*] S. Kéna-Cohen,[1] V. M. Menon,[2] and S. R. Forrest[3,†]

[1]*Princeton Institute for the Science and Technology of Materials (PRISM), Department of Electrical Engineering, Princeton University, Princeton, New Jersey 08544, USA*

[2]*Department of Physics, Queens College of the City University of New York (CUNY), Flushing, New York 11367, USA*

[3]*Department of Electrical Engineering and Department of Computer Science, Physics, and Materials Science and Engineering, University of Michigan, Ann Arbor, Michigan 48109, USA*

(Received 16 October 2006; published 13 December 2006)

We demonstrate strong exciton-photon coupling and photon-mediated hybridization between the Frenkel and Wannier-Mott excitons of an organic-inorganic hybrid optical microcavity. Hybridization occurs between the Frenkel excitons of the small molecular weight organic tetraphenylporphyrin and the Wannier-Mott excitons of InGaP quantum wells. This mixed state consists of 10% Frenkel and Wannier-Mott exciton and 80% cavity photon character, and persists up to temperatures of 100 K.

DOI: 10.1103/PhysRevB.74.235211 PACS number(s): 71.35.Gg, 71.35.Lk, 71.36.+c, 72.80.Le

I. INTRODUCTION

The absorption of light in a semiconductor can lead to the creation of a bound electron-hole pair, known as an exciton. Frenkel-type excitons are commonly found in organic semiconductors and have large binding energies (~1 eV) and small Bohr radii (~1 nm). In contrast, W annier-Mott excitons are associated with inorganic semiconductors and are weakly bound (~10 meV) with large Bohr radii (~10 nm). An exciton placed in an optical microcavity can interact with the photon mode of the cavity.[1] If the resonance leads to a splitting (anticrossing) between the coupled exciton and cavity-photon eigenstates, the system is identified as "strongly coupled."[2] Furthermore, when multiple excitons of a single type (either Frenkel or Wannier-Mott) are confined within the microcavity, they may hybridize by each strongly coupling to the cavity photon field.[3–7] The eigenstates of the strongly coupled exciton-photon system are called microcavity polaritons.[2,8]

Microcavity polaritons were first reported in inorganic (GaAs-based) semiconductor structures at low temperature.[2] Observations of the strongly coupled state are generally limited to low temperature in inorganic materials as a result of thermal linewidth broadening and the small Wannier-Mott oscillator strength. In contrast, the study of strong coupling in organic materials has only recently received attention. Organic materials are interesting in this context due to their large exciton oscillator strengths and binding energies. These properties lead to a stronger interaction with the cavity mode, and a stable, strongly coupled state at room temperature. Strong coupling has been reported in a variety of spun-cast and solution-processed organic materials,[9–13] as well as in thermally evaporated thin films.[4,14]

When multiple excitonic resonances are coupled using a single cavity mode, the excitons are said to be hybridized (or mixed). In inorganic semiconductors, exciton hybridization has been explored by coupling quantum wells of varying thicknesses to a cavity,[6] and also by simultaneously coupling the light and heavy-hole excitonic transitions of a single quantum well (QW) to a common cavity photon mode.[15] Hybridization has been observed in organic materials between detuned molecular absorbers in a cavity,[5,16] and between the neighboring vibronic transitions of a single molecular material.[4]

In addition, the existence of a hybrid Frenkel/Wannier-Mott polariton state has been predicted theoretically and is expected to exhibit unique nonlinear optical properties.[17,18] The study of hybrid cavity polaritons can also lead to an improved understanding of energy transfer between semiconductor systems with vastly different properties. However, to our knowledge, prior to this work there has not been an experimental demonstration of hybridization between the Frenkel exciton resonance of an organic material and the Wannier-Mott exciton resonance of an inorganic QW. In contrast to earlier work with polaritonic states, this state would involve the coupling of two fundamentally different excitonic oscillators.

Here, we provide evidence for coupling between an exciton in tetraphenylporphyrin (TPP), a red absorbing, small molecular weight organic material, and that in the QWs of $In_{0.52}Ga_{0.48}P$ via a common optical cavity mode. The poor intermolecular overlap present in small molecular weight organic materials such as TPP leads to the formation of Frenkel excitons upon optical excitation. In a Group III–V inorganic semiconductor such as InGaP, optical excitation leads to the formation of highly delocalized Wannier-Mott excitons due to the large-scale order and periodicity of the crystal lattice.

This paper is organized as follows. Section II contains the experimental details describing the fabrication of various microcavity structures. The experimental results are presented in Sec. III. The theoretical framework for interpreting the results followed by a discussion of the results is given in Sec. IV. Conclusions are presented in Sec. V.

II. EXPERIMENTAL

The device structure is shown in Fig. 1 and consists of two optically active semiconductor regions (an InGaP QW structure and a film of the fluorescent organic TPP) sandwiched between dielectric and semiconductor distributed

 ©2006 The American Physical Society

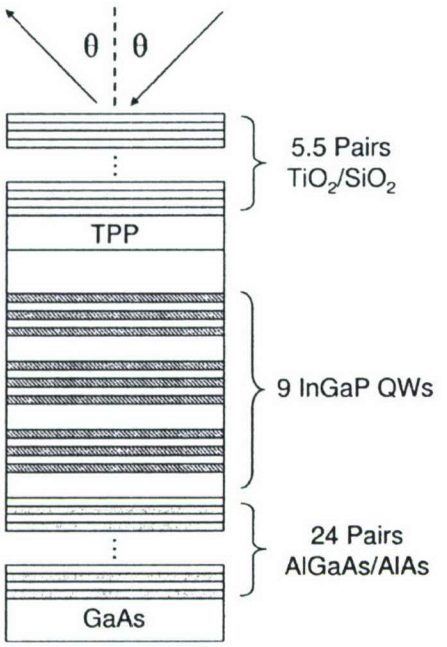

FIG. 1. The organic-inorganic semiconductor microcavity structure used to observe strong coupling between Frenkel and Wannier-Mott excitons through their mutual interaction with a common cavity mode.

Bragg reflectors (DBRs). The QWs were placed in sets of three at the electric field antinodes of the structure to maximize the interaction between the cavity photon and the QW exciton. The bottom DBR mirror consists of a 24-pair DBR composed of undoped $Al_{0.46}Ga_{0.54}As$ ($n_{AlGaAs}=3.45$) and AlAs ($n_{AlAs}=3.04$), grown by gas source molecular beam epitaxy (GSMBE), on a (100) GaAs substrate. Following this, nine 12-nm-thick $In_{0.52}Ga_{0.48}P$ QWs with 12.5-nm-thick $(Al_{0.4}Ga_{0.6})In_{0.5}P$ barriers were similarly grown to form the inorganic active region. A 320-nm-thick layer of TPP was deposited on a room temperature substrate onto the (AlGa)InP spacer layer by vacuum thermal sublimation in a chamber with a base pressure of approximately 10^{-7} Torr. The deposition conditions result in highly polycrystalline films. The (AlGa)InP spacer thickness (75 nm) is sufficient to prevent Förster energy transfer between the QWs and TPP.[19] To complete the structure, a 5.5 pair DBR consisting of TiO_2 ($n_{TiO_2}=2.30$) and SiO_2 ($n_{SiO_2}=1.46$) was deposited on top of the TPP by rf magnetron sputtering. Angularly resolved reflectivity spectra for the full organic-inorganic microcavity were collected as a function of temperature under white light excitation through the TiO_2/SiO_2 DBR stack.[20]

The refractive index profile and the spatial variation of the optical field intensity within the microcavity are shown in Fig. 2. The spacing and placement of the InGaP quantum well sets were optimized to provide maximum overlap between the QWs and the optical field profile.

To understand the nature of the Wannier-Mott polariton states, an inorganic microcavity was also fabricated by first growing the AlGaAs/GaAs DBR, followed by the InGaP MQW structure. The sample was capped by depositing a dielectric mirror [seven pairs of SiN_x ($n_{SiN_x}=2.10$) and SiO_2 ($n_{SiO_2}=1.46$)] on top of the inorganic QW structure by plasma-enhanced chemical vapor deposition. Angularly resolved reflectivity spectra were collected through the SiN_x/SiO_2 DBR stack.

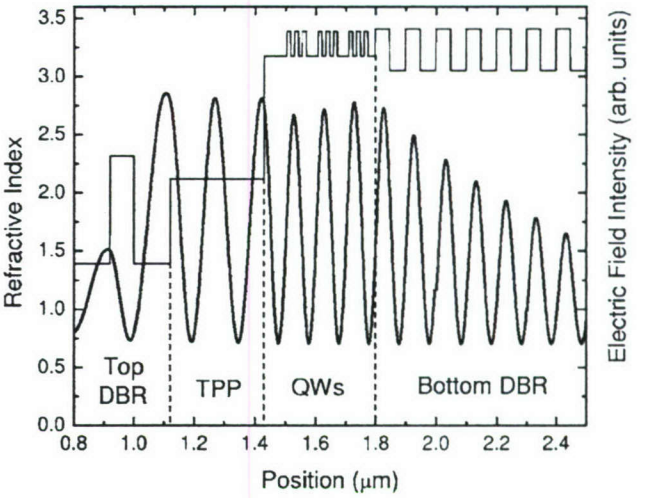

FIG. 2. The refractive index profile and calculated electric field intensity distribution (normal incidence) in the structure of Fig. 1.

III. RESULTS

Quantum wells comprised of InGaP are a suitable partner for TPP ($E_{Frenkel}=1.90\pm0.02$ eV, measured at 300 K), given their heavy-hole excitonic absorption in the red at $E_{Wannier\text{-}Mott}=(1.972\pm0.002$ eV) at 4 K. Figure 3 shows the absorbance spectrum of TPP at room temperature, as well as the reflectivity spectrum of the inorganic component of the hybrid microcavity structure at an angle of 65° at 4 K. The

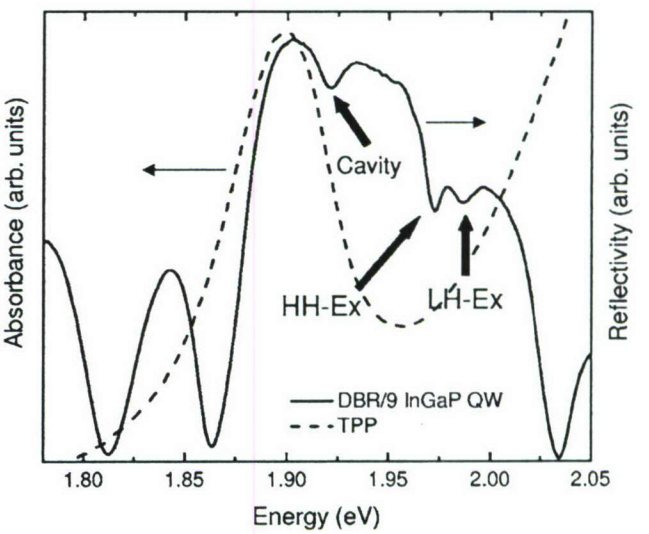

FIG. 3. The room temperature absorbance of tetraphenylporphyrin, and the low-temperature (4 K) reflectivity of the inorganic InGaP/(AlGa)InP quantum well component of the hybrid structure at an angle of 65°. Excitonic absorption features in the inorganic quantum wells are denoted by solid arrows.

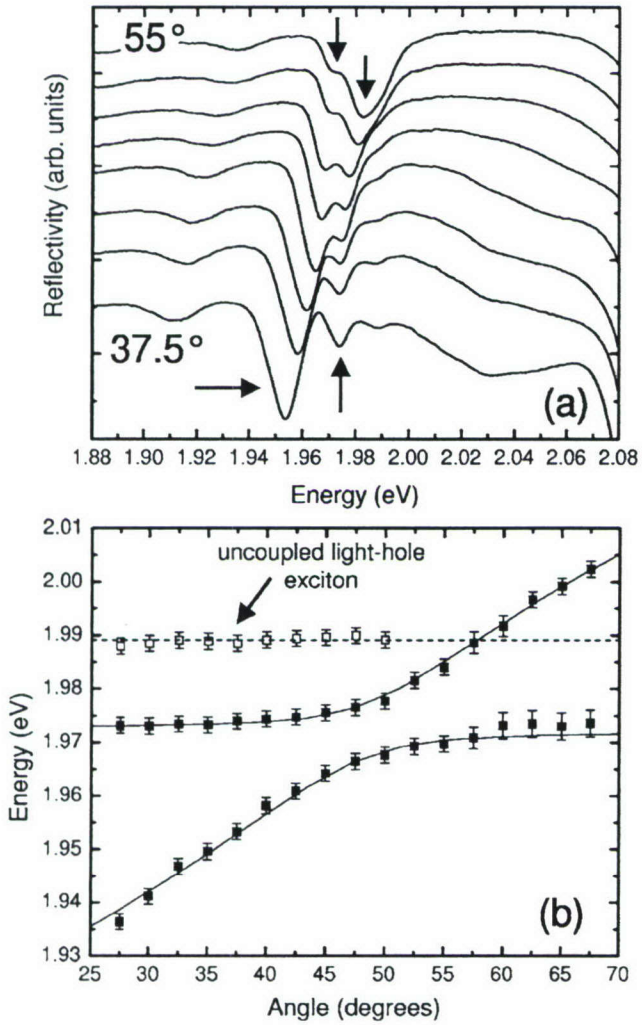

FIG. 4. (a) Reflectivity spectra at 4 K from an InGaP/(AlGa)InP semiconductor quantum well microcavity structure for angles of incidence ranging from 37.5° to 55°. The arrows denote features resulting from the strong coupling of the cavity mode and the heavy-hole exciton transition of InGaP at $E_{\text{Wannier-Mott}}=1.972$ eV. (b) The dispersion relation extracted from the reflectivity spectra of (a). The fits (solid lines) are obtained using a coupled oscillator model (see text) with a splitting of $\Omega_{\text{InGaP}}=10$ meV.

stop band of the AlGaAs/AlAs DBR is clearly visible from 1.86 eV to 2.03 eV, as are three separate dips in the reflectivity spectrum. The large dip centered in the DBR stopband is a weak cavity mode resulting from reflection between the AlGaAs/AlAs DBR and the spacer/air interface. The two smaller dips on the high-energy side of the DBR correspond to heavy-hole and light-hole excitonic absorption. Previous work has demonstrated that TPP can effectively form polaritons in an optical microcavity at room temperature.[14]

As a precursor to the study of the hybrid structure, the angularly resolved reflectivity of a purely inorganic microcavity was measured at 4 K [see Fig. 4(a)]. The resulting dispersion curve is shown in Fig. 4(b) and is fit using a coupled oscillator model. To our knowledge, there has been

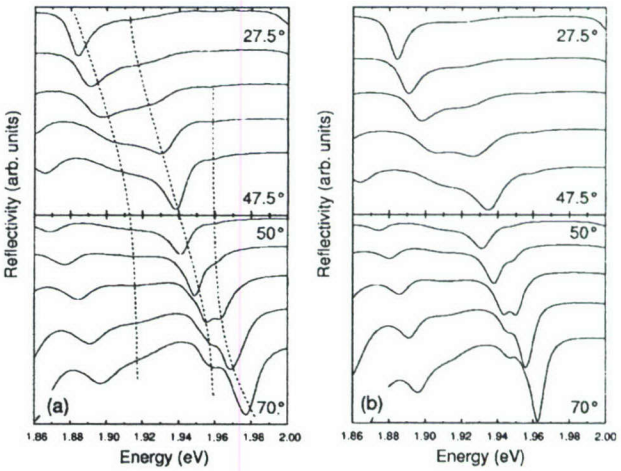

FIG. 5. (a) Reflectivity spectra at 100 K for the hybrid organic-inorganic semiconductor microcavity structure of Fig. 1. The three-body coupling between the Frenkel and Wannier-Mott excitons and the cavity mode is denoted by the broken lines. (b) Transfer matrix simulations of the reflectivity of the hybrid organic-inorganic microcavity structure in Fig. 1. Qualitative agreement is obtained with the experimental spectra of (a).

no report on the use of the red-emitting InGaP as an active material for strongly coupled devices.

Angularly resolved reflectivity spectra collected at 100 K for the full hybrid organic-inorganic structure are shown in Fig. 5(a). In the transfer matrix simulations of Fig. 5(b), the Wannier-Mott excitonic transition of InGaP is modeled as a Lorentzian oscillator[1] with a heavy hole oscillator strength of $f_{\text{hh}}=4.9\times10^{12}$ cm^{-2}, a full width at half maximum (FWHM) of $\gamma_{\text{hh}}=7$ meV, a background dielectric constant of $\varepsilon_{\text{b}}=11.5$, and a center transition energy of 1.957 eV. The values of f_{hh} and γ_{hh} are determined by fitting the transfer matrix simulation to reflectivity spectra collected from the inorganic-only structure of Fig. 4 as well as the hybrid structure of Fig. 5(a). The Frenkel excitonic transition of TPP is modeled using a peak absorbance of $\alpha=2.8\times10^{4}$ cm^{-1}, $\gamma_{\text{TPP}}=42$ meV, a background index of refraction of $n_{\text{TPP}}=2.12$, and a center transition energy of 1.917 eV. The values of α and γ_{TPP} were determined from low-temperature transmission measurements made on a film of TPP deposited on a quartz substrate.

In cases where the Rabi splitting is comparable to the polaritonic linewidth, absorbance measurements (A) are favored over reflectivity (R) as the most quantitative measure of strong exciton-photon coupling.[1,21] In the hybrid organic-inorganic microcavity studied here, the structure is purposely unbalanced, with the reflectivity of the AlGaAs/AlAs back mirror exceeding that of the TiO_2/SiO_2 front mirror. This imbalance leads to the transmission, $T \ll R$ for this structure on resonance, such that the absorbance is $A \sim 1-R$. Transmission spectra were calculated for the hybrid structure as a function of angle using transfer matrices, and in all cases $T < 1\%$ on resonance. This result further validates the use of reflectivity measurements in Fig. 5(a) to examine the strongly coupled state.

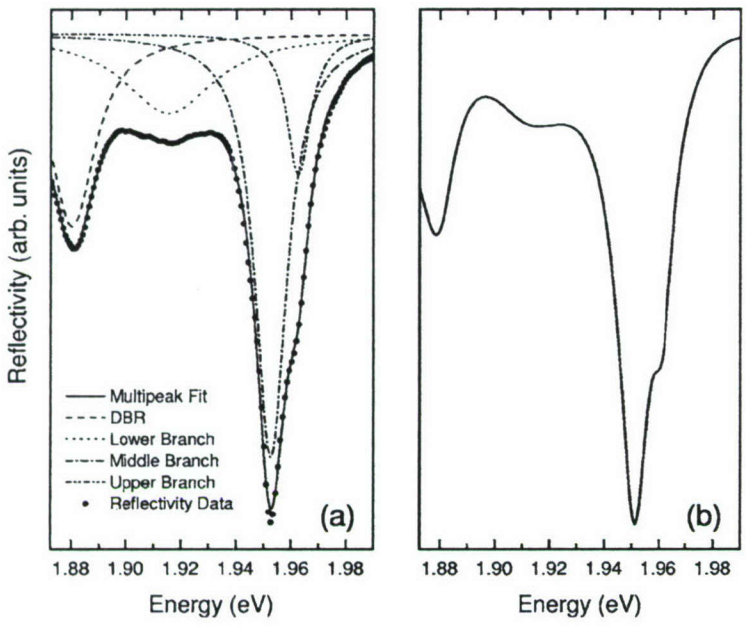

FIG. 6. (a) Measured reflectivity spectrum at 100 K at an angle of 57.5°. Also shown is the multiple Lorentzian function deconvolution of the spectrum used to extract the peak positions of each feature. Some raw data points have been omitted in order to increase the visibility of the Lorentzian fits. (b) Simulated reflectivity spectrum at the same angle. All three coupled features are clearly visible in both the measured and simulated spectra.

IV. DISCUSSION

In Fig. 4(a), a clear anticrossing is observed that results from strong coupling between the cavity photon and the heavy-hole excitonic transition of the InGaP QWs at 4 K. The resulting dispersion [Fig. 4(b)] can be modeled using coupled oscillators with a cavity cutoff energy $E_0 = 1.920$ eV, an average cavity refractive index of 3.27, and a splitting of $\Omega_{\mathrm{InGaP}} = 10$ meV. The uncoupled light-hole excitonic transition is also observed in the reflectivity spectra of Fig. 4(a), and is included in the dispersion curve.

In the hybrid structure, three separate features are observed in reflectivity at 100 K [Fig. 5(a)]. For small angles ($\theta < 47.5°$), two features dominate the spectra and show a pronounced anticrossing. These features result from strong coupling between the Frenkel exciton and the cavity mode. As the angle of incidence is further increased, a third feature emerges near the excitonic resonance of the inorganic QWs, and all three features anticross with increasing angle of incidence. For these intermediate angles ($47.5° < \theta < 60°$), the two excitons of the system are mixed with each other, and with the cavity photon. The positions of the three coupled features are denoted by the broken lines in Fig. 5(a). At large angles ($\theta > 60°$), two features dominate the spectrum, namely, coupling between the Wannier-Mott exciton and the cavity mode. The polaritonic linewidths observed at high angles are significantly narrower than those encountered at low angles because the uncoupled Wannier-Mott exciton linewidth is much narrower than that of the uncoupled Frenkel exciton (see Fig. 3).

Figure 5(b) shows transfer matrix simulations of the reflectivity at angles of incidence corresponding to those in Fig. 5(a). In these simulations, both excitons are modeled as Lorentz oscillators using the parameters discussed in Sec. III. The simulations qualitatively agree with experimental data. Slight discrepancies result from uncertainties in the low-temperature refractive indices used in the calculation.

Figures 6(a) and 6(b) compare in detail the experimental data collected at 100 K at an angle of 57.5° with the simulated reflectivity spectrum at the same angle, respectively. All three coupled features are clearly visible in both spectra. In Fig. 6(b), the multiple Lorentzian function deconvolution of the spectrum used to extract the peak positions of each feature is also shown. Lorentzian functions were used to fit and extract the peak centers of each feature in the reflectivity spectra of Fig. 5(a) as functions of the angle of incidence.

For a microcavity with coupling between a cavity photon, and Frenkel and Wannier-Mott excitons, the dispersion relation is modeled as a three-body coupled oscillator,[4–6,22]

$$\begin{bmatrix} E_p & V_{\mathrm{Frenkel}} & V_{\mathrm{Wannier\text{-}Mott}} \\ V_{\mathrm{Frenkel}} & E_{\mathrm{Frenkel}} & 0 \\ V_{\mathrm{Wannier\text{-}Mott}} & 0 & E_{\mathrm{Wannier\text{-}Mott}} \end{bmatrix} \begin{bmatrix} \alpha \\ \beta \\ \gamma \end{bmatrix} = \varepsilon \begin{bmatrix} \alpha \\ \beta \\ \gamma \end{bmatrix}, \quad (1)$$

where α, β, and γ are the mixing coefficients of the new eigenvectors of the strongly coupled system. Here, two interaction potentials (V_{Frenkel}, $V_{\mathrm{Wannier\text{-}Mott}}$) are included in the Hamiltonian, as are the two uncoupled exciton energies (E_{Frenkel}, $E_{\mathrm{Wannier\text{-}Mott}}$). The cavity photon dispersion, E_p, can be expressed in terms of the angle of incidence as $E_p = E_0(1-\sin^2\theta/n^2)^{-1/2}$, where E_0 is the cutoff energy and n is the cavity index of refraction.[8]

The dispersion relations for the hybrid structure are shown in Figs. 7(a) and 8(a) for temperatures of 100 K and 4 K, respectively. For the dispersion of Fig. 7(a), the energy eigenvalues (ε) were determined numerically using Eq. (1), where $E_0 = 1.861$ eV, $E_{\mathrm{Frenkel}} = 1.917$ eV, $E_{\mathrm{Wannier\text{-}Mott}} = 1.957$ eV, $n = 2.79$, $V_{\mathrm{Frenkel}} = 10$ meV, and $V_{\mathrm{Wannier\text{-}Mott}} = 4$ meV. The dispersion curve at 4 K [Fig. 8(a)] is fit using $E_0 = 1.865$ eV, $E_{\mathrm{Frenkel}} = 1.918$ eV, $E_{\mathrm{Wannier\text{-}Mott}} = 1.970$ eV, $n = 2.81$, $V_{\mathrm{Frenkel}} = 11$ meV and $V_{\mathrm{Wannier\text{-}Mott}} = 4$ meV. The value of the interaction potential, $V_{\mathrm{Wannier\text{-}Mott}} = 4$ meV, is consistent with that of $\Omega_{\mathrm{InGaP}}/2 = 5$ meV obtained from the inorganic InGaP microcavity of Fig. 4. The uncoupled Frenkel

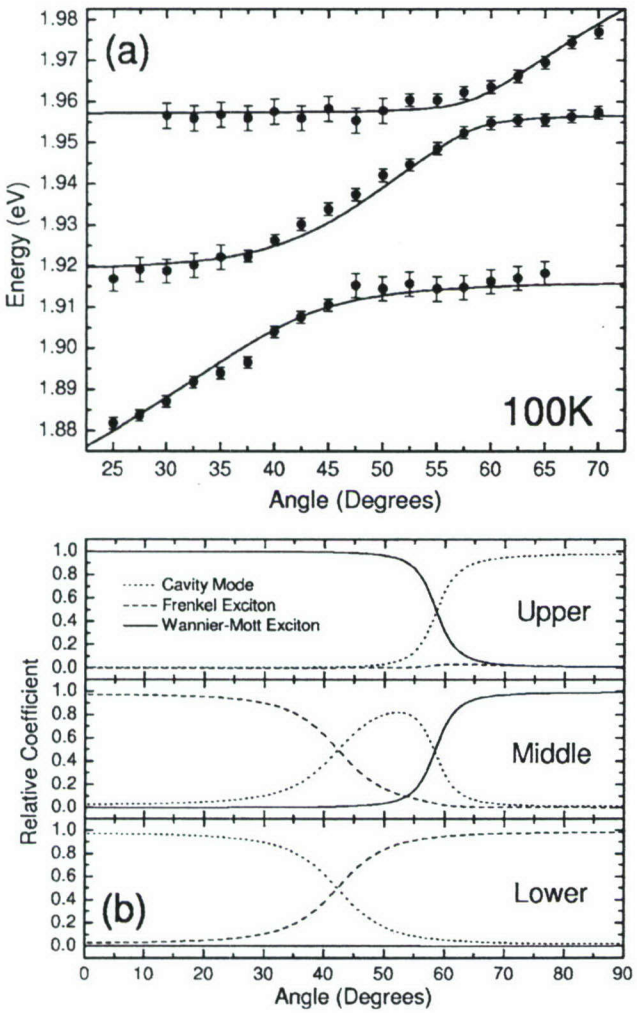

FIG. 7. (a) Dispersion relation extracted from the reflectivity spectra of Fig. 5. The pronounced anticrossings result from strong coupling to both the organic Frenkel exciton and the inorganic Wannier-Mott exciton. A three-body coupled oscillator model (solid lines) yields interaction potentials of $V_{\text{Frenkel}}=10$ meV and $V_{\text{Wannier-Mott}}=4$ meV. (b) Mixing coefficients $|\alpha|^2$, $|\beta|^2$, and $|\gamma|^2$ extracted from the fits of (a). The middle branch shows significant mixing between both the Frenkel and Wannier-Mott excitons and the cavity photon.

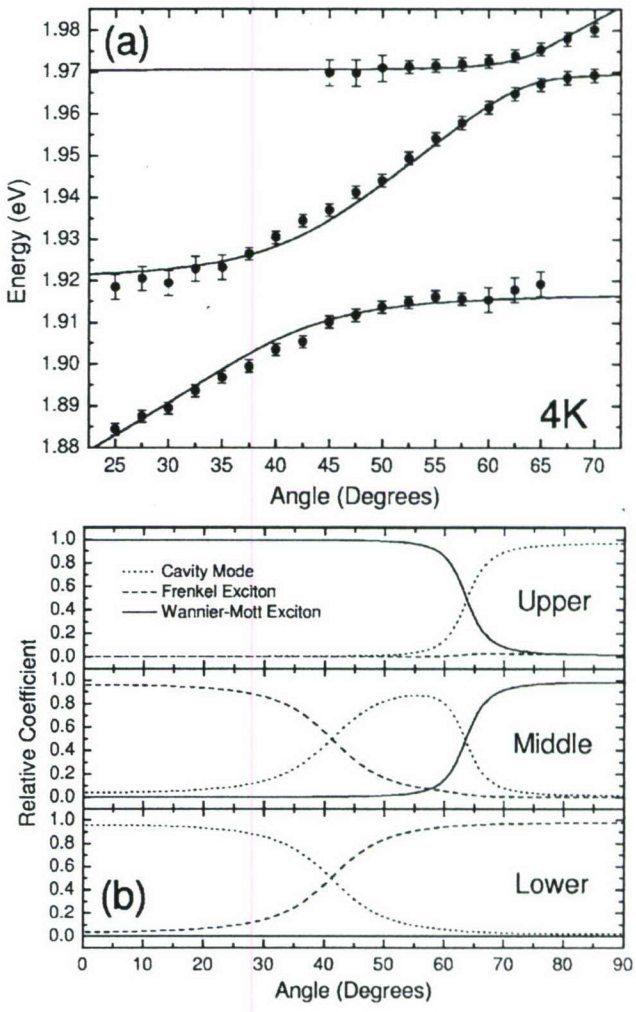

FIG. 8. (a) Dispersion relation obtained for the hybrid structure of Fig. 1 at temperature of 4 K. A three-body coupled oscillator model (solid lines) yields interaction potentials of $V_{\text{Frenkel}}=11$ meV and $V_{\text{Wannier-Mott}}=4$ meV. (b) Mixing coefficients $|\alpha|^2$, $|\beta|^2$, and $|\gamma|^2$ extracted from the fits of (a).

exciton energy used in the fit is blue-shifted in comparison to its value at room temperature. This shift is consistent with temperature-dependent transmission measurements separately performed on films of TPP deposited on quartz substrates. The uncoupled Wannier-Mott energy used in the fit agrees with the value determined from Fig. 3.

In Fig. 7(b), the mixing coefficients $|\alpha|^3$, $|\beta|^2$, and $|\gamma|^2$ [from Eq. (1)] are plotted versus angle for each branch of the hybrid dispersion relation of Fig. 7(a). The lower polariton branch [bottom, Fig. 7(b)] has symmetrically varying amounts of cavity photon and Frenkel exciton character. The middle polariton branch exhibits significant mixing between the cavity photon and both excitons with the point of strongest coupling occurring at $\theta\sim 54°$, where the branch character consists of equal parts Frenkel and Wannier-Mott ($\sim$10%), and $\sim$80% cavity photon [middle, Fig. 7(b)]. In the upper branch, mixing is observed between the cavity photon and the Wannier-Mott excitonic resonance [top, Fig. 7(b)], and at large angles some mixing of the Frenkel exciton also occurs as a result of the strong coupling between the cavity and the Frenkel state.

At 4 K, the absorbance of the InGaP QWs is blue-shifted, and hence we expect a reduction in the mixing between the two excitonic states. Indeed, the exciton hybridization of the middle branch in the hybrid structure is weaker at 4 K than at 100 K, with the branch character consisting of equal parts Frenkel and Wannier-Mott ($\sim$7%), and $\sim$86% cavity photon, as shown in Fig. 8(b). For temperatures above 100 K, the three-body coupling becomes increasingly difficult to resolve since the linewidth of the Wannier-Mott exciton becomes comparable to the splitting between the middle and the upper branches.

V. CONCLUSION

We have demonstrated strong exciton-photon coupling between the Frenkel exciton of an organic semiconductor and the Wannier-Mott exciton of inorganic QWs through their mutual interaction with a cavity photon. The hybridized exciton-polariton state is modeled as a three-body coupled oscillator. Hybrid Frenkel-Wannier-Mott polaritonic states are expected to exhibit nonlinear optical behavior that draws on the properties of both component excitons. Namely, this unusual eigenstate has been predicted to possess the large exciton oscillator strength of a molecular Frenkel exciton and the low saturation density typical of inorganic Wannier-Mott excitons.[17] In addition, the hybrid state may provide a path for exciting the organic polariton by either optical or electrical means.[18] This is especially significant as there has yet to be a successful demonstration of an electrically pumped organic laser. In addition to being useful in the design of unique optoelectronic devices, hybrid states provide an opportunity to study the storage and transfer of energy between different excitonic species.

ACKNOWLEDGMENTS

The authors thank Universal Display Corporation and the Air Force Office of Scientific Research for partial financial support of this work. S.K.C. acknowledges support from the Natural Sciences and Engineering Research Council of Canada.

---

*Present address: Department of Chemical Engineering and Materials Science, University of Minnesota, Minneapolis, Minnesota 55455, USA.

†Author to whom correspondence should be addressed. Email address: stevefor@umich.edu

[1] V. Savona, L. C. Andreani, P. Schwendimann, and A. Quattropani, Solid State Commun. **93**, 733 (1995).

[2] C. Weisbuch, M. Nishioka, A. Ishikawa, and Y. Arakawa, Phys. Rev. Lett. **69**, 3314 (1992).

[3] R. Houdre, R. P. Stanley, and M. Ilegems, Phys. Rev. A **53**, 2711 (1996).

[4] R. J. Holmes and S. R. Forrest, Phys. Rev. Lett. **93**, 186404 (2004).

[5] D. G. Lidzey, D. D. C. Bradley, A. Armitage, S. Walker, and M. S. Skolnick, Science **288**, 1620 (2000).

[6] J. Wainstain, C. Delalande, D. Gendt, M. Voos, J. Bloch, V. Thierry-Mieg, and R. Planel, Phys. Rev. B **58**, 7269 (1998).

[7] P. G Lagoudakis, M. D. Martin, J. J. Baumberg, G. Malpuech, and A. Kavokin, J. Appl. Phys. **95**, 2487 (2004).

[8] M. S. Skolnick, T. A. Fisher, and D. M. Whittaker, Semicond. Sci. Technol. **13**, 645 (1998).

[9] D. G. Lidzey, D. D. C. Bradley, M. S. Skolnick, T. Virgili, S. Walker, and D. M. Whittaker, Nature (London) **395**, 53 (1998).

[10] D. G. Lidzey, D. D. C. Bradley, T. Virgili, A. Armitage, M. S. Skolnick, and S. Walker, Phys. Rev. Lett. **82**, 3316 (1999).

[11] N. Takada, T. Kamata, and D. D. C. Bradley, Appl. Phys. Lett. **82**, 1812 (2003).

[12] P. Schouwink, H. von Berlepsch, L. Dahne, and R. F. Mahrt, J. Lumin. **94-95**, 821 (2001).

[13] J. R. Tischler, M. S. Bradley, V. Bulovic, J.-H. Song, and A. Nurmikko, Phys. Rev. Lett. **95**, 036401 (2005).

[14] R. J. Holmes and S. R. Forrest, Phys. Rev. B **71**, 235203 (2005).

[15] E. Goobar, R. J. Ram, J. Ko, G. Bjork, M. Oestreich, and A. Imamoglu, Appl. Phys. Lett. **69**, 3465 (1996).

[16] D. G. Lidzey, J. Wenus, D. M. Whittaker, G. Itskos, P. N. Stavrinou, D. D. C. Bradley, and R. Murray, J. Lumin. **110**, 347 (2004).

[17] V. M. Agranovich, D. M. Basko, G. C. La Rocca, and F. Bassani, J. Phys. Condens. Matter **10**, 9369 (1998).

[18] V. M. Agranovich, H. Benisty, and C. Weisbuch, Solid State Commun. **102**, 631 (1997).

[19] V. M. Agranovich, D. M. Basko, G. C. La Rocca, and F. Bassani, Synth. Met. **116**, 349 (2001).

[20] R. Houdre, C. Weisbuch, R. P. Stanley, U. Oesterle, P. Pellandini, and M. Ilegems, Phys. Rev. Lett. **73**, 2043 (1994).

[21] R. Houdre, Phys. Status Solidi B **242**, 2167 (2005).

[22] A. Armitage, M. S. Skolnick, A. Kavokin, D. M. Whittaker, V. N. Astratov, G. A. Gehring, and J. S. Roberts, Phys. Rev. B **58**, 15367 (1998).